

<sup>1</sup>

©Copyright 2021

<sup>2</sup>

Sean Gasiorowski

# $HH \rightarrow b\bar{b}b\bar{b}$ or How I Learned to Stop Worrying and Love the QCD Background

Sean Gasiorowski

A dissertation  
submitted in partial fulfillment of the  
requirements for the degree of

## Doctor of Philosophy

University of Washington

2021

### Reading Committee:

Anna Goussiou, Chair

Jason Detwiler

Shih-Chieh Hsu

David Kaplan

Henry Lubatti

Thomas Quinn

Gordon Watts

Program Authorized to Offer Degree:  
Physics

22

University of Washington

23

**Abstract**

24

$HH \rightarrow b\bar{b}b\bar{b}$  or How I Learned to Stop Worrying and Love the QCD Background

25

Sean Gasiorowski

26

Chair of the Supervisory Committee:

27

Professor Anna Goussiou

28

Physics

29

Insert abstract here

## TABLE OF CONTENTS

	Page
<a href="#">31 List of Figures</a>	iii
<a href="#">32 Glossary</a>	xv
<a href="#">33 Chapter 1: The Standard Model of Particle Physics</a>	1
<a href="#">34 1.1 Introduction: Particles and Fields</a>	1
<a href="#">35 1.2 Quantum Electrodynamics</a>	4
<a href="#">36 1.3 An Aside on Group Theory</a>	9
<a href="#">37 1.4 Quantum Chromodynamics</a>	11
<a href="#">38 1.5 The Weak Interaction</a>	14
<a href="#">39 1.6 The Higgs Potential and the SM</a>	20
<a href="#">40 1.7 The Standard Model: A Summary</a>	26
<a href="#">41 Chapter 2: Di-Higgs Phenomenology and Physics Beyond the Standard Model</a>	28
<a href="#">42 2.1 Intro to Di-Higgs</a>	28
<a href="#">43 2.2 Resonant <math>HH</math> Searches</a>	29
<a href="#">44 2.3 Non-resonant <math>HH</math> Searches</a>	31
<a href="#">45 Chapter 3: Experimental Apparatus</a>	35
<a href="#">46 3.1 The Large Hadron Collider</a>	35
<a href="#">47 3.2 The ATLAS Experiment</a>	38
<a href="#">48 Chapter 4: Simulation</a>	47
<a href="#">49 4.1 Event Generation</a>	47
<a href="#">50 4.2 Detector Simulation</a>	50
<a href="#">51 4.3 Correlated Fluctuations in FastCaloSim</a>	52
<a href="#">52 4.4 Outlook</a>	60

53	Chapter 5: Reconstruction . . . . .	62
54	5.1 Jets . . . . .	62
55	5.2 Flavor Tagging . . . . .	64
56	Chapter 6: The Anatomy of an LHC Search . . . . .	74
57	6.1 Object Selection and Identification . . . . .	74
58	6.2 Defining a Signal Region . . . . .	74
59	6.3 Background Estimation . . . . .	74
60	6.4 Uncertainty Estimation . . . . .	74
61	6.5 Hypothesis Testing . . . . .	74
62	Chapter 7: Search for pair production of Higgs bosons in the $b\bar{b}b\bar{b}$ final state . . . . .	75
63	7.1 Data and Monte Carlo Simulation . . . . .	77
64	7.2 Triggers and Object Definitions . . . . .	79
65	7.3 Analysis Selection . . . . .	81
66	7.4 Background Reduction and Top Veto . . . . .	87
67	7.5 Kinematic Region Definition . . . . .	89
68	7.6 Background Estimation . . . . .	95
69	7.7 Uncertainties . . . . .	156
70	7.8 Background Validation . . . . .	166
71	7.9 Overview of Other $b\bar{b}b\bar{b}$ Channels . . . . .	169
72	7.10 $m_{HH}$ Distributions . . . . .	171
73	7.11 Statistical Analysis . . . . .	182
74	7.12 Results . . . . .	183
75	Chapter 8: Future Ideas for $HH \rightarrow b\bar{b}b\bar{b}$ . . . . .	188
76	8.1 pairAGraph: A New Method for Jet Pairing . . . . .	188
77	8.2 Background Estimation with Mass Plane Interpolation . . . . .	191
78	Chapter 9: Conclusions . . . . .	202

## LIST OF FIGURES

	Figure Number	Page
80	1.1 Diagram of the elementary particles described by the Standard Model [1]. . . . .	3
81	2.1 Representative diagrams for the gluon-gluon fusion production of spin-0 ( $X$ ) and spin-2 ( $G_{KK}^*$ ) resonances which decay to two Standard Model Higgs bosons. The spin-0 resonance considered for this thesis is a generic narrow width resonance which may be interpreted in the context of two Higgs doublet models [18], whereas the spin-2 resonance is considered as a Kaluza-Klein graviton within the bulk Randall-Sundrum (RS) model [19, 20]. . . . .	29
87	2.2 Dominant contributing diagrams for non-resonant gluon-gluon fusion production of $HH$ . $\kappa_\lambda$ and $\kappa_t$ represent variations of the Higgs self-coupling and coupling to top quarks respectively, relative to that predicted by the Standard Model. . . . .	30
91	2.3 Illustration of dominant $HH$ branching ratios. $HH \rightarrow b\bar{b}b\bar{b}$ is the most common decay mode, representing 34 % of all $HH$ events produced at the LHC. . . . .	31
93	2.4 Monte Carlo generator level $m_{HH}$ distributions for various values of $\kappa_\lambda$ , demonstrating the impact of the interference between the two diagrams of Figure 2.2 on the resulting $m_{HH}$ distribution. For $\kappa_\lambda = 0$ there is no triangle diagram contribution, demonstrating the shape of the box diagram contribution, whereas for $\kappa_\lambda = 10$ , the triangle diagram dominates, with a strong low mass peak. The interplay between the two is quite evident for other values, resulting in, e.g., the double peaked structure present for $\kappa_\lambda = 2$ (near maximal destructive interference) and $\kappa_\lambda = -5$ . [21] . . . . .	33
101	3.1 Diagram of the ATLAS detector [41] . . . . .	38
102	3.2 Cross section of the ATLAS detector showing how particles interact with various detector components [43] . . . . .	40
104	3.3 2D projections of the ATLAS coordinate system . . . . .	41

105	4.1	Schematic diagram of the Monte Carlo simulation of a hadron-hadron collision. The incoming hadrons are the green blobs with the arrows on the left and right, with the red blob in the center representing the hard scatter event, and the purple representing a secondary hard scatter. Radiation from both incoming and outgoing particles is shown, and the light green blobs represent hadronization, with the outermost dark green circles corresponding to the final state hadrons. Yellow lines are radiated photons. [57] . . . . .	49
112	4.2	The projected ATLAS computational requirements for Run 3 and the HL-LHC relative to the projected computing budget. Aggressive R&D is required to keep resources within budget [60]. . . . .	51
115	4.3	Energy and variable weta2, defined as the energy weighted lateral width of a shower in the second electromagnetic calorimeter layer, for 16 GeV photons with full simulation (G4) and FastCaloSimV2 (FCSV2) [62]. . . . .	53
118	4.4	Example of photon and pion average shapes in $5 \times 5$ calorimeter cells. The left column shows the average shape over a sample of 10000 events, while the right column shows the energy ratio, in each cell, of single GEANT4 events with respect to this average. The photon ratios are all close to 1, while the pion ratios show significant deviation from the average. . . . .	55
123	4.5	Distribution of the ratio of voxel energy in single events to the corresponding voxel energy in the average shape, with GEANT4 events in blue and Gaussian model events in orange, for 65 GeV central pions in EMB2. Moving top to bottom corresponds to increasing $\alpha$ , left to right corresponds to increasing $R$ , with core voxels numbered 1, 10, 19, . . . . Agreement is quite good across all voxels. Results are similar for the VAE method. . . . .	56
129	4.6	Correlation coefficient of ratios of voxel energy in single events to the corresponding voxel energy in the average shape, examined between the core bin from $\alpha = 0$ to $2\pi/8$ and each of the other voxels. The periodic structure represents the binning in $\alpha$ , and the increasing numbers in each of these periods correspond to increasing $R$ , where the eight points with correlation coefficient 1 are the eight core bins. Both the Gaussian and VAE generated toy events are able to reproduce the major correlation structures for 65 GeV central pions in EMB2. . . . .	57
137	4.7	Comparison of the RMS fluctuations about the average shape with the Gaussian fluctuation model (red), the VAE fluctuation model (green), and without correlated fluctuations (blue) for a range of pion energies, $\eta$ points, and layers.	58

140	4.8 Comparison of the Gaussian fluctuation model to the default FCSV2 version	59
141	and to G4 simulation, using pions of 65 GeV energy and $0.2 <  \eta  < 0.25$ .	
142	Variables shown relate to calorimeter clusters, three-dimensional spatial group-	
143	ings of cells [68] which provide powerful insight on the structure of energy	
144	deposits in the calorimeter. Variables considered include number and energy	
145	of clusters, the 2nd moment in lambda, ( $\langle \lambda^2 \rangle$ ), which describes the square	
146	of the longitudinal extension of a cluster, where $\lambda$ is the distance of a cell from	
147	the shower center along the shower axis, and a cluster moment is defined as	
148	$\langle x^n \rangle = \frac{\sum E_i x_i}{\sum E_i}$ , and the distance $\Delta R$ , between the cluster and the true pion.	
149	With the correlated fluctuations, variables demonstrate improved modeling	
150	relative to default FastCaloSimV2. . . . .	
151	5.1 Illustration of an interaction producing two light jets and one $b$ -jet in the	67
152	transverse plane. While the light jets decay “promptly”, coinciding with	
153	the primary vertex of the proton-proton interaction, the longer lifetime of $B$	
154	hadrons leads to a secondary decay vertex, displaced from the primary vertex	
155	by length $L_{xy}$ . This is typically a few mm, and therefore is not directly visible	
156	in the detector, but leads to a large transverse impact parameter, $d_0$ , for the	
157	resulting tracks. [76] . . . . .	
158	5.2 Performance of the various low and high level flavor tagging algorithms in	71
159	$t\bar{t}$ simulation, demonstrating the tradeoff between $b$ -jet efficiency and light	
160	and $c$ -jet rejection. The high level taggers demonstrate significantly better	
161	performance than any of the individual low level taggers, with DL1 offering	
162	slight improvements over MV2 due to the inclusion of additional input variables.	
163	5.3 Performance of the MV2, DL1, and DL1r algorithms in $t\bar{t}$ simulation, demon-	72
164	strating the tradeoff between $b$ -jet efficiency and light and $c$ -jet rejection. $f_c$	
165	controls the importance of $c$ -jet rejection in the discriminating variable, and	
166	values shown have been optimized separately for each DL1 configuration. DL1r	
167	demonstrates a significant improvement in both light and $c$ jet rejection over	
168	MV2 and DL1. [81] . . . . .	
169	7.1 Comparison of $m_{H1}$ vs $m_{H2}$ planes for the full Run 2 $2b$ dataset with different	85
170	pairings. As evidenced, this choice significantly impacts where events fall in	
171	this plane, and therefore which events fall into the various kinematic regions	
172	defined in this plane (see Section 7.5). Respective signal regions are shown for	
173	reference, with the min $\Delta R$ signal region shifted slightly up and to the right to	
174	match the non-resonant selection. Note that the band structure around 80 GeV	
175	in both $m_{H1}$ and $m_{H2}$ is introduced by the top veto described in Section 7.4.	

176	7.2 Comparison of signal distributions in the respective signal regions for the min $\Delta R$ and $D_{HH}$ pairing for various values of the Higgs trilinear coupling in the respective signal regions. The distributions are quite similar at the Standard Model point, but for other variations, min $\Delta R$ does not pick up the low mass features. . . . .	86
181	7.3 Regions used for the resonant search, shown on the $2b$ data mass plane. The outermost region (the “control region”) is used for derivation of the nominal background estimate. The innermost region is the signal region, where the signal extraction fit is performed. The region in between (the “validation region”) is used for the assessment of an uncertainty. . . . .	90
186	7.4 Regions used for the non-resonant search. The “top” and “bottom” quadrants together comprise the control region, in which the nominal background estimate is derived. The “left” and “right” quadrants together comprise the validation region, which is used to assess an uncertainty. The signal region, in the center, is where the signal extraction fit is performed. . . . .	92
191	7.5 Impact of the $m_{HH}$ correction on a range of spin-0 resonant signals. The corrected $m_{HH}$ distributions (solid lines) are much sharper and more centered on the corresponding resonance masses than the uncorrected $m_{HH}$ distributions (dashed). . . . .	93
195	<b>7.6 Resonant Search:</b> Distributions of $\Delta R$ between the closest Higgs Candidate jets, $\Delta R$ between the other two, and average absolute value of HC jet $\eta$ before and after CR derived reweighting for the 2018 Control Region. . . . .	102
198	<b>7.7 Resonant Search:</b> Distributions of $p_T$ of the 2nd and 4th leading Higgs Candidate jets and the $p_T$ of the di-Higgs system before and after CR derived reweighting for the 2018 Control Region. . . . .	103
201	<b>7.8 Resonant Search:</b> Distributions of the number of jets before and after CR derived reweighting for the 2018 Control Region. A minimum of 4 jets is required in each event in order to form Higgs candidates. . . . .	104
204	<b>7.9 Resonant Search:</b> Distributions of $p_T$ of the 1st and 3rd leading Higgs Candidate jets and $\Delta R$ between Higgs candidates before and after CR derived reweighting for the 2018 Control Region. . . . .	105
207	<b>7.10 Resonant Search:</b> Distributions of $\eta$ of the 1st, 2nd, and 3rd leading Higgs Candidate jets before and after CR derived reweighting for the 2018 Control Region. . . . .	106
210	<b>7.11 Resonant Search:</b> Distributions of $\eta$ of the 4th leading Higgs Candidate jet and the $p_T$ of the leading and subleading Higgs candidates before and after CR derived reweighting for the 2018 Control Region. . . . .	107

213	<b>7.12 Resonant Search:</b> Distributions of mass of the leading and subleading Higgs candidates and of the di-Higgs system before and after CR derived reweighting for the 2018 Control Region. . . . .	108
216	<b>7.13 Resonant Search:</b> Distributions of $\Delta\phi$ between jets in the leading and subleading Higgs candidates before and after CR derived reweighting for the 2018 Control Region. . . . .	109
219	<b>7.14 Resonant Search:</b> Distributions of the top veto variable, $X_{Wt}$ , before and after CR derived reweighting for the 2018 Control Region. Reweighting is done after the cut on this variable is applied . . . . .	110
222	<b>7.15 Resonant Search:</b> Distributions of $\Delta R$ between the closest Higgs Candidate jets, $\Delta R$ between the other two, and average absolute value of HC jet $\eta$ before and after CR derived reweighting for the 2018 Validation Region. . . . .	111
225	<b>7.16 Resonant Search:</b> Distributions of $p_T$ of the 2nd and 4th leading Higgs Candidate jets and the $p_T$ of the di-Higgs system before and after CR derived reweighting for the 2018 Validation Region. . . . .	112
228	<b>7.17 Resonant Search:</b> Distributions of the number of jets before and after CR derived reweighting for the 2018 Validation Region. A minimum of 4 jets is required in each event in order to form Higgs candidates. . . . .	113
231	<b>7.18 Resonant Search:</b> Distributions of $p_T$ of the 1st and 3rd leading Higgs Candidate jets and $\Delta R$ between Higgs candidates before and after CR derived reweighting for the 2018 Validation Region. . . . .	114
234	<b>7.19 Resonant Search:</b> Distributions of $\eta$ of the 1st, 2nd, and 3rd leading Higgs Candidate jets before and after CR derived reweighting for the 2018 Validation Region. . . . .	115
237	<b>7.20 Resonant Search:</b> Distributions of $\eta$ of the 4th leading Higgs Candidate jet and the $p_T$ of the leading and subleading Higgs candidates before and after CR derived reweighting for the 2018 Validation Region. . . . .	116
240	<b>7.21 Resonant Search:</b> Distributions of mass of the leading and subleading Higgs candidates and of the di-Higgs system before and after CR derived reweighting for the 2018 Validation Region. . . . .	117
243	<b>7.22 Resonant Search:</b> Distributions of $\Delta\phi$ between jets in the leading and subleading Higgs candidates before and after CR derived reweighting for the 2018 Validation Region. . . . .	118
246	<b>7.23 Resonant Search:</b> Distributions of the top veto variable, $X_{Wt}$ , before and after CR derived reweighting for the 2018 Validation Region. Reweighting is done after the cut on this variable is applied . . . . .	119

249	<b>7.24 Non-resonant Search (4b):</b> Distributions of $\Delta R$ between the closest Higgs Candidate jets, $\Delta R$ between the other two, and average absolute value of HC jet $\eta$ before and after CR derived reweighting for the 2018 4b Control Region.	120
250		
251		
252	<b>7.25 Non-resonant Search (4b):</b> Distributions of $p_T$ of the 2nd and 4th leading Higgs Candidate jets and the $p_T$ of the di-Higgs system before and after CR derived reweighting for the 2018 4b Control Region.	121
253		
254		
255	<b>7.26 Non-resonant Search (4b):</b> Distributions of the number of jets before and after CR derived reweighting for the 2018 4b Control Region. A minimum of 4 jets is required in each event in order to form Higgs candidates.	122
256		
257		
258	<b>7.27 Non-resonant Search (4b):</b> Distributions of $p_T$ of the 1st and 3rd leading Higgs Candidate jets and $\Delta R$ between Higgs candidates before and after CR derived reweighting for the 2018 4b Control Region.	123
259		
260		
261	<b>7.28 Non-resonant Search (4b):</b> Distributions of $\eta$ of the 1st, 2nd, and 3rd leading Higgs Candidate jets before and after CR derived reweighting for the 2018 4b Control Region.	124
262		
263		
264	<b>7.29 Non-resonant Search (4b):</b> Distributions of $\eta$ of the 4th leading Higgs Candidate jet and the $p_T$ of the leading and subleading Higgs candidates before and after CR derived reweighting for the 2018 4b Control Region.	125
265		
266		
267	<b>7.30 Non-resonant Search (4b):</b> Distributions of mass of the leading and sub-leading Higgs candidates and of the di-Higgs system before and after CR derived reweighting for the 2018 4b Control Region.	126
268		
269		
270	<b>7.31 Non-resonant Search (4b):</b> Distributions of $\Delta\phi$ between jets in the leading and subleading Higgs candidates before and after CR derived reweighting for the 2018 4b Control Region.	127
271		
272		
273	<b>7.32 Non-resonant Search (4b):</b> Distributions of the top veto variable, $X_{Wt}$ , before and after CR derived reweighting for the 2018 4b Control Region. Reweighting is done after the cut on this variable is applied.	128
274		
275		
276	<b>7.33 Non-resonant Search (4b):</b> Distributions of $\Delta R$ between the closest Higgs Candidate jets, $\Delta R$ between the other two, and average absolute value of HC jet $\eta$ before and after CR derived reweighting for the 2018 4b Validation Region.	129
277		
278		
279	<b>7.34 Non-resonant Search (4b):</b> Distributions of $p_T$ of the 2nd and 4th leading Higgs Candidate jets and the $p_T$ of the di-Higgs system before and after CR derived reweighting for the 2018 4b Validation Region.	130
280		
281		
282	<b>7.35 Non-resonant Search (4b):</b> Distributions of the number of jets before and after CR derived reweighting for the 2018 4b Validation Region. A minimum of 4 jets is required in each event in order to form Higgs candidates.	131
283		
284		

285	<b>7.36 Non-resonant Search (4b):</b> Distributions of $p_T$ of the 1st and 3rd leading Higgs Candidate jets and $\Delta R$ between Higgs candidates before and after CR derived reweighting for the 2018 4b Validation Region. . . . .	132
288	<b>7.37 Non-resonant Search (4b):</b> Distributions of $\eta$ of the 1st, 2nd, and 3rd leading Higgs Candidate jets before and after CR derived reweighting for the 2018 4b Validation Region. . . . .	133
291	<b>7.38 Non-resonant Search (4b):</b> Distributions of $\eta$ of the 4th leading Higgs Candidate jet and the $p_T$ of the leading and subleading Higgs candidates before and after CR derived reweighting for the 2018 4b Validation Region. . . . .	134
294	<b>7.39 Non-resonant Search (4b):</b> Distributions of mass of the leading and sub-leading Higgs candidates and of the di-Higgs system before and after CR derived reweighting for the 2018 4b Validation Region. . . . .	135
297	<b>7.40 Non-resonant Search (4b):</b> Distributions of $\Delta\phi$ between jets in the leading and subleading Higgs candidates before and after CR derived reweighting for the 2018 4b Validation Region. . . . .	136
300	<b>7.41 Non-resonant Search (4b):</b> Distributions of the top veto variable, $X_{Wt}$ , before and after CR derived reweighting for the 2018 4b Validation Region. Reweighting is done after the cut on this variable is applied. . . . .	137
303	<b>7.42 Non-resonant Search (3b1l):</b> Distributions of $\Delta R$ between the closest Higgs Candidate jets, $\Delta R$ between the other two, and average absolute value of HC jet $\eta$ before and after CR derived reweighting for the 2018 3b1l Control Region. . . . .	138
307	<b>7.43 Non-resonant Search (3b1l):</b> Distributions of $p_T$ of the 2nd and 4th leading Higgs Candidate jets and the $p_T$ of the di-Higgs system before and after CR derived reweighting for the 2018 3b1l Control Region. . . . .	139
310	<b>7.44 Non-resonant Search (3b1l):</b> Distributions of the number of jets before and after CR derived reweighting for the 2018 3b1l Control Region. A minimum of 4 jets is required in each event in order to form Higgs candidates. . . . .	140
313	<b>7.45 Non-resonant Search (3b1l):</b> Distributions of $p_T$ of the 1st and 3rd leading Higgs Candidate jets and $\Delta R$ between Higgs candidates before and after CR derived reweighting for the 2018 3b1l Control Region. . . . .	141
316	<b>7.46 Non-resonant Search (3b1l):</b> Distributions of $\eta$ of the 1st, 2nd, and 3rd leading Higgs Candidate jets before and after CR derived reweighting for the 2018 3b1l Control Region. . . . .	142
319	<b>7.47 Non-resonant Search (3b1l):</b> Distributions of $\eta$ of the 4th leading Higgs Candidate jet and the $p_T$ of the leading and subleading Higgs candidates before and after CR derived reweighting for the 2018 3b1l Control Region. . . . .	143

322	<b>7.48 Non-resonant Search (3b1l):</b> Distributions of mass of the leading and 323 subleading Higgs candidates and of the di-Higgs system before and after CR 324 derived reweighting for the 2018 3b1l Control Region. . . . .	144
325	<b>7.49 Non-resonant Search (3b1l):</b> Distributions of $\Delta\phi$ between jets in the lead- 326 ing and subleading Higgs candidates before and after CR derived reweighting 327 for the 2018 3b1l Control Region. . . . .	145
328	<b>7.50 Non-resonant Search (3b1l):</b> Distributions of the top veto variable, $X_{Wt}$ , 329 before and after CR derived reweighting for the 2018 3b1l Control Region. 330 Reweighting is done after the cut on this variable is applied. . . . .	146
331	<b>7.51 Non-resonant Search (3b1l):</b> Distributions of $\Delta R$ between the closest 332 Higgs Candidate jets, $\Delta R$ between the other two, and average absolute value of 333 HC jet $\eta$ before and after CR derived reweighting for the 2018 3b1l Validation 334 Region. . . . .	147
335	<b>7.52 Non-resonant Search (3b1l):</b> Distributions of $p_T$ of the 2nd and 4th leading 336 Higgs Candidate jets and the $p_T$ of the di-Higgs system before and after CR 337 derived reweighting for the 2018 3b1l Validation Region. . . . .	148
338	<b>7.53 Non-resonant Search (3b1l):</b> Distributions of the number of jets before 339 and after CR derived reweighting for the 2018 3b1l Validation Region. A 340 minimum of 4 jets is required in each event in order to form Higgs candidates.	149
341	<b>7.54 Non-resonant Search (3b1l):</b> Distributions of $p_T$ of the 1st and 3rd leading 342 Higgs Candidate jets and $\Delta R$ between Higgs candidates before and after CR 343 derived reweighting for the 2018 3b1l Validation Region. . . . .	150
344	<b>7.55 Non-resonant Search (3b1l):</b> Distributions of $\eta$ of the 1st, 2nd, and 3rd 345 leading Higgs Candidate jets before and after CR derived reweighting for the 346 2018 3b1l Validation Region. . . . .	151
347	<b>7.56 Non-resonant Search (3b1l):</b> Distributions of $\eta$ of the 4th leading Higgs 348 Candidate jet and the $p_T$ of the leading and subleading Higgs candidates before 349 and after CR derived reweighting for the 2018 3b1l Validation Region. . . . .	152
350	<b>7.57 Non-resonant Search (3b1l):</b> Distributions of mass of the leading and 351 subleading Higgs candidates and of the di-Higgs system before and after CR 352 derived reweighting for the 2018 3b1l Validation Region. . . . .	153
353	<b>7.58 Non-resonant Search (3b1l):</b> Distributions of $\Delta\phi$ between jets in the lead- 354 ing and subleading Higgs candidates before and after CR derived reweighting 355 for the 2018 3b1l Validation Region. . . . .	154
356	<b>7.59 Non-resonant Search (3b1l):</b> Distributions of the top veto variable, $X_{Wt}$ , 357 before and after CR derived reweighting for the 2018 3b1l Validation Region. 358 Reweighting is done after the cut on this variable is applied. . . . .	155

359	7.60 Illustration of the approximate bootstrap band procedure, shown as a ratio to 360 the nominal estimate for the 2017 non-resonant background estimate. Each grey 361 line is from the $m_{HH}$ prediction for a single bootstrap training. Figure 7.60(a) 362 shows the variation histograms constructed from median weight $\pm$ the IQR of 363 the replica weights. It can be seen that this captures the rough shape of the 364 bootstrap envelope, but is not good estimate for the overall magnitude of the 365 variation. Figure 7.60(b) demonstrates the applied normalization correction, 366 and Figure 7.60(c) shows the final band (normalized Figure 7.60(a) + Figure 367 7.60(b)). Comparing this with the IQR variation for the prediction from each 368 bootstrap in each bin in Figure 7.60(d), the approximate envelope describes a 369 very similar variation. . . . .	160
370	7.61 <b>Resonant Search:</b> Example of CR vs VR variation in each $H_T$ region for 371 2018. The variation nicely factorizes into low and high mass components. . . . .	162
372	7.62 <b>Non-resonant Search (4b):</b> Example of CR vs VR variation in each signal 373 region quadrant for 2018. Significantly different behavior is seen between 374 quadrants, with the largest variation in quadrant 1 and the smallest in quadrant 375 4. . . . .	163
376	7.63 <b>Resonant Search:</b> Performance of the background estimation method in the 377 resonant analysis reversed $\Delta\eta_{HH}$ kinematic signal region. A new background 378 estimate is trained following nominal procedures entirely within the reversed 379 $\Delta\eta_{HH}$ region, and the resulting model, including uncertainties, is compared 380 with $4b$ data in the corresponding signal region. Good agreement is shown. 381 The quoted $p$ -value uses the $\chi^2$ test statistic, and demonstrates no evidence 382 that the data differs from the assessed background. . . . .	167
383	7.64 <b>Non-resonant Search:</b> Performance of the background estimation method 384 in the $3b + 1$ fail validation region. A new background estimate is trained 385 following nominal procedures but with a reweighting from $2b$ to $3b + 1$ fail 386 events. Generally good agreement is seen, though there is some deviation at 387 very low masses in the low $\Delta\eta_{HH}$ low $X_{HH}$ category. . . . .	168
388	7.65 <b>Resonant Search:</b> Demonstration of the performance of the nominal reweight- 389 ing in the control region on corrected $m_{HH}$ , with Figure 7.65(a) showing 390 $2b$ events normalized to the total $4b$ yield and Figure 7.65(b) applying the 391 reweighting procedure. Agreement is much improved with the reweighting. 392 Note that overall reweighted $2b$ yield agrees with $4b$ yield in the control region 393 by construction. . . . .	172

394	7.66 <b>Resonant Search:</b> Demonstration of the performance of the control region derived reweighting in the validation region on corrected $m_{HH}$ . Agreement is generally good for this extrapolated estimate. Note that the uncertainty band includes the extrapolation systematic, which is defined by a reweighting trained in the validation region. . . . .	173
399	7.67 <b>Resonant Search:</b> Signal region agreement of the background estimate and observed data after a background-only profile likelihood fit. The closure is generally quite good, though there is an evident deficit in the background estimate relative to the data for higher values of corrected $m_{HH}$ . . . . .	174
403	7.68 <b>Non-resonant Search (4b):</b> Demonstration of the performance of the nomi- nal reweighting in the control region on $m_{HH}$ , split into the two $\Delta\eta_{HH}$ regions. Closure is generally good, with some residual mismodeling in the low $\Delta\eta_{HH}$ region near 600 GeV. . . . .	176
407	7.69 <b>Non-resonant Search (3b1l):</b> Demonstration of the performance of the nominal reweighting in the control region on $m_{HH}$ , split into the two $\Delta\eta_{HH}$ regions. Closure is generally good, with similar conclusions as for the 4b region.	177
410	7.70 <b>Non-resonant Search (4b):</b> Demonstration of the performance of the nomi- nal reweighting in the validation region on $m_{HH}$ , split into the two $\Delta\eta_{HH}$ regions. The low $\Delta\eta_{HH}$ region is consistently overestimated, but, systematic uncertainties are defined via the difference between VR and CR estimates. .	178
414	7.71 <b>Non-resonant Search (3b1l):</b> Demonstration of the performance of the nominal reweighting in the validation region on $m_{HH}$ , split into the two $\Delta\eta_{HH}$ regions. A deficit is present near 600 GeV, but agreement is fairly good otherwise.	179
417	7.72 <b>Non-resonant Search (4b):</b> Signal region agreement of the background estimate and observed data after a background-only profile likelihood fit for the 4b channels, with Standard Model and $\kappa_\lambda = 6$ signal overlaid for reference. Modeling is generally quite good near the Standard Model peak, but disagreements are seen at very low and high masses. A deficit is present in low $\Delta\eta_{HH}$ bins near 600 GeV. . . . .	180
423	7.73 <b>Non-resonant Search (3b1l):</b> Signal region agreement of the background estimate and observed data after a background-only profile likelihood fit for the 3b1l channels, with Standard Model and $\kappa_\lambda = 6$ signal overlaid for reference. Conclusions are very similar to the 4b channels, with generally good modeling near the Standard Model peak, but disagreements at very low and high masses. A deficit is present near 600 GeV. . . . .	181

429	7.74 Expected (dashed black) and observed (solid black) 95% CL upper limits 430 on the cross-section times branching ratio of resonant production for spin-0 431 ( $X \rightarrow HH$ ) and spin-2 $G_{KK}^* \rightarrow HH$ . The $\pm 1\sigma$ and $\pm 2\sigma$ ranges for the 432 expected limits are shown in the colored bands. The resolved channel expected 433 limit is shown in dashed pink and covers the range from 251 and 1500 GeV. It 434 is combined with the boosted channel (dashed blue) between 900 and 1500 GeV. 435 The theoretical prediction for the bulk RS model with $k/\bar{M}_{\text{Pl}} = 1$ [20] (solid 436 red line) is shown, with the decrease below 350 GeV due to a sharp reduction 437 in the $G_{KK}^* \rightarrow HH$ branching ratio. The nominal $H \rightarrow b\bar{b}$ branching ratio is 438 taken as 0.582. . . . .	185
439	7.75 Expected (dashed black) and observed (solid black) 95% CL upper limits on 440 the cross-section times branching ratio of non-resonant production for a range 441 of values of the Higgs self-coupling, with the Standard Model value ( $\kappa_\lambda = 1$ ) 442 illustrated with a star. The $\pm 1\sigma$ and $\pm 2\sigma$ ranges for the expected limits are 443 shown in the colored bands. The cross section limit for $HH$ production is set 444 at 140 fb (180 fb) observed (expected), corresponding to an observed (expected) 445 limit of 4.4 (5.9) times the Standard Model prediction. $\kappa_\lambda$ is constrained to 446 be within the range $-4.9 \leq \kappa_\lambda \leq 14.4$ observed ( $-3.9 \leq \kappa_\lambda \leq 10.9$ expected). 447 The nominal $H \rightarrow b\bar{b}$ branching ratio is taken as 0.582. We note that the 448 excess present for $\kappa_\lambda \geq 5$ is thought to be due to a low mass background 449 mis-modeling, present due to the optimization of this analysis for the Standard 450 Model point, and is not present in more sensitive channels in this same region 451 (e.g. $HH \rightarrow bb\gamma\gamma$ ). . . . .	186
452	7.76 Comparison of the limits in Figure 7.75 with an equivalent set of limits that 453 drop the $m_{HH}$ bins below 381 GeV, with the value of 381 GeV determined 454 by the optimized variable width binning. The expected limit band with this 455 mass cut is shown in dashed blue, and the observed is shown in solid blue. 456 The excess at and above $\kappa_\lambda = 5$ is significantly reduced, demonstrating that 457 this is driven by low mass. Notably, there is minimal impact on the expected 458 sensitivity with this $m_{HH}$ cut. . . . .	187
459	8.1 Gaussian process sampling prediction of marginals $m_{H_1}$ and $m_{H_2}$ for 2b signal 460 region events compared to real 2b signal region events for the 2018 dataset. 461 Good agreement is seen. Only a small fraction (0.01) of the 2b dataset is used 462 for both training and this final comparison to mimic 4b statistics. . . . .	197
463	8.2 Gaussian process sampling prediction for the mass plane compared to the real 464 2b dataset for 2018. Only a small fraction (0.01) of the 2b dataset is used for 465 both training and this final comparison to mimic 4b statistics. Good agreement 466 is seen. . . . .	199

467	8.3 Gaussian process sampling prediction of marginals $m_{H1}$ and $m_{H2}$ for $4b$ signal	
468	region events compared to both control and validation reweighting predictions.	
469	While there are some differences, the estimates are compatible. . . . .	200
470	8.4 Gaussian process sampling prediction for the $4b$ mass plane compared to the	
471	reweighted $2b$ estimate in the signal region. Both estimates are compatible. .	201

## GLOSSARY

473 ARGUMENT: replacement text which customizes a L<sup>A</sup>T<sub>E</sub>X macro for each particular usage.

## ACKNOWLEDGMENTS

475 Five years is both a short time and a long time – many things have happened and many  
476 have stayed the same. I certainly know much more physics than I did at the outset, but also  
477 have learned to ski, discovered a love for hiking, eaten large amounts of cheese, and survived  
478 a pandemic by making sourdough and cinnamon rolls. Of course, the most important part of  
479 any journey is the friends we made along the way – the utmost gratitude and appreciation  
480 goes to the Seattle friends, for the many nights both hard at work and at College Inn, to  
481 the CERN friends, for adventures around Europe and days by the lake, the Chicago friends,  
482 for my position as European correspondent for the Dum Dum Donut Intellectuals, and the  
483 friends from home, for New Years Eve parties and visits in between. Though we’re scattered  
484 across the world, I hope to see you all soon.

485 A thank you, of course, to my family for their continued and constant support, for trying  
486 their best to learn physics along with me, and going along on this Ph.D. adventure every  
487 step of the way.

488 I am only writing this thesis because of the incredible support of my research group, so a  
489 massive thank you to Anna, for your guidance and compassion, for advising me as both a  
490 physicist and a person, and for always being available, and Jana, for shaping who I am as a  
491 physicist and providing feedback on almost literally every talk that I’ve written – I knew I  
492 was getting ready to graduate when you started running out of comments.

493 A special set of thank yous to the SLAC group, namely Nicole, Michael, and Rafael, for  
494 being an excellent set of collaborators with an excellent set of ideas to push the analysis  
495 forward, many of which are in this thesis, and for being my second research family.

496 And last but not least, a thank you to the entire  $HH \rightarrow 4b$  group, of course to Max

497 and Rafael for their guidance and direction, Bejan for being an excellent collaborator and  
498 co-editor for the resonant search, Dale and Alex for excelling on the boosted side of things,  
499 Lucas, for great work on triggers and for diving headfirst into all of my code, the ggF push  
500 squad, for a huge amount of hard work on the non-resonant, and of course the  $HH \rightarrow 4\text{beers}$   
501 team, many of whom have already been mentioned, but who deserve an extra shout out for  
502 keeping things fun even during stressful times.

503 The physics is done, the rest is paperwork. Let us begin.

504

## DEDICATION

505

To family, both given and found

506

## Chapter 1

507

### THE STANDARD MODEL OF PARTICLE PHYSICS

508

The Standard Model of Particle Physics (SM) is a monumental historical achievement, providing a formalism with which one may describe everything from the physics of everyday experience to the physics that is studied at very high energies at the Large Hadron Collider (Chapter 3). In this chapter, we will provide a brief overview of the pieces that go into the construction of such a model. The primary focus of this thesis is searches for pair production of Higgs bosons decaying to four  $b$ -quarks. Consequently, we will pay particular attention to the relevant pieces of the Higgs Mechanism, as well as the theory behind searches at a hadronic collider.

516

#### **1.1 Introduction: Particles and Fields**

517

What is a particle? The Standard Model describes a set of fundamental, point-like, objects shown in Figure 1.1. These objects have distinguishing characteristics (e.g., mass and spin). These objects interact in very specific ways. The set of objects and their interactions result in a set of observable effects, and these effects are the basis of a field of experimental physics.

521

The effects of these objects and their interactions are familiar as fundamental forces: electromagnetism (photons, electrons), the strong interaction (quarks, gluons), the weak interaction (neutrinos,  $W$  and  $Z$  bosons). Gravity is not described in this model, as the weakest, with effects most relevant on much larger distance scales than the rest. However, the description of these other three is powerful – verifying and searching for cracks in this description is a large effort, and the topic of this thesis.

527

The formalism for describing these particles and their interactions is that of quantum field theory. Classical field theory is most familiar in the context of, e.g., electromagnetism – an

529 electric field exists in some region of space, and a charged point-particle experiences a force  
530 characterized by the charge of the point-particle and the magnitude of the field at the location  
531 of the point-particle in spacetime. The same language translates to quantum field theory.  
532 Here, particles are described in terms of quantum fields in some region of spacetime. These  
533 fields have associated charges which describe the forces they experience when interacting  
534 with other quantum fields. Most familiar is electric charge – however this applies to e.g., the  
535 strong interaction as well, where quantum fields have an associated *color charge* describing  
536 behavior under the strong force.

537 Particles are observed to behave in different ways under different forces. These behaviors  
538 respect certain *symmetries*, which are most naturally described in the language of group  
539 theory. The respective fields, charges, and generators of these symmetry groups are the basic  
540 pieces of the SM Lagrangian, which describes the full dynamics of the theory. In the following,  
541 we will build up the basic components of this Lagrangian. The treatment presented here relies  
542 heavily on Jackson's Classical Electrodynamics [2] for the build-up, and Thomson's Modern  
543 Particle Physics [3] for the rest, with reference to Srednicki's Quantum Field Theory [4], and  
544 some personal biases and interjections.

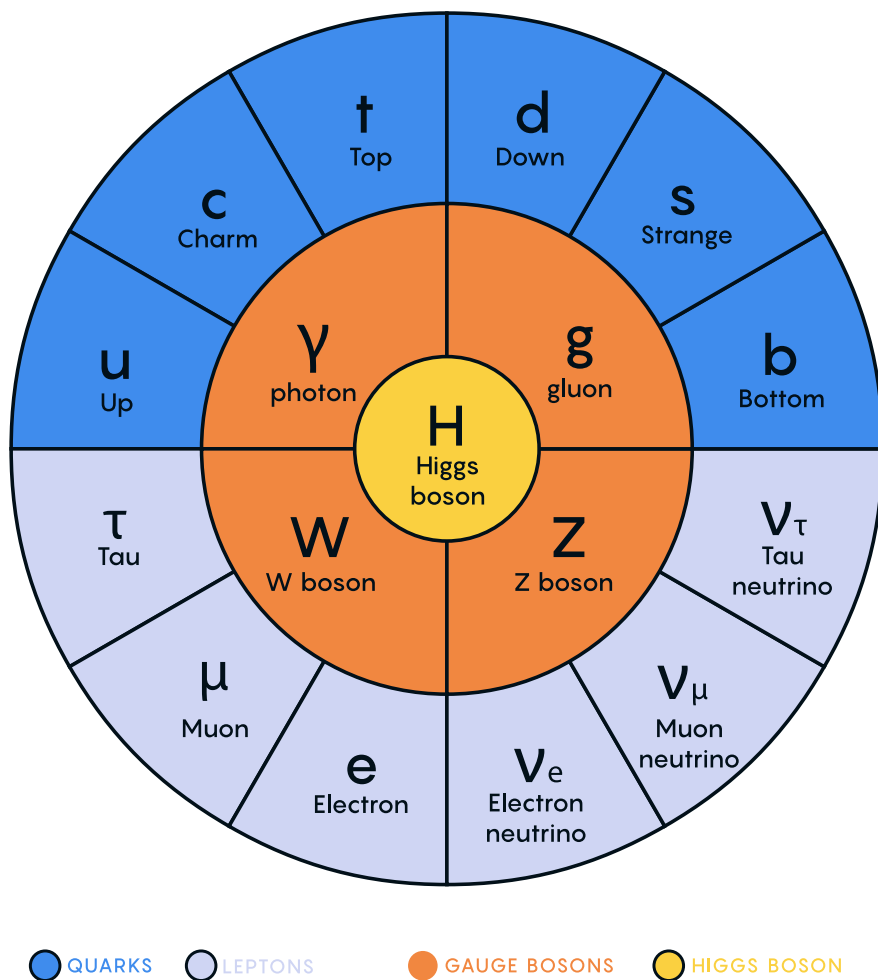


Figure 1.1: Diagram of the elementary particles described by the Standard Model [1].

545 **1.2 Quantum Electrodynamics**

Classical electrodynamics is familiar to the general physics audience: electric ( $\vec{E}$ ) and magnetic ( $\vec{B}$ ) fields are used to describe behavior of particles with charge  $q$  moving with velocity  $\vec{v}$ , with forces described as  $\vec{F} = q\vec{E} + q\vec{v} \times \vec{B}$ . Hints at some more fundamental properties of electric and magnetic fields come via a simple thought experiment: in a frame of reference moving along with the particle at velocity  $\vec{v}$ , the particle would appear to be standing still, and therefore have no magnetic force exerted. Therefore a *relativistic* formulation of the theory is required. This is most easily accomplished with a repackaging: the fundamental objects are no longer classical fields but the electric and magnetic *potentials*:  $\phi$  and  $\vec{A}$  respectively, with

$$\vec{E} = -\nabla\phi - \frac{\partial\vec{A}}{\partial t} \quad (1.1)$$

$$\vec{B} = \nabla \times \vec{A} \quad (1.2)$$

It is then natural to fully repackage into a relativistic *four-vector*:  $A^\mu = (\phi, \vec{A})$ . Considering  $\partial^\mu = (\frac{\partial}{\partial t}, \nabla)$ , the  $x$  components of these above two equations become:

$$E_x = -\frac{\partial\phi}{\partial x} - \frac{\partial A_x}{\partial t} = -(\partial^0 A^1 - \partial^1 A^0) \quad (1.3)$$

$$B_x = \frac{\partial A_z}{\partial y} - \frac{\partial A_y}{\partial z} = -(\partial^2 A^3 - \partial^3 A^2) \quad (1.4)$$

546 where we have used the sign convention  $(+, -, -, -)$ , such that  $\partial^\mu = (\frac{\partial}{\partial x_0}, -\nabla)$ .

This is naturally suggestive of a second rank, antisymmetric tensor to describe both the electric and magnetic fields (the *field strength tensor*), defined as:

$$F^{\alpha\beta} = \partial^\alpha A^\beta - \partial^\beta A^\alpha \quad (1.5)$$

Defining a four-current as  $J_\mu = (q, \vec{J})$ , with  $q$  standard electric charge,  $\vec{J}$  standard electric current, conservation of charge may be expressed via the continuity equation

$$\partial_\mu J^\mu = 0 \quad (1.6)$$

and all of classical electromagnetism may be packaged into the Lagrangian density:

$$\mathcal{L} = -\frac{1}{4} F_{\mu\nu} F^{\mu\nu} - J^\mu A_\mu. \quad (1.7)$$

547 This gets us partway to our goal, but is entirely classical - the description is of classical  
 548 fields and point charges, not of quantum fields and particles. To reframe this, let us go back  
 549 to the zoomed out view of the particles of the Standard Model. Two of the most familiar  
 550 objects associated with electromagnetism are electrons: spin-1/2 particles with charge  $e$ , mass  
 551  $m$ , and photons: massless spin-1 particles which are the "pieces" of electromagnetic radiation.

552 We know that electrons experience electromagnetic interactions with other objects. Given  
 553 this, and the fact that such interactions must be transmitted *somewhat* between e.g. two  
 554 electrons, it seems natural that these interactions are facilitated by electromagnetic radiation.  
 555 More specifically, we may think of photons as *mediators* of the electromagnetic force. It  
 556 follows, then, that a description of electromagnetism on the level of particles must involve a  
 557 description of both the "source" particles (e.g. electrons), the mediators (photons), and their  
 558 interactions. Further, this description must be (1) relativistic and (2) consistent with the  
 559 classically derived dynamics described above.

The beginnings of a relativistic description of spin-1/2 particles is due to Paul Dirac, with the famous Dirac equation:

$$(i\gamma^\mu \partial_\mu - m)\psi = 0 \quad (1.8)$$

where  $\partial_\mu$  is as defined above,  $\psi$  is a Dirac *spinor*, i.e. a four-component wavefunction,  $m$  is the mass of the particle, and  $\gamma^\mu$  are the Dirac gamma matrices, which define the algebraic structure of the theory. For the following, we also define a conjugate spinor,

$$\bar{\psi} = \psi^\dagger \gamma^0 \quad (1.9)$$

which satisfies the conjugate Dirac equation

$$\bar{\psi}(i\gamma^\mu \partial_\mu - m) = 0 \quad (1.10)$$

560 where the derivative acts to the left.

The Dirac equation is the dynamical equation for spin-1/2, but we'd like to express these dynamics via a Lagrangian density. Further, to have a relativistic description, we'd like to

have this be density be Lorentz invariant. These constraints lead to a Lagrangian of the form

$$\mathcal{L} = \bar{\psi}(i\gamma^\mu \partial_\mu - m)\psi \quad (1.11)$$

561 where the Euler-Lagrange equation exactly recovers the Dirac equation.

The question now becomes how to marry the two Lagrangian descriptions that we have developed. Returning for a moment to classical electrodynamics, we know that the Hamiltonian for a charged particle in an electromagnetic field is described by

$$H = \frac{1}{2m}(\vec{p} - q\vec{A})^2 + q\phi. \quad (1.12)$$

Comparing this to the Hamiltonian for a free particle, we see that the modifications required are  $\vec{p} \rightarrow \vec{p} - q\vec{A}$  and  $E \rightarrow E - q\phi$ . Using the canonical quantization trick of identifying  $\vec{p}$  with operator  $-i\nabla$  and  $E$  with operator  $i\frac{\partial}{\partial t}$ , this identification becomes

$$i\partial_\mu \rightarrow i\partial_\mu - qA_\mu \quad (1.13)$$

Allowing for the naive substitution in the Dirac Lagrangian:

$$\mathcal{L} = \bar{\psi}(i\gamma^\mu(\partial_\mu + iqA_\mu) - m)\psi - \frac{1}{4}F_{\mu\nu}F^{\mu\nu}. \quad (1.14)$$

562 where the source term may be interpreted as coming from the Dirac fields themselves, namely,

563  $-q\bar{\psi}\gamma^\mu\psi A_\mu$ .

Setting  $q = e$  here (as appropriate for the case of an electron), and defining  $D_\mu \equiv \partial_\mu + ieA_\mu$ , this may then be written in the form

$$\mathcal{L} = \bar{\psi}(i\gamma^\mu D_\mu - m)\psi - \frac{1}{4}F_{\mu\nu}F^{\mu\nu}. \quad (1.15)$$

564 which is exactly the quantum electrodynamics Lagrangian.

565 We have swept a few things under the rug here, however. Recall that the general form  
566 of a Lagrangian is conventionally  $\mathcal{L} = T - V$ , where  $T$  is the kinetic term, and thus ought  
567 to contain a derivative with respect to time (c.f. the standard  $\frac{1}{2}m\frac{\partial x}{\partial t}$  familiar from basic  
568 kinematics). More particularly, given the definition of conjugate momentum as  $\partial\mathcal{L}/\partial\dot{q}$  for

569  $\mathcal{L}(q, \dot{q}, t)$  and  $\dot{q} = \frac{\partial q}{\partial t}$ , any field  $q$  which has no time derivative in the Lagrangian has 0  
570 conjugate momentum, and thus no dynamics.

571 Looking at this final form, there is an easily identifiable kinetic term for the spinor fields  
572 (just applying the  $D_\mu$  operator). However trying to identify something similar for the  $A$  fields,  
573 one comes up short – the antisymmetric nature of  $F^{\mu\nu}$  term means that there is no time  
574 derivative applied to  $A^0$ .

575 What does this mean?  $A^\mu$  is a four component object, but it would appear that only three  
576 of the components have dynamics: we have too many degrees of freedom in the theory. This  
577 is the principle behind *gauge symmetry* – an extra constraint on  $A^\mu$  (a *gauge condition*) must  
578 be defined such that a unique  $A^\mu$  defines the theory and satisfies the condition. However,  
579 we are free to choose this extra condition – the physics content of the theory should be  
580 independent of this choice (that is, it should be *gauge invariant*).

To ground this a bit, let us return to basic electric and magnetic fields. These are physical quantities that can be measured, and are defined in terms of potentials as

$$\vec{E} = -\nabla\phi - \frac{\partial\vec{A}}{\partial t} \quad (1.16)$$

$$\vec{B} = \nabla \times \vec{A}. \quad (1.17)$$

581 It is easy to show, for any scalar function  $\lambda$ , that  $\nabla \times \nabla\lambda = 0$ . This implies that the physical  
582  $\vec{B}$  field is invariant under the transformation  $\vec{A} \rightarrow \vec{A} + \nabla\lambda$  for any scalar function  $\lambda$ .

583 Under the same transformation of  $\vec{A}$ , the electric field  $\vec{E}$  becomes  $-\nabla\phi - \frac{\partial\vec{A}}{\partial t} - \frac{\partial\nabla\lambda}{\partial t} =$   
584  $-\nabla(\phi + \frac{\partial\lambda}{\partial t}) - \frac{\partial\vec{A}}{\partial t}$ , such that, for the  $\vec{E}$  field to be unchanged, we must additionally apply  
585 the transformation  $\phi \rightarrow \phi - \frac{\partial\lambda}{\partial t}$ .

This set of transformations to the potentials that leave the physical degrees of freedom invariant is expressed in our four vector notation naturally as

$$A_\mu \rightarrow A_\mu - \partial_\mu \lambda \quad (1.18)$$

586 where  $A_\mu = (\phi, -\vec{A})$  with our sign convention. It should be noted that this function  $\lambda$  is an  
587 arbitrary function of *local* spacetime, and thus expresses invariance of the physics content

588 under a local transformation.

Let us return to the Lagrangian for QED. In particular, focusing on the free Dirac piece

$$\mathcal{L} = \bar{\psi}(i\gamma^\mu \partial_\mu - m)\psi \quad (1.19)$$

we note that if we apply a local transformation of the form  $\psi \rightarrow e^{iq\lambda(x)}\psi$  (and correspondingly  $\bar{\psi} \rightarrow \bar{\psi}e^{-iq\lambda(x)}$ , by definition), the Lagrangian becomes

$$\bar{\psi}e^{-iq\lambda(x)}(i\gamma^\mu \partial_\mu - m)e^{iq\lambda(x)}\psi = \bar{\psi}e^{-iq\lambda(x)}(i\gamma^\mu \partial_\mu)e^{iq\lambda(x)}\psi - m\bar{\psi}\psi. \quad (1.20)$$

As  $\partial_\mu(e^{iq\lambda(x)}\psi) = iq e^{iq\lambda(x)}(\partial_\mu \lambda(x))\psi + e^{iq\lambda(x)}\partial_\mu \psi$ , this becomes

$$\bar{\psi}(i\gamma^\mu(\partial_\mu + iq\partial_\mu \lambda(x)) - m)\psi. \quad (1.21)$$

Thus, the free Dirac Lagrangian on its own is not invariant under this transformation. We may note, however, that on interaction with an electromagnetic field, as described above, this transformed Lagrangian may be packaged as:

$$\bar{\psi}(i\gamma^\mu(\partial_\mu + iq\partial_\mu \lambda(x) + iqA_\mu) - m)\psi = \bar{\psi}(i\gamma^\mu(\partial_\mu + iq(A_\mu + \partial_\mu \lambda(x))) - m)\psi. \quad (1.22)$$

589 since by the arguments above, the physics content of the Lagrangian is invariant under the  
590 transformation  $A_\mu \rightarrow A_\mu - \partial_\mu \lambda$ , we may directly make this transformation, and remove this  
591 extra  $\partial_\mu \lambda(x)$  term. It is straightforward to verify that the  $\frac{1}{4}F_{\mu\nu}F^{\mu\nu}$  term is invariant under  
592 this same transformation of  $A_\mu$ , so we may say that the QED Lagrangian is invariant under  
593 local transformations of the form  $\psi \rightarrow e^{iq\lambda(x)}\psi$ .

594 These arguments illuminate some important concepts which will serve us well going forward.  
595 First, while we have remained grounded in the “familiar” physics of electromagnetism for the  
596 above, arguments of the “top down” variety would lead us to the exact same conclusions.  
597 That is, suppose we wanted to construct a theory of spin-1/2 particles that was invariant  
598 under local transformations of the form  $\psi \rightarrow e^{iq\lambda(x)}\psi$ . More broadly, we could say that we  
599 desire this theory to be invariant under local  $U(1)$  transformations, where  $U(1)$  is exactly  
600 this group, under multiplication, of complex numbers with absolute value 1. By very similar

arguments as above, we would see that, to achieve invariance, this theory would necessitate an additional degree of freedom,  $A_\mu$ , with the exact properties that are familiar to us from electrodynamics. These arguments based on symmetries are extremely powerful in building theories with a less familiar grounding, as we will see in the following.

Second, we defined this quantity  $D_\mu \equiv \partial_\mu + ieA_\mu$  above, seemingly as a matter of notational convenience. However, from the latter set of arguments, such a packaging takes on a new power: by explicitly including this gauge field  $A_\mu$  which transforms in such a way as to keep invariance under a given transformation, the invariance is immediately more manifest. That is, to pose the  $U(1)$  invariance in a more zoomed out way, under the transformation  $\psi \rightarrow e^{iq\lambda(x)}\psi$ , while

$$\bar{\psi}\partial_\mu\psi \rightarrow \bar{\psi}(\partial_\mu + iq\partial_\mu\lambda(x))\psi \quad (1.23)$$

with the extra term that gets canceled out by the gauge transformation of  $A_\mu$ ,

$$\bar{\psi}D_\mu\psi \rightarrow \bar{\psi}D_\mu\psi \quad (1.24)$$

where this transformation is already folded in. This repackaging, called a *gauge covariant derivative* is much more immediately expressive of the symmetries of the theory.

Finally, to emphasize how fundamental these gauge symmetries are to the corresponding theory, let us examine the additional term needed for  $U(1)$  invariance,  $q\bar{\psi}\gamma^\mu A_\mu\psi$ . While a first principles examination of Feynman rules is beyond the scope of this thesis, it is powerful to note that this is expressive of a QED vertex: the  $U(1)$  invariance of the theory and the interaction between photons and electrons are inextricably tied together.

### 1.3 An Aside on Group Theory

Quantum electrodynamics is very familiar and well covered, and provides (both historically and in this thesis) a nice bridge between “standard” physics and the language of symmetries and quantum field theory. However, now that we are acquainted with the language, we may set up to dive a bit deeper. To begin, let us look again at the  $U(1)$  group that is so fundamental to QED. We have expressed this via a set of transformations on our Dirac spinor

618 objects,  $\psi$ , of the form  $e^{iq\lambda(x)}$ . Note that such transformations, though they are local (i.e. a  
 619 function of spacetime) are purely *phase* transformations. Relatedly,  $U(1)$  is an Abelian group,  
 620 meaning that group elements commute.

621 To set up language to generalize beyond  $U(1)$ , note that we may equivalently write  $U(1)$   
 622 elements as  $e^{ig\vec{\alpha}(x)\cdot\vec{T}}$ ,  $\vec{\alpha}(x)$  and  $\vec{T}$  and are vectors in the space of *generators* of the group,  
 623 with each  $\alpha^a(x)$  an associated scalar function to generator  $t^a$ , and  $g$  is some scalar strength  
 624 parameter. Of course this is a bit silly for  $U(1)$ , which has a single generator, and thus  
 625 reduces to the transformation we discussed above. However, this becomes much more useful  
 626 for groups of higher degree, with more generators and degrees of freedom.

627 To discuss these groups in a bit more detail, note that  $U(n)$  is the unitary group of degree  
 628  $n$ , and corresponds to the group of  $n \times n$  unitary matrices (that is,  $U^\dagger U = UU^\dagger = 1$ ). Given  
 629 that group elements are  $n \times n$ , this means that there are  $n^2$  degrees of freedom:  $n^2$  generators  
 630 are needed to characterize the group.

631 For  $U(1)$ , this is all consistent with what we have said above – the group of  $1 \times 1$  unitary  
 632 matrices have a single generator, and the phases we identify above clearly satisfy unitarity.  
 633 Note that these degrees of freedom for the gauge group also characterize the number of gauge  
 634 bosons we need to satisfy the local symmetry: for  $U(1)$ , we need one gauge boson, the photon.

635 Of relevance for the Standard Model are also the special unitary groups  $SU(n)$ . These  
 636 are defined similarly to the unitary groups, with the additional requirement that group  
 637 elements have determinant 1. This extra constraint removes 1 degree of freedom: groups are  
 638 characterized by  $n^2 - 1$  generators.

639 In particular, we will examine the groups  $SU(2)$  in the context of the weak interaction,  
 640 with an associated  $2^2 - 1 = 3$  gauge bosons (cf. the  $W^\pm$  and  $Z$  bosons), and  $SU(3)$ , with an  
 641 associated  $3^2 - 1 = 8$  gauge bosons (cf. gluons of different flavors). Note that these groups  
 642 are non-Abelian ( $2 \times 2$  or  $3 \times 3$  matrices do not, in general, commute), leading to a variety of  
 643 complications. However, both of these theories feature interactions with spin-1/2 particles,  
 644 with transformations of a very similar form:  $\psi \rightarrow e^{ig\vec{\alpha}(x)\cdot\vec{T}}\psi$ , and the general framing of the  
 645 arguments for QED will serve us well in the following.

646 **1.4 Quantum Chromodynamics**

647 In some sense, the simplest extension the development of QED is quantum chromodynamics  
648 (QCD). QCD is a theory in which, once the basic dynamics are framed (a non-trivial task!)  
649 the group structure becomes apparent. The quark model, developed by Murray Gell-Mann [5]  
650 and George Zweig [6], provided the fundamental particles involved in the theory, and had  
651 great success in explaining the expanding zoo of experimentally observed hadronic states.

652 Some puzzles were still apparent – the  $\Delta^{++}$  baryon, e.g., is composed of three up quarks,  
653  $u$ , with aligned spins. As quarks are fermions, such a state should not be allowed by the  
654 Pauli exclusion principle. The existence of such a state in nature implies the existence of  
655 another quantum number, and a triplet of values, called *color charge* was proposed by Oscar  
656 Greenberg [7]. With these pieces in place, the structure becomes more apparent, as elucidated  
657 by Han and Nambu [8].

658 Let us reason our way to the symmetries using color charge. Experimentally, we know  
659 that there is this triplet of color charge values  $r, g, b$  (the “plus” values, cf. electric charge)  
660 and correspondingly anti-color charge  $\bar{r}, \bar{g}, \bar{b}$  (the “minus” values). Supposing that the force  
661 behind QCD (the *strong force*) is, similar to QED, interactions between fermions mediated  
662 by gauge bosons (quarks and gluons respectively), we can start to line up the pieces.

663 What color charge does a gluon have? Similarly to electric charge, we may associate  
664 particles with color charge, anti-particles with anti-color charge. Notably, free particles  
665 observed experimentally are colorless (have no color charge). Thus, in order for charge to  
666 be conserved throughout such processes, this already implies that there are charged gluons.  
667 Further, examining color flow diagrams such as *TODO: insert*, it is apparent first that a  
668 gluon has not one but two associated color charges and second that these two must be one  
669 color charge and one anti-color charge.

670 Counting up the available types of gluons, then, we come up with nine. Six of mixed  
671 color type:  $r\bar{b}, r\bar{g}, b\bar{r}, b\bar{g}, g\bar{b}$ , and  $g\bar{r}$ , and three of same color type:  $r\bar{r}, g\bar{g}$ , and  $b\bar{b}$ . In practice,  
672 however, these latter three are a bit redundant: all express a colorless gluon, which, if we

673 could observe this as a free particle, would be indistinguishable from each other. The *color*  
 674 *singlet* state is then a mix of these,  $\frac{1}{\sqrt{3}}(r\bar{r} + g\bar{g} + b\bar{b})$ , leaving two unclaimed degrees of  
 675 freedom, which may be satisfied by the linearly independent combinations  $\frac{1}{\sqrt{2}}(r\bar{r} - g\bar{g})$  and  
 676  $\frac{1}{\sqrt{6}}(r\bar{r} + g\bar{g} - 2b\bar{b})$ .

677 We thus have an octet of color states plus a colorless singlet state. If this colorless singlet  
 678 state existed, however, we would be able to observe it, not only via interactions with quarks,  
 679 but as a free particle. Since do not observe this in nature, this restricts us to 8 gluons. The  
 680 simplest group with a corresponding 8 generators is  $SU(3)$ . Under the assumption that  
 681  $SU(3)$  is the local gauge symmetry of the strong interaction, we may proceed in a similar  
 682 way as we did for QED. The gauge transformation is  $\psi \rightarrow e^{ig_S \vec{\alpha}(x) \cdot \vec{T}} \psi$ , where  $\vec{T}$  is an eight  
 683 component vector of the generators of  $SU(3)$ , often expressed via the Gell-Mann matrices,  
 684  $\lambda^a$ , as  $t^a = \frac{1}{2}\lambda^a$ , and the spinor  $\psi$  represents the fields corresponding to quarks.

685 This  $SU(3)$  symmetry exactly expresses the color structure elucidated above – the Gell-  
 686 Mann matrices are an equivalent presentation of the color combinations described above.  
 687 Proceeding by analogy to QED, gauge invariance is achieved by introducing eight new degrees  
 688 of freedom,  $G_\mu^a$ , which are the gauge fields corresponding to the gluons, with the gauge  
 689 covariant derivative then analogously taking the form  $D_\mu \equiv \partial_\mu + ig_S G_\mu^a t^a$ .

Recall from the QED derivation that the field strength tensor,  $F^{\mu\nu}$  is a rank two antisymmetric tensor which is manifestly gauge invariant and which describes the physical dynamics of the  $A_\mu$  field. We would like to analogously define a term for the gluon fields. Repackaging this QED tensor, it is apparent that

$$[D_\mu, D_\nu] = D_\mu D_\nu - D_\nu D_\mu \quad (1.25)$$

$$= (\partial_\mu + iqA_\mu)(\partial_\nu + iqA_\nu) - (\partial_\nu + iqA_\nu)(\partial_\mu + iqA_\mu) \quad (1.26)$$

$$= \partial_\mu \partial_\nu + iq\partial_\mu A_\nu + iqA_\mu \partial_\nu + (iq)^2 A_\mu A_\nu - (\partial_\nu \partial_\mu + iq\partial_\nu A_\mu + iqA_\nu \partial_\mu + (iq)^2 A_\nu A_\mu) \quad (1.27)$$

$$= iq(\partial_\mu A_\nu - \partial_\nu A_\mu) + (iq)^2 (A_\mu A_\nu - A_\nu A_\mu) \quad (1.28)$$

$$= iq(\partial_\mu A_\nu - \partial_\nu A_\mu) + (iq)^2 [A_\mu, A_\nu]. \quad (1.29)$$

We proceed through this derivation to highlight that, in the specific case of QED, with its Abelian  $U(1)$  gauge symmetry, the field commutator vanishes, leaving exactly the definition of  $F_{\mu\nu}$  as described above, i.e.,

$$F_{\mu\nu} = \frac{1}{iq}[D_\mu, D_\nu]. \quad (1.30)$$

We may proceed to define an analogous field strength term for  $G_\mu^a$  in a similar way:

$$G_{\mu\nu} = \frac{1}{ig_S}[D_\mu, D_\nu] \quad (1.31)$$

This has an extremely nice correspondence, but is complicated by the non-Abelian nature of  $SU(3)$ , with

$$G_{\mu\nu} = \partial_\mu(G_\nu^a t^a) - \partial_\nu(G_\mu^a t^a) + ig_s[G_\mu^a t^a, G_\nu^a t^a]. \quad (1.32)$$

in which the field commutator term is non-zero. In particular (since each term is summing over  $a$ , so we may relabel) as

$$[G_\mu^a t^a, G_\nu^b t^b] = [t^a, t^b]G_\mu^a G_\nu^b \quad (1.33)$$

and as  $[t^a, t^b] = if^{abc}t^c$  for the Gell-Mann matrices, where  $f^{abc}$  are the structure constants of  $SU(3)$ , we have

$$G_{\mu\nu} = \partial_\mu(G_\nu^a t^a) - \partial_\nu(G_\mu^a t^a) - g_s f^{abc} t^c G_\mu^a G_\nu^b \quad (1.34)$$

$$= t^a(\partial_\mu G_\nu^a - \partial_\nu G_\mu^a - f^{bca} G_\mu^b G_\nu^c) \quad (1.35)$$

$$= t^a G_{\mu\nu}^a \quad (1.36)$$

for  $G_{\mu\nu}^a = \partial_\mu G_\nu^a - \partial_\nu G_\mu^a - f^{abc} G_\mu^b G_\nu^c$ .

This gives the component of the field strength corresponding to a particular gauge field  $a$ , where the first two terms have the familiar form of the QED field strength, while the last term is new, and explicitly related to the group structure via the  $f^{abc}$  constants. In terms of the physics content of the theory, this latter term gives rise to a gluon *self-interaction*, a distinguishing feature of QCD.

Similarly as in QED, a Lorentz invariant combination of field strength tensors may be made as  $G_{\mu\nu} G^{\mu\nu}$ . However, this is not manifestly gauge invariant. Under a gauge transformation

698  $U$ , the covariant derivative behaves as  $D^\mu \rightarrow UD^\mu U^{-1}$ , corresponding to  $G^{\mu\nu} \rightarrow UG^{\mu\nu}U^{-1}$ .  
699 The cyclic property of the trace thus ensures the gauge invariance of  $\text{tr}(G_{\mu\nu}G^{\mu\nu})$ , which we  
700 will write as  $G_{\mu\nu}^a G_a^{\mu\nu}$  with the implied sum over generators  $a$ .

Packaging up the theory, it is tempting to copy the form of the QED Lagrangian, with the identifications we have made above:

$$\mathcal{L} = \bar{\psi}(i\gamma^\mu D_\mu - m)\psi - \frac{1}{4}G_{\mu\nu}^a G_a^{\mu\nu}. \quad (1.37)$$

However this is not quite correct due to the  $SU(3)$  nature of the theory. In terms of the physics, the Dirac fields  $\psi$  have associated color charge, which must interact appropriately with the  $G_\mu$  fields. Mathematically, the generators  $t^a$  are  $3 \times 3$  matrices, while the  $\psi$  are four component spinors. Adding a color index to the Dirac fields, i.e.,  $\psi_i$  where  $i$  runs over the three color charges, and similarly indexing the generators  $t_{ij}^a$ , we may then express the  $SU(3)$  gauge covariant derivative component-wise as

$$(D_\mu)_{ij} = \partial_\mu \delta_{ij} + ig_S G_\mu^a t_{ij}^a \quad (1.38)$$

701 where  $\delta_{ij}$  is the Kronecker delta, as  $\partial_\mu$  does not participate in the  $SU(3)$  structure.

The Lagrangian then becomes

$$\mathcal{L} = \bar{\psi}_i(i(\gamma^\mu D_\mu)_{ij} - m\delta_{ij})\psi_j - \frac{1}{4}G_{\mu\nu}^a G_a^{\mu\nu}. \quad (1.39)$$

702 and we have constructed QCD.

### 703 1.5 The Weak Interaction

704 One of the first theories of the weak interaction was from Enrico Fermi [9], in an effort to  
705 explain beta decay, a process in which an electron or positron is emitted from an atomic  
706 nucleus, resulting in the conversion of a neutron to a proton or proton to a neutron respectively.  
707 Fermi's hypothesis was of a direct interaction between four fermions. However, in the advent of  
708 QED, it is natural to wonder if a theory based on mediator particles and gauge symmetries  
709 applies to the weak force as well. The modern formulation of such a theory is due to Sheldon

<sup>710</sup> Glashow, Steven Weinberg, and Abdus Salam [10], and is what we will describe in the  
<sup>711</sup> following.

<sup>712</sup> Considering emission of an electron, Fermi's theory involves an initial state neutron that  
<sup>713</sup> transitions to a proton with the emission of an electron and a neutrino. This transition  
<sup>714</sup> gives a hint that something slightly more complicated is happening than in QED: there is an  
<sup>715</sup> apparent mixing between particle types.

<sup>716</sup> Now, with the assumption there are mediators for such an interaction, we further know  
<sup>717</sup> from beta decay and charge conservation that there must be at least two such degrees of  
<sup>718</sup> freedom: e.g. one that decays to an electron and neutrino ( $W^-$ ) and one that decays to a  
<sup>719</sup> positron and neutrino ( $W^+$ ). From consideration of the process  $e^+e^- \rightarrow W^+W^-$ , it turns  
<sup>720</sup> out that with just these two degrees of freedom, the cross section for this process increases  
<sup>721</sup> without limit as a function of center-of-mass energy, ultimately violating unitarity (more  
<sup>722</sup>  $W^+W^-$  pairs come out than  $e^+e^-$  pairs go in). This is resolved with a third, neutral degree  
<sup>723</sup> of freedom, the  $Z$  boson, whose contribution interferes negatively, regulating this process.

<sup>724</sup> This leads to three degrees of freedom for the gauge symmetry of the weak interactions, so  
<sup>725</sup> we thus need a theory which is locally invariant under transformations of a group with three  
<sup>726</sup> generators. The simplest such choice is  $SU(2)$ . We may follow a very similar prescription as  
<sup>727</sup> for QED and QCD:  $SU(2)$  has three generators, which implies the existence of three gauge  
<sup>728</sup> bosons, call them  $W_\mu^k$ . The gauge transformation may be expressed as  $\psi \rightarrow e^{ig_W \vec{\alpha}(x) \cdot \vec{T}} \psi$ , where  
<sup>729</sup> in this case the generators are for  $SU(2)$ , which may be written in terms of the familiar Pauli  
<sup>730</sup> matrices:  $\vec{T} = \frac{1}{2}\vec{\sigma}$ . The structure constants for  $SU(2)$  are the antisymmetric Levi-Civita  
<sup>731</sup> tensor, so the corresponding gauge covariant derivative is  $D_\mu \equiv \partial_\mu + ig_W W_\mu^k t^k$ , and the field  
<sup>732</sup> strength tensor is  $W_{\mu\nu}^k = \partial_\mu W_\nu^k - \partial_\nu W_\mu^k - \epsilon^{ijk} W_\mu^k W_\nu^k$ .

The corresponding Lagrangian would thus be

$$\mathcal{L} = \bar{\psi}_i (i(\gamma^\mu D_\mu)_{ij} - m\delta_{ij}) \psi_j - \frac{1}{4} W_{\mu\nu}^k W_k^{\mu\nu} \quad (1.40)$$

<sup>733</sup> where indices  $i$  and  $j$  run over  $SU(2)$  charges.

<sup>734</sup> On considering some of the details, the universe unfortunately turns out to be a bit

more complicated. However, this still provides a useful starting place for elucidating the theory of weak interactions. First off, let us consider the particle content, namely, what do the Dirac fields correspond to? This is still a theory of fermionic interactions with gauge bosons. However, we might notice that the fermion content of this theory is both a) broader than QCD, as we know experimentally (cf. beta decay) that both quarks and leptons (e.g. electrons) participate in the weak interaction and b) this fermion content seemingly has a large overlap with QED. In terms of the gauge bosons, we know that at both  $W^+$  and  $W^-$  are electrically charged – this means that we expect some interaction of the weak theory with electromagnetism.

However, before diving deeper into this apparent connection between the weak interaction and QED, let us focus on the gauge symmetry. In QCD, the  $SU(3)$  content of the theory is expressed via a contraction of color indices – the theory allows for transitions between quarks of one color and quarks of another. Thinking similarly in terms of  $SU(2)$  transitions, the beta decay example is already fruitful – there is a transition between an electron and its corresponding neutrino, as well as between two types of quark. In particular, for the case of neutron (with quark content  $udd$ ) and proton (with quark content  $udu$ ), the weak interaction provides for a transition from down to up quark.

Such  $SU(2)$  dynamics are described via a quantity called *weak isospin*, denoted  $I_W$  with third component  $I_W^{(3)}$ , and can be thought of in a very similar way as color charge in QCD (i.e. as the charge corresponding to the weak interaction). Since  $SU(2)$  is  $2 \times 2$ , there are two such charge states for the fermions, denoted as  $I_W^{(3)} = \pm\frac{1}{2}$ . This means that the bosons must have  $I_W = 1$  such that, by sign convention corresponding to electric charge, the  $W^+$  boson has  $I_W^{(3)} = +1$ , the  $Z$  boson has  $I_W^{(3)} = 0$ , and the  $W^-$  boson has  $I_W^{(3)} = -1$ .

From conservation of electric charge, this means that transitions involving a  $W^\pm$  are between particles that differ by  $\pm 1$  in both weak isospin  $I_W^{(3)}$  and electric charge. We may thus line up all such doublets as:

$$\begin{pmatrix} \nu_e \\ e^- \end{pmatrix}, \begin{pmatrix} \nu_\mu \\ \mu^- \end{pmatrix}, \begin{pmatrix} \nu_\tau \\ \tau^- \end{pmatrix}, \begin{pmatrix} u \\ d' \end{pmatrix}, \begin{pmatrix} c \\ s' \end{pmatrix}, \begin{pmatrix} t \\ b' \end{pmatrix} \quad (1.41)$$

758 with the top corresponding to the lower weak isospin and electric charge particles, and the  
 759 lower quark entries ( $d'$ , etc) corresponding to the weak quark eigenstates (which are related  
 760 to the mass eigenstates by the CKM matrix *TODO: more detail*). Similar doublets may be  
 761 constructed for the corresponding anti-particles.

The fundamental structuring of these transitions around both electric and weak charge is again indicative of a natural connection. However, nature is again a bit more complicated than we have described. This is because the weak interaction is a *chiral* theory. For massless particles, chirality is the same as the perhaps more intuitive *helicity*. This describes the relationship between a particle's spin and momentum: if the spin vector points in the same direction as the momentum vector, helicity is positive (the particle is “right-handed”), and if the two point in opposite directions, the helicity is negative (the particle is “left-handed”). More concretely:

$$H = \frac{\vec{s} \cdot \vec{p}}{|\vec{s} \cdot \vec{p}|}. \quad (1.42)$$

For massive particles, this generalizes a bit – in the language of Dirac fermions that we have developed, we define projection operators

$$P_R = \frac{1}{2}(1 + \gamma^5) \quad \text{and} \quad P_L = \frac{1}{2}(1 - \gamma^5) \quad (1.43)$$

762 for right and left-handed chiralities respectively – acting on a Dirac field with such operators  
 763 projects the field onto the corresponding chiral state.

Experimentally, this pops up via parity violation and the famous  $V - A$  theory. For the scope of this thesis, it is sufficient to say that the weak interaction is only observed to take place for left-handed particles (and correspondingly, right-handed anti-particles). We therefore modify the theory stated above by projecting all fermions participating in the weak interaction onto respective chiral states – in particular, the  $SU(2)$  gauge symmetry only acts on left-handed particles and right-handed anti-particles. We therefore modify the theory appropriately, denoting the chiral projected gauge symmetry as  $SU(2)_L$ , and similarly for the

Dirac fields. In particular, the weak isospin doublets listed above must now be left-handed:

$$\begin{pmatrix} \nu_e \\ e^- \end{pmatrix}_L, \begin{pmatrix} \nu_\mu \\ \mu^- \end{pmatrix}_L, \begin{pmatrix} \nu_\tau \\ \tau^- \end{pmatrix}_L, \begin{pmatrix} u \\ d' \end{pmatrix}_L, \begin{pmatrix} c \\ s' \end{pmatrix}_L, \begin{pmatrix} t \\ b' \end{pmatrix}_L \quad (1.44)$$

<sup>764</sup> and right-handed particle states are placed in singlets and assigned 0 charge under  $SU(2)_L$   
<sup>765</sup> ( $I_W = I_W^{(3)} = 0$ ).

With all of these assignments, let us revisit our guess at the form of the weak interaction Lagrangian. First, dwelling on the kinetic term  $\bar{\psi}_i(i(\gamma^\mu D_\mu)_{ij}\psi_j)$ , we note that the assigning of left-handed fermions to isospin doublets and right-handed fermions to isospin singlets allows us to remove explicit  $SU(2)$  indices by treating these as the fundamental objects, that is, for a single *generation* of fermions, we may write:

$$\bar{Q}i\gamma^\mu D_\mu Q + \bar{u}i\gamma^\mu D_\mu u + \bar{d}i\gamma^\mu D_\mu d + \bar{L}i\gamma^\mu D_\mu L + \bar{e}i\gamma^\mu D_\mu e \quad (1.45)$$

<sup>766</sup> for left-handed doublets  $Q$  and  $L$  for quarks and electron fields respectively and right handed  
<sup>767</sup> singlets  $u$  and  $d$  for up and down quark fields and  $e$  for electrons.

More concisely, and summing over the three generations of fermions, we may write

$$\sum_f \bar{f}i\gamma^\mu D_\mu f \quad (1.46)$$

<sup>768</sup> where the  $f$  are understood to run over the fermion chiral doublets and singlets as above.

This then leaves our Lagrangian as

$$\mathcal{L} = \sum_f \bar{f}i\gamma^\mu D_\mu f - \frac{1}{4}W_{\mu\nu}^k W_k^{\mu\nu} \quad (1.47)$$

$$= \sum_f \bar{f}\gamma^\mu(i\partial_\mu - \frac{1}{2}g_W W_\mu^k \sigma_k)f - \frac{1}{4}W_{\mu\nu}^k W_k^{\mu\nu}, \quad (1.48)$$

<sup>769</sup> where we have expanded the covariant derivative for clarity. You may note that we have  
<sup>770</sup> dropped the mass term in the equation above – we will discuss this in detail in just a moment.

First, however, we return to the above comment about fermion content – we neglected to include the sum over fermions in our QED derivation for simplicity. However, all of the

fermions considered in the discussion of the weak interaction have an electric charge (except for the neutrinos). It would be nice to repackage the theory into a coherent *electroweak* theory. This is fairly straightforward when considering the gauge approach – from the discussion above we should expect the electroweak gauge group to be something like  $SU(2) \times U(1)$ , with four corresponding gauge bosons. Consider a gauge theory with group  $SU(2)_L \times U(1)_Y$  – that is, the same weak interaction as discussed previously, but a new  $U(1)_Y$  gauge group for electromagnetism, with transformations defined as

$$\psi \rightarrow e^{ig' \frac{Y}{2} \lambda(x)} \psi \quad (1.49)$$

<sup>771</sup> with *weak hypercharge*  $Y$ .

Similarly to our discussion of QED, we may write the  $U(1)_Y$  gauge field as  $B_\mu$ , and interactions with the Dirac fields take the form  $g' \frac{Y}{2} \gamma^\mu B_\mu \psi$ . The relationship between this hypercharge and new  $B_\mu$  field and classical electrodynamics is not so obvious – however it is convenient to parametrize as

$$\begin{pmatrix} A_\mu \\ Z_\mu \end{pmatrix} = \begin{pmatrix} \cos \theta_W & \sin \theta_W \\ -\sin \theta_W & \cos \theta_W \end{pmatrix} \begin{pmatrix} B_\mu \\ W_\mu^3 \end{pmatrix} \quad (1.50)$$

<sup>772</sup> where  $A_\mu$  and  $Z_\mu$  are the physical fields, and we pick  $W_\mu^3$  as the neutral weak boson.

<sup>773</sup> Note that in the  $SU(2)_L \times U(1)_Y$  theory, the Lagrangian must be invariant under all of  
<sup>774</sup> the local gauge transformations. In particular, this means that the hypercharge must be the  
<sup>775</sup> same for fermion fields in each weak doublet to preserve  $U(1)_Y$  invariance. This gives insight  
<sup>776</sup> into the relation between the charges of  $SU(2)_L \times U(1)_Y$  and electric charge. In particular  
<sup>777</sup> we know that the hypercharge,  $Y$ , of  $e^-$  ( $I_W^{(3)} = -\frac{1}{2}$ ) and  $\nu_e$  ( $I_W^{(3)} = +\frac{1}{2}$ ) is the same.

Supposing that  $Y = \alpha I_W^{(3)} + \beta Q$ , we must have  $-\alpha \frac{1}{2} - \beta = \alpha \frac{1}{2} \implies \beta = -\alpha$ . Therefore, choosing an overall scaling from convention,

$$Y = 2(Q - I_W^{(3)}). \quad (1.51)$$

<sup>778</sup> Some of these particular forms are best understood in the context of the Higgs mechanism  
<sup>779</sup> – we will return to this discussion below.

780 **1.6 The Higgs Potential and the SM**

781 In the above, we have neglected a discussion of masses. However there are several things to  
782 sort out here. In the first place, we know experimentally that the weak interactions occur  
783 over very short ranges at low energies (e.g., why Fermi's effective four fermion interaction was  
784 such a good description). This is consistent with massive  $W^\pm$  and  $Z$  bosons (and indeed, this  
785 is seen experimentally). However, requiring local gauge invariance forbids mass terms in the  
786 Lagrangian. In the simple  $U(1)$  QED example, such a term would have the form  $\frac{1}{2}m_\gamma^2 A_\mu A^\mu$ ,  
787 which is not invariant under the transformation  $A_\mu \rightarrow A_\mu - \partial_\mu \lambda$ , and similar arguments hold  
788 for gauge bosons in the electroweak theory and QCD.

Similar issues are encountered with fermions – in the electroweak theory above, the gauge symmetries are separated into left and right handed chirality via doublet and singlet states. This means that a mass term would need to be separated as well. Such a term would have the form:

$$m\bar{f}f = m(\bar{f}_L + \bar{f}_R)(f_L + f_R) \quad (1.52)$$

$$= m(\bar{f}_L f_L + \bar{f}_L f_R + \bar{f}_R f_L + \bar{f}_R f_R) \quad (1.53)$$

$$= m(\bar{f}_L f_R + \bar{f}_R f_L) \quad (1.54)$$

789 where we have used that  $f_{L,R} = P_{L,R}f$ ,  $\bar{f}_{L,R} = \bar{f}P_{R,L}$ , and  $P_R P_L = P_L P_R = 0$ . As left  
790 and right-handed particles transform differently under  $SU(2)_L$ , this is manifestly not gauge  
791 invariant.

792 The question then becomes: how do we include particle masses while preserving the  
793 gauge properties of our theory? The answer, due to Robert Brout and François Englert [11],  
794 Peter Higgs [12], and Gerald Guralnik, Richard Hagen, and Tom Kibble [13] comes via the  
795 Higgs mechanism, which we will describe in the following. Importantly for this thesis, this  
796 mechanism predicts the existence of a physical particle, the Higgs boson, and a particle  
797 consistent with the Higgs boson was seen by both ATLAS [14] and CMS [15] in 2012.

To explain the Higgs, we focus first on generating masses for the electroweak gauge bosons.

Consider adding two complex scalar fields  $\phi^+$  and  $\phi^0$  to the Standard Model embedded in a weak isospin doublet  $\phi$ . We may write the doublet as

$$\phi = \begin{pmatrix} \phi^+ \\ \phi^0 \end{pmatrix} = \frac{1}{\sqrt{2}} \begin{pmatrix} \phi_1 + i\phi_2 \\ \phi_3 + i\phi_4 \end{pmatrix} \quad (1.55)$$

798 where we explicitly note the four available degrees of freedom.

The Lagrangian for such a doublet takes the form

$$\mathcal{L} = (\partial_\mu \phi)^\dagger (\partial^\mu \phi) - V(\phi) \quad (1.56)$$

where  $V$  is the corresponding potential. Considering the particular form

$$V(\phi) = \mu^2 \phi^\dagger \phi + \lambda (\phi^\dagger \phi)^2 \quad (1.57)$$

799 we may notice that this has some interesting properties. Considering, as illustration, a similar  
800 potential for a real scalar field,  $\mu^2 \chi^2 + \lambda \chi^4$ , taking the derivative and setting it equal to 0  
801 yields extrema when  $\chi = 0$  and  $(\mu^2 + 2\lambda\chi^2) = 0 \implies \chi^2 = -\frac{\mu^2}{2\lambda}$ . For  $\mu^2 > 0$ , there is a  
802 unique minimum at  $\chi = 0$ , and for  $\mu^2 < 0$  there are degenerate minima at  $\chi = \pm\sqrt{-\frac{\mu^2}{2\lambda}}$ .  
803 Note that we take  $\lambda > 0$ , otherwise the only minima in the theory are trivial.

The same simple calculus for the complex Higgs doublet above yields degenerate minima for  $\mu^2 < 0$  at

$$\phi^\dagger \phi = \frac{1}{2} (\phi_1^2 + \phi_2^2 + \phi_3^2 + \phi_4^2) = \frac{v}{2} = -\frac{\mu^2}{2\lambda} \quad (1.58)$$

However, though there is this degenerate set of minima, there can only be a single *physical* vacuum state (we say that the symmetry is *spontaneously broken*). Without loss of generality, we may align our axes such that the physical vacuum state is at

$$\langle 0 | \phi | 0 \rangle = \frac{1}{\sqrt{2}} \begin{pmatrix} 0 \\ v \end{pmatrix} \quad (1.59)$$

804 where we have explicitly chosen a real, non-zero vacuum expectation value for the neutral  
805 component of the Higgs doublet to maintain a massless photon, as we shall see. Physically,  
806 however, this makes sense - the vacuum is not electrically charged.

The vacuum is a classical state – we want a quantum one. We may express fluctuations about this nonzero expectation value via an expansion as  $v + \eta(x) + i\xi(x)$ . However, renaming of fields is only meaningful for the non-zero vacuum component - we thus have:

$$\phi = \frac{1}{\sqrt{2}} \begin{pmatrix} \phi_1 + i\phi_2 \\ v + \eta(x) + i\phi_4 \end{pmatrix}. \quad (1.60)$$

where we may expand the Lagrangian listed above:

$$\mathcal{L} = (\partial_\mu \phi)^\dagger (\partial^\mu \phi) - \mu^2 \phi^\dagger \phi - \lambda(\phi^\dagger \phi)^2. \quad (1.61)$$

It is an exercise in algebra to plug in the expansion about  $v$  into this Lagrangian: first expanding the potential

$$V(\phi) = \mu^2 \phi^\dagger \phi + \lambda(\phi^\dagger \phi)^2 \quad (1.62)$$

$$= \mu^2 \left( \sum_i \phi_i(x)^2 + (v + \eta(x))^2 \right) + \lambda \left( \sum_i \phi_i(x)^2 + (v + \eta(x))^2 \right) \quad (1.63)$$

$$= -\frac{1}{4} \lambda v^4 + \lambda v^2 \eta^2 + \lambda v \eta^3 + \frac{1}{4} \lambda \eta^4 \quad (1.64)$$

$$+ \frac{1}{2} \lambda \sum_{i \neq j} \phi_i^2 \phi_j^2 + \lambda v \eta \sum_i \phi_i(x)^2 + \frac{1}{2} \lambda \eta^2 \sum_i \phi_i(x)^2 + \frac{1}{4} \sum_i \phi_i(x)^4 \quad (1.65)$$

where the sums are over the  $i \in 1, 2, 4$ , that is, the fields with 0 vacuum expectation, and we have used the definition  $\mu^2 = -\lambda v^2$ .

Within this potential, we note a quadratic term in  $\eta(x)$  which we may identify with a mass, namely  $m_\eta = \sqrt{2\lambda v^2}$ , whereas the  $\phi_i$  are massless. These  $\phi_i$  are known as *Goldstone bosons*, and correspond to quantum fluctuations along the minimum of the potential. Of particular note for this thesis are the interaction terms  $\lambda v \eta^3$  and  $\frac{1}{4} \lambda \eta^4$ , expressing trilinear and quartic self-interactions of the  $\eta$  field.

Expanding the kinetic term

$$(\partial_\mu \phi)^\dagger (\partial^\mu \phi) = \frac{1}{2} \sum_i (\partial_\mu \phi_i)(\partial^\mu \phi_i) + \frac{1}{2} (\partial_\mu(v + \eta(x)))(\partial^\mu(v + \eta(x))) \quad (1.66)$$

$$= \frac{1}{2} \sum_i (\partial_\mu \phi_i)(\partial^\mu \phi_i) + \frac{1}{2} (\partial_\mu \eta)(\partial^\mu \eta) \quad (1.67)$$

<sup>814</sup> in a similar way, completing the story of three massless degrees of freedom (Goldstone bosons)  
<sup>815</sup> and one massive one.

Now, this doublet is embedded in an  $SU(2)_L \times U(1)$  theory, so we would like to preserve that gauge invariance. This is achieved in the same way as for the Dirac fields, with the introduction of the electroweak gauge covariant derivative such that the Lagrangian for the Higgs doublet and the electroweak bosons is just

$$\mathcal{L} = (D_\mu \phi)^\dagger (D^\mu \phi) - \mu^2 \phi^\dagger \phi - \lambda (\phi^\dagger \phi)^2 - \frac{1}{4} W_{\mu\nu}^k W_k^{\mu\nu} - \frac{1}{4} F_{\mu\nu} F^{\mu\nu} \quad (1.68)$$

<sup>816</sup> with  $D_\mu = \partial_\mu + ig_W W_\mu^k t^k + ig' \frac{Y}{2} B_\mu$ .

We note that it is convenient to pick a gauge such that the Goldstone fields do not appear in the Lagrangian, upon which we may identify the field  $\eta(x)$  with the physical Higgs field,  $h(x)$ . The field mass terms then very apparently come via the covariant derivative, namely, as

$$W_\mu^k \sigma^k + B_\mu = \begin{pmatrix} W_\mu^3 + B_\mu & W_\mu^1 - iW_\mu^2 \\ W_\mu^1 + iW_\mu^2 & -W_\mu^3 + B_\mu \end{pmatrix} \quad (1.69)$$

we may then write

$$D_\mu \phi = \frac{1}{2\sqrt{2}} \begin{pmatrix} 2\partial_\mu + ig_W W_\mu^3 + ig' Y B_\mu & ig_W W_\mu^1 + \frac{1}{2} g_W W_\mu^2 \\ ig_W W_\mu^1 - g_W W_\mu^2 & 2\partial_\mu - ig_W W_\mu^3 + ig' Y B_\mu \end{pmatrix} \begin{pmatrix} 0 \\ v + h \end{pmatrix} \quad (1.70)$$

$$= \frac{1}{2\sqrt{2}} \begin{pmatrix} ig_W (W_\mu^1 - iW_\mu^2)(v + h) \\ (2\partial_\mu - ig_W W_\mu^3 + ig' Y B_\mu)(v + h) \end{pmatrix} \quad (1.71)$$

<sup>817</sup> As identified above,  $Y = 2(Q - I_W^{(3)})$ . The Higgs has 0 electric charge, and the lower doublet  
<sup>818</sup> component has  $I_W^{(3)} = -\frac{1}{2}$ , yielding  $Y = 1$ .

Computing  $(D_\mu \phi)^\dagger (D^\mu \phi)$ , then, yields

$$\frac{1}{8} g_W^2 (W_\mu^1 + iW_\mu^2)(W^{\mu 1} - iW^{\mu 2})(v + h)^2 + \frac{1}{8} (2\partial_\mu + ig_W W_\mu^3 - ig' B_\mu)(2\partial^\mu - ig_W W^{\mu 3} + ig' B^\mu)(v + h)^2 \quad (1.72)$$

and extracting terms quadratic in the fields gives

$$\frac{1}{8} g_W^2 v^2 (W_{\mu 1} W^{\mu 1} + W_{\mu 2} W^{\mu 2}) + \frac{1}{8} v^2 (g_W W_\mu^3 - g' B_\mu)(g_W W^{\mu 3} - g' B^\mu) \quad (1.73)$$

meaning that  $W_\mu^1$  and  $W_\mu^2$  have masses  $m_W = \frac{1}{2}g_W v$ . The neutral boson case is a bit more complicated. Writing the corresponding term as

$$\frac{1}{8}v^2 \begin{pmatrix} W_\mu^3 & B_\mu \end{pmatrix} \begin{pmatrix} g_W^2 & -g_W g' \\ -g_W g' & g'^2 \end{pmatrix} \begin{pmatrix} W^{\mu 3} \\ B^\mu \end{pmatrix} \quad (1.74)$$

we note that we must diagonalize this mass matrix to get the physical mass eigenstates. Doing so in the usual way yields eigenvalues  $0$ ,  $g'^2 + g_W^2$ , thus corresponding to  $m_\gamma = 0$  and  $m_Z = \frac{1}{2}v\sqrt{g'^2 + g_W^2}$ , with physical fields as the (normalized) eigenvectors

$$A_\mu = \frac{g'W_\mu^3 + g_W B_\mu}{\sqrt{g_W^2 + g'^2}} \quad (1.75)$$

$$Z_\mu = \frac{g_W W_\mu^3 - g' B_\mu}{\sqrt{g_W^2 + g'^2}} \quad (1.76)$$

From this form, the angular parametrization of the physical fields is very apparent, namely, defining

$$\tan \theta_W = \frac{g'}{g_W}, \quad (1.77)$$

these equations may be written in terms of the single parameter  $\theta_W$  as

$$A_\mu = \cos \theta_W B_\mu + \sin \theta_W W_\mu^3 \quad (1.78)$$

$$Z_\mu = -\sin \theta_W B_\mu + \cos \theta_W W_\mu^3 \quad (1.79)$$

and, notably, from the above equations,

$$\frac{m_W}{m_Z} = \cos \theta_W. \quad (1.80)$$

To get the mass terms from Equation 1.72, we extracted those terms quadratic in fields, i.e., the  $v^2$  terms within  $(v + h)^2$ . However there are also terms of the form  $VVh$  and  $VVhh$  that arise, which describe the Higgs interactions with the corresponding vector bosons  $V = W^\pm, Z$ . Namely, identifying physical  $W$  bosons as

$$W^\pm = \frac{1}{\sqrt{2}}(W^1 \mp iW^2) \quad (1.81)$$

we may express the first term of Equation 1.72 as

$$\frac{1}{4}g_W^2 W_\mu^- W^{+\mu} (v + h)^2 = \frac{1}{4}g_W^2 v^2 W_\mu^- W^{+\mu} + \frac{1}{2}g_W^2 v W_\mu^- W^{+\mu} h + \frac{1}{4}g_W^2 W_\mu^- W^{+\mu} h^2 \quad (1.82)$$

with the first term corresponding to the mass term  $m_W = \frac{1}{2}g_W v$ , and the second two terms corresponding to  $hW^+W^-$  and  $hhW^+W^-$  vertices. Of particular note is the coupling strength

$$g_{HWW} = \frac{1}{2}g_W^2 v = g_W m_W \quad (1.83)$$

819 which is proportional to the  $W$  mass – an analysis with the form of the physical  $Z$  boson  
820 finds that the coupling  $g_{HZZ}$  is also proportional to the  $Z$  mass.

The Higgs coupling to fermions (in particular to quarks) is of particular interest for this thesis. We showed above that a naive introduction of a mass term

$$m\bar{f}f = m(\bar{f}_L f_R + \bar{f}_R f_L) \quad (1.84)$$

821 is manifestly not gauge invariant because right and left handed particles transform differently  
822 under  $SU(2)_L$ . However, because the Higgs is constructed via an  $SU(2)_L$  doublet,  $\phi$ , writing  
823 a fermion doublet as  $L$  and conjugate  $\bar{L}$ , it is apparent that  $\bar{L}\phi$  is invariant under  $SU(2)_L$ .

Combining with the right handed singlet,  $R$ , creates a term invariant under  $SU(2)_L \times U(1)_Y$ ,  $\bar{L}\phi R$  (and correspondingly  $(\bar{L}\phi R)^\dagger$ ), such that we may include Yukawa [16] terms

$$\mathcal{L}_{Yukawa} = -g_f \left[ \begin{pmatrix} \bar{f}_1 & \bar{f}_2 \end{pmatrix}_L \begin{pmatrix} \phi^+ \\ \phi^0 \end{pmatrix} f_R + \bar{f}_R \begin{pmatrix} \phi^{+*} & \phi^{0*} \end{pmatrix} \begin{pmatrix} f_1 \\ f_2 \end{pmatrix}_L \right] \quad (1.85)$$

824 where  $g_f$  is a corresponding Yukawa coupling,  $f_1$  and  $f_2$  have been used to denote components  
825 of the left-handed doublet and  $f_R$  the corresponding right-handed singlet.

After spontaneous symmetry breaking, with the gauge as described above to remove the Goldstone fields, the Higgs doublet becomes

$$\phi(x) = \begin{pmatrix} 0 \\ v + h(x) \end{pmatrix} \quad (1.86)$$

giving rise to terms such as

$$-\frac{1}{\sqrt{2}}g_f v(\bar{f}_{2L}\bar{f}_R + \bar{f}_R f_{2L}) - \frac{1}{\sqrt{2}}g_f h(\bar{f}_{2L}\bar{f}_R + \bar{f}_R f_{2L}) \quad (1.87)$$

where we have kept the subscript  $f_{2L}$  to emphasize that these terms *only* impact the lower component of the left-handed doublet because of the 0 in the upper component of the Higgs doublet. Leaving this aside for a second, we note that the first term has the form of the desired mass term above (identifying  $f_{2L}$  to  $f_L$ ) while the second term describes the coupling of the fermion to the physical Higgs field. The corresponding Yukawa coupling may be chosen to be consistent with the observed fermion mass, namely

$$g_f = \sqrt{2} \frac{m_f}{v} \quad (1.88)$$

such that

$$\mathcal{L}_f = -m_f \bar{f}f - \frac{m_f}{v} \bar{f}fh. \quad (1.89)$$

<sup>826</sup> Notably here, the fermion coupling to the Higgs boson scales with the mass of the fermion, a  
<sup>827</sup> fact that is extremely relevant for this thesis analysis.

As we said above, these terms *only* impact the lower component of the left-handed doublet. The inclusion of terms for the upper component is accomplished via the introduction of a Higgs conjugate doublet, defined as

$$\phi_c = -i\sigma_2\phi^* = \begin{pmatrix} -\phi^{0*} \\ \phi^- \end{pmatrix}. \quad (1.90)$$

<sup>828</sup> The argument proceeds similarly to the above, with similar results for couplings and masses  
<sup>829</sup> of upper components.

### <sup>830</sup> 1.7 The Standard Model: A Summary

After all of the above, we may write the Standard Model as a theory with a local  $SU(3) \times SU(2)_L \times U(1)_Y$  gauge symmetry, described by the Lagrangian

$$\mathcal{L} = \sum_f \bar{f}i\gamma^\mu D_\mu f - \frac{1}{4} \sum_{gauges} F_{\mu\nu}F^{\mu\nu} + (D_\mu\phi)^\dagger(D^\mu\phi) - \mu^2\phi^\dagger\phi - \lambda(\phi^\dagger\phi)^2 \quad (1.91)$$

where  $D_\mu = \partial_\mu + ig_W W_\mu^k t^k + ig' \frac{Y}{2} B_\mu + ig_S G_\mu^a t^a$ , in addition to the Yukawa terms, which we write generally as

$$\mathcal{L}_{Yukawa} = - \sum_{f,\phi=\phi,-\phi_c} y_f (\bar{f}\phi f + (\bar{f}\phi f)^\dagger) \quad (1.92)$$

831 with the sum running over running over appropriate chiral fermion and Higgs doublets.

832 The  $SU(2)_L \times U(1)_Y$  subgroup is spontaneously broken to a  $U(1)$  symmetry, lending mass  
833 to the associated gauge bosons and fermions. Of relevance for this thesis is the resulting  
834 physical Higgs field, with a predicted trilinear self-interaction and associated coupling  $\lambda v$ ,  
835 related to the experimentally observed Higgs boson mass by  $m_H = \sqrt{2\lambda v^2}$ , as well as the fact  
836 that the strength of the Higgs coupling to fermions scales proportionally with the fermion  
837 mass.

838 The Standard Model has been monumentally successful, with predictions consistent across  
839 many varied experimental cross-checks. This thesis participates in one such cross check.  
840 However, the Standard Model is notably not a complete theory of the universe – there is  
841 no inclusion of gravity, for instance, though a consistent description may be provided with  
842 the introduction of a spin-2 particle. Neutrino oscillations demonstrate that neutrinos have  
843 mass, but right-handed neutrinos have not been observed, leading to questions about whether  
844 there is a different mechanism to provide neutrinos with mass than that described above.  
845 Cosmology tells us that dark matter exists, but there is no corresponding particle within the  
846 Standard Model. This thesis therefore also participates in searches for physics beyond the  
847 Standard Model. We will provide a sketch of the relevant theories in the following chapter,  
848 though a detailed theoretical discussion is beyond the scope of this work.

849

## Chapter 2

850

### DI-HIGGS PHENOMENOLOGY AND PHYSICS BEYOND THE STANDARD MODEL

851

852 This thesis focuses on searches for di-Higgs production in the  $b\bar{b}b\bar{b}$  final state. In this  
 853 chapter, we will provide a brief overview of the practical theoretical information motivating  
 854 such searches. Though the searches test for physics beyond the Standard Model, particularly  
 855 in the search for resonances, the goal of the experimental results is to be somewhat agnostic  
 856 to particular theoretical frameworks. An in depth treatment of such models is therefore  
 857 beyond the scope of this thesis, though we will attempt to provide a grounding for the models  
 858 that we consider.

859 **2.1 Intro to Di-Higgs**

860 Di-Higgs searches can be split into two major theoretical categories: *resonant searches*, in  
 861 which a physical resonance is produced that subsequently decays into two Higgs bosons, and  
 862 a *non-resonant searches* in which no physical resonance is produced, but where the  $HH$   
 863 production cross section has a contribution from an exchange of a *virtual* or *off-shell* particle.

864 The focus of this thesis is gluon initiated processes – in the case of di-Higgs this is termed  
 865 gluon-gluon fusion (ggF).  $HH$  production may also occur via vector boson fusion [17]. However  
 866 the cross section for such production is significantly smaller. Representative Feynman diagrams  
 867 are shown for gluon-gluon fusion resonant production in Figure 2.1 and for non-resonant  
 868 production in Figure 2.2.

869 As shown in Chapter 1, the Higgs coupling to fermions scales with particle mass. As the  
 870 top quark has a mass of 173 GeV, whereas the  $H$  has a mass of 125 GeV, such that  $H \rightarrow t\bar{t}$  is  
 871 kinematically disfavored,  $H \rightarrow b\bar{b}$  is the dominant fermionic Higgs decay mode, and, in fact,

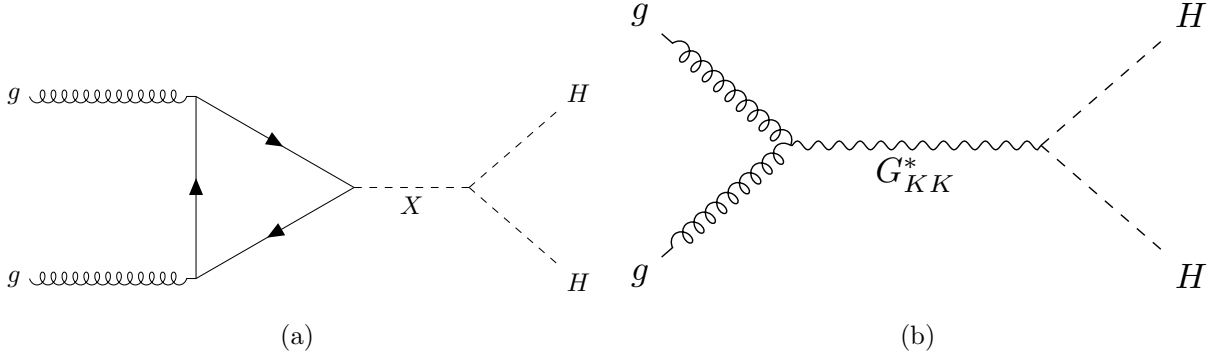


Figure 2.1: Representative diagrams for the gluon-gluon fusion production of spin-0 ( $X$ ) and spin-2 ( $G_{KK}^*$ ) resonances which decay to two Standard Model Higgs bosons. The spin-0 resonance considered for this thesis is a generic narrow width resonance which may be interpreted in the context of two Higgs doublet models [18], whereas the spin-2 resonance is considered as a Kaluza-Klein graviton within the bulk Randall-Sundrum (RS) model [19, 20].

the dominant overall decay mode, with a branching fraction of around 58 %. The dominant top quark Yukawa coupling to the  $H$  does play a role in  $H$  production, however – gluon-gluon fusion is dominated by processes including a top loop.

The single  $H$  properties translate to  $HH$  production, with  $HH \rightarrow b\bar{b}b\bar{b}$  accounting for around 34 % of all  $HH$  decays. The  $H$   $H$  branching fractions are shown in Figure 2.3.

## 2.2 Resonant $HH$ Searches

Resonant di-Higgs production is predicted in a variety of extensions to the Standard Model. In particular, this thesis presents searches for both spin-0 and spin-2 resonances. The decay of spin-1 resonances to two identical spin-0 bosons is prohibited, as the final state must correspondingly be symmetric under particle exchange, but this process would require orbital angular momentum  $\ell = 1$ , and thus an anti-symmetric final state. Each model considered here is implemented in a particular theoretical context, but set up experimental results for generic searches.

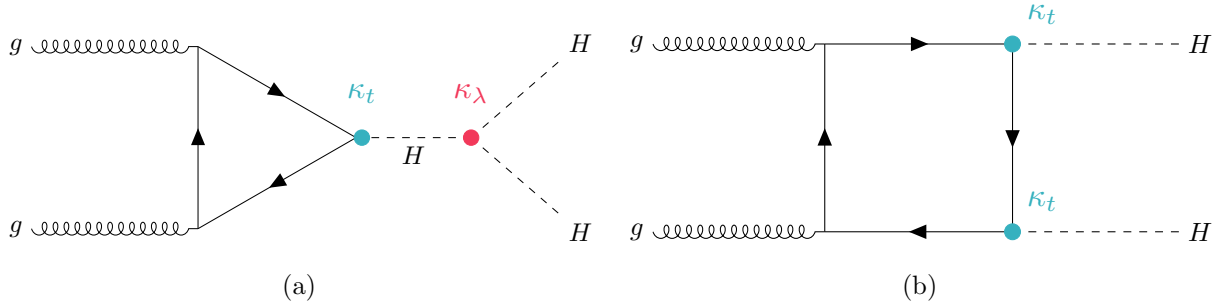


Figure 2.2: Dominant contributing diagrams for non-resonant gluon-gluon fusion production of  $HH$ .  $\kappa_\lambda$  and  $\kappa_t$  represent variations of the Higgs self-coupling and coupling to top quarks respectively, relative to that predicted by the Standard Model.

The spin-2 signal considered is implemented within the bulk Randall-Sundrum (RS) model [19, 20], which features spin-2 Kaluza-Klein gravitons,  $G_{KK}^*$ , that are produced via gluon-fusion and which may decay to a pair of Higgs bosons. The model predicts such gravitons as a consequence of warped extra dimensions, and is correspondingly parametrized by a value  $c = k/\overline{M}_{\text{Pl}} = 1$ , where  $k$  describes a curvature scale for the extra dimension and  $\overline{M}_{\text{Pl}}$  is the Planck mass. The model considered here has  $c = 1.0$ . However, this model was considered in the early Run 2  $HH$  analyses [21], and was excluded across much of the relevant mass range.

The primary theoretical focus of this work is therefore the spin-0 result, which is implemented as a generic resonance with width below detector resolution. Scalar resonances are interesting, for instance, in the context of two Higgs doublet models [18], which posit the existence of a second Higgs doublet. This leads to the existence of five scalar particles in the Higgs sector – roughly, two complex doublets provide eight degrees of freedom, three of which are “eaten” by the electroweak bosons, leaving five degrees of freedom which may correspond to physical fields.

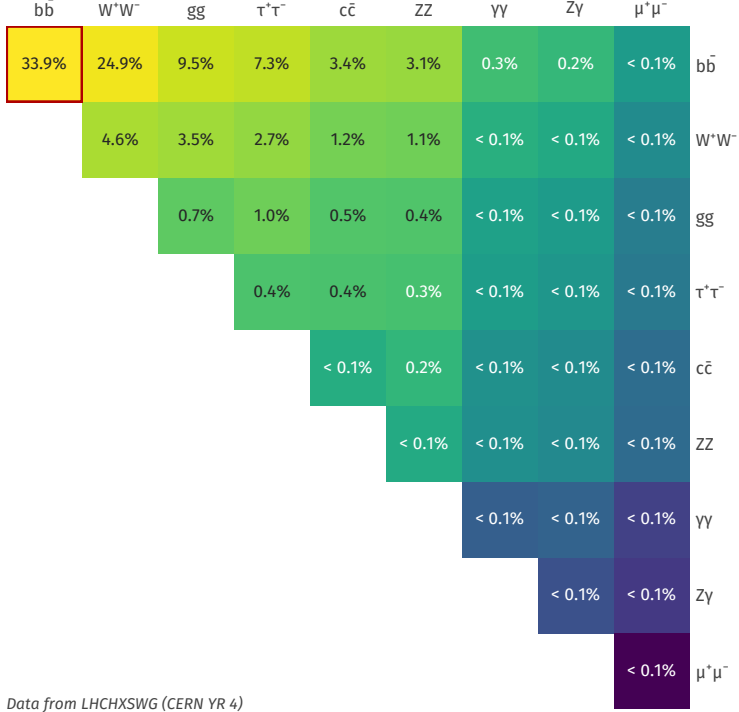


Figure 2.3: Illustration of dominant  $HH$  branching ratios.  $HH \rightarrow b\bar{b}b\bar{b}$  is the most common decay mode, representing 34 % of all  $HH$  events produced at the LHC.

### 900 2.3 Non-resonant $HH$ Searches

Non-resonant  $HH$  production is predicted by the Standard Model via the trilinear coupling discussed above, as well as via production in a fermion loop. More explicitly, after electroweak symmetry breaking, we have

$$\mathcal{L}_{SM} \supset -\lambda v^2 h^2 - \lambda v h^3 - \frac{1}{4} \lambda h^4 \quad (2.1)$$

$$= -\frac{1}{2} m_H^2 - \lambda_{HHH}^{SM} v h^3 - \lambda_{HHHH}^{SM} h^4 \quad (2.2)$$

where  $m_H = \sqrt{2\lambda v^2}$  so that

$$\lambda_{HHH}^{SM} = \frac{m_H^2}{2v^2}. \quad (2.3)$$

901 The mass of the SM Higgs boson has been experimentally measured to be 125 GeV [22],  
 902 and the vacuum expectation value  $v = 246$  GeV has a precise determination from the muon  
 903 lifetime [23]. This coupling is therefore precisely predicted in the Standard Model, such that  
 904 an observed deviation from this prediction would be a clear sign of new physics.

905 The relevant diagrams for non-resonant  $HH$  production are shown in Figure 2.2. Notably,  
 906 the diagrams *interfere* with each other, which can be easily seen by counting the fermion  
 907 lines. A detailed theoretical discussion is provided by, e.g. [24].

908 For the searches presented here, the quark couplings to the Higgs are considered to be  
 909 consistent with the Standard Model value, with measurements of the dominant top Yukawa  
 910 coupling left to more sensitive direct measurements, e.g. from  $t\bar{t}$  final states [25]. Variations of  
 911 the trilinear coupling away from the Standard Model are considered, however. Such variations  
 912 are parametrized via

$$\kappa_\lambda = \frac{\lambda_{HHH}}{\lambda_{HHH}^{SM}} \quad (2.4)$$

913 where  $\lambda_{HHH}$  is a varied coupling and  $\lambda_{HHH}^{SM}$  is the Standard Model prediction. As this  
 914 variation only comes as a prefactor only with the *triangle* diagram, significant and interesting  
 915 effects are observed due to the interference. Examples of the impact of this tradeoff on the  
 916 di-Higgs invariant mass are shown in Figure 2.4. Generally speaking, the triangle diagram  
 917 contributes more at low mass, while the box diagram contributes more at high mass.

From a quick analysis of Figure 2.2, one may see that, at leading order, the box diagram,  $B$  has amplitude proportional to  $\kappa_t^2$ , defined as the ratio of the top Yukawa coupling to the value predicted by the Standard Model, whereas the triangle diagram,  $T$  has amplitude proportional to  $\kappa_t \kappa_\lambda$ . Therefore, the cross section is proportional to

$$\sigma(\kappa_t, \kappa_\lambda) = |A(\kappa_t, \kappa_\lambda)|^2 \quad (2.5)$$

$$\sim |\kappa_t^2 B + \kappa_t \kappa_\lambda T|^2 \quad (2.6)$$

$$= \kappa_t^4 |B|^2 + \kappa_t^3 \kappa_\lambda (BT + TB) + \kappa_t^2 \kappa_\lambda^2 |T|^2, \quad (2.7)$$

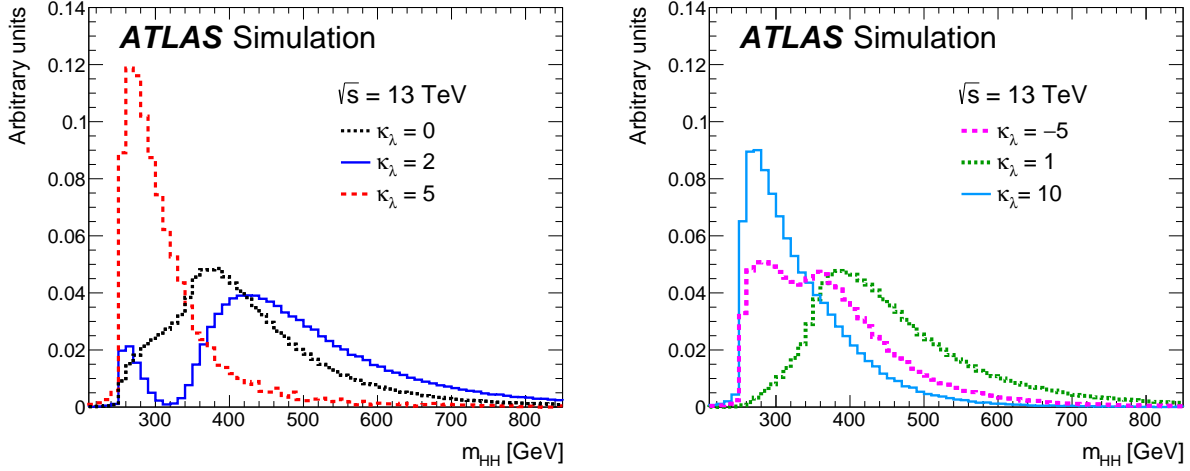


Figure 2.4: Monte Carlo generator level  $m_{HH}$  distributions for various values of  $\kappa_\lambda$ , demonstrating the impact of the interference between the two diagrams of Figure 2.2 on the resulting  $m_{HH}$  distribution. For  $\kappa_\lambda = 0$  there is no triangle diagram contribution, demonstrating the shape of the box diagram contribution, whereas for  $\kappa_\lambda = 10$ , the triangle diagram dominates, with a strong low mass peak. The interplay between the two is quite evident for other values, resulting in, e.g., the double peaked structure present for  $\kappa_\lambda = 2$  (near maximal destructive interference) and  $\kappa_\lambda = -5$ . [21]

and thus non-resonant  $HH$  production cross section may be parametrized as a second order polynomial in  $\kappa_\lambda$ .

For positive values of  $\kappa_\lambda$ , due to the relative minus sign between the triangle and box diagrams, the interference between the two diagrams is *destructive*, with a maximum interference near  $\kappa_\lambda = 2.3$ , corresponding to the minimum cross section prediction. One may note that the Standard Model value of  $\kappa_\lambda = 1$  is not far away from this minimum – correspondingly the Standard Model cross section for  $HH$  production is quite small, namely 31.05 fb at  $\sqrt{s} = 13 \text{ TeV}$  for production via gluon-gluon fusion [26–33] compared to, e.g. single Higgs production, with a gluon-gluon fusion production cross section of 46.86 pb at

927  $\sqrt{s} = 13 \text{ TeV}$  [34] roughly 1500 times larger! For negative values of  $\kappa_\lambda$ , the interference is  
928 constructive.

929 ATLAS projections [35] of  $b\bar{b}b\bar{b}$ ,  $b\bar{b}\gamma\gamma$ , and  $b\bar{b}\tau^+\tau^-$  predict an expected signal strength  
930 for Standard Model  $HH$  of  $3.5\sigma$  with no systematic uncertainties and  $3.0\sigma$  with systematic  
931 uncertainties using the  $3000 \text{ fb}^{-1}$  of data from the HL-LHC (around  $20\times$  the full Run 2  
932 dataset considered in this thesis), constituting an *observation* of  $HH$ . As the cross section  
933 for Standard Model  $HHH$  production, corresponding to the quartic Higgs interaction, is  
934 much smaller (around  $0.1 \text{ fb}$  at  $\sqrt{s} = 14 \text{ TeV}$  [36]), observation of triple Higgs production is  
935 even farther in the future, and so is not considered here. However this may be interesting for  
936 future work in a variety of Beyond the Standard Model scenarios (e.g. [37–39]).

937

## Chapter 3

938

### EXPERIMENTAL APPARATUS

939     What machines must we build to examine the smallest pieces of the universe? The famous  
 940     equation  $E = m$  provides that to create massive particles, we need to provide enough energy.  
 941     In order to give kinematic phase space to the types of processes that are examined in this  
 942     thesis (and many others besides), a system must be created in which there is enough energy  
 943     to (at bare minimum), overcome kinematic thresholds: if you want to search for  $HH$  decays,  
 944     you should have at least 250 GeV ( $= 2 \times m_H$ ) to work with. It is not enough to simply induce  
 945     such processes, however. These processes need to be captured in some way, emitted energy  
 946     and particles must be characterized and identified, and in the end all of this information must  
 947     be put into a useful and useable form such that selections can be made, statistics can be run,  
 948     and a meaningful statement can be made about the universe. In this chapter, we describe the  
 949     machines behind the physics, namely the Large Hadron Collider and the ATLAS experiment.

950     **3.1 The Large Hadron Collider**

951     The Large Hadron Collider is a particle accelerator near Geneva, Switzerland. In broad scope,  
 952     it is a ring with a 27 kilometer circumference. Hadrons (usually protons or heavy ions) move  
 953     in two counter-circulating beams, which are made to collide at four collision points at various  
 954     points on the ring. These four collision points correspond to the four detectors placed around  
 955     the ring: two “general purpose” experiments: ATLAS and CMS; LHCb, focused primarily on  
 956     flavor physics; and ALICE, focused primarily on heavy ions.

957     The focus of this thesis is proton-proton collisions at center of mass energy  $\sqrt{s} = 13$  TeV.  
 958     The process to achieve such collisions proceeds as follows: first, an electric field strips hydrogen  
 959     of its electrons, creating protons. A linear accelerator, LINAC 2, accelerates protons to

960 50 MeV. The resulting beam is injected into the Proton Synchrotron Booster (PSB), which  
 961 pushes the protons to 1.4 GeV, and then the Proton Synchrotron, which brings the beam to  
 962 25 GeV.

963 Protons are then transferred to the Super Proton Synchrotron (SPS), which ramps up  
 964 the energy to 450 GeV. Finally, the protons enter the LHC itself, bringing the beam up to  
 965 6.5 TeV [40].

966 While there is, of course, much that goes into the Large Hadron Collider development and  
 967 operation, perhaps two of the most fundamental ideas are (1) how are the beams directed  
 968 and manipulated and (2) what do we mean when we say “protons are accelerated”. These  
 969 questions both are directly answered by pieces of hardware, namely (1) magnets and (2)  
 970 radiofrequency (RF) cavities.

971 One of fundamental components of the LHC is a large set of superconducting niobium-  
 972 titanium magnets. These are cooled by liquid helium to achieve superconducting temperatures,  
 973 and there are several types with very specific purposes. The obvious first question with a  
 974 circular accelerator is how to keep the particle beam moving around in that circle. This job  
 975 is done via a set of dipole magnets placed around the *beam pipes*: the tubes containing the  
 976 beam. These are designed such that the magnetic field in the center of the beam pipe runs  
 977 perpendicular to the velocity of the charged particles, providing the necessary centripetal  
 978 force for the synchrotron motion.

979 A proton beam is not made of a single proton, however, but of many protons, grouped  
 980 into a series of *bunches*. As all of these are positively charged, if unchecked, these bunches  
 981 would become diffuse and break apart. What we want is a stable beam with tightly clustered  
 982 protons to maximize the chance of a high energy collision. Such clustering is done via a series  
 983 of quadropole magnets, with field distributed as in *TODO: grab image from General Exam.*  
 984 Alternating sets of quadropoles provide the necessary forces for a tight, stable beam. While  
 985 these are the two major components of the LHC magnet system, it is not the full story –  
 986 higher order magnets are used to correct for small imperfections in the beam.

987 Magnetic fields do no work, however, so the magnet system is unable to do the job of the

actual acceleration. This is accomplished via a set of radiofrequency (RF) cavities. Within these cavities, an electric field is made to oscillate (switch direction) at a precise rate. These rates interact with the beam via in RF *buckets*, with bunches corresponding to groups of protons that fill a given bucket. The timing is such that protons will always experience an accelerating voltage, corresponding to the 25 ns bunch spacing used at the LHC.

A nice property of this bucket/bunch configuration is that there is some self-correction – there is some finite spread in the grouping of particles. If a particle arrives too early, it will experience some decelerating voltage; if too late, it will experience a higher accelerating voltage.

### 3.1.1 The LHC Schedule

The physics program at the Large Hadron Collider is split into a variety of data taking periods called *runs*. These runs correspond to various detector/accelerator configurations, and are interspersed with *long shutdowns* – periods used for detector/accelerator upgrades in preparation for the next run. The LHC timeline is as follows

1. Run 1 (2010–2013): First run of the LHC, operating at center of mass energy  $\sqrt{s} = 7 \text{ TeV}$ , increased to  $8 \text{ TeV}$  in 2012. ATLAS recorded  $4.57 \text{ fb}^{-1}$  and  $20.3 \text{ fb}^{-1}$  of data usable for physics at  $\sqrt{s} = 7 \text{ TeV}$  and  $8 \text{ TeV}$  respectively.
2. Long Shutdown 1 (LS1; 2013–2015): Upgrades to accelerator complex, magnet system, to allow for increase in energy. Design energy was  $\sqrt{s} = 14 \text{ TeV}$ , delays in “training” of superconducting magnets led to decrease to  $\sqrt{s} = 13 \text{ TeV}$ .
3. Run 2 (2015–2018): Second run of the LHC, operating at center of mass energy  $\sqrt{s} = 13 \text{ TeV}$ . Data from this run is used in this thesis, with  $139 \text{ fb}^{-1}$  of data available for physics from the ATLAS experiment.
4. Long Shutdown 2 (LS2; 2019–2021): Upgrades to ATLAS muon spectrometer (New

1012 Small Wheel), liquid argon calorimeter; upgrades in preparation for the High Luminosity  
1013 LHC (HL-LHC).

1014 5. Run 3 (2021–2023?): Third run of the LHC, target center of mass energy  $\sqrt{s} =$   
1015  $13 - 14 \text{ TeV}$ , total target luminosity  $300 \text{ fb}^{-1}$ .

1016 6. Long Shutdown 3 (LS3; 2024?–2026?): Further upgrades for the HL-LHC.

1017 7. Run 4, 5, ... (2026? onward): High Luminosity LHC – goal is to achieve instantaneous  
1018 luminosities by a factor of five, massively enlarging available statistics for physics.  
1019 Projected 3000 to  $4000 \text{ fb}^{-1}$ ,  $> 20$  times the full Run 2 ATLAS dataset.

### 1020 3.2 The ATLAS Experiment

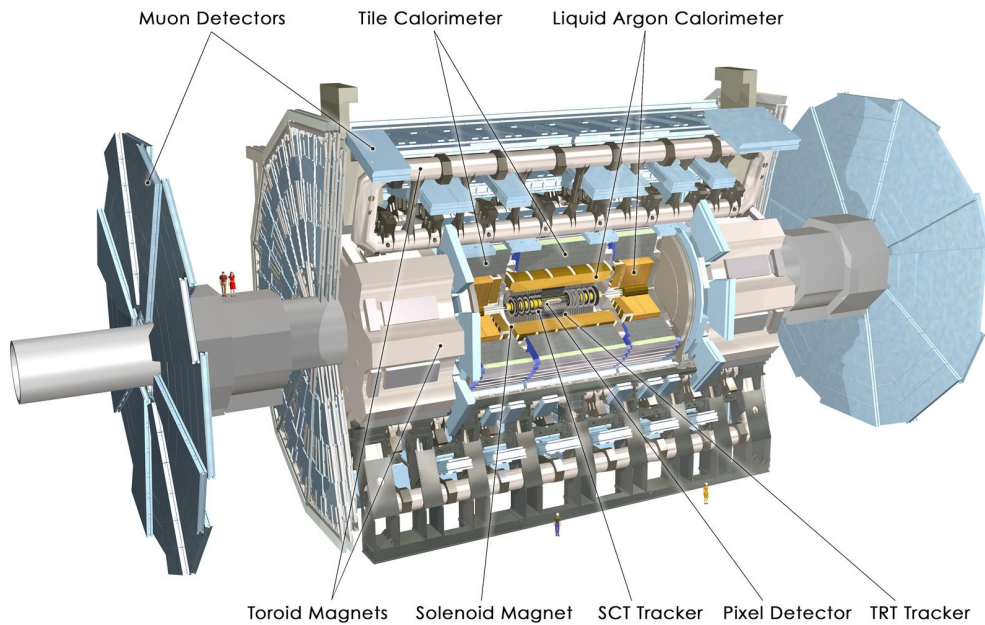


Figure 3.1: Diagram of the ATLAS detector [41]

1021 This thesis focuses on searches done with the ATLAS experiment. As mentioned, this is one

of two “general purpose” experiments at the LHC, by which we mean there is a very large and broad variety of physics done within the experimental collaboration. This broad physics focus has a direct relation to the design of the ATLAS detector [42], pictured in Figure 3.1, which is composed of a sophisticated set of subsystems designed to fully characterize the physics of a given high energy particle collision. It consists of an inner tracking detector surrounded by a thin superconducting solenoid, electromagnetic and hadronic calorimeters, and a muon spectrometer incorporating three large superconducting toroidal magnets. The ATLAS detector covers nearly the entire solid angle around the collision point, fully characterizing the “visible” components of a collision and allowing for indirect sensitivity to particles that do not interact with the detector (e.g. neutrinos) via “missing” energy (roughly momentum balance). We will go through the design and physics contribution of each of the detector components in the following. A schematic of how various particles interact with the detector is shown in Figure 3.2.

### 3.2.1 ATLAS Coordinate System

Of relevance for the following discussion, as well as for the analysis presented in Chapter 7, is the ATLAS coordinate system. ATLAS uses a right-handed coordinate system with its origin at the nominal interaction point (IP) in the center of the detector and the  $z$ -axis along the beam pipe. The  $x$ -axis points from the IP to the centre of the LHC ring, and the  $y$ -axis points upwards. Cylindrical coordinates  $(r, \phi)$  are used in the transverse plane,  $\phi$  being the azimuthal angle around the  $z$ -axis. The pseudorapidity is defined in terms of the polar angle  $\theta$  as  $\eta = -\ln \tan(\theta/2)$ . Angular distance is measured in units of  $\Delta R \equiv \sqrt{(\Delta\eta)^2 + (\Delta\phi)^2}$ . These coordinates are shown in Figure 3.3.

### 3.2.2 Inner Detector

The purpose of the inner detector is the reconstruction of the trajectory of charged particles, called *tracking*. This is accomplished primarily through the collection of electrons displaced when a charged particle passes through a tracking detector. By setting up multiple layers of

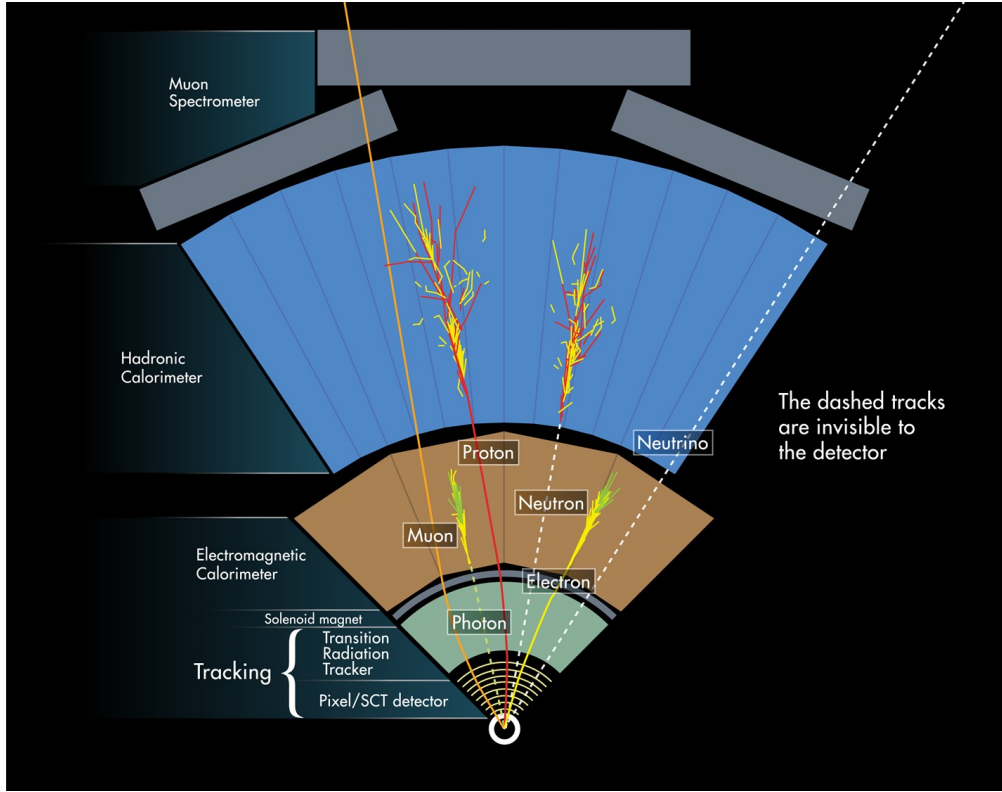


Figure 3.2: Cross section of the ATLAS detector showing how particles interact with various detector components [43]

1048 such detectors, such that a given particle leaves a signature, known as a “hit”, in each layer,  
 1049 the trajectory of the particle may be inferred via “connecting the dots” between these hits.

1050 The raw trajectory of a particle only provides positional information. However, the  
 1051 trajectory of a charged particle in a known magnetic field additionally provides information on  
 1052 particle momentum and charge via the curvature of the corresponding track (cf.  $\vec{F} = q\vec{v} \times \vec{B}$ ).  
 1053 The inner detector system is therefore surrounded by a solenoid magnet, providing a 2 T  
 1054 magnetic field along the  $z$ -axis (yielding curvature in the transverse  $x - y$  plane).

1055 The inner detector provides charged particle tracking in the range  $|\eta| < 2.5$  via a series of  
 1056 detector layers. The innermost of these is the high-granularity silicon pixel detector which  
 1057 typically provides four measurements per track, with the first hit in the insertable B-layer

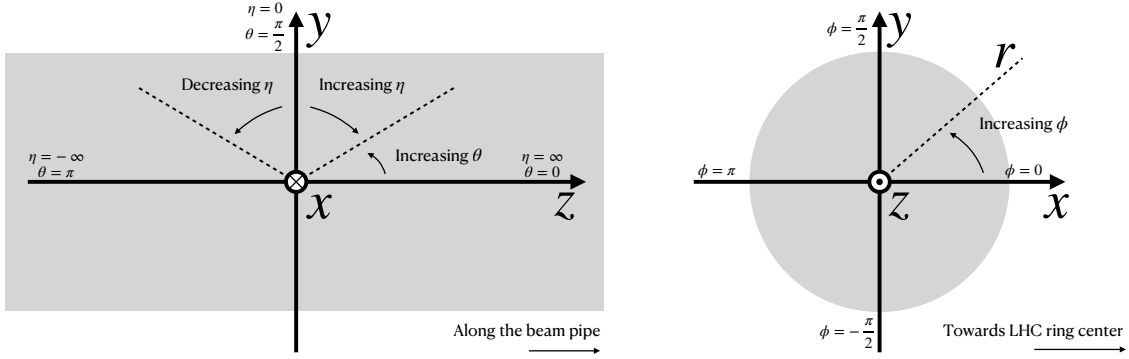


Figure 3.3: 2D projections of the ATLAS coordinate system

1058 (IBL) installed before Run 2 [44, 45]. This is very close to the interaction point with a  
 1059 high degree of positional information, and is therefore very important for e.g.  $b$ -tagging (see  
 1060 Chapter 5). It is followed by the silicon microstrip tracker (SCT), which usually provides  
 1061 eight measurements per track. This is lower granularity, but similar in concept to the pixel  
 1062 detector.

1063 Both of these silicon detectors are complemented by the transition radiation tracker  
 1064 (TRT), which extends the radial track reconstruction within the range  $|\eta| < 2.0$ . This is  
 1065 a different design, composed of *drift tubes*, i.e. straws filled with Xenon gas with a wire  
 1066 in the center, but similarly collects electrons displaced by ionizing particles. In addition,  
 1067 the TRT includes materials with widely varying indices of refraction, which leads to the  
 1068 production of transition radiation, namely radiation produced by a charged particle passing  
 1069 through an inhomogeneous medium. The energy loss on such a transition is proportional  
 1070 to the Lorentz factor  $\gamma = E/m$  – correspondingly, lighter particles (e.g. electrons) tend to  
 1071 lose more energy and emit more photons compared to heavier particles (e.g. pions). In the  
 1072 detector, this corresponds to a larger fraction of hits (typically 30 in total) above a given

1073 high energy-deposit threshold for electrons, providing particle identification information.

1074 *3.2.3 Calorimeter*

1075 Surrounding the inner detector in ATLAS is the calorimeter. The principle of the calorimeter  
1076 is to completely absorb the energy of a produced particle in order to measure it. However,  
1077 a pure block of absorber does not provide much information about the particle interaction  
1078 with the material. The ATLAS calorimeter therefore has a *sampling calorimeter* structure,  
1079 namely, layers of absorber interspersed with layers of sensitive material, giving the calorimeter  
1080 “stopping power” while allowing detailed measurement of the resulting particle shower and  
1081 corresponding deposited energy.

1082 The ATLAS calorimetersystem covers the pseudorapidity range  $|\eta| < 4.9$ , and is primarily  
1083 composed of two components, an electromagnetic calorimeter, designed to measure particles  
1084 which primarily interact via electromagnetism (e.g. photons and electrons), and a hadronic  
1085 calorimeter, designed to measure particles which interact via the strong force (e.g. pions,  
1086 other hadrons). We will return to the differences between these in a moment.

1087 In ATLAS, the electromagnetic calorimeter covers the region of  $|\eta| < 3.2$ , and uses  
1088 lead for the absorbers and liquid-argon for the sensitive material. It is high granularity  
1089 and, geometrically, has two components: the “barrel”, which covers the cylindrical body of  
1090 the detector volume and the “endcap”, covering the ends. An additional thin liquid-argon  
1091 presampler covers  $|\eta| < 1.8$  to correct for energy loss in material upstream of the calorimeters.

1092 The hadronic calorimeter is composed of alternating steel and plastic scintillator tiles,  
1093 segmented into three barrel structures within  $|\eta| < 1.7$ , in addition to two copper/liquid-argon  
1094 endcap calorimeters.

1095 The solid angle coverage is completed with forward copper/liquid-argon and tungsten/liquid-  
1096 argon calorimeter modules optimized for electromagnetic and hadronic energy measurements  
1097 respectively.

1098    3.2.4    *Muon Spectrometer*

1099    While muons interact electromagnetically, they are around 200 times heavier than electrons  
 1100    ( $m_\mu = 106 \text{ MeV}$ , while  $m_e = 0.510 \text{ MeV}$ ). Therefore, electromagnetic interactions with ab-  
 1101    sorbers in the calorimeter are not sufficient to stop them, and, as they do not interact via the  
 1102    strong force, hard scattering with nuclei is rare. A dedicated system for muon measurements  
 1103    is therefore required.

1104    The muon spectrometer (MS) is the outermost layer of ATLAS and is designed for this  
 1105    purpose. It is composed of three parts: a set of triggering chambers, which detect if there is  
 1106    a muon and provide a coordinate measurement, in conjunction with high-precision tracking  
 1107    chambers, which measure the deflection of muons in a magnetic field to measure muon  
 1108    momentum, similar to the inner detector solenoid. The magnetic field is generated by the  
 1109    superconducting air-core toroidal magnets, with a field integral between 2.0 and 6.0 T m  
 1110    across most of the detector. The toroid magnetic field runs roughly in a circle in the  $x - y$   
 1111    plane around the beam line, leading to muon curvature along the z-axis.

1112    The precision tracking system covers the region  $|\eta| < 2.7$  via three layers of monitored  
 1113    drift tubes, and is complemented by cathode-strip chambers in the forward region, where the  
 1114    background is highest. The muon trigger system covers the range  $|\eta| < 2.4$  with resistive-plate  
 1115    chambers in the barrel, and thin-gap chambers in the endcap regions.

1116    3.2.5    *Triggering*

1117    During a typical run of the LHC, there are roughly 1 billion collisions in ATLAS per second  
 1118    (1 GHz), corresponding to a 40 MHz bunch crossing rate [46]. Saving the information from  
 1119    all of them is not only unnecessary, but infeasible. The ATLAS trigger system provides a  
 1120    sophisticated set of selections to filter the collision data and only keep those collision events  
 1121    useful for downstream analysis.

1122    These events are selected by the first-level trigger system, which is implemented in custom  
 1123    hardware, and accepts events at a rate below 100 kHz. Selections are then made by algorithms

1124 implemented in software in the high-level trigger [47], reducing this further, and, in the end,  
1125 events are recorded to disk at much more manageable rate of about 1 kHz.

1126 An extensive set of ATLAS software [48] is open source, including the software used for  
1127 real and simulated data reconstruction and analysis and that used in the trigger and data  
1128 acquisition systems of the experiment.

### 1129 3.2.6 Particle Showers and the Calorimeter

1130 The design of the ATLAS detector is directly tied to the physics it is trying to detect. Of these,  
1131 possibly the most non-trivial distinction is in the calorimeter design. It is therefore useful to  
1132 discuss in more detail the various properties of electromagnetic and hadronic interactions  
1133 with material, and how these correspond to the particle showers measured by the detector  
1134 described above.

1135 Electromagnetic showers in ATLAS predominantly occur via bremsstrahlung, or “braking  
1136 radiation”, and electron-positron pair production. This proceeds roughly as follows: an electron  
1137 entering a material is deflected by the electromagnetic field of a heavy nucleus. This results in  
1138 the radiation of a photon. That photon produces an electron-positron pair, and the process  
1139 repeats, resulting in a shower structure. At each step, characterized by *radiation length*,  $X_0$ ,  
1140 the number of particles approximately doubles and the average particle energy decreases by  
1141 approximately a factor of two. *TODO: Include nice Thomson image*

Note that bremsstrahlung and pair production only dominate in specific energy regimes, with other processes taking over depending on particle energy. For electrons, bremsstrahlung only dominates for higher energies, as low energy electrons will form ions with the atoms of the material. The point where the rates for the two processes are equal is called the *critical energy*, and is roughly

$$E_c \approx \frac{800 \text{ MeV}}{Z} \quad (3.1)$$

1142 where  $Z$  is the nuclear charge. From a similar analysis of rates, we may see that the  
1143 bremsstrahlung rate is inversely proportional to the square of the mass of the particle. This

<sub>1144</sub> explains why muons do not shower in a similar way, as the rate of bremsstrahlung is suppressed  
<sub>1145</sub> by  $(m_e/m_\mu)^2$  relative to electrons.

For lead, the absorber used for the ATLAS electromagnetic calorimeter, which has  $Z = 82$ , this critical energy is therefore around 10 MeV. Electrons resulting from LHC collisions are of a  $1.3 \times 10^3$  GeV scale. With the approximation of a reduction in particle energy by a factor of two every radiation length, the number of radiation lengths before the critical energy is reached is

$$x = \frac{\ln(E/E_c)}{\ln 2} \quad (3.2)$$

<sub>1146</sub> such that for a 100 GeV shower in lead,  $x \sim 13$ . The radiation length for lead is around  
<sub>1147</sub> 0.56 cm, such that an electromagnetic shower could be expected to be captured within 10 cm  
<sub>1148</sub> of lead.

<sub>1149</sub> Electromagnetic showers are therefore characterized by depositing much of their energy  
<sub>1150</sub> within a small region of space. As we show below (Chapter 4) though electromagnetic  
<sub>1151</sub> showering is not deterministic, the large number of particles and the restricted set of processes  
<sub>1152</sub> involved means that the shower development as a whole is very similar between individual  
<sub>1153</sub> electromagnetic showers of the same energy.

<sub>1154</sub> For completeness, note as well that pair production dominates for photons of energy greater  
<sub>1155</sub> than around 10 MeV, whereas for lower energies (below around 1 MeV), the photoelectric  
<sub>1156</sub> effect, namely atomic photon absorption and electron emission, dominates.

<sub>1157</sub> Hadronic showers are distinguished by the fact that they interact strongly with atomic  
<sub>1158</sub> nuclei. They are correspondingly more complex because (1) they involve a wider variety  
<sub>1159</sub> of processes than electromagnetic showers, and (2) these processes have a wide variety of  
<sub>1160</sub> associated length scales. Because these are heavier than electrons (e.g. protons and charged  
<sub>1161</sub> pions) bremsstrahlung is suppressed, but ionization interactions with the electrons will cause  
<sub>1162</sub> these particles to lose energy as they pass through the material. Hadronic showering occurs  
<sub>1163</sub> on interaction with atomic nuclei. This may lead to production of, e.g. both charged ( $\pi^\pm$ )  
<sub>1164</sub> and neutral ( $\pi^0$ ) pions. The  $\pi^0$  lifetime is much much shorter than that of the charged pions  
<sub>1165</sub> (around a factor of  $10^8$ ), and immediately decays to two photons, starting an electromagnetic

<sub>1166</sub> shower, as described above. The longer lived  $\pi^\pm$  travel further in the detector before  
<sub>1167</sub> experiencing another strong interaction with more particles produced, also with varying  
<sub>1168</sub> lifetimes and decay properties.

<sub>1169</sub> It is therefore immediately apparent that hadronic showers are more complex than  
<sub>1170</sub> electromagnetic ones (electromagnetic showers can be a subset of the hadronic!), and therefore  
<sub>1171</sub> much more variable from shower to shower. The length scales involved are also significantly  
<sub>1172</sub> larger due to the reliance on nuclear interactions, characterized by length  $\lambda_I$ , which is around  
<sub>1173</sub> 17 cm for iron (used in the ATLAS hadronic calorimeter). This motivates the calorimeter  
<sub>1174</sub> design, and results in the properties demonstrated in Figure 3.2.

1175

## Chapter 4

1176

# SIMULATION

1177 Simulated physics samples are a core piece of the physics output of the Large Hadron  
 1178 Collider, providing a map from a physics theory into what is observed in our detector. This  
 1179 is crucial for searches for new physics, where simulation is necessary to describe what a given  
 1180 signal model looks like, but also extremely valuable for describing the physics of the Standard  
 1181 Model, providing detailed predictions of background processes for use in everything from  
 1182 designing simple cuts to training multivariate discriminators. Broadly, simulation can be split  
 1183 into two stages: *event generation*, in which physics theory is used to generate a description of  
 1184 particles present after a proton-proton collision, and *detector simulation*, which passes this  
 1185 particle description through a simulation of the detector material, providing a view of the  
 1186 physics event as it would be seen in ATLAS data. Such simulation is often called Monte Carlo  
 1187 in reference to the underlying mathematical framework, which relies on random sampling.

1188 **4.1 Event Generation**

1189 A variety of tools are used to simulate various aspects of event generation. One such aspect  
 1190 is generation of the “hard scatter” event, i.e., two protons collide and some desired physics  
 1191 process happens. In practice, this is not quite as simple as two quarks or gluons interacting.  
 1192 Protons are composed of three “valence” quarks with various momenta interacting with each  
 1193 other via exchange of gluons, but also a sea of virtual gluons which may decay into other  
 1194 quarks. A hard scatter event is therefore characterized by the corresponding particle level  
 1195 diagrams, but additionally by a set of *parton distribution functions* (PDFs), which describe  
 1196 the probability to find constituent quarks or gluons at carrying various momenta at a given  
 1197 energy scale (often written  $Q^2$ ). Such PDFs are measured experimentally *TODO: cite* and

the selection of a “PDF set” and a given physics process characterizes the hard scatter. Depending on the model being considered and the particular theoretical constraints, processes are often simulated at either leading (LO) or next to leading order (NLO), corresponding to the order of the perturbative expansion (i.e. tree level or 1 loop diagrams). Various additional tools are developed for such NLO calculations, including POWHEG Box v2 [49–51], which is used for this thesis. MADGRAPH [52] is used in this thesis for leading order simulation.

The hard scatter is not the only component of a given collider event, however. Incoming and outgoing particles are themselves very energetic and may radiate particles along their trajectory. In particular, gluons, which have a self-interaction term as described in Chapter 1, may be radiated, which subsequently themselves radiate gluons or decay to quarks which can also radiate gluons, in a whole mess of QCD that both contributes to the particle content of a collider event and is not directly described by the hard scatter. This cascade, called a *parton shower*, has a dedicated set of simulation tools. For this thesis, HERWIG 7 [53][54] and PYTHIA 8 [55] are used, which interface with tools such as MADGRAPH for simulation.

Due to color confinement (Chapter 1), quarks and gluons cannot be observed free particles, but rather undergo a process called hadronization, in which they are grouped into colorless hadrons (e.g. *mesons*, consisting of one quark and one antiquark). In simulation, this is also handled with tools such as HERWIG 7 or PYTHIA 8.

The physics of  $b$ -quarks is quite important for a variety of searches for new physics and measurements of the Standard Model, including this thesis work. Correspondingly, the decay of “heavy flavor” particles (e.g.  $B$  and  $D$  mesons, containing  $b$  and  $c$  quarks respectively) has been very well studied, and a dedicated simulation tool, EVTGEN [56], is used for such processes.

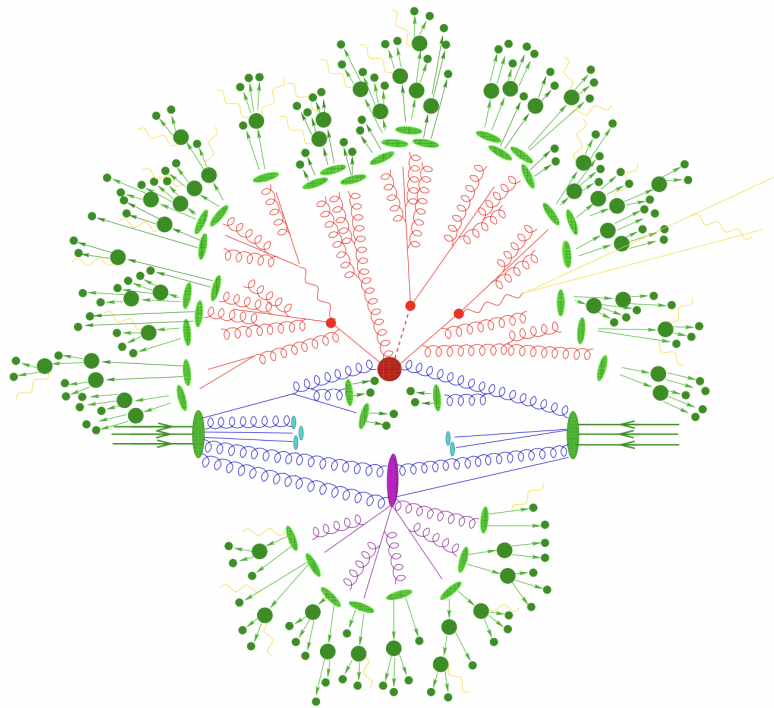


Figure 4.1: Schematic diagram of the Monte Carlo simulation of a hadron-hadron collision. The incoming hadrons are the green blobs with the arrows on the left and right, with the red blob in the center representing the hard scatter event, and the purple representing a secondary hard scatter. Radiation from both incoming and outgoing particles is shown, and the light green blobs represent hadronization, with the outermost dark green circles corresponding to the final state hadrons. Yellow lines are radiated photons. [57]

1221 **4.2 Detector Simulation**

1222 Event generation provides a full and exact description of the particle content of a given  
1223 collider event. This description is useful, but is an artifact of the simulation – for real physics  
1224 events, we must rely on the information collected by sophisticated detectors (Chapter 3) to  
1225 make statements about the physics content of collider events. The simulation of how particles  
1226 interact with the physical detector and of the corresponding information that is collected is  
1227 therefore a necessary step of physics simulation at the LHC. The design and components of  
1228 the ATLAS detector are described in Chapter 3. Simulation of this detector quickly becomes  
1229 complicated – there are a variety of different materials and subdetectors, each with particular  
1230 configurations and resolutions. Interactions of particles with the detector materials can cause  
1231 showering, and such showers must be simulated and characterized.

1232 In ATLAS, the GEANT4 [58] simulation toolkit is used for detailed simulation of the  
1233 ATLAS detector, often referred to as *full simulation*. The method can be thought of as  
1234 proceeding step by step as a particle moves through the detector, simulating the interaction  
1235 of the material at each stage, and following each branch of each resulting shower with a  
1236 similarly detailed step by step simulation.

1237 This type of simulation is very computationally intensive, especially in the calorimeter,  
1238 which has a high density of material, leading to an extremely large set of material interactions  
1239 to simulate. There is correspondingly a large effort within ATLAS to develop techniques to  
1240 decrease the computational load – these techniques will be of increasing importance for Run  
1241 3 and the HL-LHC, which will have increased computational need due to the high complexity  
1242 and large volume of collected physics events, along with the corresponding set of simulated  
1243 physics events [59]. The divergence of the baseline computing model from the projected  
1244 computing budget is shown in Figure 4.2.

1245 The fast simulation used for this thesis, AtlFast-II [61], is one such technique, which uses  
1246 a parametrized simulation of the calorimeter, called FastCaloSim, in conjunction with full  
1247 simulation of the inner detector, to achieve an order of magnitude speed up in simulation

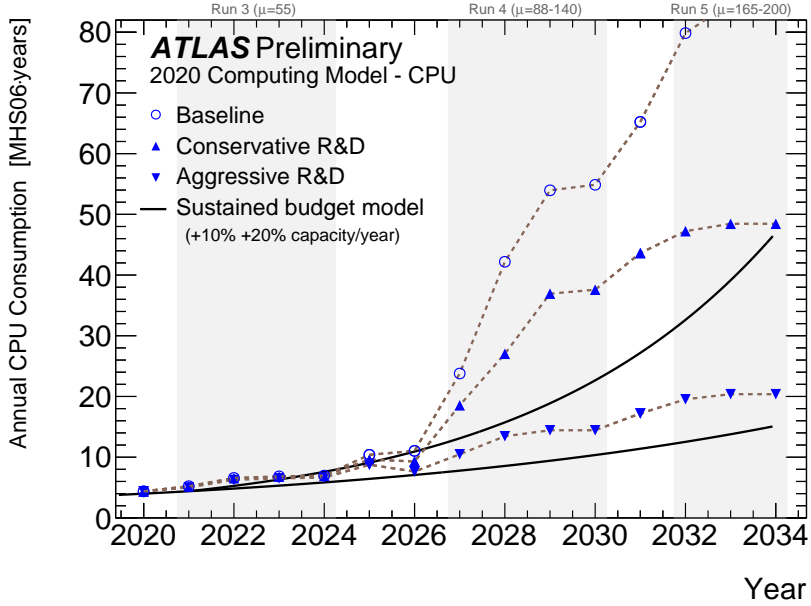


Figure 4.2: The projected ATLAS computational requirements for Run 3 and the HL-LHC relative to the projected computing budget. Aggressive R&D is required to keep resources within budget [60].

time. This parametrized simulation uses a simplified detector geometry, in conjunction with a simulation of particle shower development based on statistical sampling of distributions from fully simulated events, to massively speed up simulation time and computational load.

Such a speed up comes at a bit of a cost in performance. In particular, the modeling of jet substructure (see Chapter 5) historically has been an issue for FastCaloSim. The ATLAS authorship qualification work supporting this thesis is an effort to improve such modeling, and is part of a suite of updates being considered for a new fast simulation targeting Run 3. We briefly describe this work in the following.

1256 **4.3 Correlated Fluctuations in FastCaloSim**

1257 A variety of developments have been made to FastCaloSim, improving on the version used for  
1258 AtlFast-II. This new fast calorimeter simulation [62] is largely based on two components: one  
1259 which describes the *total energy* deposited in each calorimeter layer as a shower moves from  
1260 the interaction point outward, and one which describes the *shape*, i.e., the pattern of energy  
1261 deposits, of a shower in each respective calorimeter layer. Both methods are parametrizations  
1262 of the full simulation, and therefore are considered to be performing well if they are able  
1263 to reproduce corresponding full simulation distributions. Of course, directly sampling from  
1264 a library of showers would identically reproduce such distributions – however a statistical  
1265 sampling of various shower *properties* provides much more generality in the simulation.

1266 For the simulation of total energy in each given layer, the primary challenge is that such  
1267 energy deposits are highly correlated. The new FastCaloSim thus relies on a technique called  
1268 Principal Component Analysis (PCA) [63] to de-correlate the layers, aiding parametrization.

1269 The PCA chain transforms  $N$  energy inputs into  $N$  Gaussians and projects these Gaussians  
1270 onto the eigenvectors of the corresponding covariance matrix. This results in  $N$  de-correlated  
1271 components, as the eigenvectors are orthogonal. The component of the PCA decomposition  
1272 with the largest corresponding eigenvalue is then used to define bins, in which showers  
1273 demonstrate similar patterns of energy deposition across the calorimeter layers. To further  
1274 de-correlate the inputs, the PCA chain is repeated on the showers within each such bin. This  
1275 full process is reversed for the particle simulation. A full description of the method can be  
1276 found in [62].

1277 Modeling of the lateral shower shape makes use of 2D histograms filled with GEANT4  
1278 hit energies in each layer and PCA bin. Binned in polar  $\alpha - R$  coordinates in a local plane  
1279 tangential to the surface of the calorimeter system, these histograms represent the spatial  
1280 distribution of energy deposits for a given particle shower. Such histograms are constructed  
1281 for a number of Geant4 events, and the histograms for each event are normalized to total  
1282 energy deposited in the given layer. The average of these histograms is then taken (what is

1283 called here the “average shape”).

1284 In simulation, these average shape histograms are used as probability distributions, from  
 1285 which a finite number of equal energy hits are drawn. This finite drawing of hits induces  
 1286 a statistical fluctuation about the average shape which is tuned to match the expected  
 1287 calorimeter sampling uncertainty.

1288 As an example, the intrinsic resolution of the ATLAS Liquid Argon calorimeter has a  
 1289 sampling term of  $\sigma_{\text{samp}} \approx 10\%/\sqrt{E}$  [64]. The number of hits to be drawn for each layer,  $N_{\text{hits}}^{\text{layer}}$ ,  
 1290 is thus taken from a Poisson distribution with mean  $1/\sigma_{\text{samp}}^2$ , where the energy assigned to  
 1291 each hit is then just  $E_{\text{hit}} = \frac{E_{\text{layer}}}{N_{\text{hits}}^{\text{layer}}}$ . This induces a fluctuation of the order of  $10\%/\sqrt{E_{\text{bin}}}$  for  
 1292 each bin in the average shape.

1293 Figure 4.3 shows a comparison of energy and weta2 [65], defined as the energy weighted  
 1294 lateral width of a shower in the second electromagnetic calorimeter layer, for 16 GeV photons  
 1295 simulated with the new FastCaloSim and with full GEANT4 simulation. The agreement is  
 1296 quite good, with FastCaloSim matching the Geant4 mean to within 0.3 and 0.03 percent  
 respectively. Similar results are seen for other photon energies and  $\eta$  points.

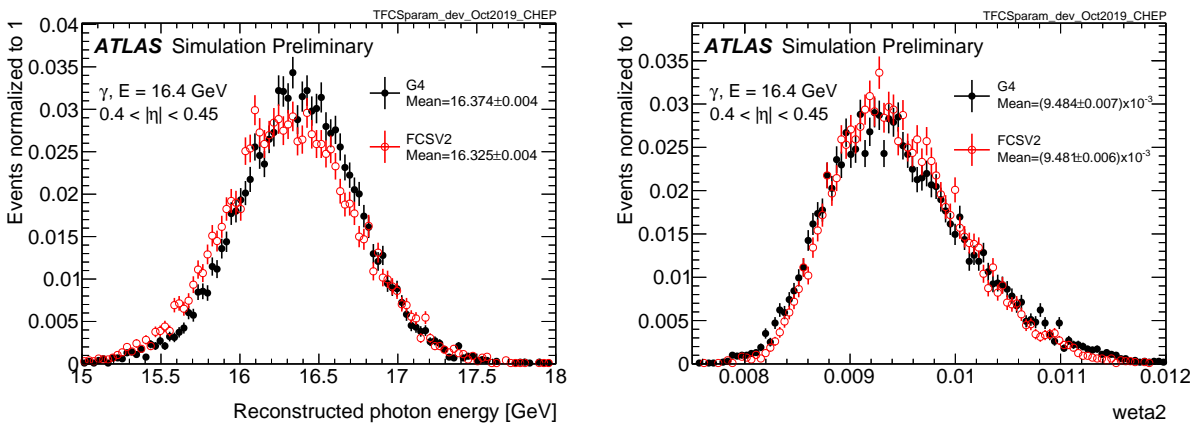


Figure 4.3: Energy and variable weta2, defined as the energy weighted lateral width of a shower in the second electromagnetic calorimeter layer, for 16 GeV photons with full simulation (G4) and FastCaloSimV2 (FCSV2) [62].

1298    4.3.1 *Fluctuation Modeling*

1299    Figure 4.4 shows the ratio of calorimeter cell energies for single GEANT4 photon and pion  
 1300    events to the corresponding cell energies in their respective average shapes. While the photon  
 1301    event is quite close to the corresponding average, the pion event shows a deviation from the  
 1302    average which is much larger and has a non-trivial structure, reflecting the different natures  
 1303    of electromagnetic and hadronic showering.

1304    While the shape parametrization described above is thus sufficient for describing electro-  
 1305    magnetic showers, we will demonstrate below that it is not sufficient for describing hadronic  
 1306    showers (Figures 4.7 and 4.8). We therefore present and validate methods to improve this  
 1307    hadronic shower modeling. Such methods have been presented as well in [66].

1308    Two methods for modeling deviations from the average shape have been studied: (1)  
 1309    a neural network based approach using a Variational Autoencoder (VAE) [67] and (2) a  
 1310    map through cumulative distributions to an  $n$ -dimensional Gaussian. With both methods,  
 1311    the shape simulation then proceeds as described in Section 4.3, with the drawing of hits  
 1312    according to the average shape. However, these hits no longer have equal energy, but have  
 1313    weights applied to increase or decrease their energy depending on their spatial position.  
 1314    This application of weights is designed to mimic a realistic shower structure and to encode  
 1315    correlations between energy deposits.

1316    Both methods are trained on ratios of energy in binned units called voxels. This voxelization  
 1317    is performed in the same polar  $\alpha - R$  coordinates as the average shape, with a 5 mm core in  
 1318     $R$  and 20 mm binning thereafter. There are a total of 8  $\alpha$  bins from 0 to  $2\pi$  and 8 additional  
 1319     $R$  bins from 5 mm to 165 mm. The 5 mm core is filled with the average value of core voxels  
 1320    across the 8  $\alpha$  bins when creating the parametrisation. However, during simulation, each of  
 1321    these 8 core bins is treated independently. The outputs of both methods mimic these energy  
 1322    ratios and are used in the shape simulation as the weights described above. In contrast to  
 1323    an approach based on, e.g., calorimeter cells, using voxels allows for flexibility in tuning the  
 1324    binning used in creating the parametrisation. Further, due to their relatively large size, using

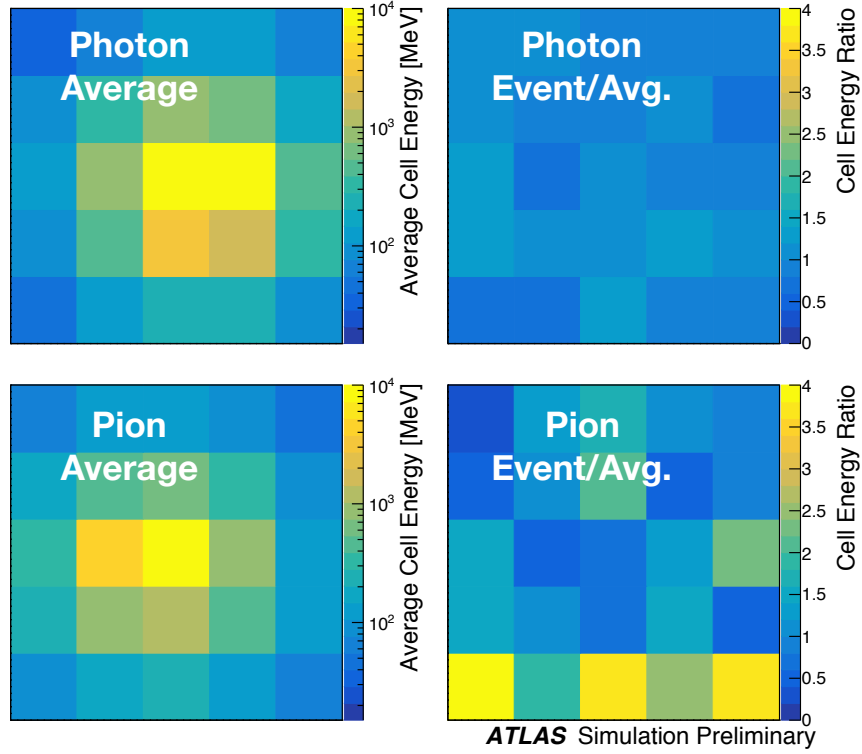


Figure 4.4: Example of photon and pion average shapes in  $5 \times 5$  calorimeter cells. The left column shows the average shape over a sample of 10000 events, while the right column shows the energy ratio, in each cell, of single GEANT4 events with respect to this average. The photon ratios are all close to 1, while the pion ratios show significant deviation from the average.

1325 calorimeter cells is subject to “edge effects”, where the splitting of energy between cells has a  
 1326 non-trivial effect on the observed energy ratio. The binning used here is of the order of half  
 1327 of a cell size, mitigating this effect.

1328 The Gaussian method operates by using cumulative distributions to map GEANT4 energy  
 1329 ratios to a multidimensional Gaussian distribution. New events are generated by randomly  
 1330 sampling from this Gaussian distribution.

1331 For the VAE method, a system of two linked neural networks is trained to generate events.

1332 The first “encoder” neural network maps input GEANT4 energy ratios to a lower dimensional  
 1333 latent space. A second “decoder” neural network then samples from that latent space and  
 1334 tries to reproduce the inputs. In simulation, events are generated by taking random samples  
 1335 from the latent space and passing them through the trained decoder.

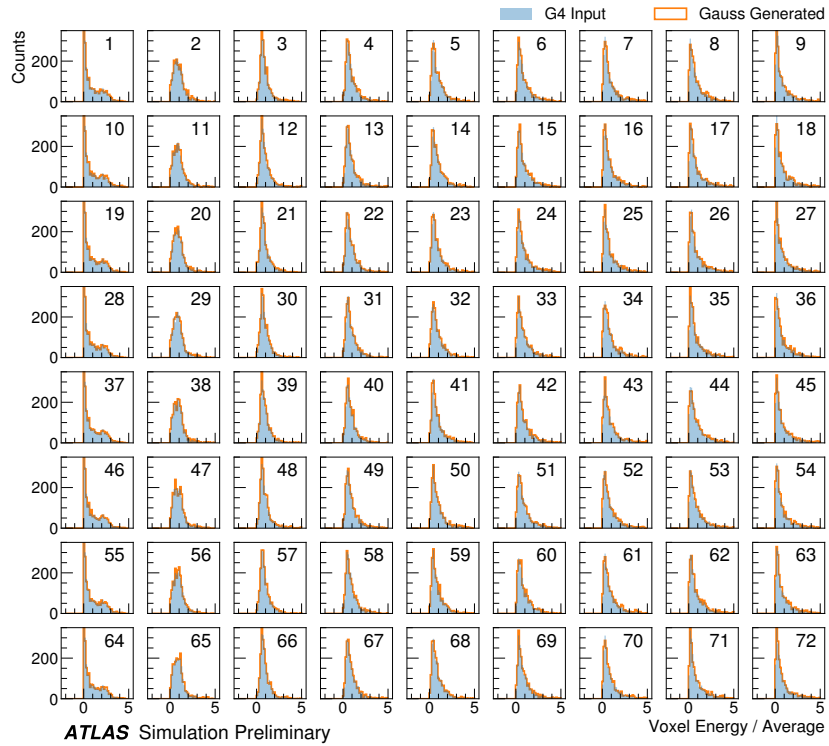


Figure 4.5: Distribution of the ratio of voxel energy in single events to the corresponding voxel energy in the average shape, with GEANT4 events in blue and Gaussian model events in orange, for 65 GeV central pions in EMB2. Moving top to bottom corresponds to increasing  $\alpha$ , left to right corresponds to increasing  $R$ , with core voxels numbered 1, 10, 19, .... Agreement is quite good across all voxels. Results are similar for the VAE method.

1336 Figure 4.5 shows the distributions of input GEANT4 and Gaussian method generated  
 1337 energy ratios in the grid of voxels. Figure 4.6 shows the correlation coefficient between the  
 1338 center voxel from  $\alpha = 0$  to  $2\pi/8$  for input GEANT4 and the Gaussian and VAE fluctuation

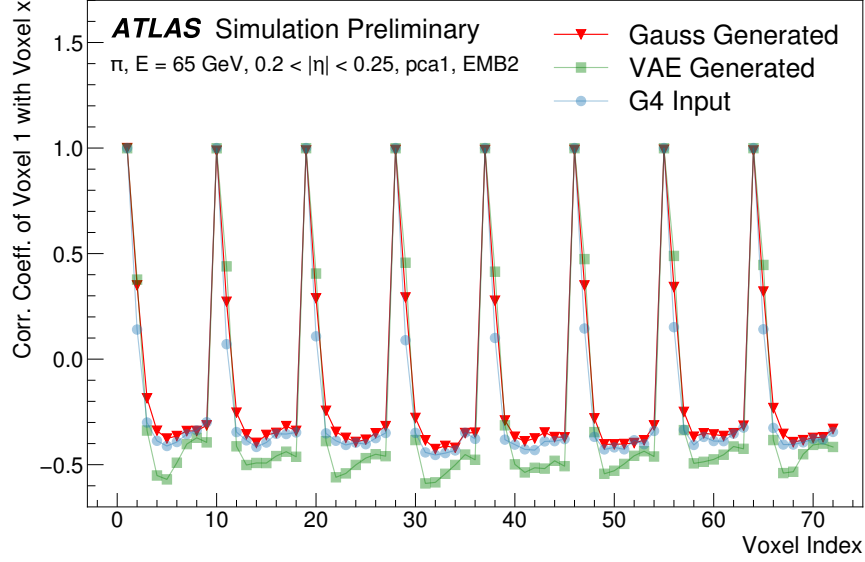


Figure 4.6: Correlation coefficient of ratios of voxel energy in single events to the corresponding voxel energy in the average shape, examined between the core bin from  $\alpha = 0$  to  $2\pi/8$  and each of the other voxels. The periodic structure represents the binning in  $\alpha$ , and the increasing numbers in each of these periods correspond to increasing  $R$ , where the eight points with correlation coefficient 1 are the eight core bins. Both the Gaussian and VAE generated toy events are able to reproduce the major correlation structures for 65 GeV central pions in EMB2.

1339 methods. Agreement is good throughout.

1340 Validation of the Gaussian and VAE fluctuation methods was performed within FastCaloSimV2.

1341 Figure 4.7 shows the energy ratio of cells for a given simulation to the corresponding cells in  
 1342 the average shape as a function of the distance from the shower center. The mean for all  
 1343 simulation methods is expected to be around 1, with deviation from the average (the RMS  
 1344 fluctuation) shown by the error bars. The Gaussian method RMS (red) and VAE method  
 1345 RMS (green) both match the GEANT4 RMS (yellow) better than the case without correlated  
 1346 fluctuations (blue) for a variety of energies,  $\eta$  points, and layers, often reproducing 80 – 100 %

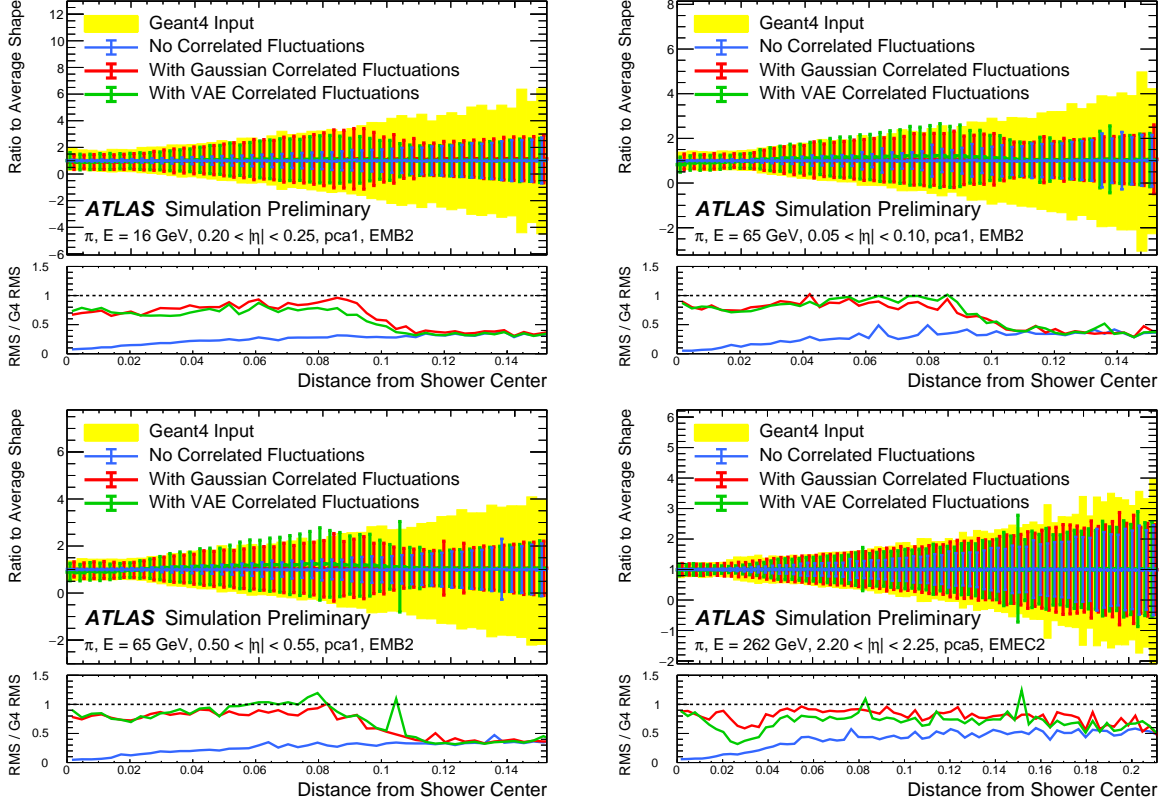


Figure 4.7: Comparison of the RMS fluctuations about the average shape with the Gaussian fluctuation model (red), the VAE fluctuation model (green), and without correlated fluctuations (blue) for a range of pion energies,  $\eta$  points, and layers.

1347 of the GEANT4 RMS magnitude, compared to the 5 – 30 % observed in the no correlated  
1348 fluctuations case.

1349 Figure 4.8 shows the result of a simulation with full ATLAS reconstruction for 65 GeV  
1350 central pions with the Gaussian fluctuation model. Here a *cluster* [68] is defined as a three-  
1351 dimensional spatial grouping of calorimeter cells which are summed based on the input signals  
1352 relative to their neighboring cells. The multiplicity, shape, and spatial distribution of such  
1353 clusters provides a powerful insight on the structure of energy deposits in the calorimeter,  
1354 and good performance in cluster variables is a promising step towards good performance

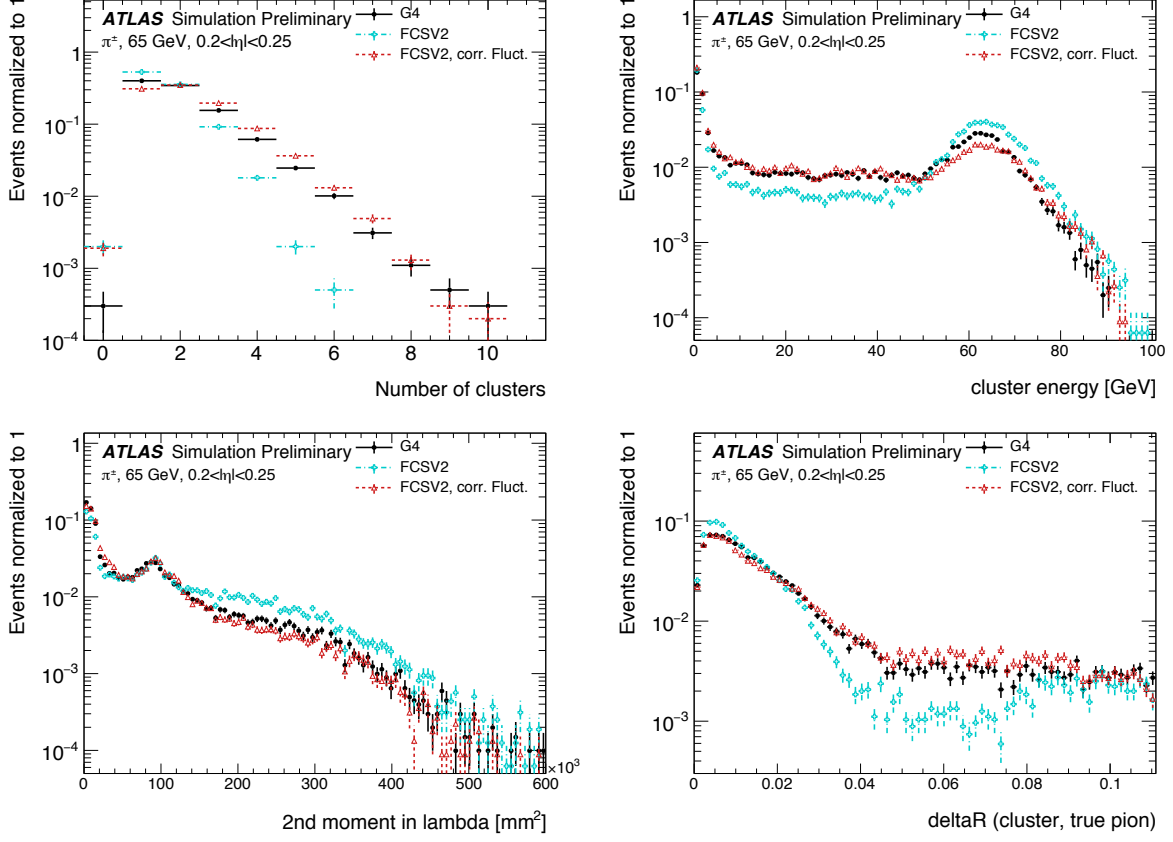


Figure 4.8: Comparison of the Gaussian fluctuation model to the default FCSV2 version and to G4 simulation, using pions of 65 GeV energy and  $0.2 < |\eta| < 0.25$ . Variables shown relate to calorimeter clusters, three-dimensional spatial groupings of cells [68] which provide powerful insight on the structure of energy deposits in the calorimeter. Variables considered include number and energy of clusters, the 2nd moment in lambda, ( $< \lambda^2 >$ ), which describes the square of the longitudinal extension of a cluster, where  $\lambda$  is the distance of a cell from the shower center along the shower axis, and a cluster moment is defined as  $< x^n > = \frac{\sum E_i x_i}{\sum E_i}$ , and the distance  $\Delta R$ , between the cluster and the true pion. With the correlated fluctuations, variables demonstrate improved modeling relative to default FastCaloSimV2.

1355 in the modeling of jet substructure, as these clusters may themselves be summed to form  
 1356 jets (see Chapter 5). The simulation with the Gaussian fluctuation model demonstrates  
 1357 improved modeling of several of these cluster variables relative to baseline FastCaloSimV2,  
 1358 reproducing the distributions of events simulated with GEANT4. These include number and  
 1359 energy of clusters, the 2nd moment in lambda, ( $\langle \lambda^2 \rangle$ ), which describes the square of the  
 1360 longitudinal extension of a cluster, where  $\lambda$  is the distance of a cell from the shower center  
 1361 along the shower axis, and a cluster moment is defined as  $\langle x^n \rangle = \frac{\sum E_i x_i}{\sum E_i}$ , and the distance  
 1362  $\Delta R$ , between the cluster and the true pion.

1363 The new fast calorimeter simulation is a crucial part of the future of simulation for the  
 1364 ATLAS Experiment at the LHC. The per event simulation time of the full detector with  
 1365 GEANT4, calculated over 100  $t\bar{t}$  events, is 228.9 s. Using FastCaloSim for the calorimeter  
 1366 simulation reduces this to 26.6 s, of which FastCaloSim itself is only 0.015 s, with the majority  
 1367 of the remaining simulation time due to GEANT4. Good physics modeling is achieved, and  
 1368 the correlated fluctuations method shows good proof of concept improvement for the modeling  
 1369 of hadronic showers.

#### 1370 **4.4 Outlook**

1371 There has been significant effort in the community to develop a set of fast simulation tools,  
 1372 with the use of machine learning methods at the forefront of such approaches (e.g. [69], [70]).  
 1373 Most fast simulation approaches generally are based on parametrizations of fully simulated  
 1374 events, but fall into two paradigms - a “by hand” simulation, which focuses on the modeling  
 1375 of individual detector effects, or a fully parametrized simulation, in which a generative model  
 1376 (e.g. a Generative Adversarial Network or Variational Autoencoder) is trained to directly  
 1377 reproduce the input events. Both approaches can be extremely powerful, but each suffer from  
 1378 certain drawbacks. The “by hand” approach offers the advantage of direct encoding of expert  
 1379 knowledge – if an effect needs to be modeled, a new parametrization is introduced. However,  
 1380 by the same token, it requires dedicated parametrizations for each effect. Fully parametrizing  
 1381 the simulation with a generative model offloads this burden onto the network itself. However,

1382 by doing so, the ability to use expert knowledge is diminished – the network is required to  
1383 learn all relevant effects.

1384 The method presented here represents an effort to step towards a hybrid between these two  
1385 approaches, leveraging the power of machine learning techniques for individual parametriza-  
1386 tions within the by hand framework. Such hybrid solutions have the potential to be extremely  
1387 powerful, and further work on the development of these solutions is an interesting direction  
1388 of future study.

1389

## Chapter 5

1390

# RECONSTRUCTION

1391 Chapter 3 discusses how a proton-proton collision may be captured by a physical detector  
 1392 and turned into data that may be stored and analyzed. Chapter 4 discusses the simulation  
 1393 of this same process. At this most basic level, however, the ATLAS detector is only a  
 1394 machine for turning particles into a set of electrical signals, albeit in a very sophisticated,  
 1395 physics motivated way. This chapter discusses the step of turning these electrical signals into  
 1396 objects which may be identified with the underlying physics processes, and therefore used to  
 1397 make statements about what occurred within a given collision event. This process is termed  
 1398 *reconstruction*, and we will focus particularly on jets and flavor tagging, as the most relevant  
 1399 pieces for this thesis work.

1400 **5.1 Jets**

1401 As discussed in Chapters 3 and 4, the production of particles with color charge from a  
 1402 proton-proton interaction is complicated both by parton showering and by confinement: a  
 1403 quark produced from a hard scatter is not seen as a quark, but rather, as a spray of particles  
 1404 with a variety of hadrons in the final state, which subsequently shower upon interaction with  
 1405 the calorimeter in a complicated way.

1406 For hard scatter electrons, photons, or muons on the other hand, the picture is much  
 1407 clearer: there is no parton showering, and each has a distinct signature in the detector:  
 1408 photons have no tracks and a very localized calorimeter shower, electrons are associated  
 1409 with tracks and are similarly localized in the calorimeter, and muons are associated with  
 1410 tracks, pass through the calorimeter due to their large mass, and leave signatures in the muon  
 1411 spectrometer.

Jets are a tool to deal with the messiness of quarks and gluons. The basic concept is to group the multitude of particles produced by hadronization into a single object. Such an object then has associated properties, including a four-vector, which may be identified with the corresponding initial state particle. In practice a variety of information from the ATLAS detector is used for such a reconstruction. The analysis considered in this thesis uses particle flow jets [71], which combines information from both the tracker and the calorimeter, where the combined objects may be identified with underlying particles. However, jets built from clusters of calorimeter cells [72] as well as from charged particle tracks [73] have also been used very effectively.

A variety of algorithms are used to associate detector level objects to a given jet. The most commonly used in ATLAS is the anti- $k_T$  algorithm [74], which is a successor to the  $k_T$  algorithm, among others [75], and develops as follows. Both algorithms are sequential recombination algorithms, which begin with the smallest distance,  $d_{ij}$  between considered objects (e.g. particles or intermediate groupings of particles). If  $d_{ij}$  is less than a parameter  $d_{iB}$  ( $B$  for “beam”) object  $i$  is combined with object  $j$ , the distance  $d_{ij}$  is recomputed, and the process repeats. This proceeds until  $d_{ij} \geq d_{iB}$ , at which point the jet is “complete” and removed from the list of considered objects.

The definitional difference between  $k_T$  and anti- $k_T$  is these distance parameters. In general form, these are defined as

$$d_{ij} = \min(p_{Ti}^{2p}, p_{Tj}^{2p}) \frac{\Delta R_{ij}^2}{R^2} \quad (5.1)$$

$$d_{iB} = p_{Ti}^{2p} \quad (5.2)$$

where  $p_{Ti}$  is the transverse momentum of object  $i$ ,  $\Delta R_{ij}$  is the angular distance between objects  $i$  and  $j$ ,  $R$  is a radius parameter, and  $p$  controls the tradeoff between the  $p_T$  and angular distance terms. For the  $k_T$  algorithm  $p = 1$ ; for the anti- $k_T$  algorithm,  $p = -1$ . This is a simple change, but results in significantly different behavior.

The anti- $k_T$  algorithm can be understood as follows: for a single high  $p_T$  particle ( $p_{T1}$ ) surrounded by a bunch of low  $p_T$  particles, the low  $p_T$  particles will be clustered with the

high  $p_T$  one if

$$d_{1j} = \frac{1}{p_{T1}^2} \frac{\Delta R_{1j}^2}{R^2} < \frac{1}{p_{T1}^2} \quad (5.3)$$

$$\implies \Delta R_{1j} < R. \quad (5.4)$$

1433 Therefore, a single high  $p_T$  particle ( $p_{T1}$ ) surrounded by a bunch of low  $p_T$  particles results in  
 1434 a perfectly conical jet. This shape may change with the presence of other high momentum  
 1435 particles, but the key feature of the dynamics is that the jet shape is determined by high  $p_T$   
 1436 objects due to the  $\frac{1}{p_T}$  nature of this definition. In contrast, the  $k_T$  algorithm results in jets  
 1437 influenced by low momentum particles, which results in a less regular shape. This property,  
 1438 of regular jet shapes determined by high momentum objects, as well as demonstrated good  
 1439 practical performance, makes the anti- $k_T$  algorithm the favored jet algorithm in ATLAS.

1440 Because jets are composed of multiple objects, a useful property of jets is jet *substructure*,  
 1441 that is, acknowledging that jets are composite objects, analyzing the structure of a given  
 1442 jet to infer physics information. This leads to the use of *subjets*; that is, after running jet  
 1443 clustering, often to create a “large-R”,  $R = 1.0$  anti- $k_T$  jet, a smaller radius jet clustering  
 1444 algorithm is run within the jet. Subjets are often chosen using the  $k_T$  algorithm, which again  
 1445 is sensitive to lower momentum particles, with  $R = 0.2$  or  $0.3$ . For the boosted version of this  
 1446 thesis analysis, such a strategy is used, in which the subjets are *variable radius* and depend  
 1447 on the momentum of the (proto)jet in question. Beyond this thesis work, substructure is  
 1448 used in a large variety of analyses, with a set of associated variables and tools developed for  
 1449 exploiting this structure *TODO: Cite some?*.

## 1450 5.2 Flavor Tagging

1451 For this this thesis, the physics process being considered is  $HH \rightarrow b\bar{b}b\bar{b}$ . From the previous  
 1452 section, we know that the standard practice is to identify these  $b$  quarks (or, rather, the  
 1453 resulting  $B$  hadrons, due to confinement) with jets – in our case, these  $b$ -*jets* are  $R=0.4$   
 1454 anti- $k_T$  particle flow jets (see Chapter 7). However, not all jets produced at the LHC are  
 1455 from  $B$  hadrons; rather, there are a variety of different types of jets corresponding to different

1456 flavors of quarks. These are often classified as light jets (from  $u$ ,  $d$ , or  $s$  quarks, or gluons)  
1457 or as other *heavy flavor* jets, e.g.  $c$ -jets, involving  $c$  quarks. Distinguishing between these  
1458 different categories is a very active area of work in ATLAS, termed *flavor tagging*, with much  
1459 focus on *b-tagging* in particular, that is, the identification of jets from  $B$  hadron decays. We  
1460 here briefly describe the techniques used for flavor tagging in ATLAS.

1461 What distinguishes a  $b$ -jet from any other jet? This question is fundamental to the  
1462 design of the various  $b$ -tagging algorithms, and has two major answers: (1)  $B$  hadrons have  
1463 long lifetimes, and (2)  $B$  hadrons have large masses. It is most illustrative to compare  
1464 the  $B$  hadron properties to a common light meson, e.g.  $\pi^0$ , the neutral pion, with quark  
1465 content  $\frac{1}{\sqrt{2}}(u\bar{u} - d\bar{d})$ .  $B$  hadrons have lifetimes around 1.5 ps, corresponding to a decay  
1466 length  $c\tau \approx 0.45$ mm. In contrast,  $\pi^0$  has a lifetime of  $8.4 \times 10^{-5}$ ps, which is around 20,000  
1467 times shorter! Theoretically, this comes from CKM suppression of the  $b$  to  $c$  transition, which  
1468 dominates the  $B$  decay modes. Experimentally, this difference pops up as shown in Figure  
1469 5.1 – light flavor initiated jets decay almost immediately at the proton-proton interaction  
1470 point, whereas  $b$ -jets are distinguished by a displaced secondary vertex, corresponding to  
1471 the 5 mm decay length calculated above. This displaced vertex falls short of the detector  
1472 itself, but may be inferred from larger transverse (perpendicular to beam) and longitudinal  
1473 (parallel to beam) impact parameters of the resulting tracks, termed  $d_0$  and  $z_0$  respectively.

1474 Coming to the mass,  $B$  mesons have masses of around 5.2 GeV, whereas the  $\pi^0$  mass  
1475 is around 0.134 GeV, (around 40 times lighter). This higher mass gives access to a larger  
1476 decay phase space, leading to a high multiplicity for  $b$ -jets (average of 5 charged particles per  
1477 decay).

1478 One final distinguishing feature of  $B$  hadrons is their *fragmentation function*, a function  
1479 describing the production of an observed final state. For  $B$  hadrons, this is particularly  
1480 “hard”, with the  $B$  hadrons themselves contributing to an average of around 75 % of the  $b$ -jet  
1481 energy. Thus, the identification of  $b$ -jets with  $B$  hadrons is, in some sense, descriptive.

1482 We have contrasted  $b$ -jets and light jets, demonstrating that there are several handles  
1483 available for making this distinction.  $c$ -jets are slightly more similar to  $b$ -jets, but the same

1484 handles still apply –  $c$ -hadron lifetimes are between 0.5 and 1 ps, a factor of 2 smaller than  $B$   
1485 hadrons. Their mass is around 1.9 GeV, 2 to 3 times smaller than  $B$  hadrons, and  $c$ -hadrons  
1486 contribute to an average of around 55 % of  $c$ -jet energy. Therefore, while the gap is slightly  
1487 smaller, a distinction may still be made.

1488 The ATLAS flavor tagging framework [77] relies on developing a suite of “low-level”  
1489 taggers, which use a variety of information about tracks and vertices as inputs. The output  
1490 of these lower level taggers are then fed into a higher level tagger, which aggregates these  
1491 results into a high level discriminant. Each of these taggers is described below.

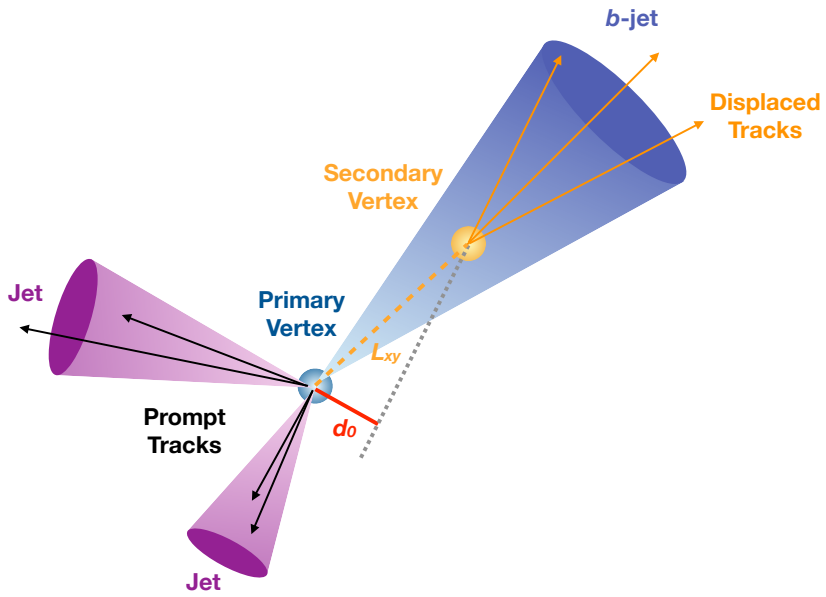


Figure 5.1: Illustration of an interaction producing two light jets and one  $b$ -jet in the transverse plane. While the light jets decay “promptly”, coinciding with the primary vertex of the proton-proton interaction, the longer lifetime of  $B$  hadrons leads to a secondary decay vertex, displaced from the primary vertex by length  $L_{xy}$ . This is typically a few mm, and therefore is not directly visible in the detector, but leads to a large transverse impact parameter,  $d_0$ , for the resulting tracks. [76]

1492 5.2.1 IP2D/3D

1493 IP2D and IP3D are taggers based on the large track impact parameter (IP) nature of  $B$   
 1494 hadron decays. Both are based on histogram templates derived from Monte Carlo simulation,  
 1495 which are used as probability density functions to construct log-likelihood discriminants.  
 1496 IP2D incorporates just the transverse impact parameter information using 1D histogram  
 1497 templates, whereas IP3D uses both transverse and longitudinal impact parameters in a 2D  
 1498 template, which accounts for correlations. Importantly, these are *signed* impact parameters,  
 1499 with sign based on the angle between the impact parameter and the considered jet – positive  
 1500 impact parameters are consistent with a track extrapolation in front of the jet (angle between  
 1501 impact parameter line and jet  $< 90^\circ$ ), and therefore more consistent with tracks originating  
 1502 from a displaced decay.

1503 Rather than using the impact parameters directly, an impact parameter *significance*  
 1504 is used which incorporates an uncertainty on the impact parameter – tracks with a lower  
 1505 uncertainty but the same impact parameter will contribute more in the calculation. This  
 1506 signed significance is what is used to sample from the PDF templates, with the resulting  
 1507 discriminants the sum of probability ratios between given jet hypotheses over tracks associated  
 1508 to a given jet, namely  $\sum_{i=1}^N \log \frac{p_b}{p_{light}}$  between  $b$ -jet and light jet hypotheses, where  $p_b$  and  
 1509  $p_{light}$  are the per-track probabilities. Similar discriminants are defined between  $b$ - and  $c$ -jets  
 1510 and  $c$  and light jets. *TODO: show distributions?*

1511 5.2.2 SV1

1512 SV1 is an algorithm which aims to find a secondary vertex (SV) in a given jet. Operating  
 1513 on all vertices associated with a considered jet, the algorithm discards tracks based on a  
 1514 variety of cleaning requirements. It then proceeds to first construct all two-track vertices,  
 1515 and then iterates over all the tracks involved in these two track vertices to try to fit a single  
 1516 secondary vertex, which would then be identified with the secondary vertex from the  $b$  or  $c$   
 1517 hadron decay. This fit proceeds by evaluating a  $\chi^2$  for the association of a track and vertex,

removing the track with the largest  $\chi^2$ , and iterating until the  $\chi^2$  is acceptable and the vertex has an invariant mass of less than 6 GeV (for consistency with  $b$  or  $c$  hadron decay).

A variety of discriminating variables may then be constructed, including (1) invariant mass of the secondary vertex, (2) number of tracks associated with the secondary vertex, (3) number of two-track vertices, (4) energy fraction of the tracks associated to the secondary vertex (relative to all of the tracks associated to the jet), and various metrics associated with the secondary vertex position and decay length, including (5) transverse distance between the primary and secondary vertex, (6) distance between the primary and secondary vertex (7) distance between the primary and secondary vertex divided by its uncertainty, and (8)  $\Delta R$  between the jet axis and the direction of the secondary vertex relative to the primary vertex.

While all eight of these variables are used as inputs to the higher level taggers, the number of two-track vertices, the vertex mass, and the vertex energy fraction are additionally used with 3D histogram templates to evaluate flavor tagging performance by constructing log-likelihood discriminants, similar to the procedure for IP2D/3D.

### 5.2.3 JetFitter

Rather than focusing on a particular aspect of the  $B$  hadron or  $D$  hadron decay topology (e.g impact parameter or secondary vertex), the third low level tagger, JETFITTER [78], tries to reconstruct the full decay chain, including all involved vertices. This is structured around a Kalman filter formalism [79], and has the strong underlying assumption that all tracks which stem from  $B$  and  $D$  hadron decay must intersect a common flight path. This assumption provides significant constraints, allowing for the reconstruction of vertices from even a single track, reducing the number of degrees of freedom in the fit, and allowing the use of “downstream” information, e.g., compatibility of tracks with a  $B \rightarrow D$ -like decay. The constructed topology, including primary vertex location and  $B$ -hadron flight path, is iteratively updated over tracks associated to a given jet, and a variety of discriminating variables related to the resulting topology and reconstructed decay are used as inputs to the high level taggers.

1545 *5.2.4 RNNIP*

1546 The IP2D and IP3D algorithms rely on per-track probabilities, and the final discriminating  
 1547 variables (and inputs to the higher level taggers) are sums (products) over these independently  
 1548 considered quantities. In practice, however, the tracks are not independent – this is merely a  
 1549 simplifying assumption to allow for the use of a binned likelihood, as treatment of all of the  
 1550 interdependencies in such a framework quickly becomes intractable. To address this issue, a  
 1551 recurrent neural network-based algorithm, RNNIP [80], is used, which takes as input a variety  
 1552 of per-track variables, including the signed impact parameter significances (as in IP3D) as  
 1553 well as track momentum fraction relative to the jet and  $\Delta R$  between the track and the jet.  
 1554 RNNs are sequence-based, and vectors of input variables corresponding to tracks for a given  
 1555 jet are ordered by magnitude of transverse impact parameter significance and then passed  
 1556 to the network, which outputs class probabilities corresponding to b-jet, c-jet, light-jet, and  
 1557  $\tau$ -jet hypotheses. Such a procedure allows the network to learn interdependencies between  
 1558 tracks, improving performance.

1559 *5.2.5 MV2 and DL1*

1560 Outputs from the above taggers are combined into high level taggers to aggregate all of the  
 1561 information and improve discriminating power relative to the respective individual taggers as,  
 1562 as shown in Figure 5.2. These high level taggers are primarily in two forms: MV2, which  
 1563 uses a Boosted Decision Tree (BDT) for this aggregation, and DL1, which uses a deep neural  
 1564 network. For the baseline versions of these taggers, only inputs from IP2D, IP3D, SV1, and  
 1565 JetFitter are used. The tagger used for this thesis analysis, DL1r, additionally incorporates  
 1566 RNNIP, demonstrating improved performance over the baseline DL1, as shown in Figure 5.3.  
 1567 All high level taggers also include jet  $p_T$  and  $|\eta|$ .

DL1 offers a variety of improvements over MV2. Rather than a single discriminant output, as with MV2, DL1 has a multidimensional output, corresponding to probabilities for a jet to be a *b*-jet, *c*-jet, or light jet. This allows the trained network to be used for both *b*- and *c*-jet

tagging. The final discriminant for  $b$ -tagging with DL1 correspondingly takes the form

$$D_{\text{DL1}} = \ln \left( \frac{p_b}{f_c \cdot p_c + (1 - f_c) \cdot p_{\text{light}}} \right) \quad (5.5)$$

where  $p_b$ ,  $p_c$ , and  $p_{\text{light}}$  are the output  $b$ ,  $c$ , and light jet probabilities, and  $f_c$  corresponds to an effective  $c$ -jet fraction, which may be tuned to optimize performance.

DL1 further includes an additional set of JETFITTER input variables relative to MV2 which correspond to  $c$ -tagging – notably properties of secondary and tertiary vertices, as would be seen in a  $B \rightarrow D$  decay chain.

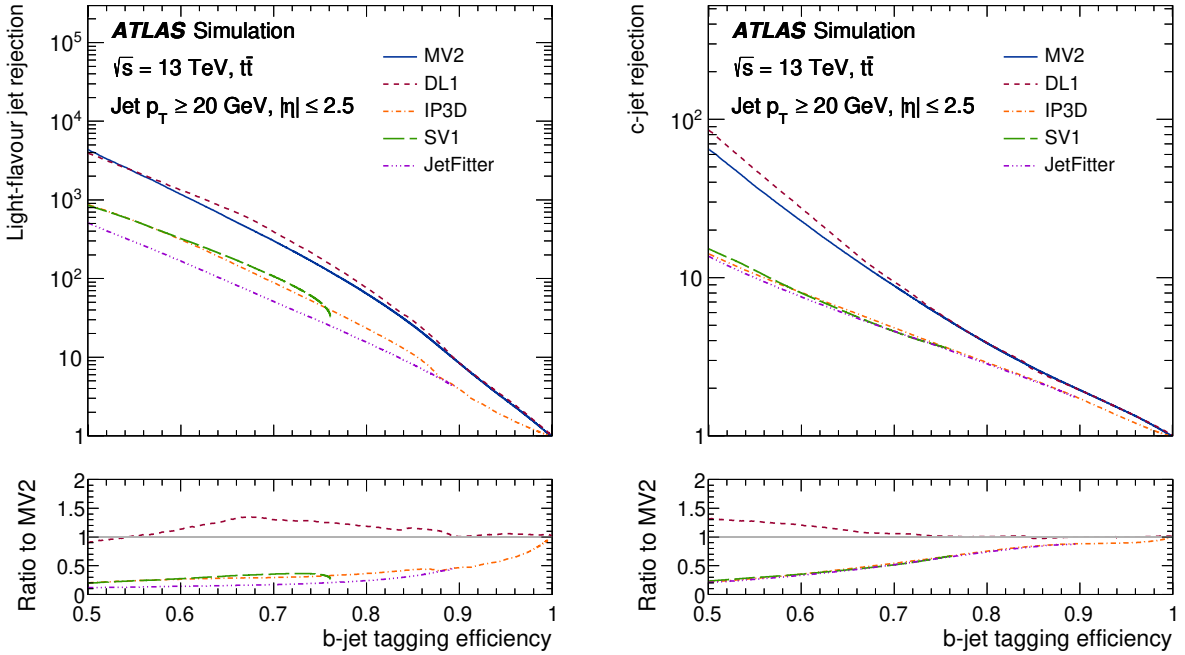


Figure 5.2: Performance of the various low and high level flavor tagging algorithms in  $t\bar{t}$  simulation, demonstrating the tradeoff between  $b$ -jet efficiency and light and  $c$ -jet rejection. The high level taggers demonstrate significantly better performance than any of the individual low level taggers, with DL1 offering slight improvements over MV2 due to the inclusion of additional input variables.

Figure 5.2 shows a comparison of the performance of the various taggers. The  $b$ -tagging performance of DL1 and MV2 is found to be similar, with some improvements in light jet and  $c$ -jet rejection from the additional variables used in DL1. The performance of these high level taggers additionally is seen to be significantly better than any of the individual low level ones, even in regimes where only a single low level tagger is relevant (such as high  $b$ -tagging efficiencies, where SV1 and JETFITTER are limited by selections on tracks entering the respective algorithms).

The inclusion of RNNIP offers a significant improvement on top of baseline DL1, as shown in Figure 5.3, strongly motivating the choice of DL1r for this thesis.

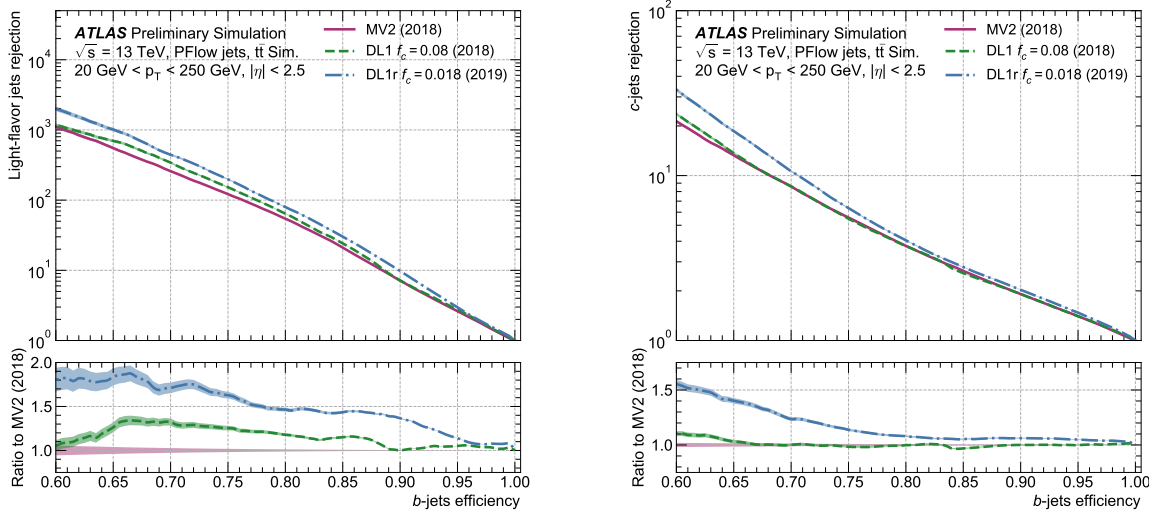


Figure 5.3: Performance of the MV2, DL1, and DL1r algorithms in  $t\bar{t}$  simulation, demonstrating the tradeoff between  $b$ -jet efficiency and light and  $c$ -jet rejection.  $f_c$  controls the importance of  $c$ -jet rejection in the discriminating variable, and values shown have been optimized separately for each DL1 configuration. DL1r demonstrates a significant improvement in both light and  $c$  jet rejection over MV2 and DL1. [81]

1582    5.2.6 *Some Practical Notes*

1583    The  $b$ -tagging metrics presented in Figures 5.2 and 5.3 correspond to evaluating a tradeoff  
1584    between  $b$ -jet efficiency and light jet and  $c$ -jet rejection. In this case,  $b$ -jet efficiency is defined  
1585    such that, e.g. for a 77 % efficiency, 77 % of the real  $b$ -jets will be tagged as such. Somewhat  
1586    counterintuitively, this means that a lower  $b$ -jet efficiency corresponds to a more aggressive  
1587    (“tighter”) selection on the discriminating variable, while a higher  $b$ -jet efficiency corresponds  
1588    to a less aggressive (“looser”) cut (100 % efficiency means no cut). Light and  $c$  jet efficiencies  
1589    are defined similarly, with rejection defined as 1/ the corresponding efficiency.

1590        In ATLAS, the respective  $b$ -tagging efficiencies are used to define various  $b$ -tagging working  
1591    points. The working point used for the nominal  $b$ -jet identification in this thesis is 77 % with  
1592    DL1r. A loosened (less aggressive) selection at the 85 % working point is additionally used.  
1593        See Chapter 7 for further details.

1594

## Chapter 6

1595

### THE ANATOMY OF AN LHC SEARCH

1596 In this thesis so far, we have set the theoretical foundation for the work carried out at the  
 1597 LHC. We have described how one may translate between this theoretical foundation and what  
 1598 we are actually able to observe with the ATLAS detector. We have further stepped through  
 1599 the process of simulating production of specific physics processes and their appearance in  
 1600 our detector, allowing us to describe how a hypothetical physics model would be seen in  
 1601 our experiment. The question then becomes: all of these pieces are on the table, what do  
 1602 we do with them? This chapter attempts to answer exactly that, setting up a roadmap for  
 1603 assembling these pieces into a statement about the universe.

1604 ***6.1 Object Selection and Identification***

1605 As described in Chapter 5, there is a complicated set of steps for going from electrical signals  
 1606 in a detector to physics objects.

1607 ***6.2 Defining a Signal Region***

1608 ***6.3 Background Estimation***

1609 ***6.4 Uncertainty Estimation***

1610 ***6.5 Hypothesis Testing***

1611

## Chapter 7

1612

### SEARCH FOR PAIR PRODUCTION OF HIGGS BOSONS IN THE $b\bar{b}b\bar{b}$ FINAL STATE

1613

This chapter presents two complementary searches for pair production of Higgs bosons in the final state. Such searches are separated based on the signal models being considered: resonant production, in which a new spin-0 or spin-2 particle is produced and decays to two Standard Model Higgs bosons, and non-resonant production, which is sensitive to the value of the Higgs self-coupling  $\lambda_{HHH}$ . Further information on the theory behind both channels can be found in Chapter 2.

While the searches face many similar challenges and proceed (in broad strokes) in a very similar manner, separate optimizations are performed to maximize the respective sensitivities for these two very different sets of signal hypotheses. More particularly, resonant signal hypotheses are (1) very peaked in values of the mass of the  $HH$  candidate system near the value of the resonance mass considered and (2) considered across a very broad range of signal mass hypotheses. The resonant searches are therefore split into resolved and boosted topologies based on Lorentz boost of the decay products, with the resolved channel as one of the primary focuses of this thesis. Further, several analysis design decisions are made to allow for sensitivity to a broad range of masses – in particular, though sensitivity is limited at lower values of  $m_{HH}$  relative to other channels *TODO: Combination, bbyy* due to the challenging background topology, retaining and properly reconstructing these low mass events allows the  $b\bar{b}b\bar{b}$  channel to retain sensitivity up until the kinematic threshold at 250 GeV.

In contrast, non-resonant signal hypotheses are quite broad in  $m_{HH}$ , and have a much more limited mass range, with Standard Model production peaking near 400 GeV, and the majority of the analysis sensitivity able to be captured with a resolved topology. Even for

1635 Beyond the Standard Model signal hypotheses, which may have more events at low  $m_{HH}$ ,  
 1636 the non-resonant nature of the production allows the  $b\bar{b}b\bar{b}$  channel to retain sensitivity while  
 1637 discarding much of the challenging low mass background. Such freedom allows for decisions  
 1638 which focus on improved background modeling for the middle to upper  $HH$  mass regime,  
 1639 resulting in improved modeling and smaller uncertainties than would be obtained with a  
 1640 more generic approach.

1641 Both searches are presented in the following, with emphasis on particular motivations for,  
 1642 and consequences of, the various design decisions involved for each respective set of signal  
 1643 hypotheses.

1644 The analyses improve upon previous work [82] in several notable ways. The resonant  
 1645 search leverages a Boosted Decision Tree (BDT) based pairing algorithm, offering improved  
 1646  $HH$  pairing efficiency over a broad mass spectrum. The non-resonant adopts a different  
 1647 approach, with a simplified algorithm based on the minimum angular distance ( $\Delta R$ ) between  
 1648 jets in a Higgs candidate. Such an approach very efficiently discards low mass background  
 1649 events, resulting in an easier to estimate background with reduced systematic uncertainties.

1650 A particular contribution of this thesis is the background estimation, which uses a novel,  
 1651 neural network based approach, offering improved modeling over previous methods, as well  
 1652 as the ability to model correlations between observables. While all aspects of the analysis of  
 1653 course contribute to the final result, the author of this thesis wishes to emphasize that the  
 1654 background estimate, with the corresponding uncertainties and all other associated decisions,  
 1655 really is the core of the  $HH \rightarrow b\bar{b}b\bar{b}$  analysis – the development of this procedure, and all  
 1656 associated decisions, is similarly the core of this thesis work.

1657 ATLAS has performed a variety of searches in complementary decay channels as well,  
 1658 notably for early Run 2 in the  $b\bar{b}W^+W^-$  [83],  $b\bar{b}\tau^+\tau^-$  [84],  $W^+W^-W^+W^-$  [85],  $b\bar{b}\gamma\gamma$  [86],  
 1659 and  $W^+W^-\gamma\gamma$  [87] final states, which were combined along with  $b\bar{b}b\bar{b}$  in [21]. ATLAS has  
 1660 also released a variety of full Run 2 results, including boosted  $b\bar{b}\tau^+\tau^-$  [88], VBF  $b\bar{b}b\bar{b}$  [17],  
 1661  $b\bar{b}\ell\nu\ell\nu$  [89], and  $b\bar{b}\gamma\gamma$  [90].

1662 CMS has also performed searches for resonant production of Higgs boson pairs in the

1663  $b\bar{b}b\bar{b}$  final state (among others) at  $\sqrt{s} = 8$  TeV [91] and  $\sqrt{s} = 13$  TeV [92]. CMS have also  
1664 performed a combination of their searches in the  $b\bar{b}b\bar{b}$ ,  $b\bar{b}\tau^+\tau^-$ ,  $b\bar{b}\gamma\gamma$ , and  $b\bar{b}VV$  channels  
1665 in [93].

1666 This analysis also benefits from improvements to ATLAS jet reconstruction and calibration,  
1667 and flavour tagging [77]. In particular, this analysis benefits from the introduction of particle  
1668 flow jets [71]. These make use of tracking information to supplement calorimeter energy  
1669 deposits, improving the angular and transverse momentum resolution of jets by better  
1670 measuring these quantities for charged particles in those jets.

1671 The analysis also benefits from the new DL1r ATLAS flavour tagging algorithm. Whereas  
1672 the flavour tagging algorithm used in the previous analysis (MV2) used a boosted decision  
1673 tree (BDT) to combine the output of various low level algorithms, DL1r (and the baseline  
1674 DL1 algorithm) uses a deep neural network to do this combination. In addition to the low  
1675 level algorithms used as inputs to MV2, DL1 includes a variety of additional variables used  
1676 for  $c$ -tagging. DL1r further incorporates RNNIP, a recurrent neural network designed to  
1677 identify  $b$ -jets using the impact parameters, kinematics, and quality information of the tracks  
1678 in the jets, while also taking into account the correlations between the track features.

1679 The overall analysis sensitivity further benefits from a factor of  $\sim 4.6$  increase in integrated  
1680 luminosity.

## 1681 7.1 Data and Monte Carlo Simulation

1682 Both the resonant and non-resonant searches are performed on the full ATLAS Run 2 dataset,  
1683 consisting of  $\sqrt{s} = 13$  TeV proton-proton collision data taken from 2016 to 2018 inclusive.  
1684 Data taken in 2015 is not used due to a lack of trigger jet matching information and  $b$ -jet  
1685 trigger scale factors. The integrated luminosity collected and usable in this analysis<sup>1</sup> was:

- 1686 •  $24.6 \text{ fb}^{-1}$  in 2016

---

<sup>1</sup>approximately  $9 \text{ fb}^{-1}$  of data was collected but could not be used in this analysis due to an inefficiency in the  $b$ -jet triggers at the start of 2016 [94]

- 1687     •  $43.65 \text{ fb}^{-1}$  in 2017

- 1688     •  $57.7 \text{ fb}^{-1}$  in 2018

1689     This gives a total integrated luminosity of  $126 \text{ fb}^{-1}$ . This is lower than the  $139 \text{ fb}^{-1}$  ATLAS  
 1690    collected during Run 2 [95] due to the inefficiency described in footnote 1 as well as the  
 1691     $3.2 \text{ fb}^{-1}$  of 2015 data which is unused due to the trigger scale factor issue mentioned above.

1692     In this analysis, Monte Carlo samples are used purely for modelling signal processes. The  
 1693    background is strongly dominated by events produced by QCD multijet processes, which  
 1694    are difficult to correctly model in simulation. This necessitates the use of a data-driven  
 1695    background modelling technique, which is described in Section 7.6.

1696     The scalar resonance signal model is simulated at leading order in  $\alpha_s$  using MADGRAPH  
 1697    [52]. Hadronization and parton showering are done using HERWIG 7 [53][54] with EVTGEN [56],  
 1698    and the nominal PDF is NNPDF 2.3 LO. In practice this is implemented as a two Higgs  
 1699    doublet model where the new neutral scalar is produced through gluon fusion and required  
 1700    to decay to a pair of SM Higgs bosons. The heavy scalar is assigned a width much smaller  
 1701    than detector resolution, and the other 2HDM particles do not enter the calculation.

1702     Scalar samples are produced at resonance masses between 251 and 900 GeV and the  
 1703    detector simulation is done using AtlFast-II [61]. In addition the samples at 400 GeV and  
 1704    900 GeV are also fully simulated to verify that the use of AtlFast-II is acceptable. For higher  
 1705    masses, as well as for the boosted analysis, samples are produced between 1000 and 5000 GeV,  
 1706    and the detector is fully simulated. As discussed in Chapter 4, an outstanding issue with  
 1707    AtlFast-II is the modeling of jet substructure. While such variables are not used for the  
 1708    resolved analysis, the boosted analysis begins at 900 GeV, motivating the different detector  
 1709    simulation in these two regimes.

1710     The spin-2 resonance signal model is also simulated at LO in  $\alpha_s$  using MADGRAPH.  
 1711    Hadronization and parton showering are done using PYTHIA 8 [55] with EVTGEN, and the  
 1712    nominal PDF is NNPDF 2.3 LO. In practice this is implemented as a Randall-Sundrum  
 1713    graviton with  $c = 1.0$ .

1714 Spin-2 resonance samples are produced at masses between 251 and 5000 GeV, and these  
1715 samples are all produced with full detector simulation.

1716 For the non-resonant search, samples are produced at values of  $\kappa_\lambda = 1.0$  and 10.0, and are  
1717 simulated using POWHEG BOX v2 generator [49–51] at next-to-leading order (NLO), with full  
1718 NLO corrections with finite top mass, using the PDF4LHC [96] parton distribution function  
1719 (PDF) set. Parton showers and hadronization are simulated with PYTHIA 8.

1720 Alternative ggF samples are simulated at NLO using POWHEG BOX v2, but instead using  
1721 HERWIG 7 [97] for parton showering and hadronization. The comparison between these two  
1722 is used to assess an uncertainty on the parton showering.

## 1723 7.2 Triggers and Object Definitions

1724 To maximize analysis sensitivity, a combination of multi- $b$ -jet triggers is used. Due to the use  
1725 of events with two  $b$ -tagged jets in the background estimate, such triggers have a maximum  
1726 requirement of two  $b$ -tagged jets. For the resonant analysis, a combination of triggers of  
1727 various topologies is used, namely

- 1728 • 2b + HT, which requires two  $b$ -tagged jets and a minimum value of of  $H_T$ , defined to  
1729 be the scalar sum of  $p_T$  across all jets in the event.
- 1730 • 2b + 2j, which requires two  $b$ -tagged jets and two other jets matching some kinematic  
1731 requirements
- 1732 • 2b + 1j, which requires two  $b$ -tagged jets and one other jet matching some kinematic  
1733 requirements
- 1734 • 1b, which requires one  $b$ -tagged jet

1735 Due to minimal contributions from some of these triggers for the Standard Model non-resonant  
1736 signal, a simplified strategy relying entirely on 2b + 1j and 2b + 2j triggers is used for the  
1737 non-resonant search.

1738 While the use of multiple triggers is beneficial for analysis sensitivity, it comes with some  
 1739 complications. Namely, a set of scale factors must be assigned to simulated events account for  
 1740 differences in trigger efficiency between real and simulated events. Because these scale factors  
 1741 may differ between triggers, the use of multiple triggers becomes complicated: an event may  
 1742 pass more than one trigger, while trigger scale factors are only provided for individual triggers.

1743 To simplify this calculation, a set of hierarchical offline selections is applied, closely  
 1744 mimicking the trigger selection. Based on these selections, events are sorted into categories  
 1745 (*trigger buckets*), after which the decision of a *single trigger* is checked.

1746 The resonant search applies such categorization in the following way, with selections  
 1747 considered in order:

- 1748 1. If the leading jet is  $b$ -tagged with  $p_T > 325 \text{ GeV}$ , the event is in the  $1b$  trigger category.
- 1749 2. Otherwise, if the leading jet is not  $b$ -tagged, but has  $p_T > 168.75 \text{ GeV}$ , the event is in  
 1750 the  $2b + 1j$  trigger category.
- 1751 3. If neither of the first two selections pass, if the scalar sum of jet  $p_T$ s,  $H_T > 900 \text{ GeV}$ ,  
 1752 the event falls into the  $2b + HT$  trigger category.
- 1753 4. Events that do not pass any of the above offline selections are in the  $2b + 2j$  trigger  
 1754 category.

1755 Corresponding triggers are then checked in each category, and the final set of events consists  
 1756 of those events that pass the trigger decision in their respective categories.

1757 For the resonant search, the  $2b + 1j$  and  $2b + 2j$  triggers are the dominant categories,  
 1758 containing roughly 26 % and 49 % of spin-2 events, evaluated on MC16d samples with  
 1759 resonance masses between 300 and 1200 GeV. Notably, the  $1b$  trigger efficiency is largest at  
 1760 high ( $> 1 \text{ TeV}$ ) resonance masses.

1761 For the non-resonant search, it was noted that the  $1b$  trigger has minimal contribution,  
 1762 while the  $2b + HT$  events are largely captured by the  $2b + 2j$  trigger. Therefore, for, a

1763 simplified scheme is considered, with selections:

- 1764 1. If the 1st leading jet has  $p_T > 170 \text{ GeV}$  and the 3rd leading jet has  $p_T > 70 \text{ GeV}$ , the event is in the  $2b + 1j$  trigger category.
- 1765
- 1766 2. Otherwise, the event is in the  $2b + 2j$  trigger category.

### 1767 7.3 Analysis Selection

1768 After the trigger selections of Section 7.2, a variety of selections on the analysis objects are made, with the goal of (1) reconstructing a  $HH$ -like topology and (2) suppressing contributions 1769 1770 from background processes.

1771 Both analyses begin with a common pre-selection, requiring at least four  $R = 0.4$  anti- $k_T$  jets with  $|\eta| < 2.5$  and  $p_T > 40 \text{ GeV}$ . The  $|\eta| < 2.5$  requirement is necessary for  $b$ -tagging due to the coverage of the ATLAS tracking detector (see Chapter 3), while the  $p_T > 40 \text{ GeV}$  requirement is motivated by the trigger thresholds. A low  $p_T$  category, which would include events failing the analysis selection due to this  $p_T$  cut, was considered for the non-resonant search, but was found to contribute minimal sensitivity. At least two of the jets passing this pre-selection are required to be  $b$ -tagged, and additional  $b$ -tagging requirements are made to define the following regions:

- 1779 • “2 $b$  Region”: require exactly two  $b$ -tagged jets, used for background estimation
- 1780 • “4 $b$  Region”: require at least (but possibly more) four  $b$ -tagged jets, used as a signal region for both resonant and non-resonant searches

1782 The non-resonant analysis additionally defines two 3 $b$  regions:

- 1783 • “3 $b+1$  loose Region”: require exactly three  $b$ -tagged jets which pass the 77 % b-tagging working point (nominal) and one additional jet that fails the 77 % b-tagging working point but passes the *looser* 85 % b-tagging working point. Used as a signal region for the non-resonant search.
- 1784
- 1785
- 1786

- 1787     • “3 $b$ +1 fail Region”: complement of 3 $b$ +1 loose. Require exactly three  $b$ -tagged jets  
 1788       which pass the 77 % b-tagging working point, but require that none of the remaining jets  
 1789       pass the 85 % b-tagging working point. Used as a validation region for the non-resonant  
 1790       search.

1791   After these requirements, four jets are chosen, ranked first by  $b$ -tagging requirement and then  
 1792   by  $p_T$  (e.g. for the 2 $b$  region, the jets chosen are the two  $b$ -tagged jets and the two highest  $p_T$   
 1793   non-tagged jets; for the 4 $b$  region, the jets are the four highest  $p_T$   $b$ -tagged jets). To match  
 1794   the topology of a  $HH \rightarrow b\bar{b}b\bar{b}$  event, these four jets are then *paired* into *Higgs candidates*: the  
 1795   four jets are split into two sets of two, and each of these pairs is used to define a reconstructed  
 1796   object that is a proxy for a Higgs in a  $HH$  event.

1797   For four jets there are three possible pairings. For signal events, a correct pairing can be  
 1798   identified (provided all necessary jets pass pre-selection) using the truth information of the  
 1799   Monte Carlo simulation, and such information may be used to design/select an appropriate  
 1800   pairing algorithm. This is only part of the story, however. The vast majority of the events in  
 1801   data do *not* include a real  $HH$  decay (this is a search for a reason!), either because the event  
 1802   originates from a background process (e.g. for 4 $b$  events), or because the selection is not  
 1803   designed to maximize the signal (e.g. 2 $b$  events). As the pairing is part of the selection, it must  
 1804   still be run on such events, such that various algorithms which achieve similar performance  
 1805   in terms of pairing efficiency may have vastly different impacts in terms of the shape of the  
 1806   background and the biases inherent in the background estimation procedure. The interplay  
 1807   between these two facets of the pairing is an important part of the choices made for this  
 1808   analysis.

1809   A comparison of different shapes due to three different paring strategies is shown in Figure  
 1810   7.1.

1811    7.3.1 *Resonant Pairing Strategy*

1812    For the resonant analysis, a Boosted Decision Tree (BDT) is used for the pairing. The boosted  
 1813    decision tree is given the total separation between the two jets in each of the two pairs ( $\Delta R_1$   
 1814    and  $\Delta R_2$ ), the pseudo-rapidity separation between the two jets in each pair ( $\Delta\eta_1$  and  $\Delta\eta_2$ ),  
 1815    and the angular separation between the two jets in each pair in the  $x - y$  plane ( $\Delta\phi_1$  and  
 1816     $\Delta\phi_2$ ). The total separations ( $\Delta R_s$ ) are provided in addition to the components in order to  
 1817    avoid requiring the boosted decision tree to reconstruct these variables in order to use them.  
 1818    For these variables, pair 1 is the pair with the highest scalar sum of jet  $p_T$ s, and pair 2 the  
 1819    other pair.

1820    The boosted decision tree is also parameterized on the di-Higgs mass ( $m_{HH}$ ) by providing  
 1821    this as an additional feature. Since the boosted decision tree is trained on correct and  
 1822    incorrect pairings in signal events, there will be exactly one correct pairing and two incorrect  
 1823    pairings in the training set for each  $m_{HH}$  value present in that set. As a result, this variable  
 1824    cannot, in itself, distinguish a correct pairing from an incorrect pairing, and therefore the  
 1825    inclusion of this variable simply serves to parameterize the BDT on  $m_{HH}$ <sup>2</sup>.

1826    The boosted decision tree was trained on one quarter of the total AFII simulated scalar  
 1827    MC statistics, using the Gradient-based One Side Sampling (GOSS) algorithm which allows  
 1828    rapid training with very large datasets. A preselection was applied requiring events to have  
 1829    four jets with a  $p_T$  of at least 35 GeV. Note that this is a looser requirement than the 40 GeV  
 1830    used in the analysis selection, and is meant to increase the available statistics for events with  
 1831    low  $m_{HH}$  and to ensure a better performance as a function of that variable. Events were also  
 1832    required to have four distinct jets that could be geometrically matched (to within  $\Delta R \leq 0.4$ )  
 1833    to the  $b$ -quarks. The events used to train the BDT were not included when the analysis was  
 1834    run on these signal simulations. The boosted decision tree was constructed with the following  
 1835    hyperparameters:

1836    `min_data_in_leaf=50,`

---

<sup>2</sup>That is, the conditions placed on the other variables by the BDT vary with  $m_{HH}$ .

1837 num\_leaves=180,  
 1838 learning\_rate=0.01

1839 These hyperparameters were optimized using a Bayesian optimization procedure [98].  
 1840 Three fold cross-validation was used to perform this optimization without the need for an  
 1841 additional sample, while avoiding over-training on signal events.

1842 *7.3.2 Non-resonant Pairing Strategy*

1843 For the non-resonant analysis, a simpler pairing algorithm is used, which proceeds as follows:  
 1844 in a given event, Higgs candidates for each possible pairing are sorted by the  $p_T$  of the vector  
 1845 sum of constituent jets. The angular separation,  $\Delta R$  is computed between jets in the each of  
 1846 the leading Higgs candidates, and the pairing with the smallest separation ( $\Delta R_{jj}$ ) is selected.  
 1847 This method will be referred to as  $\min \Delta R$  in the following.

1848 The primary motivation for the use of this pairing in the non-resonant search is a *smooth*  
 1849 *mass plane*: by efficiently discarding low mass events,  $\min \Delta R$  removes the background peak  
 1850 present in the resonant search while maintaining good pairing efficiency for the Standard  
 1851 Model non-resonant signal. This facilitates a background estimate with small kinematic bias  
 1852 – the region in which the background estimate is derived is more similar to the signal region.

1853 Along with discarding low mass background, there is a corresponding loss of low mass  
 1854 signal. This predominantly impacts points away from the Standard Model (see Figure 7.2),  
 1855 but, because the  $4b$  channel has the strongest contribution near the Standard Model and  
 1856 because of the large low mass background present with other pairing methods, the impact on  
 1857 analysis sensitivity is mitigated. The  $\min \Delta R$  pairing is thus adopted for the non-resonant  
 1858 search.

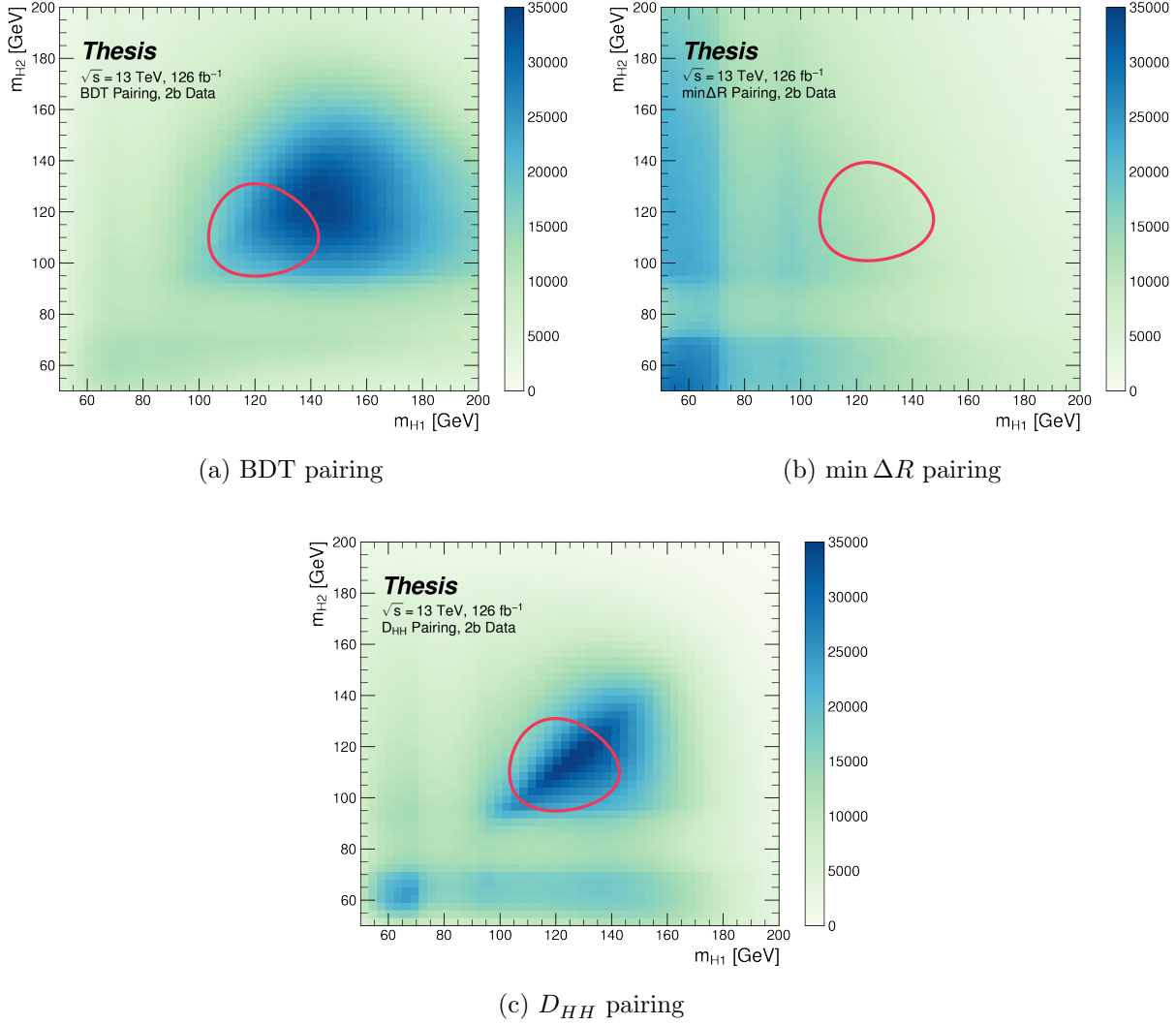


Figure 7.1: Comparison of  $m_{H1}$  vs  $m_{H2}$  planes for the full Run 2 2b dataset with different pairings. As evidenced, this choice significantly impacts where events fall in this plane, and therefore which events fall into the various kinematic regions defined in this plane (see Section 7.5). Respective signal regions are shown for reference, with the  $\min \Delta R$  signal region shifted slightly up and to the right to match the non-resonant selection. Note that the band structure around 80 GeV in both  $m_{H1}$  and  $m_{H2}$  is introduced by the top veto described in Section 7.4.

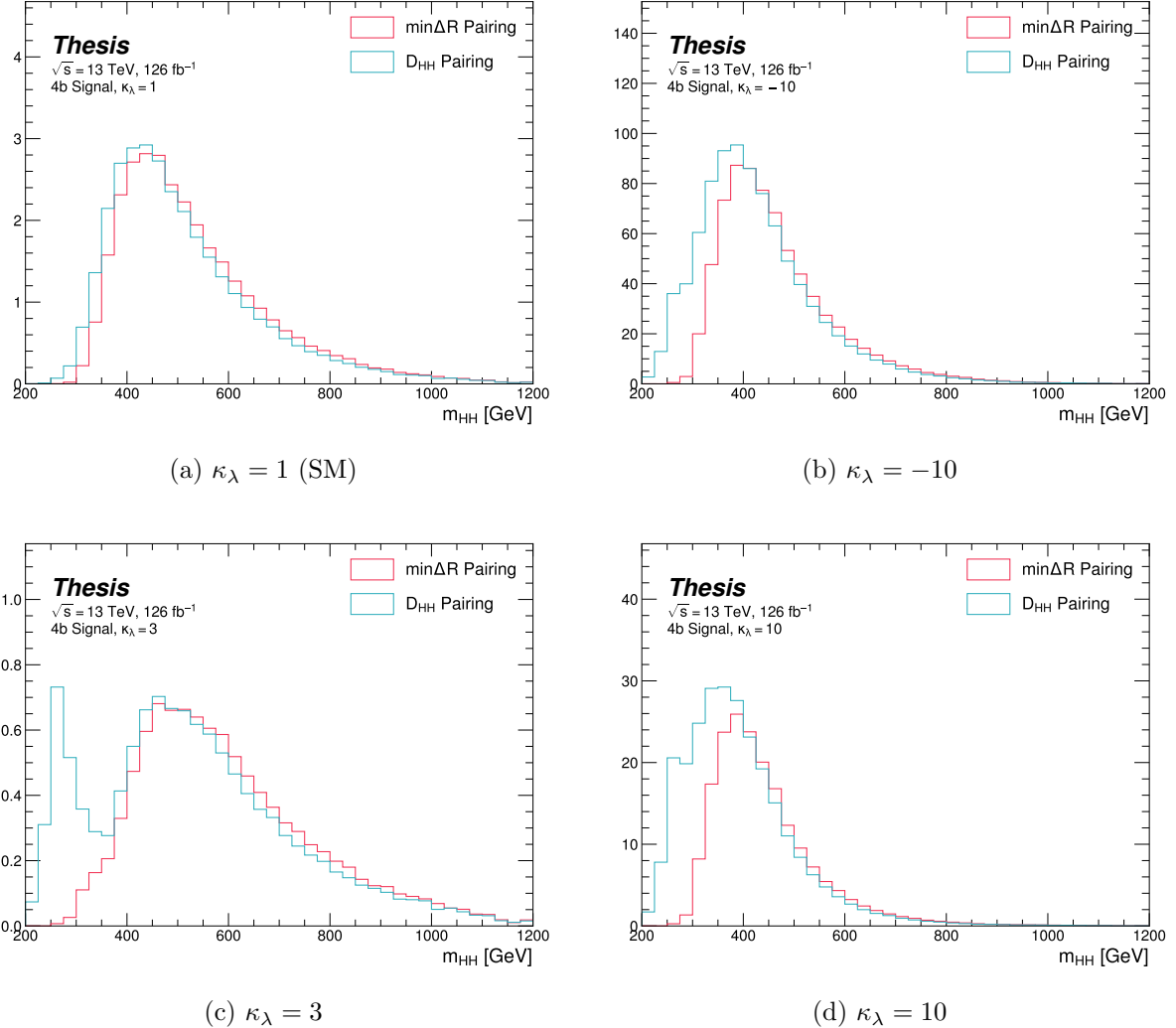


Figure 7.2: Comparison of signal distributions in the respective signal regions for the  $\min \Delta R$  and  $D_{HH}$  pairing for various values of the Higgs trilinear coupling in the respective signal regions. The distributions are quite similar at the Standard Model point, but for other variations,  $\min \Delta R$  does not pick up the low mass features.

1859 **7.4 Background Reduction and Top Veto**

1860 Choosing a pairing of the four b-tagged jets fully defines the di-Higgs candidate system used  
1861 for each event in the remainder of the analysis chain. A requirement of  $|\Delta\eta_{HH}| < 1.5$  on this  
1862 di-Higgs candidate system mitigates QCD multijet background.

1863 Figure ?? illustrates this variable in the validation region (see Section ??). It demonstrates  
1864 that this selection rejects only a small fraction of signal, but a significant fraction of data  
1865 (which, in the validation region, is a good approximation of pure background).

1866 In order to mitigate the hadronic  $t\bar{t}$  background, a top veto is then applied, removing  
1867 events consistent with a  $t \rightarrow b(W \rightarrow q_1\bar{q}_2)$  decay.

1868 The jets in the event are separated into *HC jets* which are the four jets used to build the  
1869 Higgs candidates, and *non-*HC jets**, the other jets (passing the  $p_T$  and  $|\eta|$  requirements) in  
1870 the event.

1871  $W$  candidates are built by forming all possible pairs of all jets in each event. With  $n$  jets,  
1872 there are  $\binom{n}{2}$  such pairs.  $t$  candidates are then built by pairing each  $W$  candidate with each  
1873 HC jet (for  $4\binom{n}{2}$  combinations). Note that all jets in a  $t$  candidate must be distinct (i.e. a  
1874 HC jet may not be used both on its own and in a  $W$  candidate).

With  $m_t$  denoting the invariant mass of the  $t$  candidate, and  $m_W$  the invariant mass of the  $W$  candidate, the quantity

$$X_{Wt} = \sqrt{\left(\frac{m_W - 80.4 \text{ GeV}}{0.1 \cdot m_W}\right)^2 + \left(\frac{m_t - 172.5 \text{ GeV}}{0.1 \cdot m_t}\right)^2} \quad (7.1)$$

1875 is constructed for each combination.

1876 Events are then vetoed if the minimum  $X_{Wt}$  over all combinations is less than 1.5.

1877 The same definitions and procedures are used for both the resonant and non-resonant  
1878 analyses. However, for the non-resonant search, the top candidates considered for  $X_{Wt}$  have  
1879 the additional requirement that the jet used for the  $b$  is  $b$ -tagged. While this is identical to  
1880 the resonant analysis by definition for  $4b$  events, it does change the set of events considered in  
1881 lower tag regions, in particular for the  $2b$  events considered in the derivation of the background

1882 estimate. Such a change is found to reduce the impact of background systematics by increasing

1883  $2b$  support in the high  $X_{Wt}$  kinematic region. *TODO: Insert plot*

1884 **7.5 Kinematic Region Definition**

As has been mentioned, an important piece of the analysis is the plane defined by the two Higgs candidate masses (the *Higgs candidate mass plane*). After the selection described above, a signal region is defined by requiring  $X_{HH} < 1.6$ , where:

$$X_{HH} = \sqrt{\left(\frac{m(H_1) - c_1}{0.1 \cdot m(H_1)}\right)^2 + \left(\frac{m(H_2) - c_2}{0.1 \cdot m(H_2)}\right)^2} \quad (7.2)$$

1885 with  $m(H_1)$ ,  $m(H_2)$  the leading and subleading Higgs candidate masses,  $c_1$  and  $c_2$  correspond  
1886 to the center of the signal region, and the denominator provides a Higgs candidate mass  
1887 dependent resolution of 10 %. For consistency with the  $HH$  decay hypothesis,  $c_1$  and  $c_2$   
1888 are nominally (125 GeV, 125 GeV). However, these are allowed to vary due to energy loss,  
1889 with specific values chosen described below. The selection of these values is one of several  
1890 significant differences between the regions defined for the resonant and non-resonant search.  
1891 We describe both below.

1892 **7.5.1 Resonant Kinematic Regions**

1893 For the resonant analysis, the signal region is centered at (120 GeV, 110 GeV) to account for  
1894 energy loss leading to the Higgs masses being under-reconstructed. Note that leading and  
1895 subleading Higgs candidates are defined according to the *scalar sum* of constituent jet  $p_T$ .

For the background estimation, two regions are defined which are roughly concentric around the signal region: a *validation region* which consists of those events not in the signal region, but which do pass

$$\sqrt{(m(H_1) - 1.03 \times 120 \text{ GeV})^2 + (m(H_2) - 1.03 \times 110 \text{ GeV})^2} < 30 \text{ GeV} \quad (7.3)$$

and a *control region* which consists of those events not in the signal or validation regions, but which do pass

$$\sqrt{(m(H_1) - 1.05 \times 120 \text{ GeV})^2 + (m(H_2) - 1.05 \times 110 \text{ GeV})^2} < 45 \text{ GeV} \quad (7.4)$$

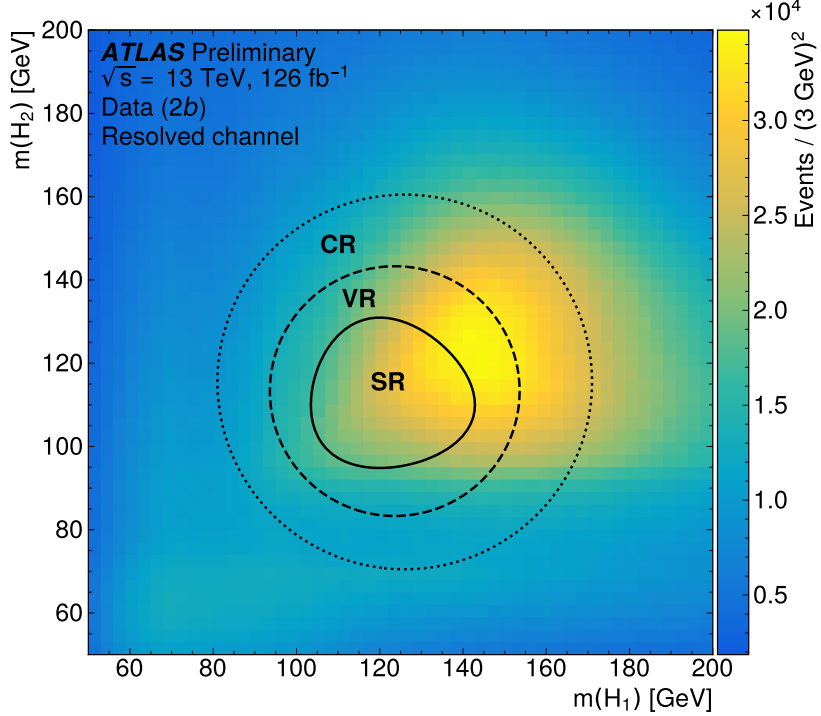


Figure 7.3: Regions used for the resonant search, shown on the  $2b$  data mass plane. The outermost region (the “control region”) is used for derivation of the nominal background estimate. The innermost region is the signal region, where the signal extraction fit is performed. The region in between (the “validation region”) is used for the assessment of an uncertainty.

1896 For simplicity, the SR/VR/CR definitions from the early Run 2 paper [82] were chosen  
1897 for the resonant analysis, but were found to be close to optimal. These regions are shown in  
1898 Figure 7.3.

### 1899 7.5.2 Non-resonant Kinematic Regions

1900 For the non-resonant analysis the signal region is centered at  $(124 \text{ GeV}, 117 \text{ GeV})$ , corre-  
1901 sponding to the means of *correctly paired* Standard Model signal events. The shape of the  
1902 signal region (other than this change of center) was found to remain optimal.

1903 For the non-resonant search, leading and subleading Higgs candidates are defined according  
 1904 to the *vector sum* of constituent jet  $p_T$ , more closely corresponding to the  $1 \rightarrow 2$  decay  
 1905 assumption behind the min  $\Delta R$  pairing algorithm.

1906 Two areas for improvement were identified in the resonant analysis, which will be dis-  
 1907 cussed in more detail below: *signal contamination* of the validation region (which impacts  
 1908 the uncertainty assessed due to extrapolation) and *large nuisance parameter pulls* on this  
 1909 uncertainty, corresponding to a rough assumption that the validation region is closer to the  
 1910 signal region in the mass plane, and so offers a better estimate of the signal region.

To mitigate these two issues, a redesign of the control and validation regions was performed for the non-resonant analysis. The outer boundary defined by the shifted resonant control region:

$$\sqrt{(m(H_1) - 1.05 \times 124 \text{ GeV})^2 + (m(H_2) - 1.05 \times 117 \text{ GeV})^2} < 45 \text{ GeV} \quad (7.5)$$

1911 is kept, roughly corresponding to combining the regions used for the resonant analysis. In  
 1912 order to assess the variation of the background estimate, two sets of regions are desired, so  
 1913 this combined region is split into *quadrants*, that is, divided into four pieces along axes that  
 1914 intersect with the signal region center. To avoid kinematic bias, quadrants on opposite sides  
 1915 of the signal region are paired, with these pairs corresponding to the non-resonant control  
 1916 and validation regions.

1917 The particular orientation of the regions is chosen such that region centers align with the  
 1918 leading and subleading Higgs candidate masses, corresponding to a set of axes rotated at  
 1919  $45^\circ$ , with the “top” and “bottom” quadrants together comprising the control region, and the  
 1920 other set (“left” and “right”) the validation region. These regions are shown in Figure 7.4

1921 This design of regions includes a set of events closer to the signal region in the mass plane,  
 1922 leveraging the assumption that these events are more similar to signal region events, while  
 1923 also including events further away from the signal region, mitigating signal contamination.  
 1924 This region selection is found to have good performance in alternate validation regions (see  
 1925 Section ??).

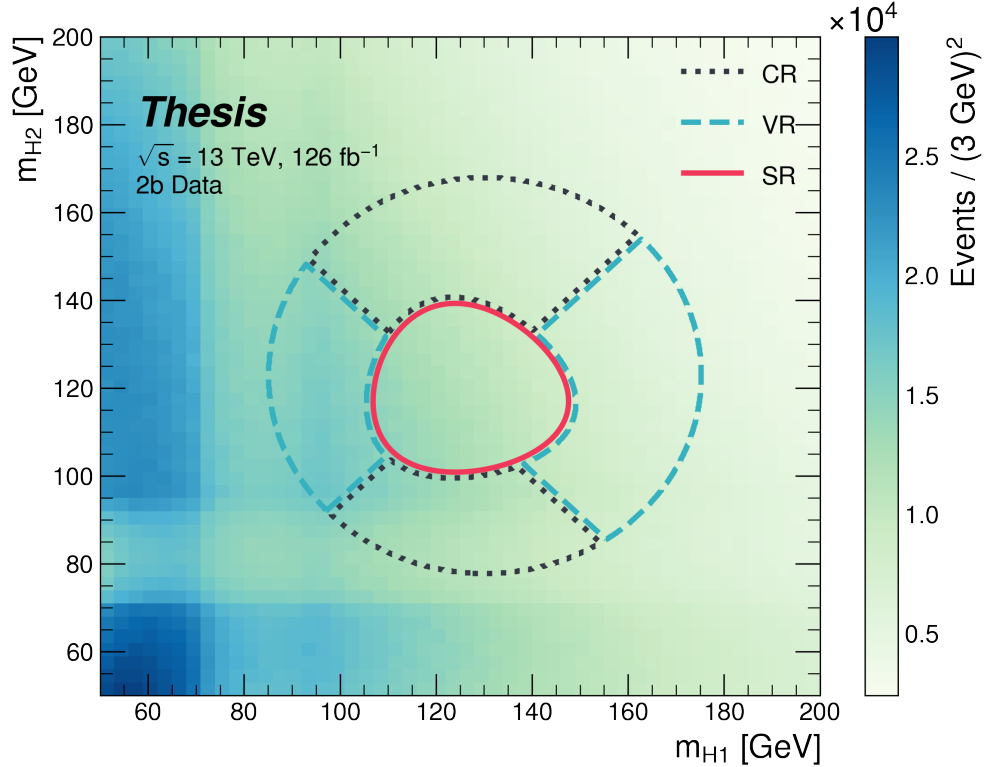


Figure 7.4: Regions used for the non-resonant search. The “top” and “bottom” quadrants together comprise the control region, in which the nominal background estimate is derived. The “left” and “right” quadrants together comprise the validation region, which is used to assess an uncertainty. The signal region, in the center, is where the signal extraction fit is performed.

1926    7.5.3    *Discriminating Variable*

1927    The discriminant used for the resonant analysis is *corrected*  $m_{HH}$ . This variable is calculated  
 1928    by re-scaling the Higgs candidate four vectors such that each  $m_H = 125 \text{ GeV}$ . These re-scaled  
 1929    four-vectors are then summed, and their invariant mass is the corrected  $m_{HH}$ . These re-scaled  
 1930    four-vectors are not used for any other purpose. The effect of this correction, which sharpens  
     the  $m_{HH}$  peak and correctly centres it, is shown in Figure 7.5.

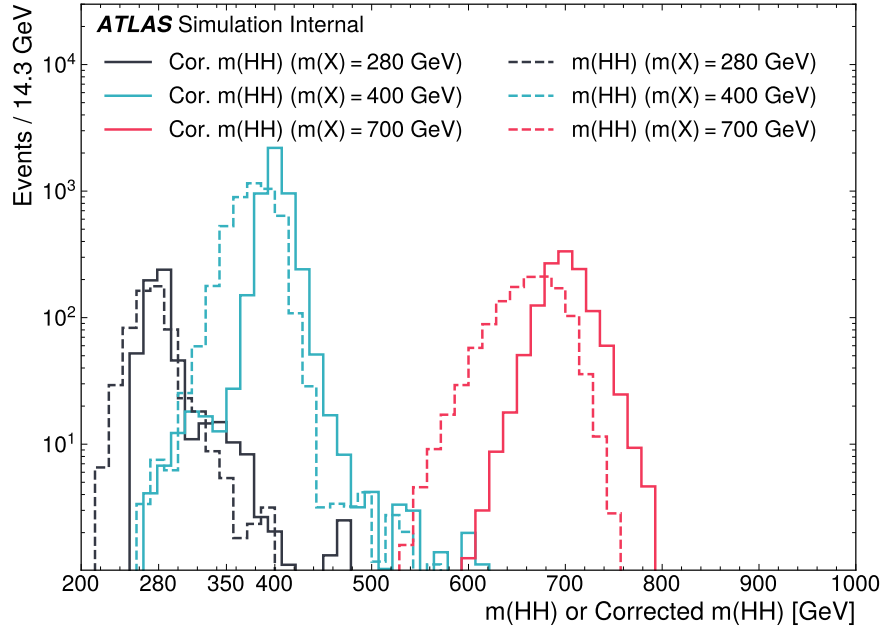


Figure 7.5: Impact of the  $m_{HH}$  correction on a range of spin-0 resonant signals. The corrected  $m_{HH}$  distributions (solid lines) are much sharper and more centered on the corresponding resonance masses than the uncorrected  $m_{HH}$  distributions (dashed).

1931

1932    For the non-resonant analysis, due to the broad nature of the signal in  $m_{HH}$ , such a  
 1933    correction is not as motivated, and, indeed, is found to have very minimal impact. The  
 1934    uncorrected  $m_{HH}$  (just referred to as  $m_{HH}$ ) is therefore used as a discriminant. To maximize

1935 sensitivity, the non-resonant analysis additionally uses two variables for categorization:  $\Delta\eta_{HH}$ ,  
 1936 an angular variable which, along with  $m_{HH}$ , fully characterizes the  $HH$  system [99], and  $X_{HH}$ ,  
 1937 the variable used for the signal region definition, which leverages the peaked structure of the  
 1938 signal in the  $(m(H_1), m(H_2))$  plane to split the signal extraction fit into lower and higher  
 1939 purity regions (highest purity near  $X_{HH} = 0$ , the center of the signal region). Distributions  
 1940 of these variables are shown in *TODO: plots*. The categorization used for this thesis has been  
 1941 optimized to be  $2 \times 2$  in these variables, with corresponding selections  $0 \leq \Delta\eta_{HH} \leq 0.75$  and  
 1942  $0.75 \leq \Delta\eta_{HH} \leq 1.5$  for  $\Delta\eta_{HH}$ , and  $0 \leq X_{HH} \leq 0.95$  and  $0.95 \leq X_{HH} \leq 1.6$  for  $X_{HH}$ .

<sup>1943</sup> **7.6 Background Estimation**

<sup>1944</sup> After the event selection described above there are two major backgrounds, QCD and  $t\bar{t}$ .  
<sup>1945</sup> A very similar approach is used for both the resonant and the non-resonant analyses, with  
<sup>1946</sup> some small modifications. This approach is notably fully data-driven, which is warranted due  
<sup>1947</sup> to the flexibility of the estimation method, as well as the high relative proportion of QCD  
<sup>1948</sup> background ( $> 90\%$ ), and allows for the use of machine learning methods in the construction  
<sup>1949</sup> of the background estimate. However, it sacrifices an explicit treatment of the  $t\bar{t}$  component.  
<sup>1950</sup> Performance of the background estimate on the  $t\bar{t}$  component is checked explicitly, and  
<sup>1951</sup> minimal impact due to  $t\bar{t}$  mismodeling is seen.

<sup>1952</sup> Contributions of single Higgs processes and  $ZZ$  are found to be negligible, and the  
<sup>1953</sup> Standard Model  $HH$  background is found to have no impact on the resonant search.

<sup>1954</sup> The foundation of the background estimate lies in the derivation of a reweighting function  
<sup>1955</sup> which matches the kinematics of events with exactly two  $b$ -tagged jets to those of events in  
<sup>1956</sup> the higher tagged regions (events with three or four  $b$ -tagged jets). The reweighting function  
<sup>1957</sup> and overall normalization are derived in the control region. Systematic bias of this estimate  
<sup>1958</sup> is assessed in the validation region.

<sup>1959</sup> For the resonant analysis, the systematic bias is a bias due to extrapolation: the validation  
<sup>1960</sup> region lies between the control and signal regions. For the non-resonant analysis, the bias  
<sup>1961</sup> instead comes from different possible interpolations of the signal region kinematics – given the  
<sup>1962</sup> choice of nominal estimate, the validation region is a conceptually equivalent, but maximally  
<sup>1963</sup> different, signal region estimate.

<sup>1964</sup> **7.6.1 The Two Tag Region**

<sup>1965</sup> Events in data with exactly two  $b$ -tagged jets are used for the data driven background estimate.  
<sup>1966</sup> The hypothesis here is that, due to the presence of multiple  $b$ -tagged jets, the kinematics of  
<sup>1967</sup> such events are similar to the kinematics of events in higher  $b$ -tagged regions (i.e. events  
<sup>1968</sup> with three and four  $b$ -tagged jets, respectively), and any differences can be corrected by a

1969 reweighting procedure. The region with three  $b$ -tagged jets is split into two  $b$ -tagging regions,  
1970 as described in Section 7.3, with the  $3b + 1$  loose region used as an additional signal region.  
1971 The lower tagged  $3b$  component ( $3b + 1$  fail) is reserved for validation of the background  
1972 modelling procedure. Events with fewer than two  $b$ -tagged jets are not used for this analysis,  
1973 as they are relatively more different from the higher tag regions.

1974 The nominal event selection requires at least four jets in order to form Higgs candidates.  
1975 For the four tag region, these are the four highest  $p_T$   $b$ -tagged jets. For the three tag regions,  
1976 these jets are the three  $b$ -tagged jets, plus the highest  $p_T$  jet satisfying a loosened  $b$ -tagging  
1977 requirement. Similarly, and following the approach of the resonant analysis, the two tag region  
1978 uses the two  $b$ -tagged jets and the two highest  $p_T$  non-tagged jets to form Higgs candidates.  
1979 Combinatoric bias from selection of different numbers of  $b$ -tagged jets is corrected as a part  
1980 of the kinematic reweighting procedure through the reweighting of the total number of jets in  
1981 the event. In this way, the full event selection may be run on two tagged events.

### 1982 7.6.2 Kinematic Reweighting

1983 The set of two tagged data events is the fundamental piece of the data driven background  
1984 estimate. However, kinematic differences from the four tag region exist and must be corrected  
1985 in order for this estimate to be useful. Binned approaches based on ratios of histograms  
1986 have been previously considered [82], [17], but are limited in their handling of correlations  
1987 between variables and by the “curse of dimensionality”, i.e. the dataset becomes sparser and  
1988 sparser in “reweighting space” as the number of dimensions in which to reweight increases,  
1989 limiting the number of variables used for reweighting. This leads either to an unstable fit  
1990 result (overfitting with finely grained bins) or a lower quality fit result (underfitting with  
1991 coarse bins).

1992 Note that even machine learning methods such as Boosted Decision Trees (BDTs) [100],  
1993 may suffer from this curse of dimensionality, as the depth of each decision tree used is limited  
1994 by the available statistics after each set of corresponding selections (cf. binning in a more  
1995 sophisticated way), limiting the expressivity of the learned reweighting function.

1996 To solve these issues, a neural network based reweighting procedure is used here. This  
 1997 is a truly multivariate approach, allowing for proper treatment of variable correlations. It  
 1998 further overcomes the issues associated with binned approaches by learning the reweighting  
 1999 function directly, allowing for greater sensitivity to local differences and helping to avoid the  
 2000 curse of dimensionality.

2001 *Neural Network Reweighting*

Let  $p_{4b}(x)$  and  $p_{2b}(x)$  be the probability density functions for four and two tag data respectively across some input variables  $x$ . The problem of learning the reweighting function between two and four tag data is then the problem of learning a function  $w(x)$  such that

$$p_{2b}(x) \cdot w(x) = p_{4b}(x) \quad (7.6)$$

from which it follows that

$$w(x) = \frac{p_{4b}(x)}{p_{2b}(x)}. \quad (7.7)$$

This falls into the domain of density ratio estimation, for which there are a variety of approaches. The method considered here is modified from [101, 102], and depends on a loss function of the form

$$\mathcal{L}(R(x)) = \mathbb{E}_{x \sim p_{2b}}[\sqrt{R(x)}] + \mathbb{E}_{x \sim p_{4b}}\left[\frac{1}{\sqrt{R(x)}}\right]. \quad (7.8)$$

where  $R(x)$  is some estimator dependent on  $x$  and  $\mathbb{E}_{x \sim p_{2b}}$  and  $\mathbb{E}_{x \sim p_{4b}}$  are the expectation values with respect to the 2b and 4b probability densities. A neural network trained with such a loss function has the objective of finding the estimator,  $R(x)$ , that minimizes this loss. It is straightforward to show that

$$\arg \min_R \mathcal{L}(R(x)) = \frac{p_{4b}(x)}{p_{2b}(x)} \quad (7.9)$$

2002 which is exactly the form of the desired reweighting function.

In practice, to avoid imposing explicit positivity constraints, the substitution  $Q(x) \equiv \log R(x)$  is made. The loss function then takes the equivalent form

$$\mathcal{L}(Q(x)) = \mathbb{E}_{x \sim p_{2b}}[\sqrt{e^{Q(x)}}] + \mathbb{E}_{x \sim p_{4b}}\left[\frac{1}{\sqrt{e^{Q(x)}}}\right], \quad (7.10)$$

with solution

$$\arg \min_Q \mathcal{L}(Q(x)) = \log \frac{p_{4b}(x)}{p_{2b}(x)}. \quad (7.11)$$

2003 Taking the exponent then results in the desired reweighting function.

2004 Note that similar methods for density ratio estimation are available [103], e.g. from a

2005 more standard binary cross-entropy loss. However, these were found to perform no better  
2006 than the formulation presented here.

2007 *Variables and Results*

2008 The neural network is trained on a variety of variables sensitive to two vs. four tag differences.

2009 To help bring out these differences, the natural logarithm of some of the variables with a  
2010 large, local change is taken. The set of training variables used for the resonant analysis is

2011 1.  $\log(p_T)$  of the 4th leading Higgs candidate jet

2012 2.  $\log(p_T)$  of the 2nd leading Higgs candidate jet

2013 3.  $\log(\Delta R)$  between the closest two Higgs candidate jets

2014 4.  $\log(\Delta R)$  between the other two Higgs candidate jets

2015 5. Average absolute value of Higgs candidate jet  $\eta$

2016 6.  $\log(p_T)$  of the di-Higgs system.

2017 7.  $\Delta R$  between the two Higgs candidates

2018 8.  $\Delta\phi$  between the jets in the leading Higgs candidate

- 2019 9.  $\Delta\phi$  between the jets in the subleading Higgs candidate
- 2020 10.  $\log(X_{Wt})$ , where  $X_{Wt}$  is the variable used for the top veto
- 2021 11. Number of jets in the event.
- 2022 The non-resonant analysis uses an identical set of variables with two notable changes
- 2023 1. The definition of  $X_{Wt}$  differs from the resonant definition (as described in Section 7.4).
- 2024 2. An integer encoding of the two trigger categories is used as an input (variable which
- 2025 takes on the value 0 or 1 corresponding to each of the two categories). This was found
- 2026 to improve a mismodeling near the tradeoff in  $m_{HH}$  of the two buckets.
- 2027 The neural network used for both resonant and non-resonant reweighting has three densely
- 2028 connected hidden layers of 50 nodes each with ReLU activation functions and a single node
- 2029 linear output. This configuration demonstrates good performance in the modelling of a variety
- 2030 of relevant variables, including  $m_{HH}$ , when compared to a range of networks of similar size.
- 2031 In practice, a given training of the reweighting neural network is subject to variation
- 2032 due to training statistics and initial conditions. An uncertainty is assigned to account for
- 2033 this (Section 7.7), which relies on training an ensemble of reweighting networks [104]. To
- 2034 increase the stability of the background estimate, the median of the predicted weight for each
- 2035 event is calculated across the ensemble. This median is then used as the nominal background
- 2036 estimate. This approach is indeed seen to be much more stable and to demonstrate a better
- 2037 overall performance than a single arbitrary training. Each ensemble used for this analysis
- 2038 consists of 100 neural networks, trained as described in Section 7.7.
- 2039 The training of the ensemble used for the nominal estimate is done in the kinematic
- 2040 Control Region. The prediction of these networks in the Signal Region is then used for the
- 2041 nominal background estimate. In addition, a separate ensemble of networks is trained in the
- 2042 Validation Region. The difference between the prediction of the nominal estimate and the

2043 estimate from the VR derived networks in the Signal Region is used to assign a systematic  
 2044 uncertainty. Further details on this systematic uncertainty are shown in Section 7.7. Note  
 2045 that although the same procedure is used for both Control and Validation Region trained  
 2046 networks, only the median estimate from the VR derived reweighting is used for assessing a  
 2047 systematic – no additional “uncertainty on the uncertainty” from VR ensemble variation is  
 2048 applied.

2049 Each reweighted estimate is normalized such that the reweighted  $2b$  yield matches the  $4b$   
 2050 yield in the corresponding training region. Note that this applies to each of the networks used  
 2051 in each ensemble, where the normalization factor is also subject to the procedure described in  
 2052 Section 7.7. As the median over these normalized weights is not guaranteed to preserve this  
 2053 normalization, a further correction is applied such that the  $2b$  yield, after the median weights  
 2054 are applied, matches the  $4b$  yield in the corresponding training region. As no preprocessing  
 2055 is applied to correct for the class imbalance between  $2b$  and  $4b$  events entering the training,  
 2056 this ratio of number of  $4b$  events ( $n(4b)$ ) over number of  $2b$  events ( $n(2b)$ ) is folded into the  
 2057 learned weights. Correspondingly, the set of normalization factors described above is near 1  
 2058 and the learned weights are centered around  $n(4b)/n(2b)$  (roughly 0.01 over the full dataset).  
 2059 This normalization procedure applies for all instances of the reweighting (e.g. those used for  
 2060 validations in Section 7.8), with appropriate substitutions of reweighting origin (here  $2b$ ) and  
 2061 reweighting target (here  $4b$ ).

2062 Note that, due to different trigger and pileup selections during each year, the reweighting  
 2063 is trained on each year separately. An approach of training all of the years together with  
 2064 a one-hot encoding was explored, but was found to have minimal benefit over the split  
 2065 years approach, and in fact to increase the systematic bias of the corresponding background  
 2066 estimate. Because of this, and because trigger selections for each year significantly impact  
 2067 the kinematics of each year, such that categorizing by year is expected to reflect groupings  
 2068 of kinematically similar events and to provide a meaningful degree of freedom in the signal  
 2069 extraction fit, the split-year approach is kept.

2070 The control region closure for the 2018 dataset is shown for the resonant search in Figures

2071 7.6 through 7.14 and for the non-resonant search in Figures 7.24 through 7.32 for 4b and  
 2072 Figures 7.42 through 7.50 for 3b1l. The impact of this control region derived reweighting  
 2073 on the validation region is shown in Figures 7.15 through 7.23 for the resonant search and  
 2074 Figures 7.33 through 7.41 for 4b and Figures 7.51 through 7.59 for 3b1l for the non-resonant  
 2075 search. Generally good performance is seen, with some occasional mis-modeling. For the  
 2076 resonant search, this is most notable in the case of individual jet  $p_T$ . Such mis-modeling  
 2077 may be corrected by including the variables in the input set, but this was found to not  
 2078 improve the modeling of  $m_{HH}$ , and so is not done here. This mis-modeling is notable for the  
 2079 non-resonant search in the leading Higgs candidate jet  $p_T$ , and is a direct consequence of the  
 2080 trigger category input, which improves modeling of  $m_{HH}$ . Results are similar for other years,  
 2081 but are not included here for brevity.

2082 One other salient feature of the non-resonant plots is the distributions of  $m_{H1}$  and  $m_{H2}$ ,  
 2083 which emphasize the quadrant region definitions – the control region has a peak around  
 2084 125 GeV in  $m_{H1}$ , which may be thought of as “signal region-like”, motivating this alignment,  
 2085 though consequently the distribution of  $m_{H2}$  is quite bimodal. The reverse is true for the  
 2086 validation region.

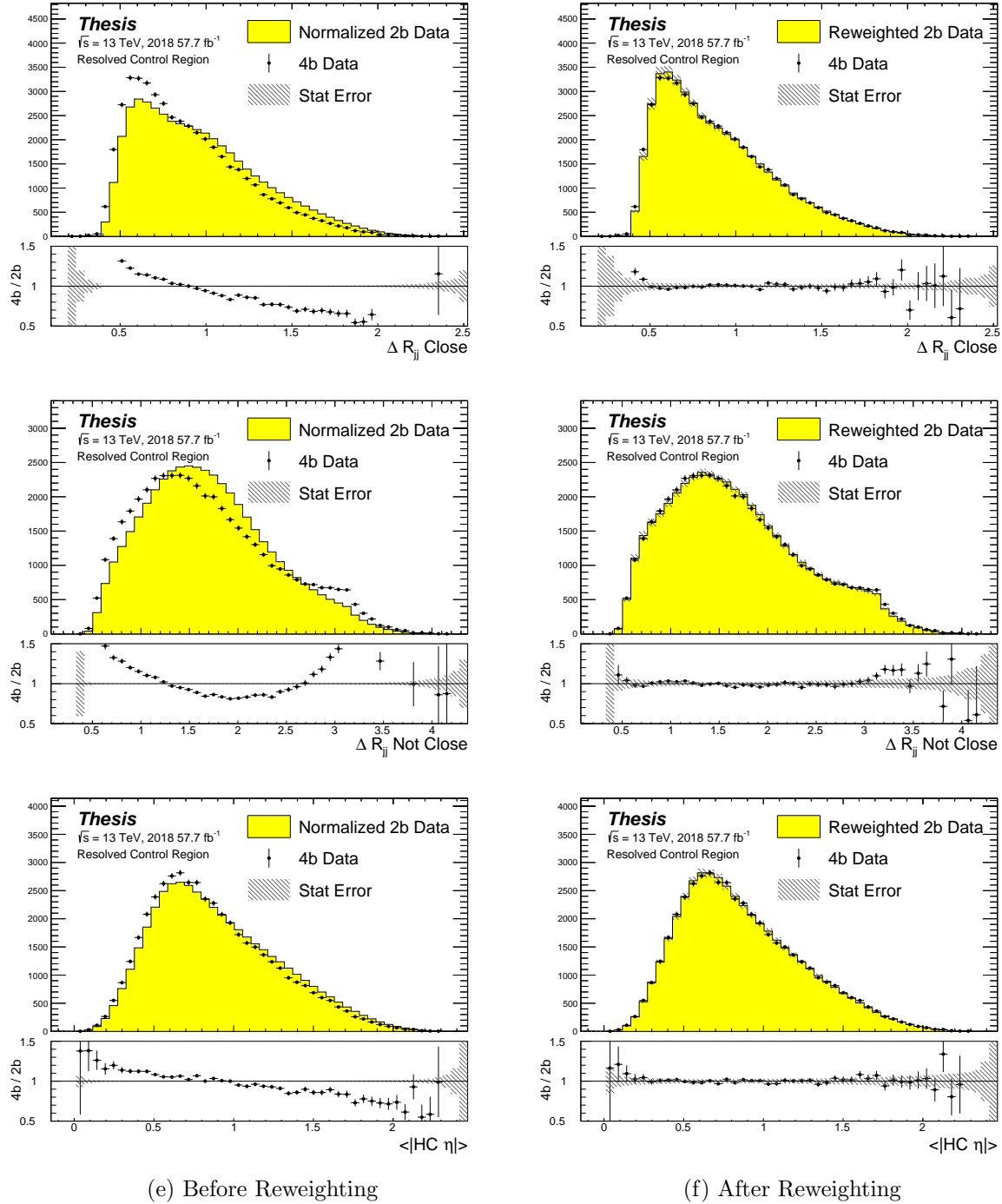


Figure 7.6: **Resonant Search:** Distributions of  $\Delta R$  between the closest Higgs Candidate jets,  $\Delta R$  between the other two, and average absolute value of HC jet  $\eta$  before and after CR derived reweighting for the 2018 Control Region.

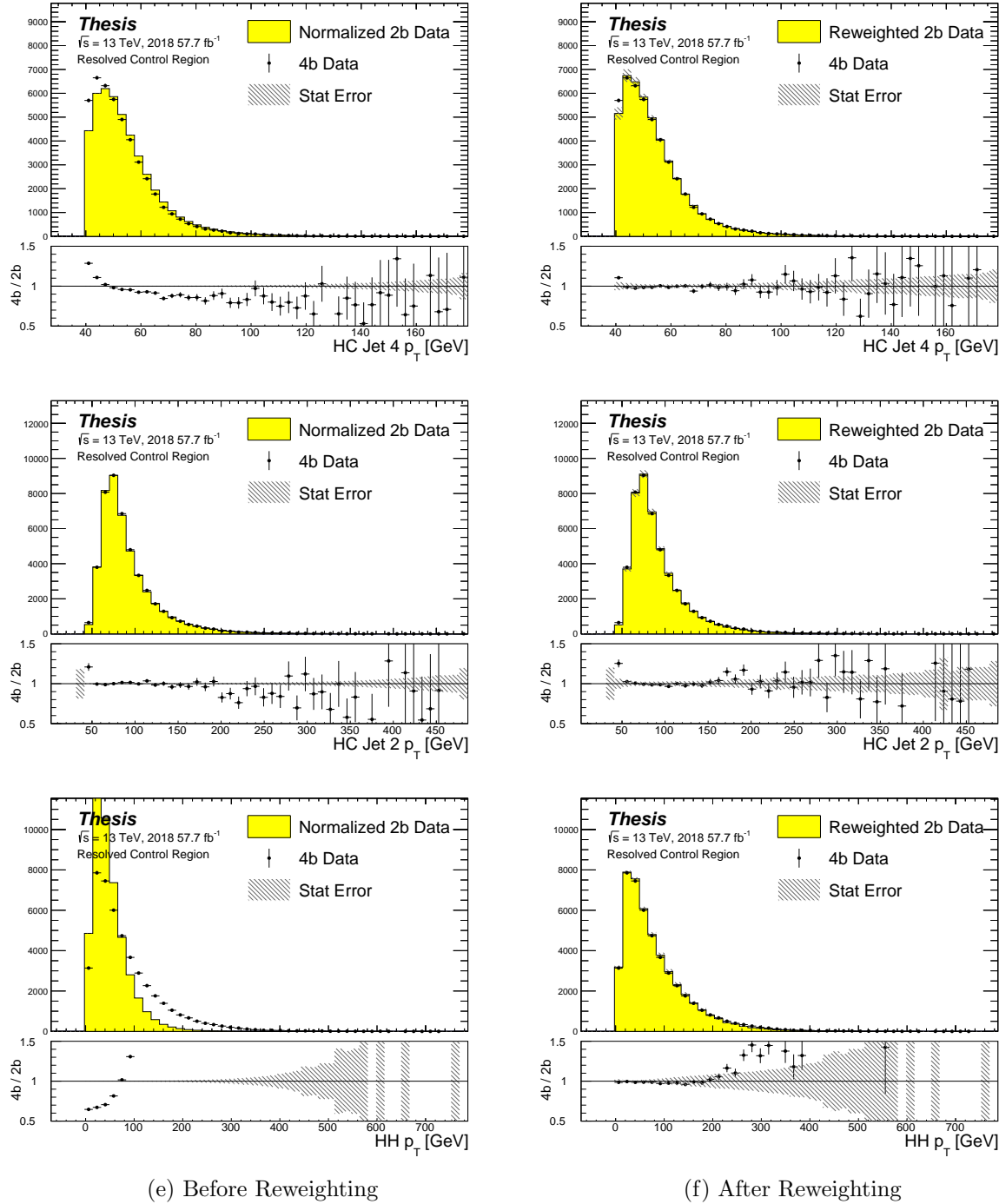
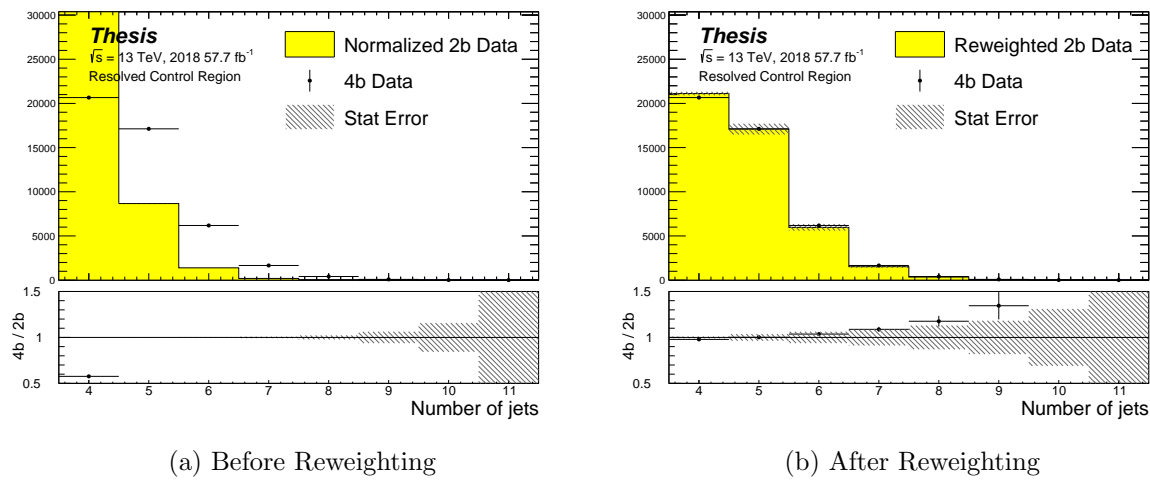


Figure 7.7: **Resonant Search:** Distributions of  $p_T$  of the 2nd and 4th leading Higgs Candidate jets and the  $p_T$  of the di-Higgs system before and after CR derived reweighting for the 2018 Control Region.



**Figure 7.8: Resonant Search:** Distributions of the number of jets before and after CR derived reweighting for the 2018 Control Region. A minimum of 4 jets is required in each event in order to form Higgs candidates.

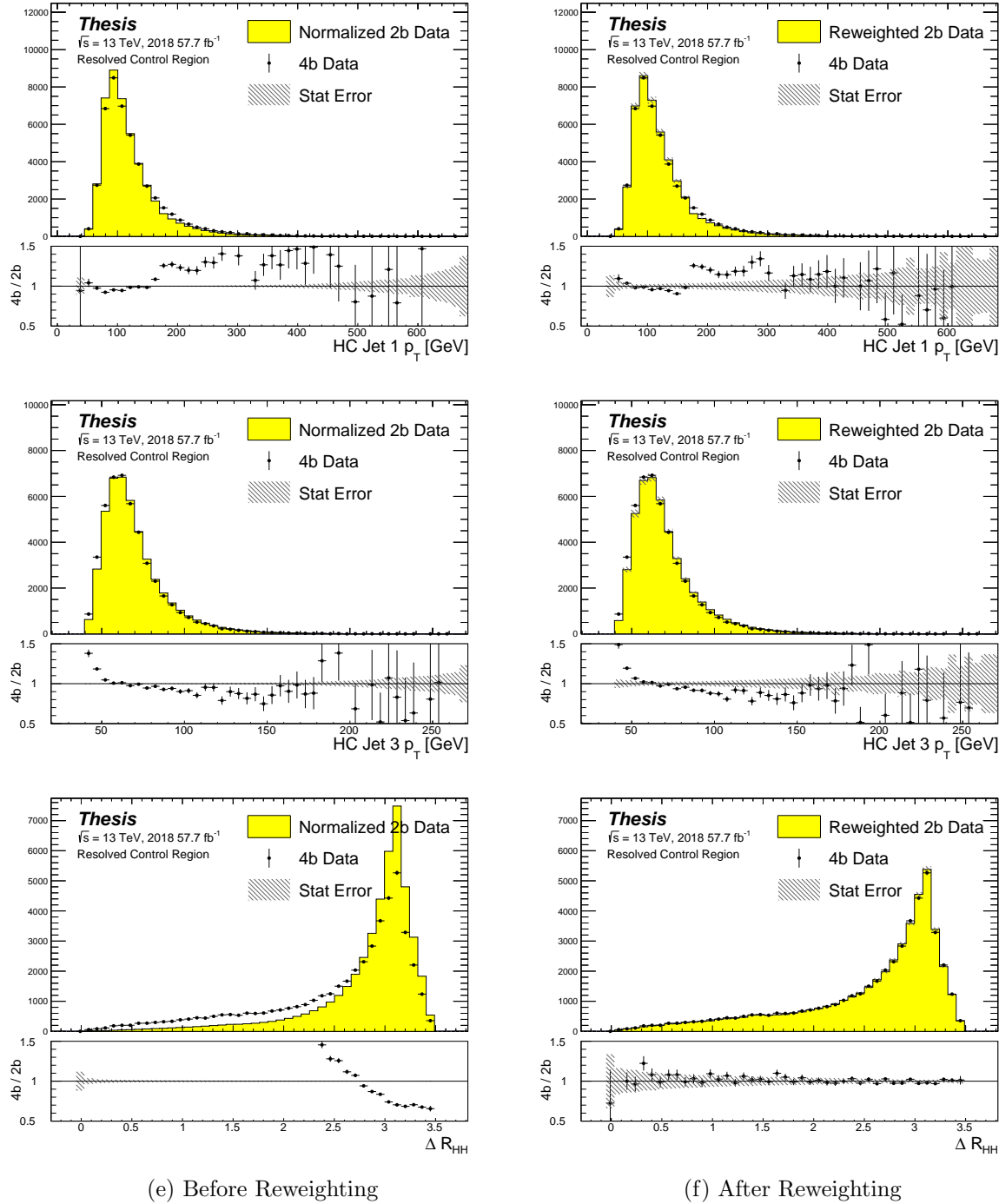


Figure 7.9: **Resonant Search:** Distributions of  $p_T$  of the 1st and 3rd leading Higgs Candidate jets and  $\Delta R$  between Higgs candidates before and after CR derived reweighting for the 2018 Control Region.

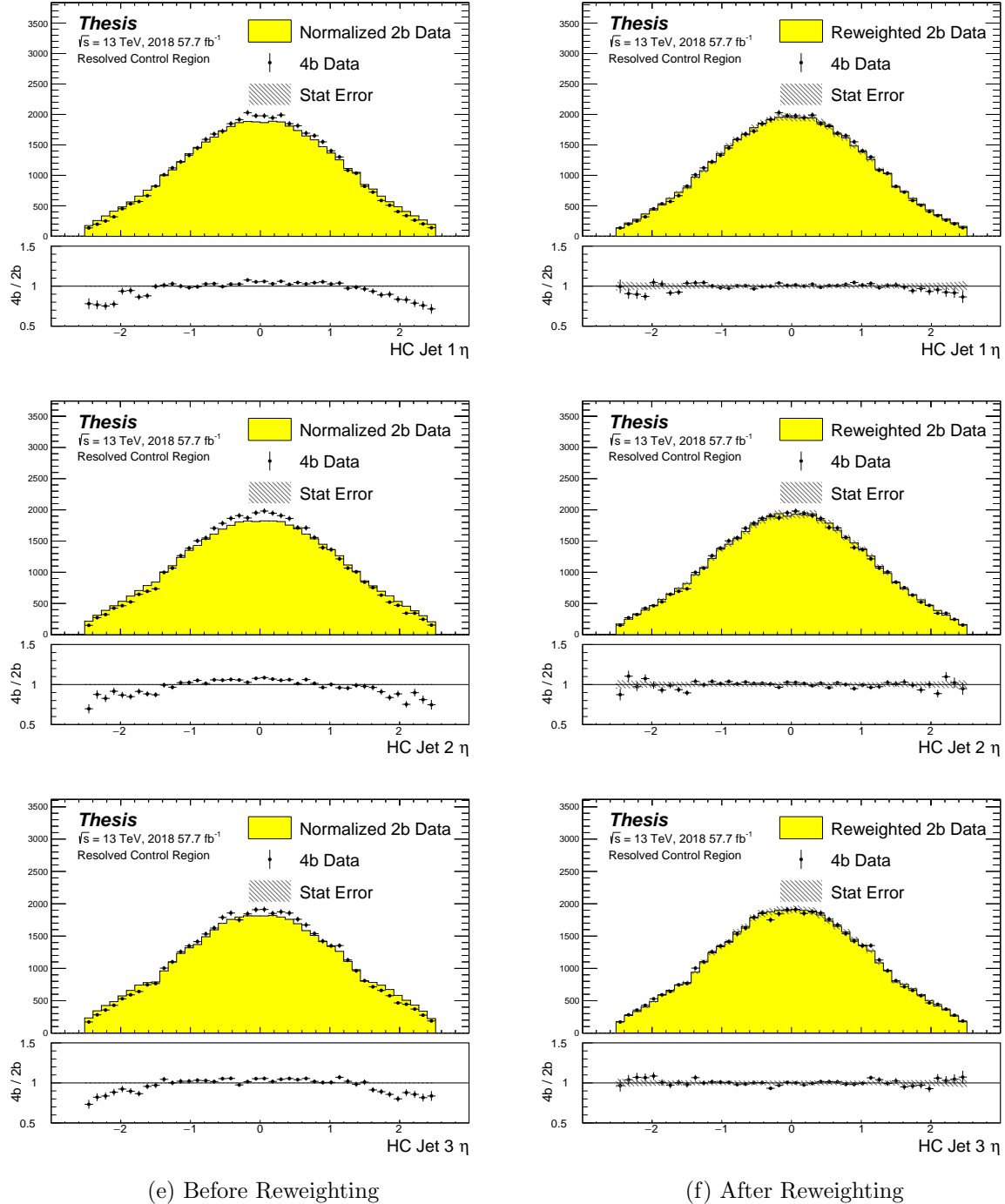


Figure 7.10: **Resonant Search:** Distributions of  $\eta$  of the 1st, 2nd, and 3rd leading Higgs Candidate jets before and after CR derived reweighting for the 2018 Control Region.

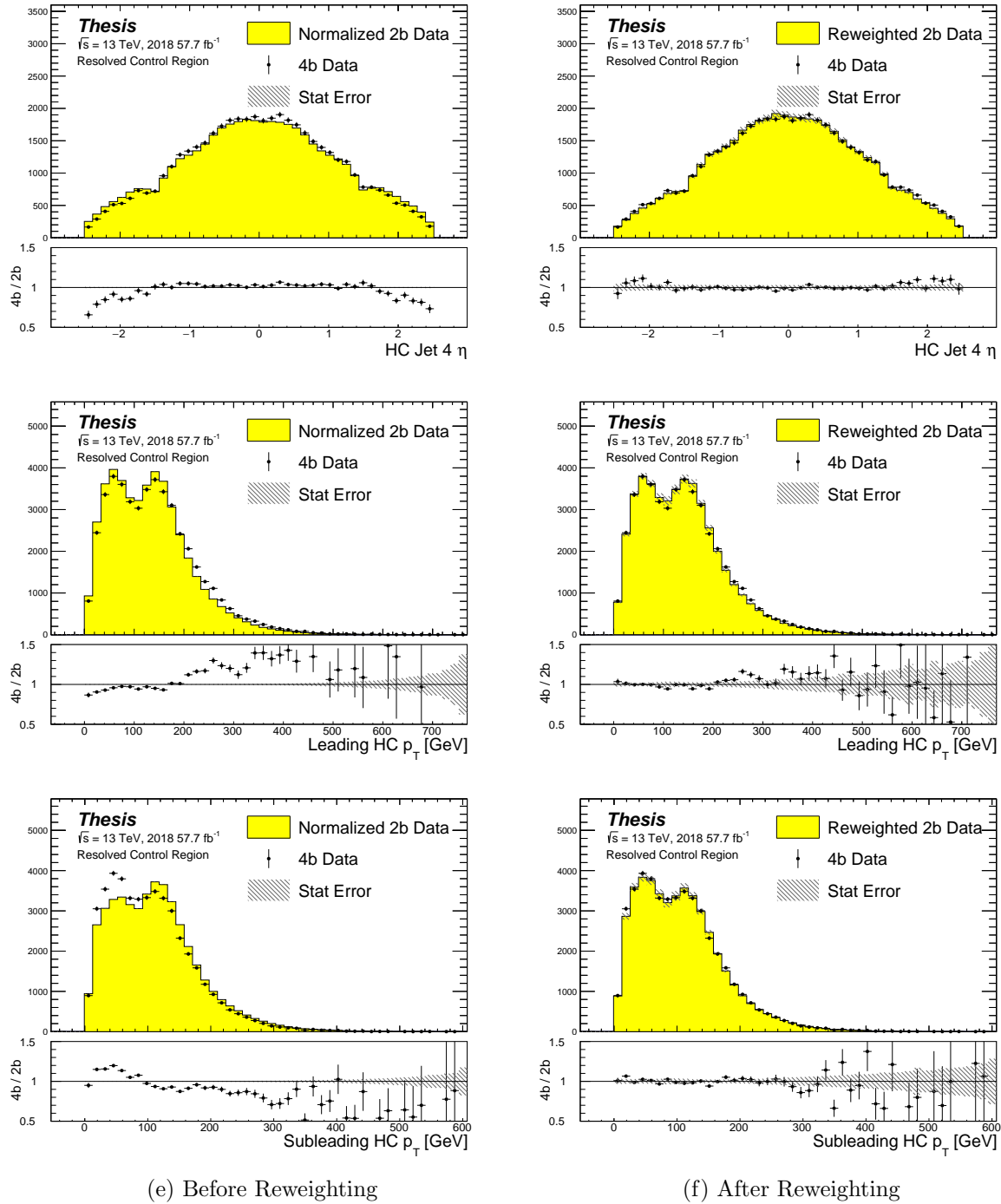


Figure 7.11: **Resonant Search:** Distributions of  $\eta$  of the 4th leading Higgs Candidate jet and the  $p_T$  of the leading and subleading Higgs candidates before and after CR derived reweighting for the 2018 Control Region.

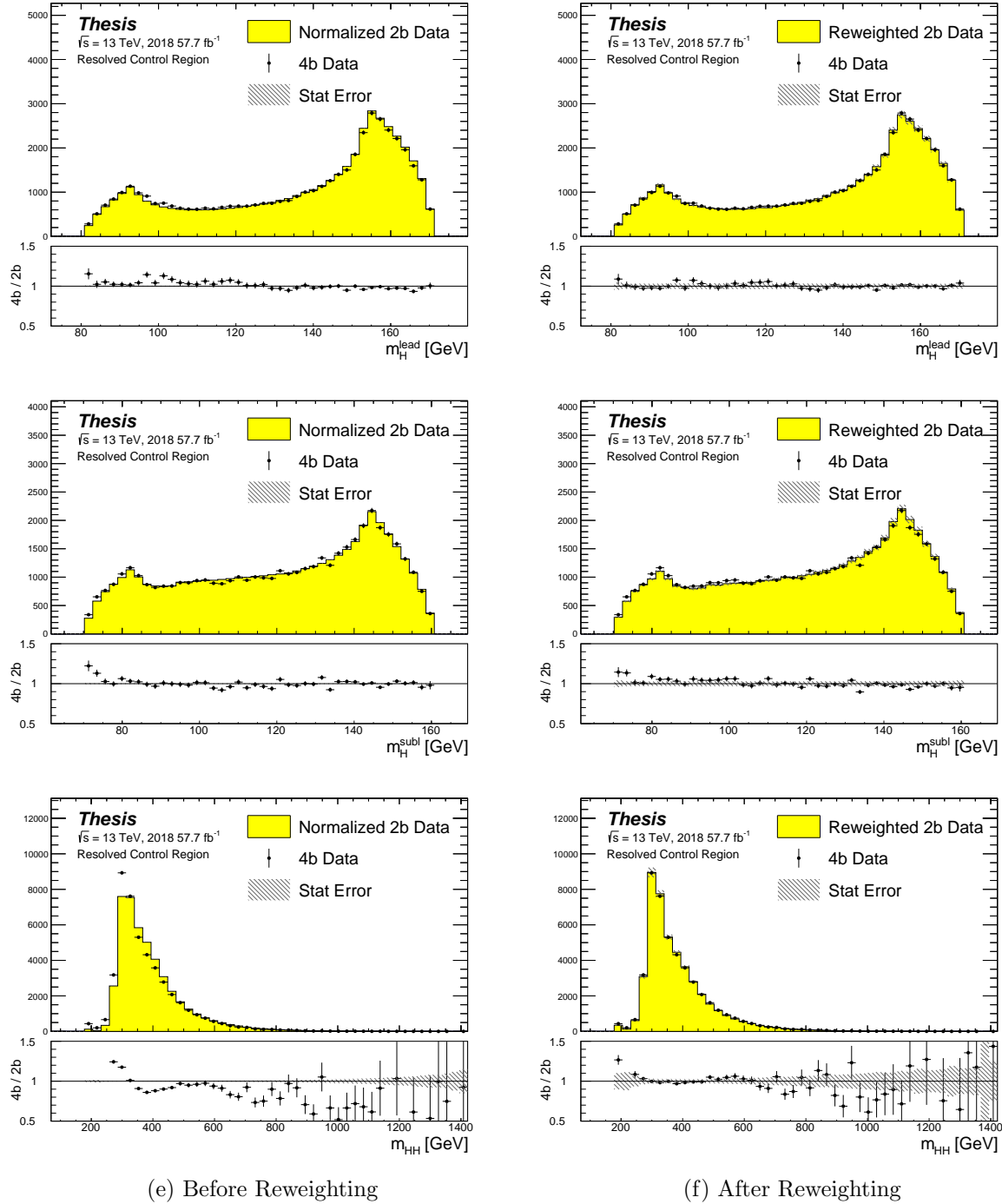


Figure 7.12: **Resonant Search:** Distributions of mass of the leading and subleading Higgs candidates and of the di-Higgs system before and after CR derived reweighting for the 2018 Control Region.

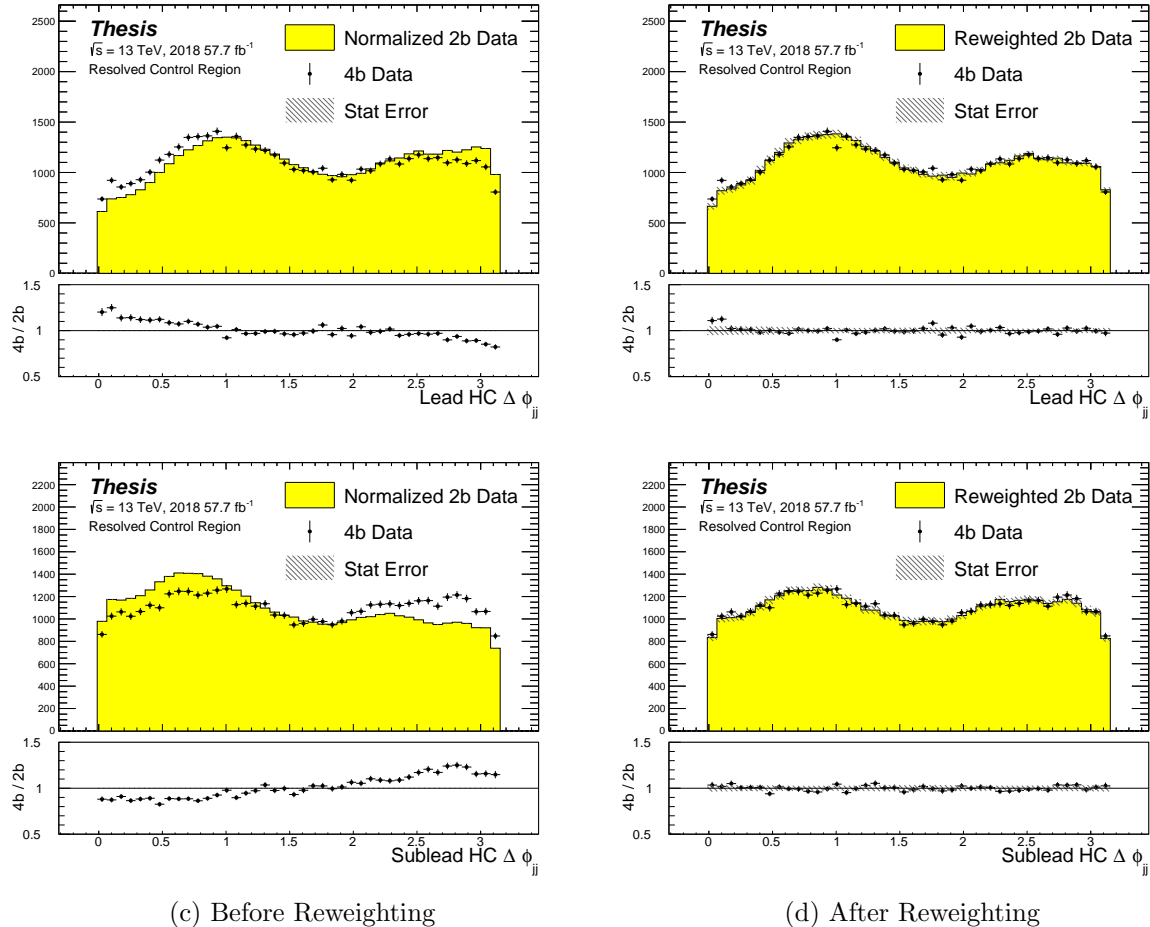


Figure 7.13: **Resonant Search:** Distributions of  $\Delta\phi$  between jets in the leading and subleading Higgs candidates before and after CR derived reweighting for the 2018 Control Region.

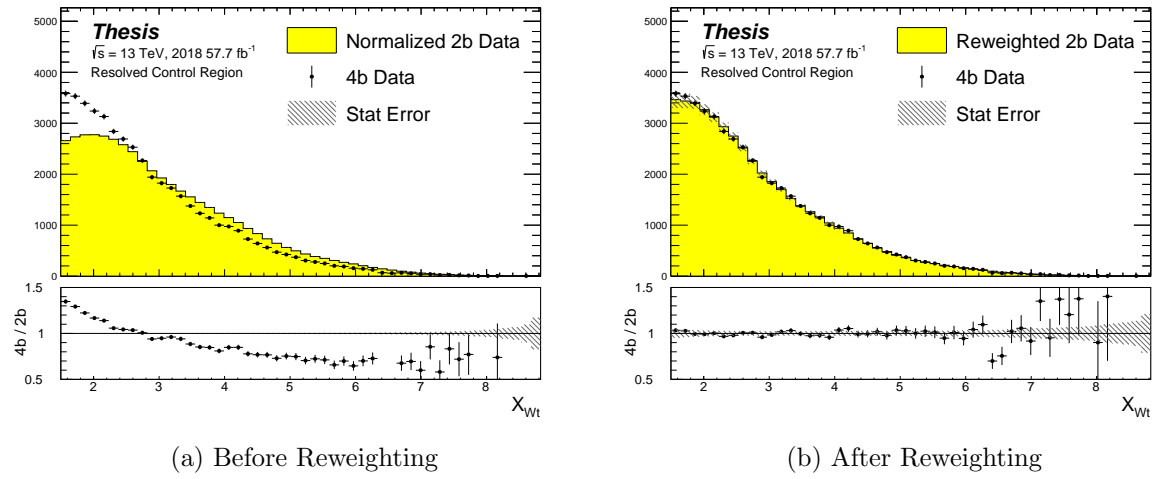


Figure 7.14: **Resonant Search:** Distributions of the top veto variable,  $X_{Wt}$ , before and after CR derived reweighting for the 2018 Control Region. Reweighting is done after the cut on this variable is applied

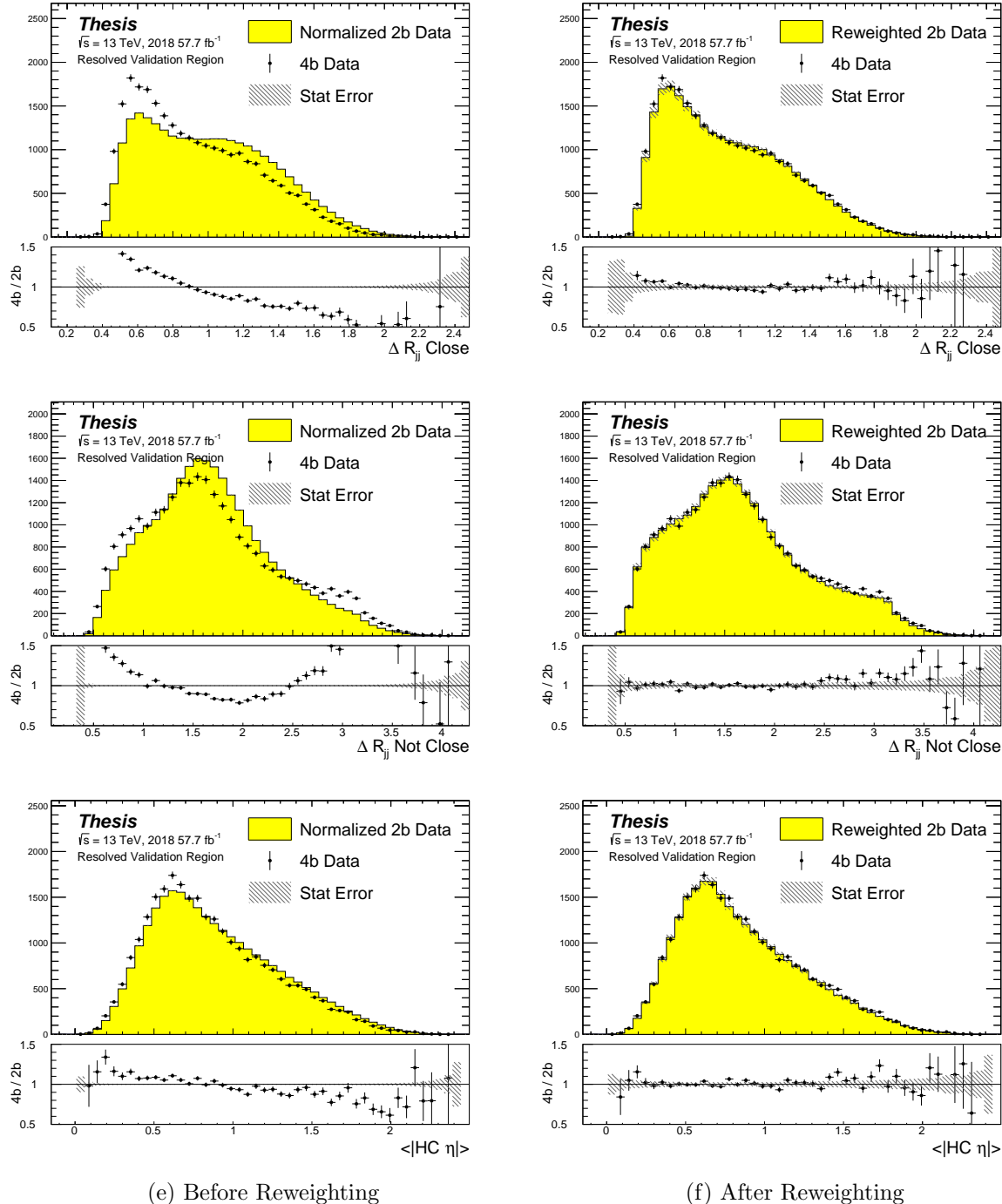


Figure 7.15: **Resonant Search:** Distributions of  $\Delta R$  between the closest Higgs Candidate jets,  $\Delta R$  between the other two, and average absolute value of HC jet  $\eta$  before and after CR derived reweighting for the 2018 Validation Region.

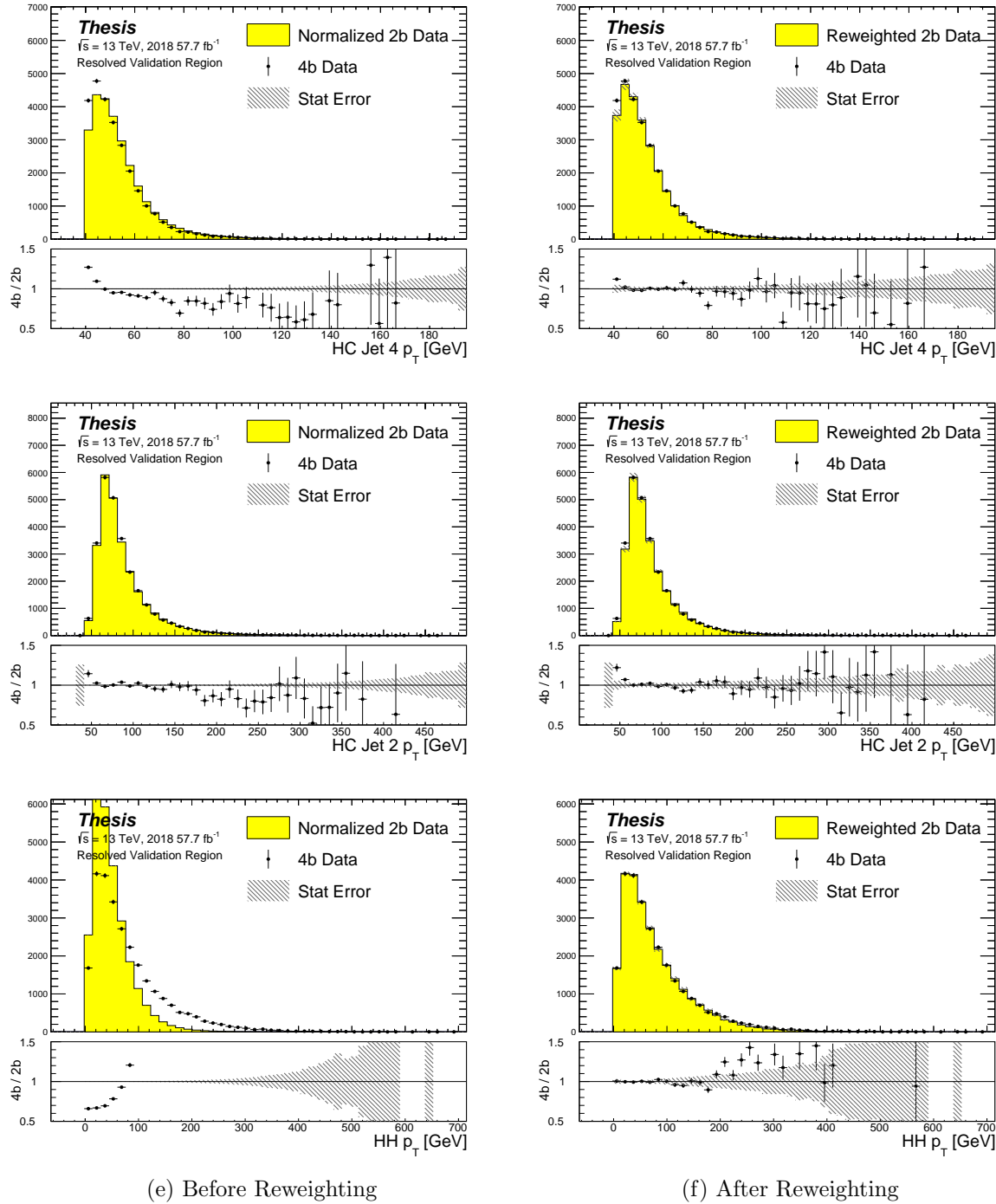


Figure 7.16: **Resonant Search:** Distributions of  $p_T$  of the 2nd and 4th leading Higgs Candidate jets and the  $p_T$  of the di-Higgs system before and after CR derived reweighting for the 2018 Validation Region.

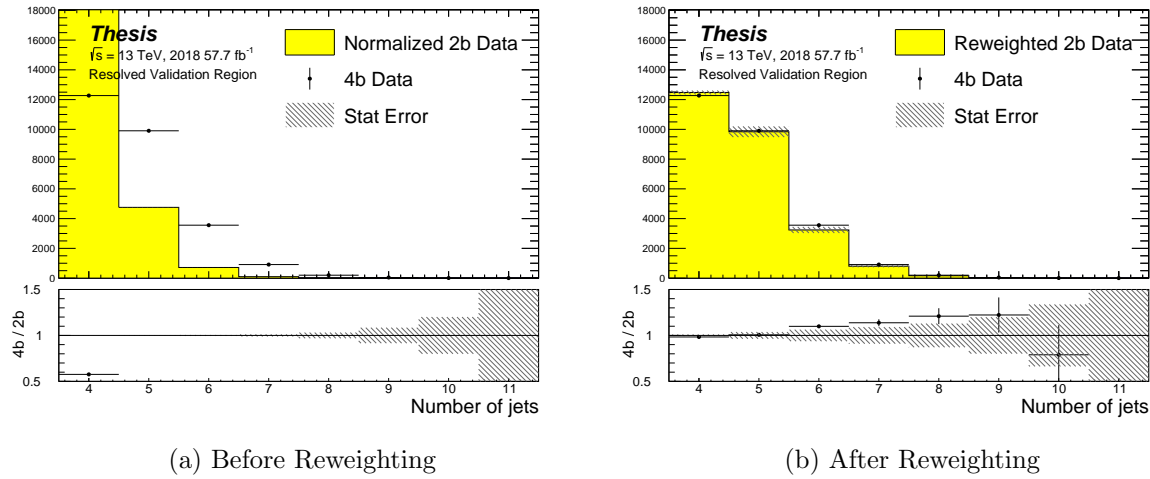


Figure 7.17: **Resonant Search:** Distributions of the number of jets before and after CR derived reweighting for the 2018 Validation Region. A minimum of 4 jets is required in each event in order to form Higgs candidates.

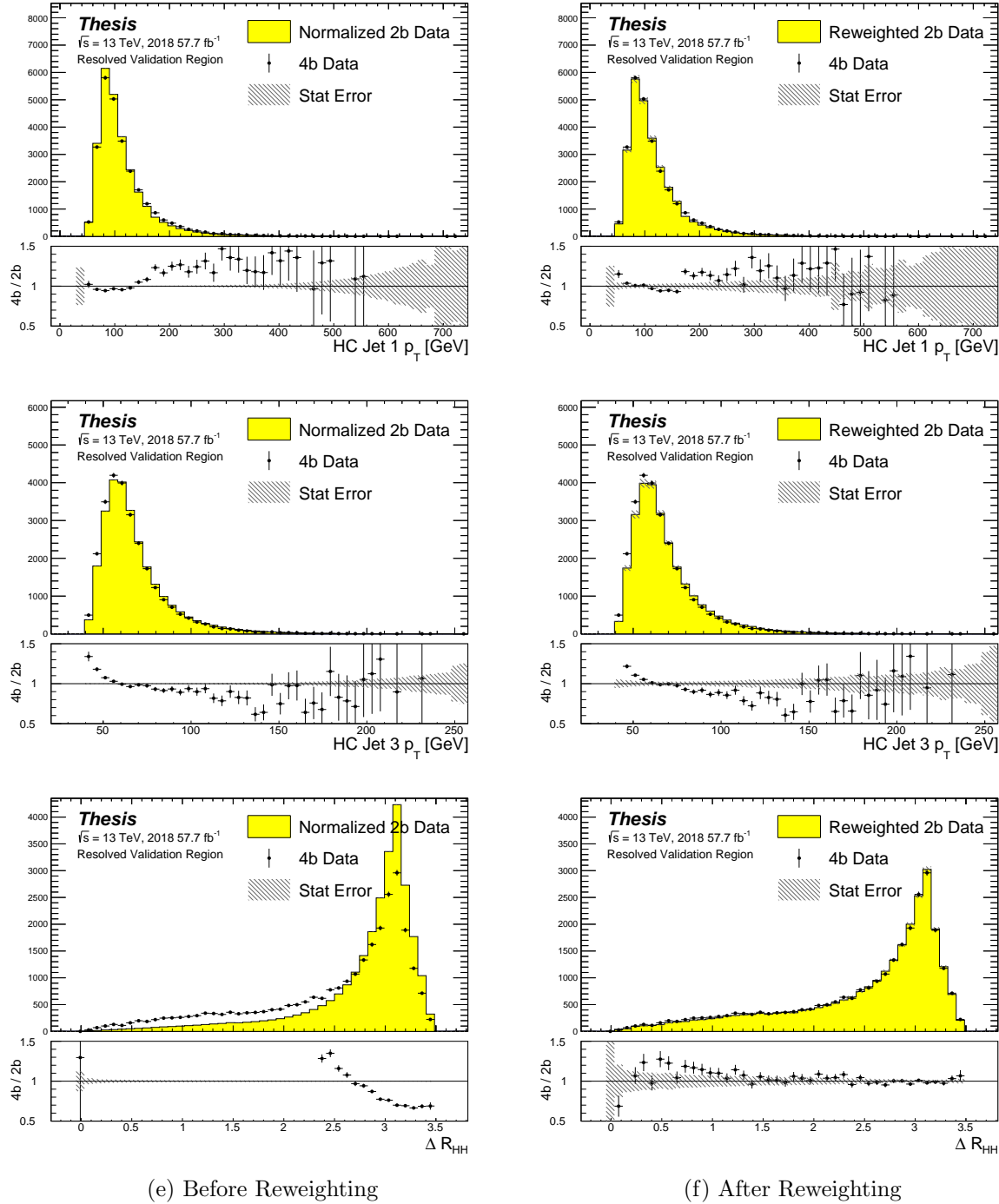


Figure 7.18: **Resonant Search:** Distributions of  $p_T$  of the 1st and 3rd leading Higgs Candidate jets and  $\Delta R$  between Higgs candidates before and after CR derived reweighting for the 2018 Validation Region.

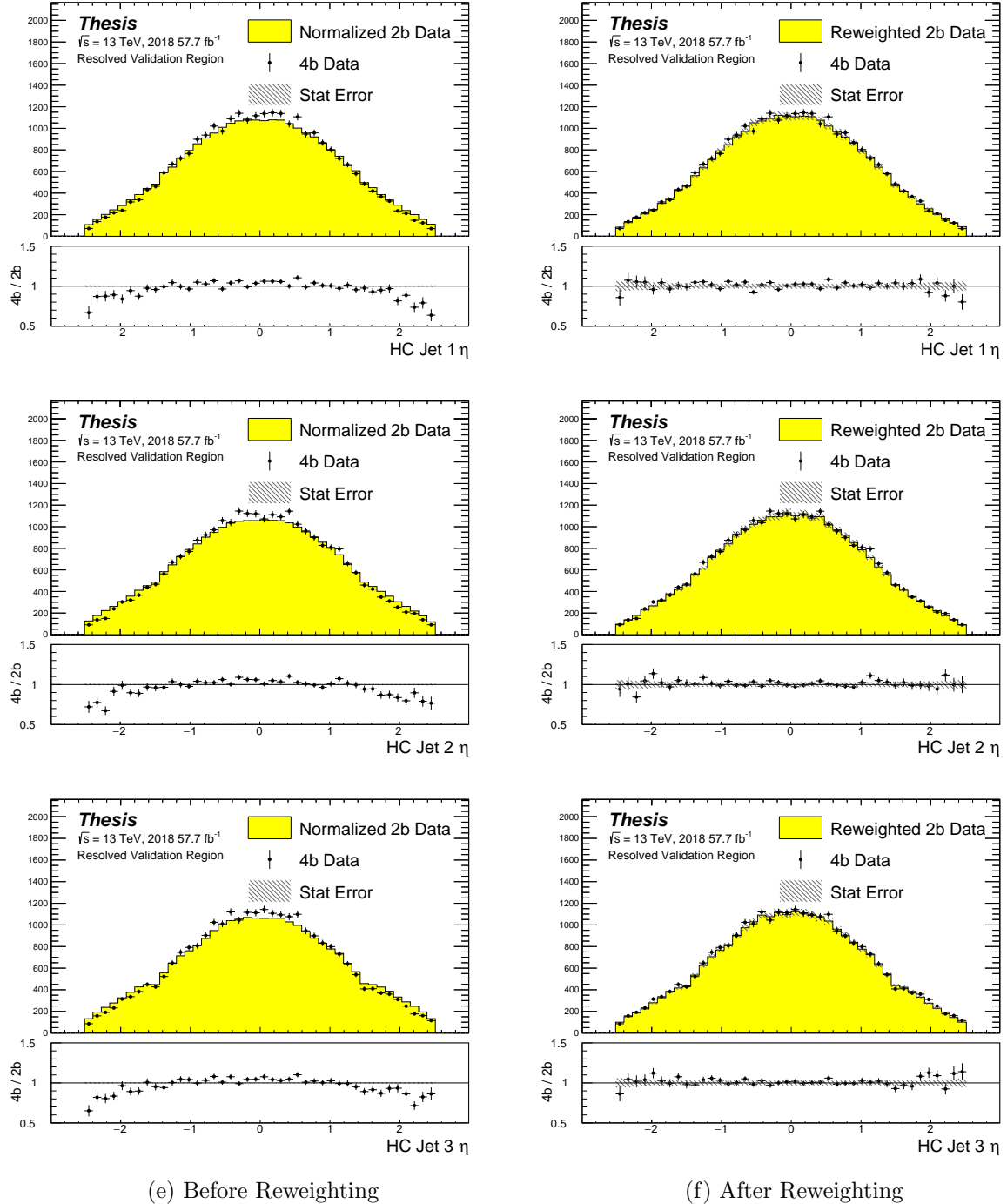


Figure 7.19: **Resonant Search:** Distributions of  $\eta$  of the 1st, 2nd, and 3rd leading Higgs Candidate jets before and after CR derived reweighting for the 2018 Validation Region.

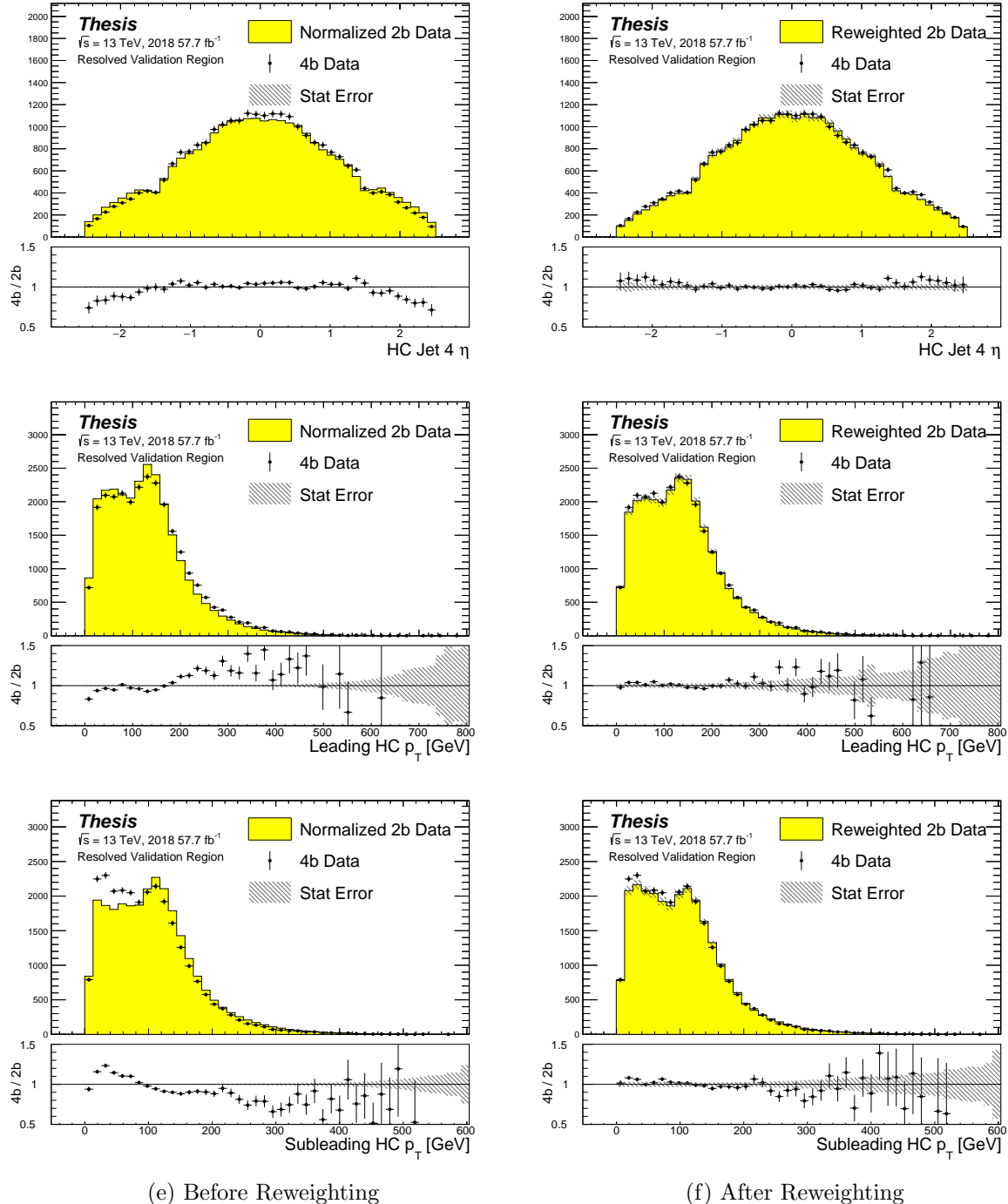


Figure 7.20: **Resonant Search:** Distributions of  $\eta$  of the 4th leading Higgs Candidate jet and the  $p_T$  of the leading and subleading Higgs candidates before and after CR derived reweighting for the 2018 Validation Region.

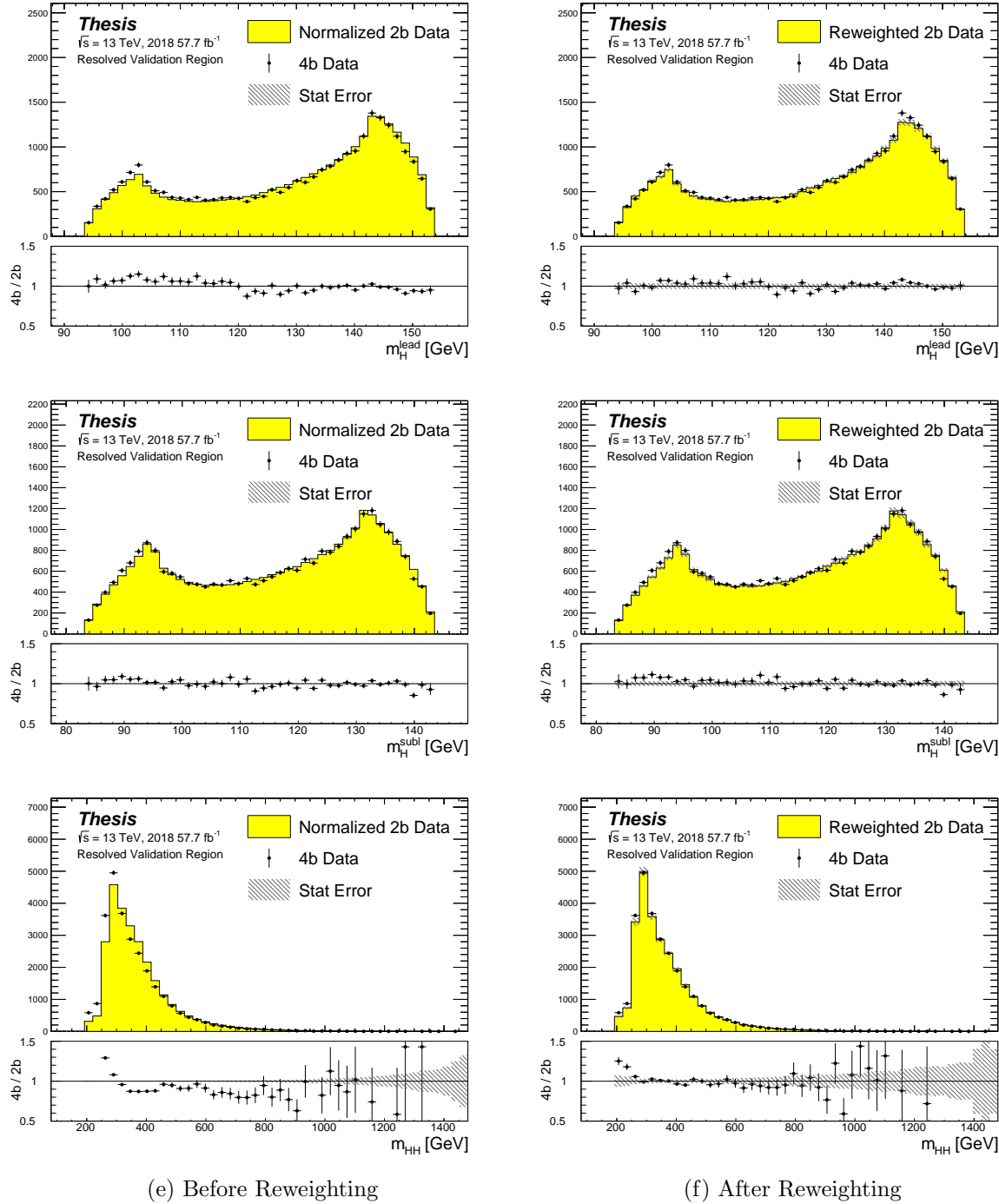


Figure 7.21: **Resonant Search:** Distributions of mass of the leading and subleading Higgs candidates and of the di-Higgs system before and after CR derived reweighting for the 2018 Validation Region.

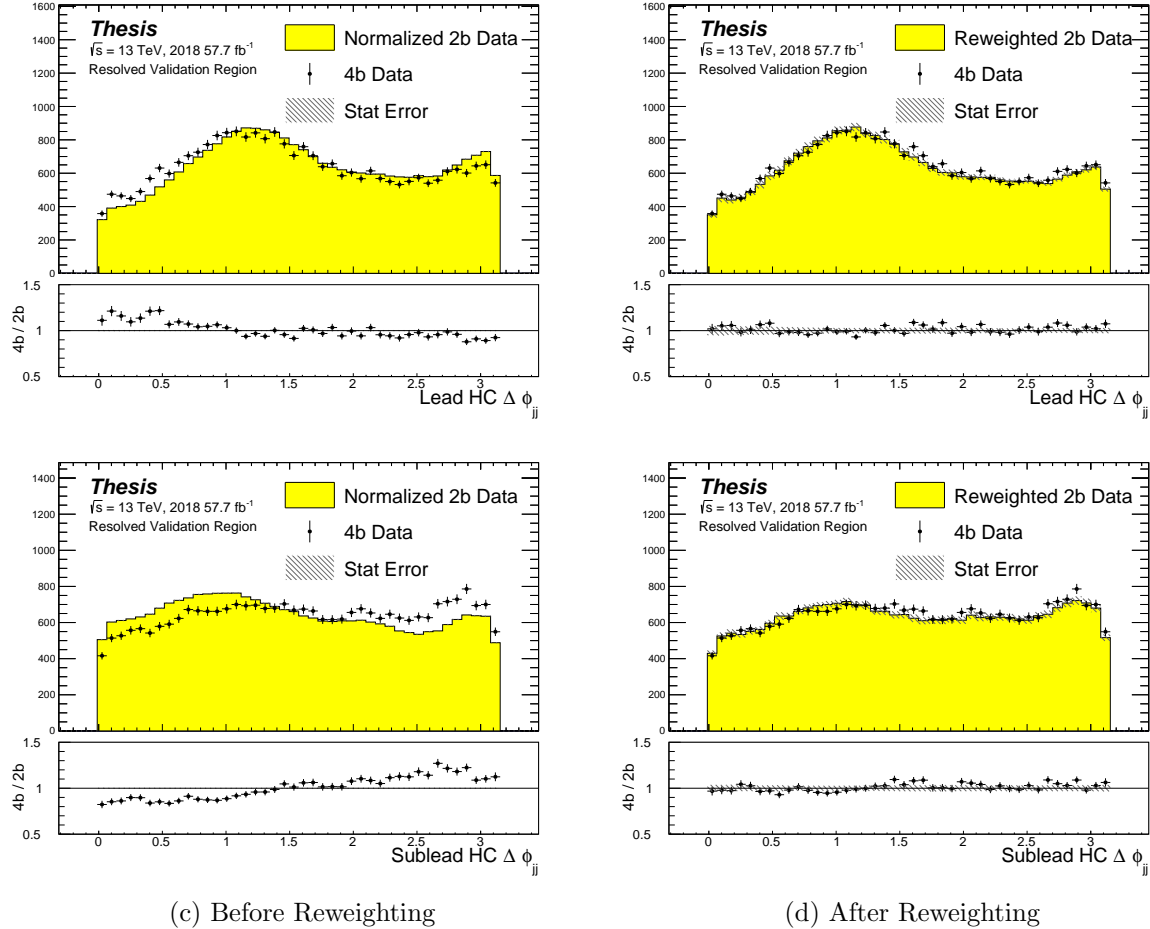


Figure 7.22: **Resonant Search:** Distributions of  $\Delta\phi$  between jets in the leading and subleading Higgs candidates before and after CR derived reweighting for the 2018 Validation Region.

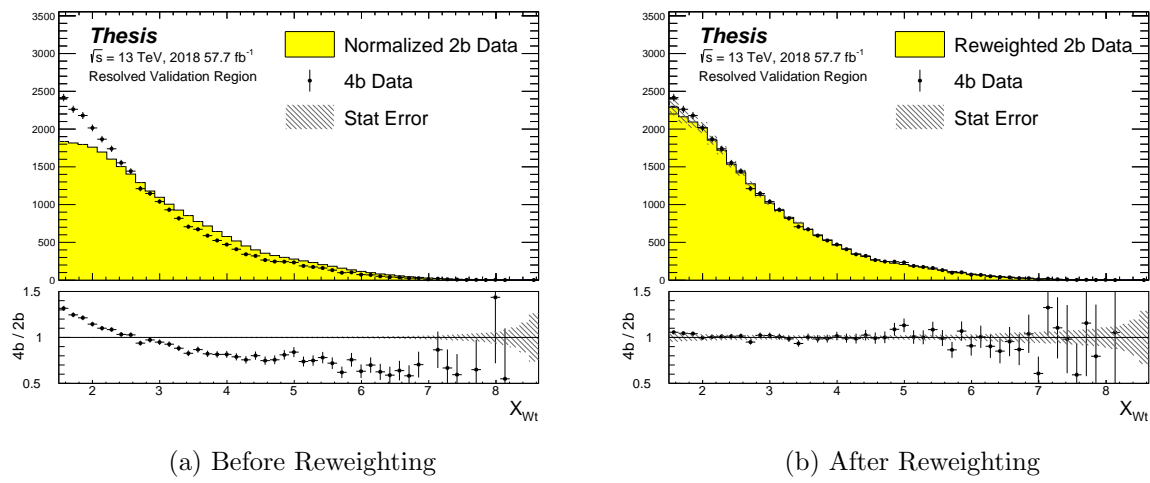


Figure 7.23: **Resonant Search:** Distributions of the top veto variable,  $X_{Wt}$ , before and after CR derived reweighting for the 2018 Validation Region. Reweighting is done after the cut on this variable is applied

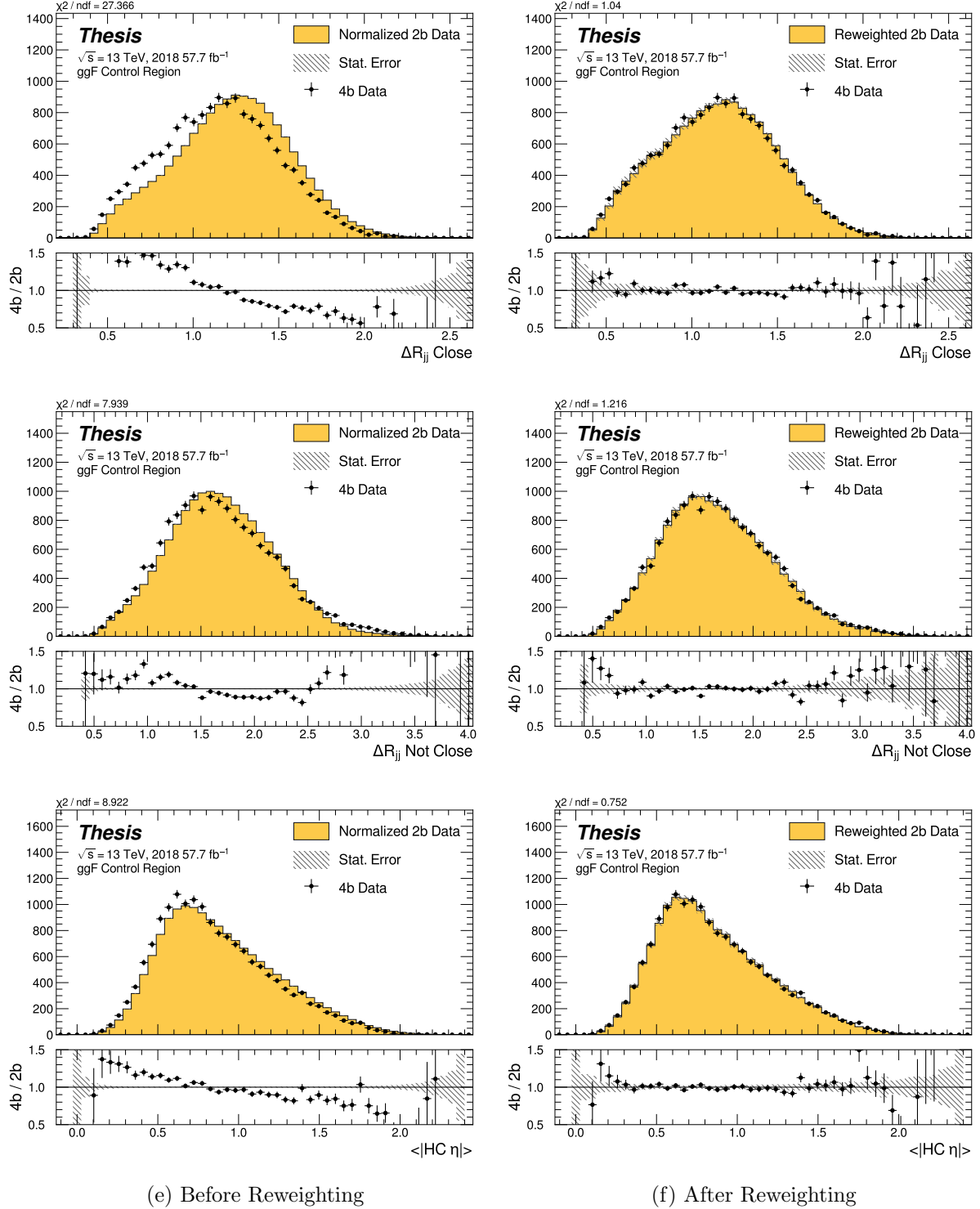
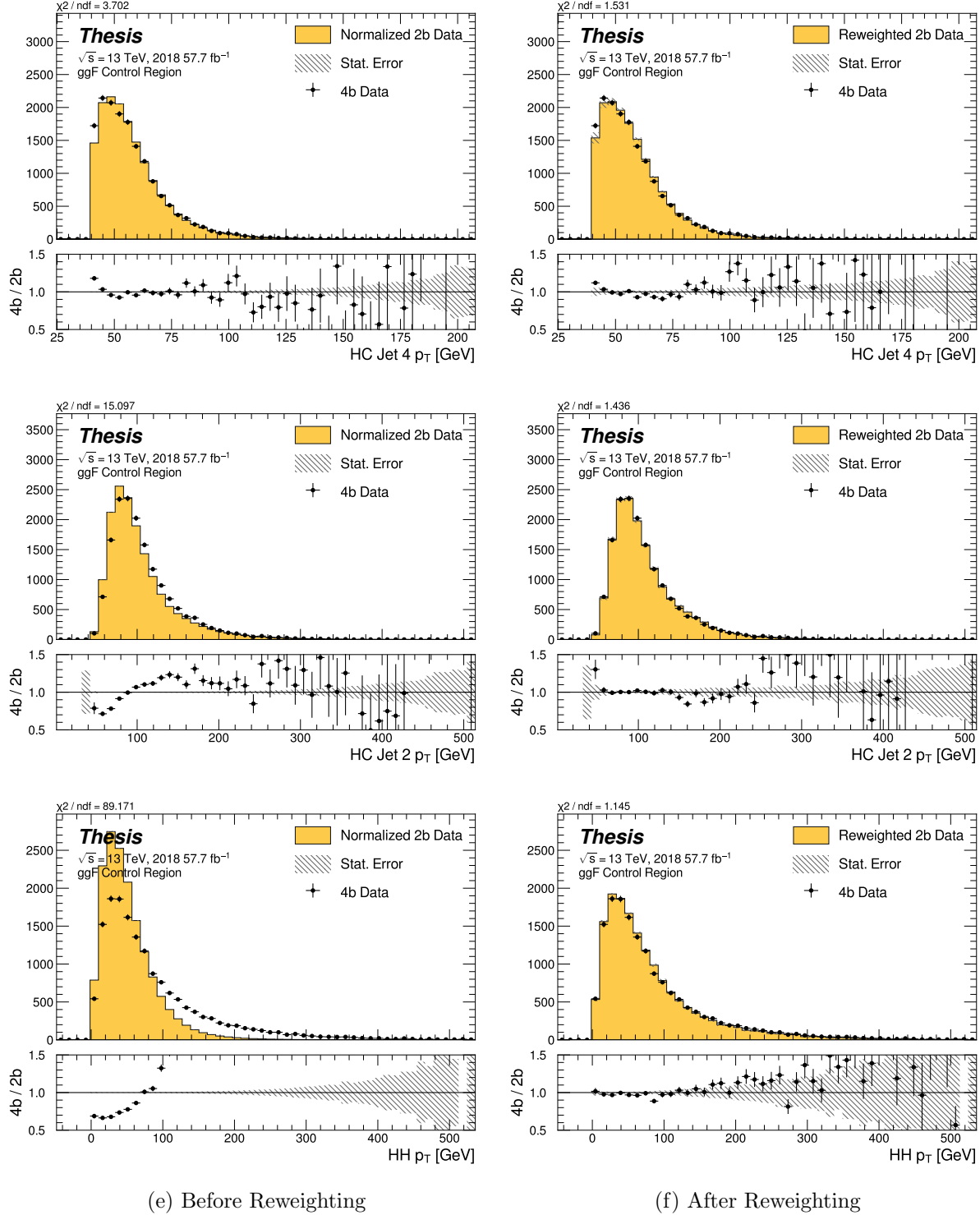


Figure 7.24: **Non-resonant Search (4b):** Distributions of  $\Delta R$  between the closest Higgs Candidate jets,  $\Delta R$  between the other two, and average absolute value of HC jet  $\eta$  before and after CR derived reweighting for the 2018 4b Control Region.



**Figure 7.25: Non-resonant Search (4b):** Distributions of  $p_T$  of the 2nd and 4th leading Higgs Candidate jets and the  $p_T$  of the di-Higgs system before and after CR derived reweighting for the 2018 4b Control Region.

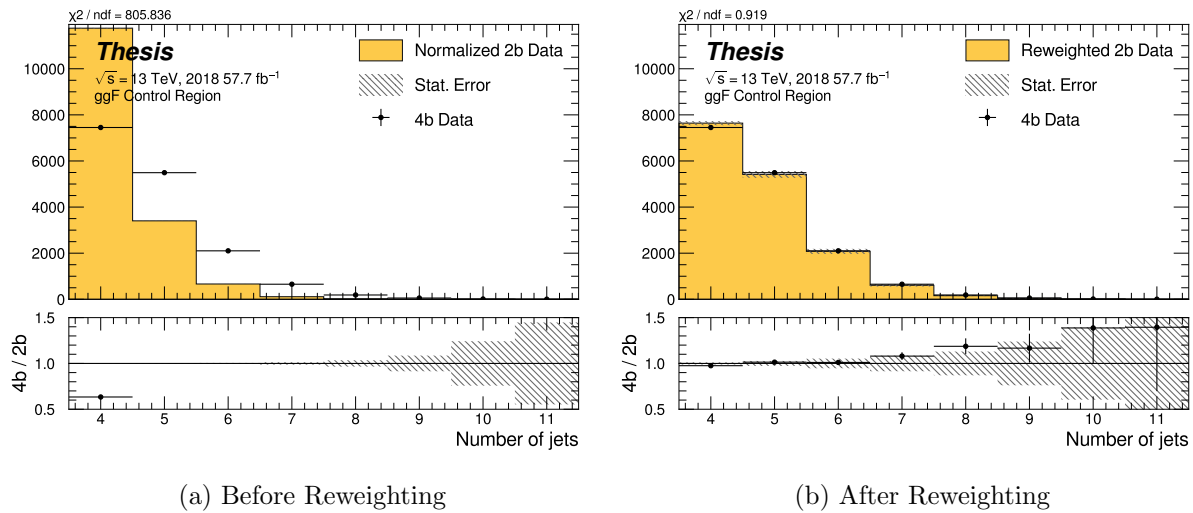


Figure 7.26: **Non-resonant Search (4b):** Distributions of the number of jets before and after CR derived reweighting for the 2018 4b Control Region. A minimum of 4 jets is required in each event in order to form Higgs candidates.

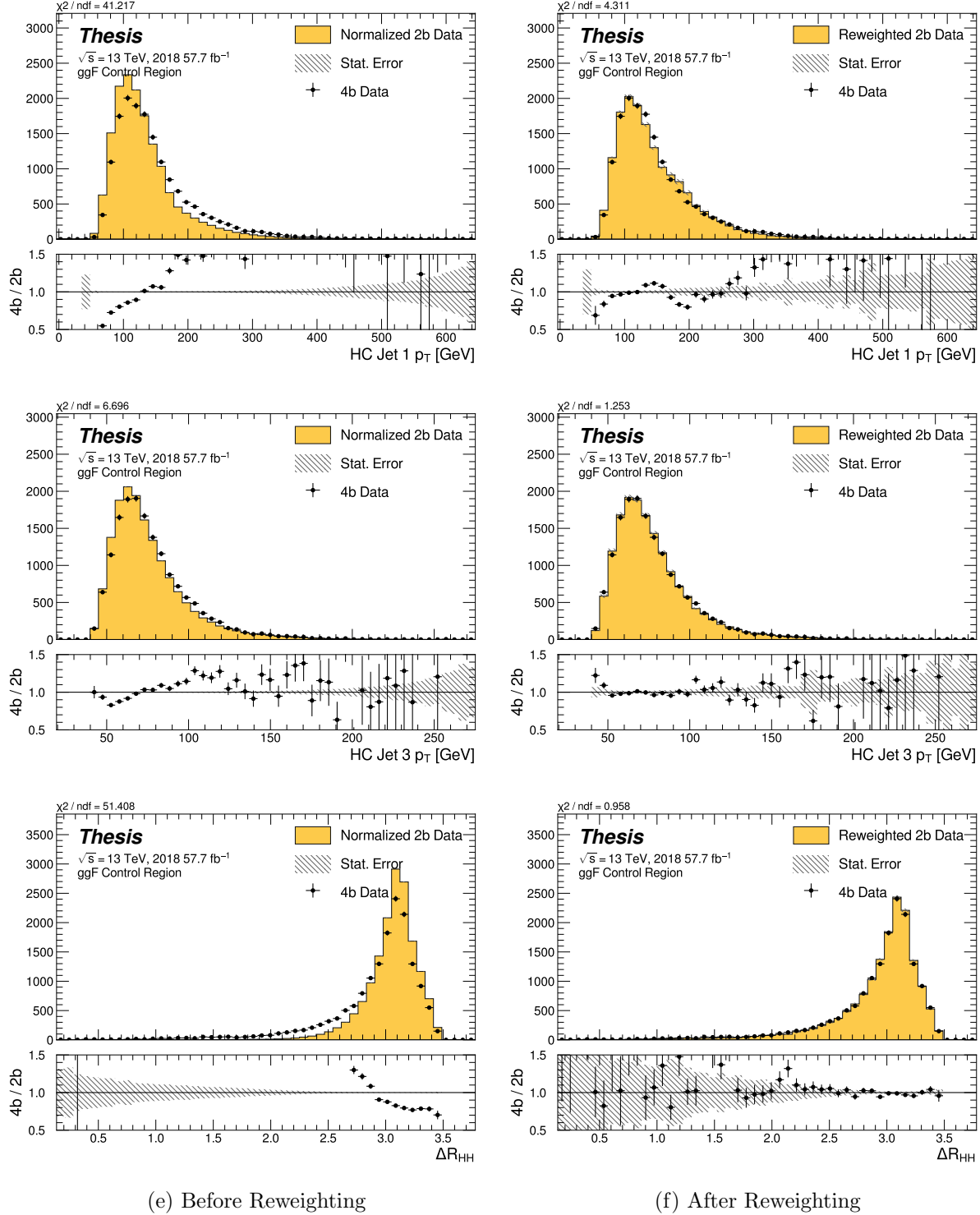


Figure 7.27: **Non-resonant Search (4b):** Distributions of  $p_T$  of the 1st and 3rd leading Higgs Candidate jets and  $\Delta R$  between Higgs candidates before and after CR derived reweighting for the 2018 4b Control Region.

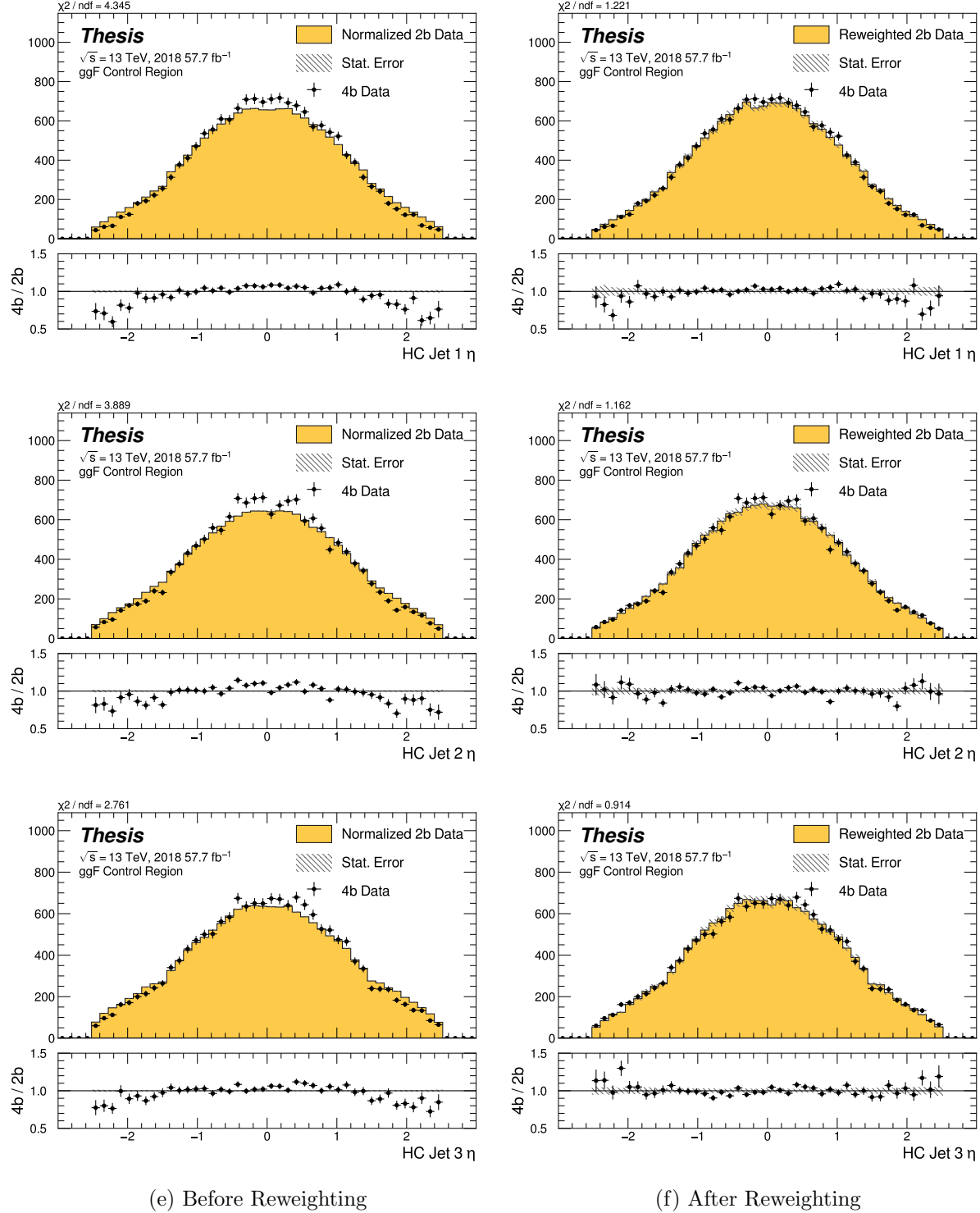


Figure 7.28: **Non-resonant Search (4b):** Distributions of  $\eta$  of the 1st, 2nd, and 3rd leading Higgs Candidate jets before and after CR derived reweighting for the 2018 4b Control Region.

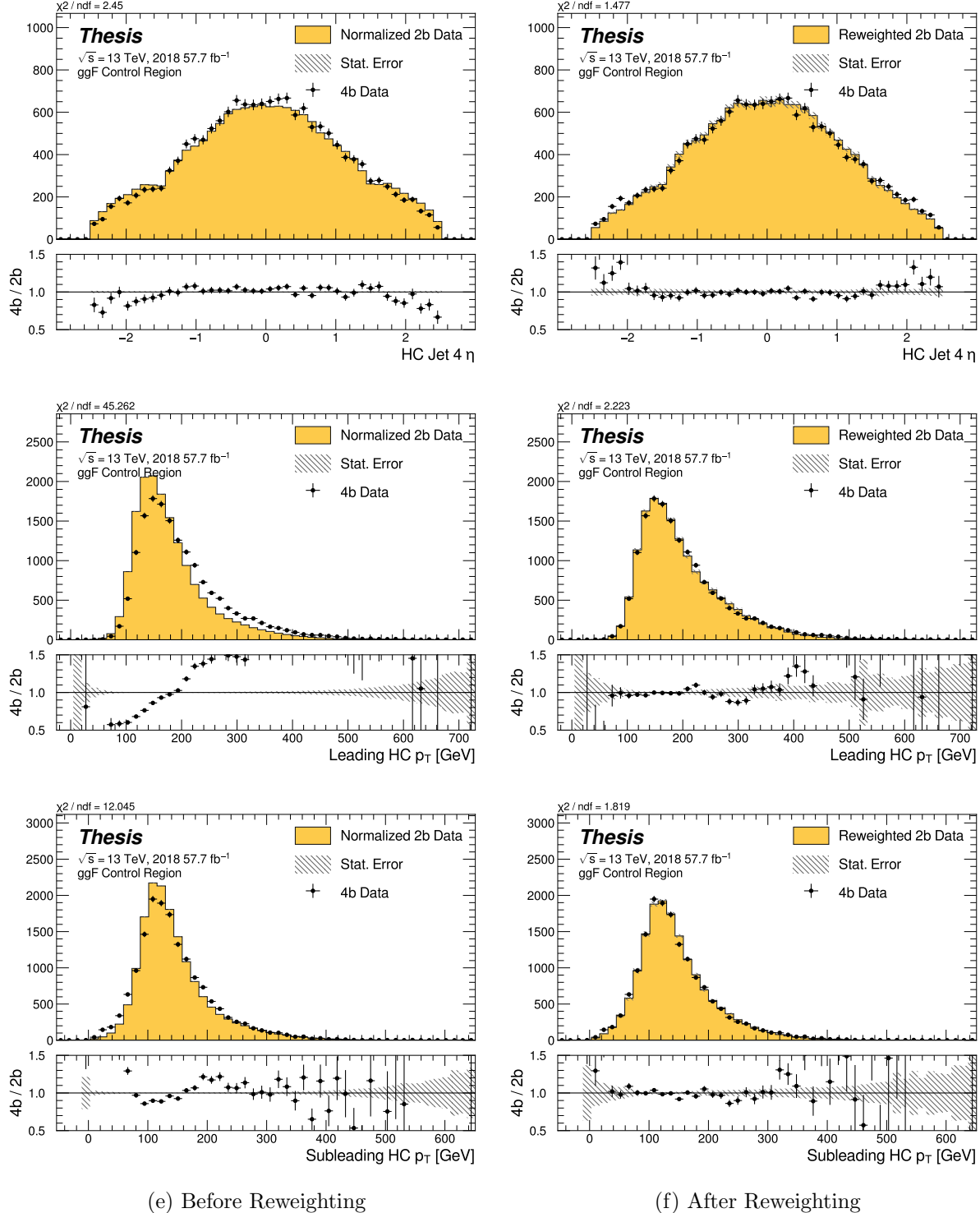


Figure 7.29: **Non-resonant Search (4b):** Distributions of  $\eta$  of the 4th leading Higgs Candidate jet and the  $p_T$  of the leading and subleading Higgs candidates before and after CR derived reweighting for the 2018 4b Control Region.

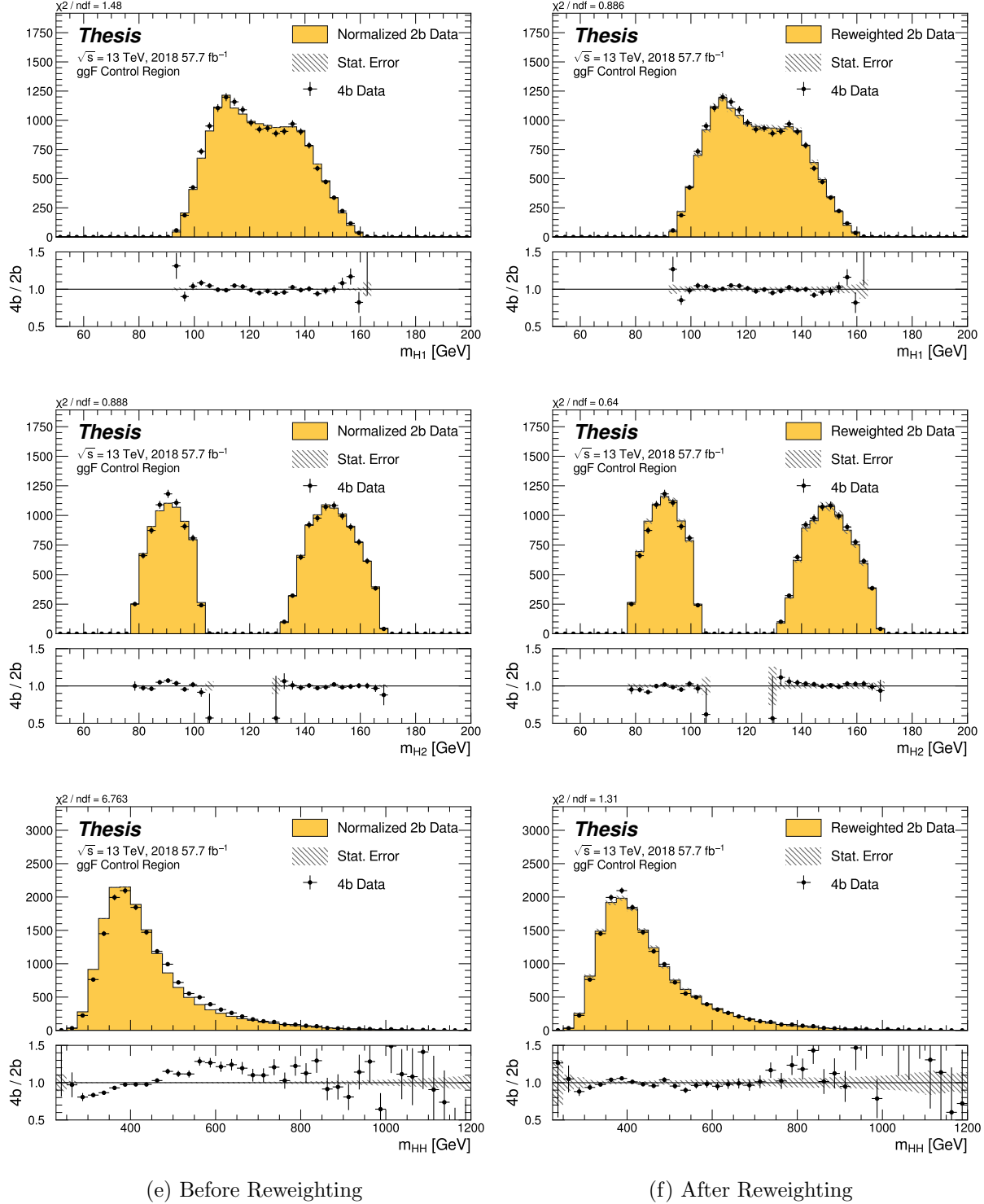


Figure 7.30: **Non-resonant Search (4b):** Distributions of mass of the leading and subleading Higgs candidates and of the di-Higgs system before and after CR derived reweighting for the 2018 4b Control Region.

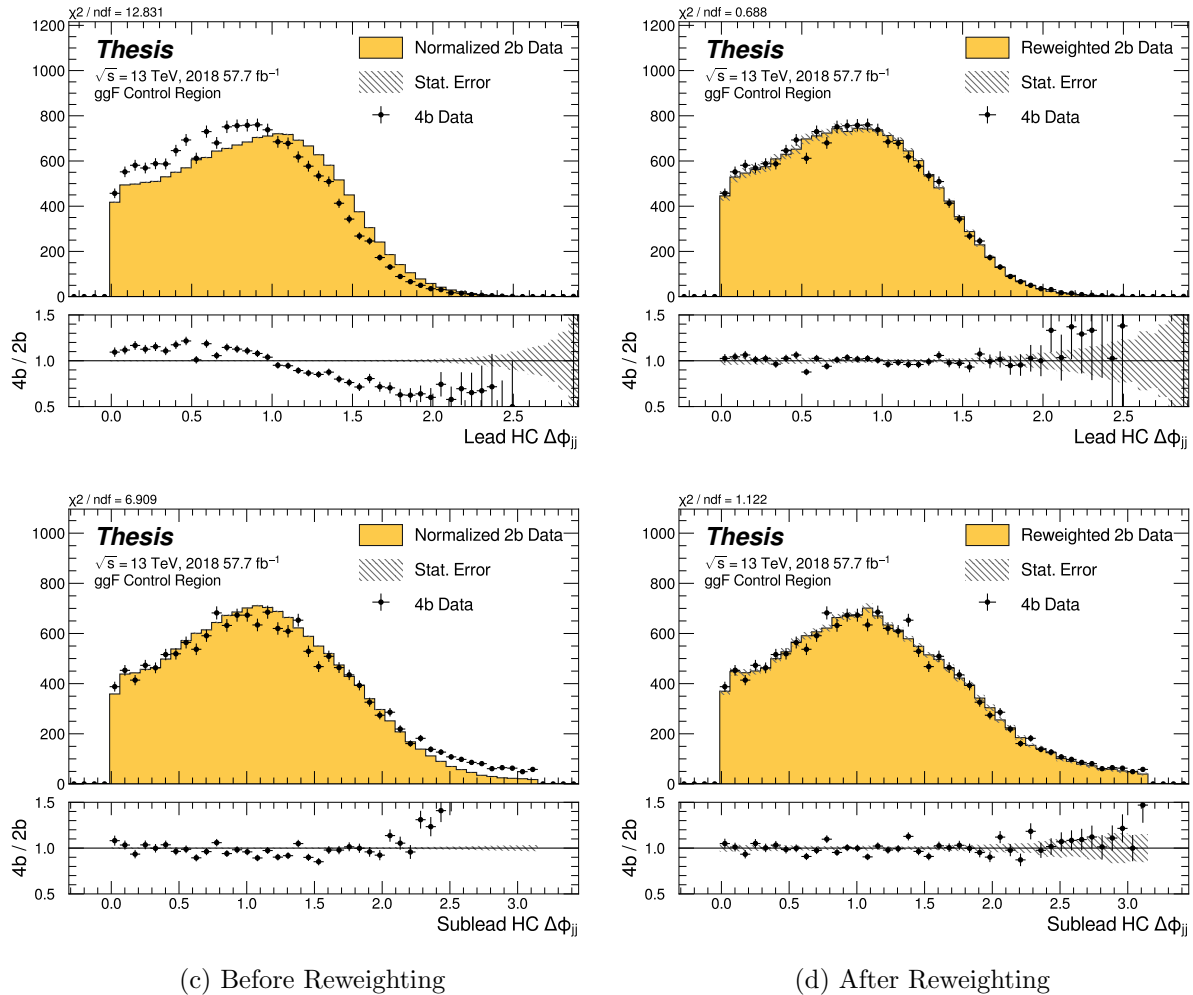


Figure 7.31: **Non-resonant Search (4b):** Distributions of  $\Delta\phi$  between jets in the leading and subleading Higgs candidates before and after CR derived reweighting for the 2018 4b Control Region.

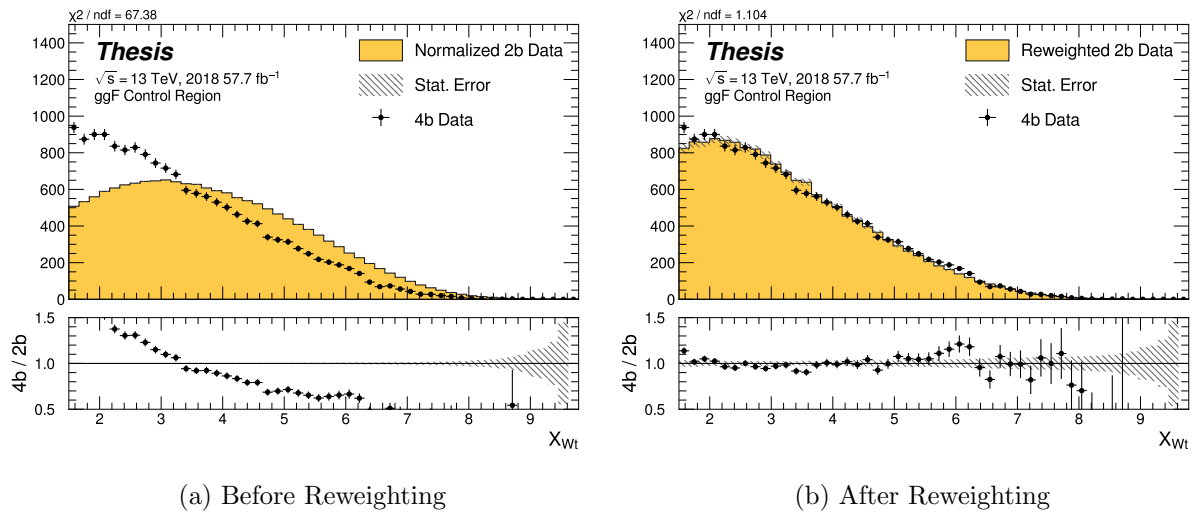


Figure 7.32: **Non-resonant Search (4b):** Distributions of the top veto variable,  $X_{Wt}$ , before and after CR derived reweighting for the 2018 4b Control Region. Reweighting is done after the cut on this variable is applied.

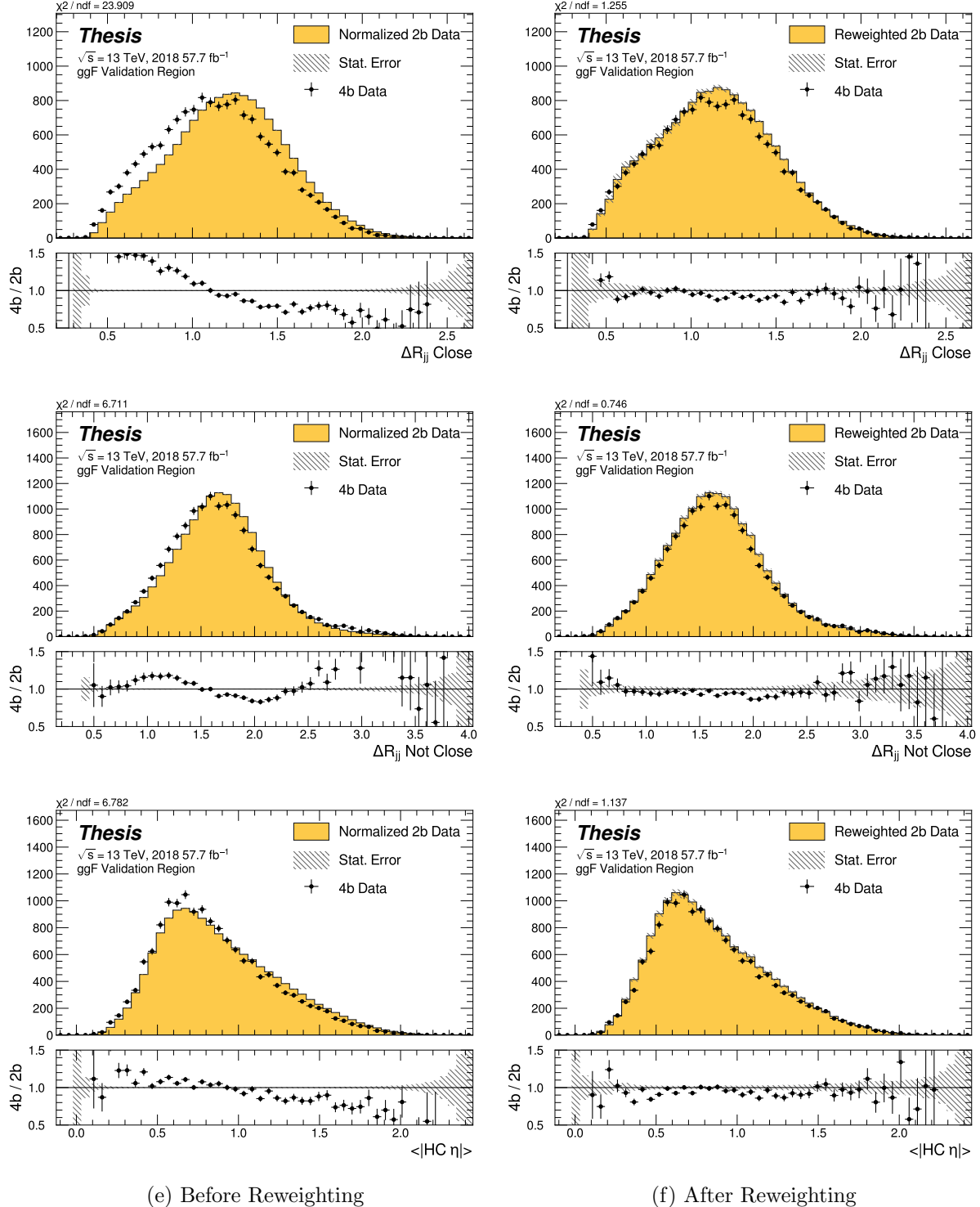


Figure 7.33: **Non-resonant Search (4b):** Distributions of  $\Delta R$  between the closest Higgs Candidate jets,  $\Delta R$  between the other two, and average absolute value of HC jet  $\eta$  before and after CR derived reweighting for the 2018 4b Validation Region.

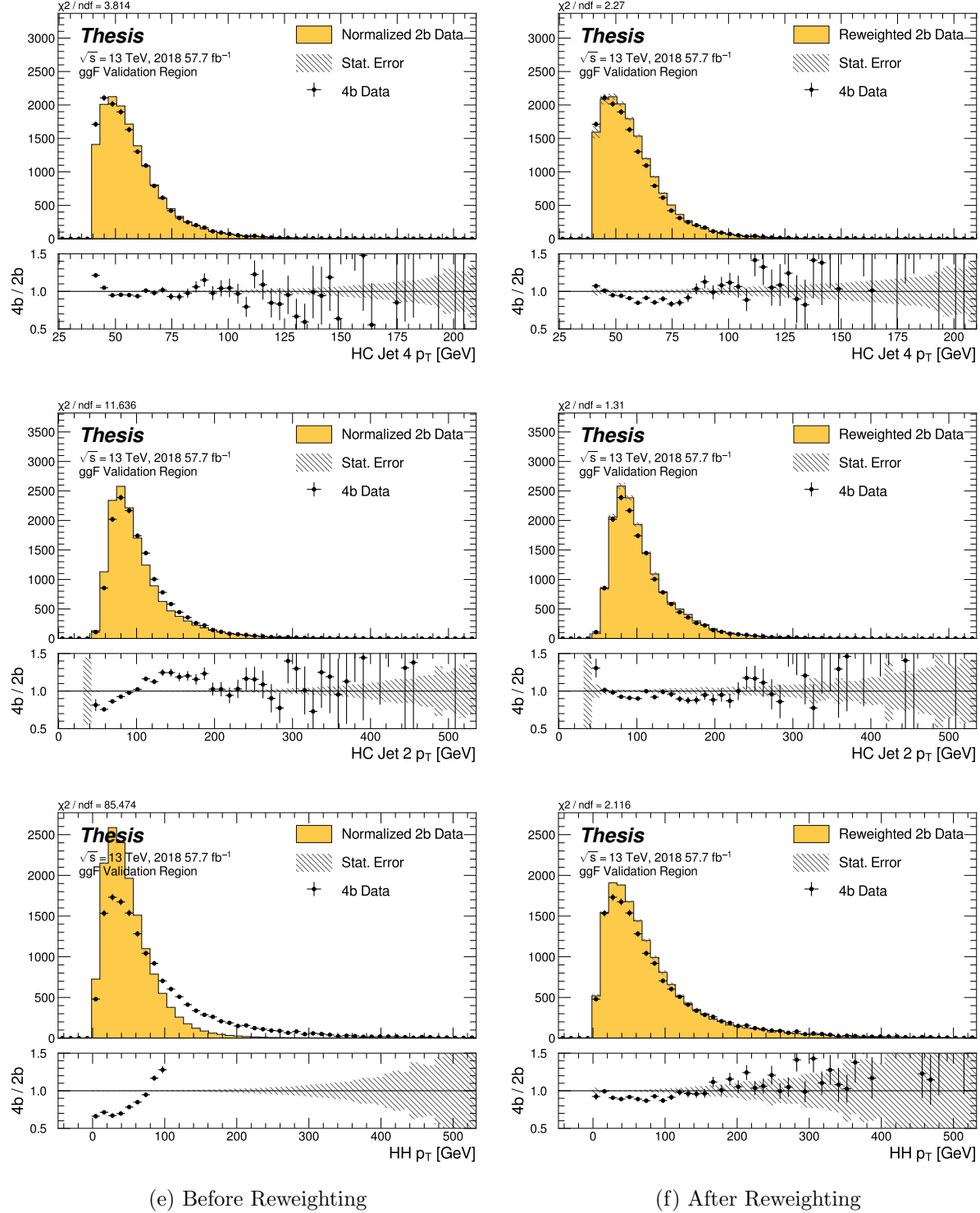


Figure 7.34: **Non-resonant Search (4b):** Distributions of  $p_T$  of the 2nd and 4th leading Higgs Candidate jets and the  $p_T$  of the di-Higgs system before and after CR derived reweighting for the 2018 4b Validation Region.

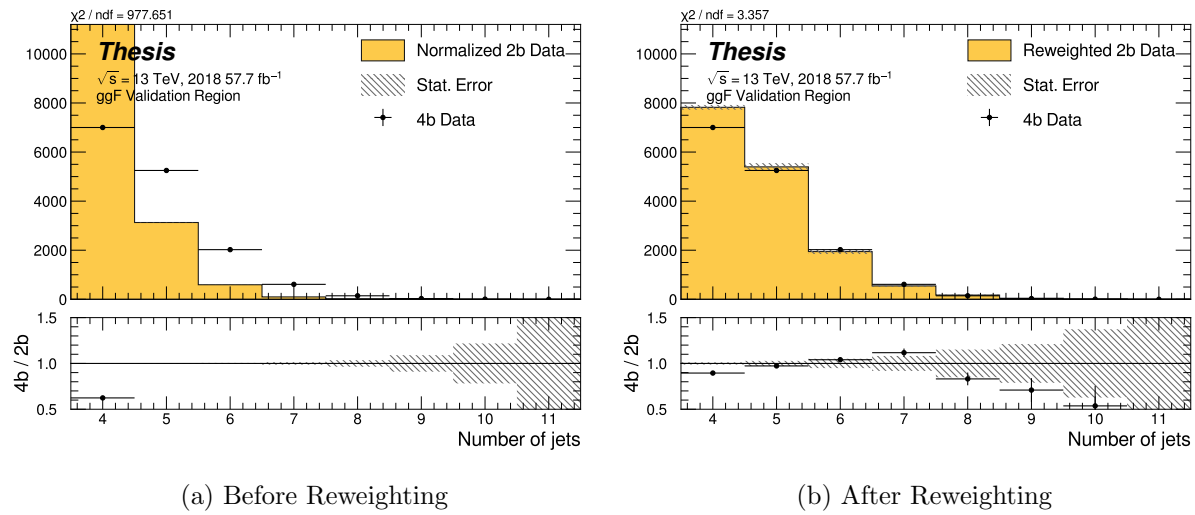


Figure 7.35: **Non-resonant Search (4b):** Distributions of the number of jets before and after CR derived reweighting for the 2018 4b Validation Region. A minimum of 4 jets is required in each event in order to form Higgs candidates.

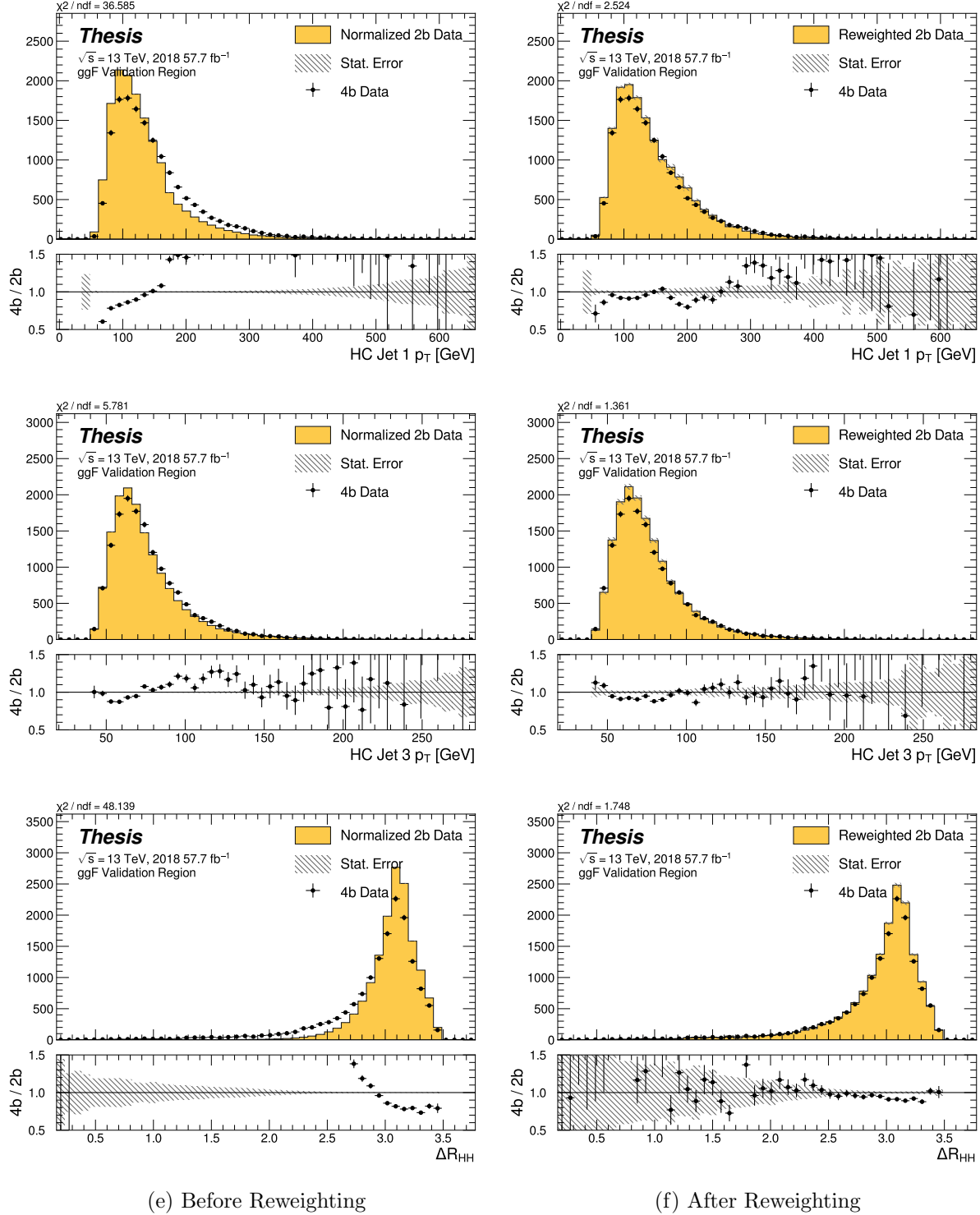


Figure 7.36: **Non-resonant Search (4b):** Distributions of  $p_T$  of the 1st and 3rd leading Higgs Candidate jets and  $\Delta R$  between Higgs candidates before and after CR derived reweighting for the 2018 4b Validation Region.

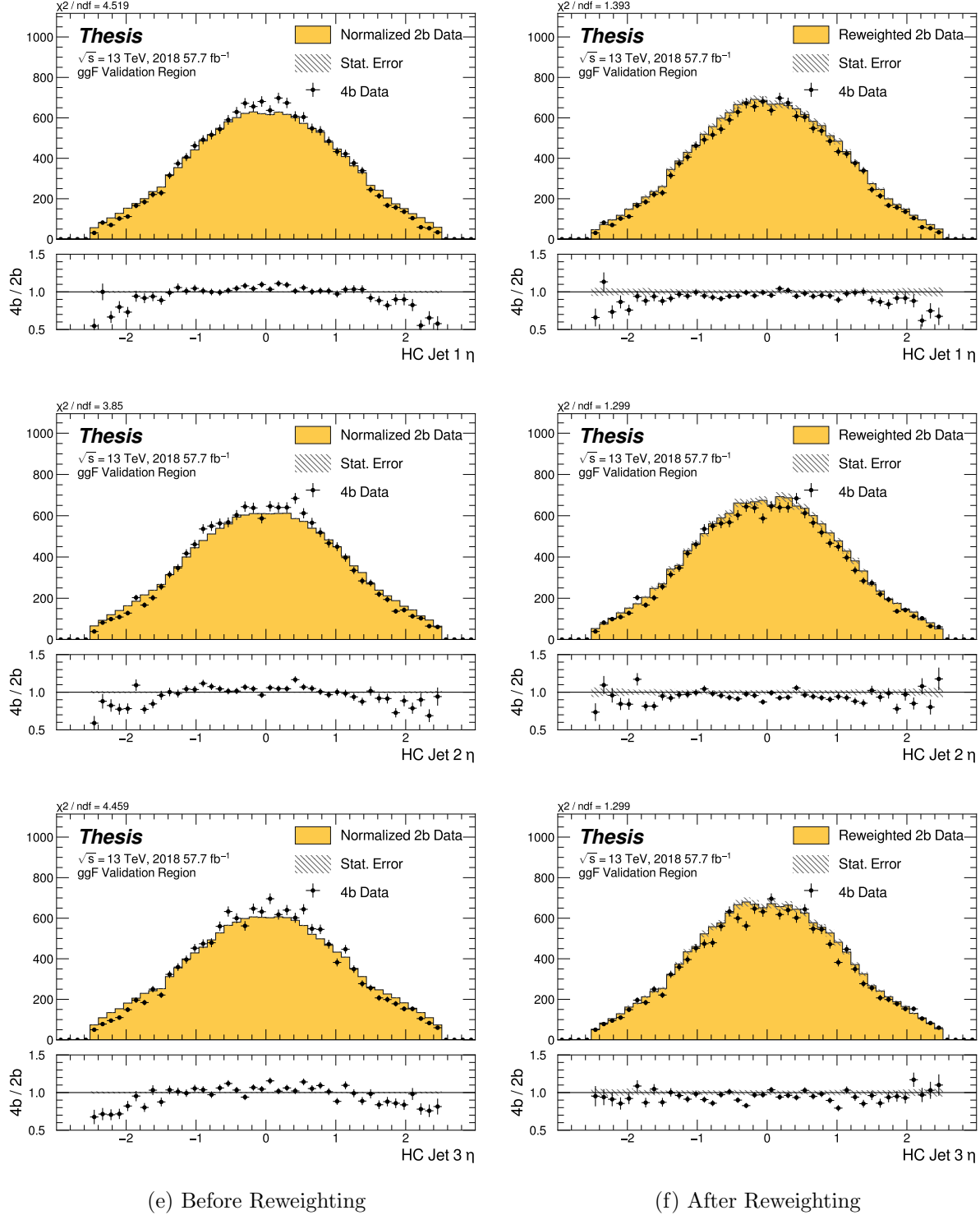


Figure 7.37: **Non-resonant Search (4b):** Distributions of  $\eta$  of the 1st, 2nd, and 3rd leading Higgs Candidate jets before and after CR derived reweighting for the 2018 4b Validation Region.

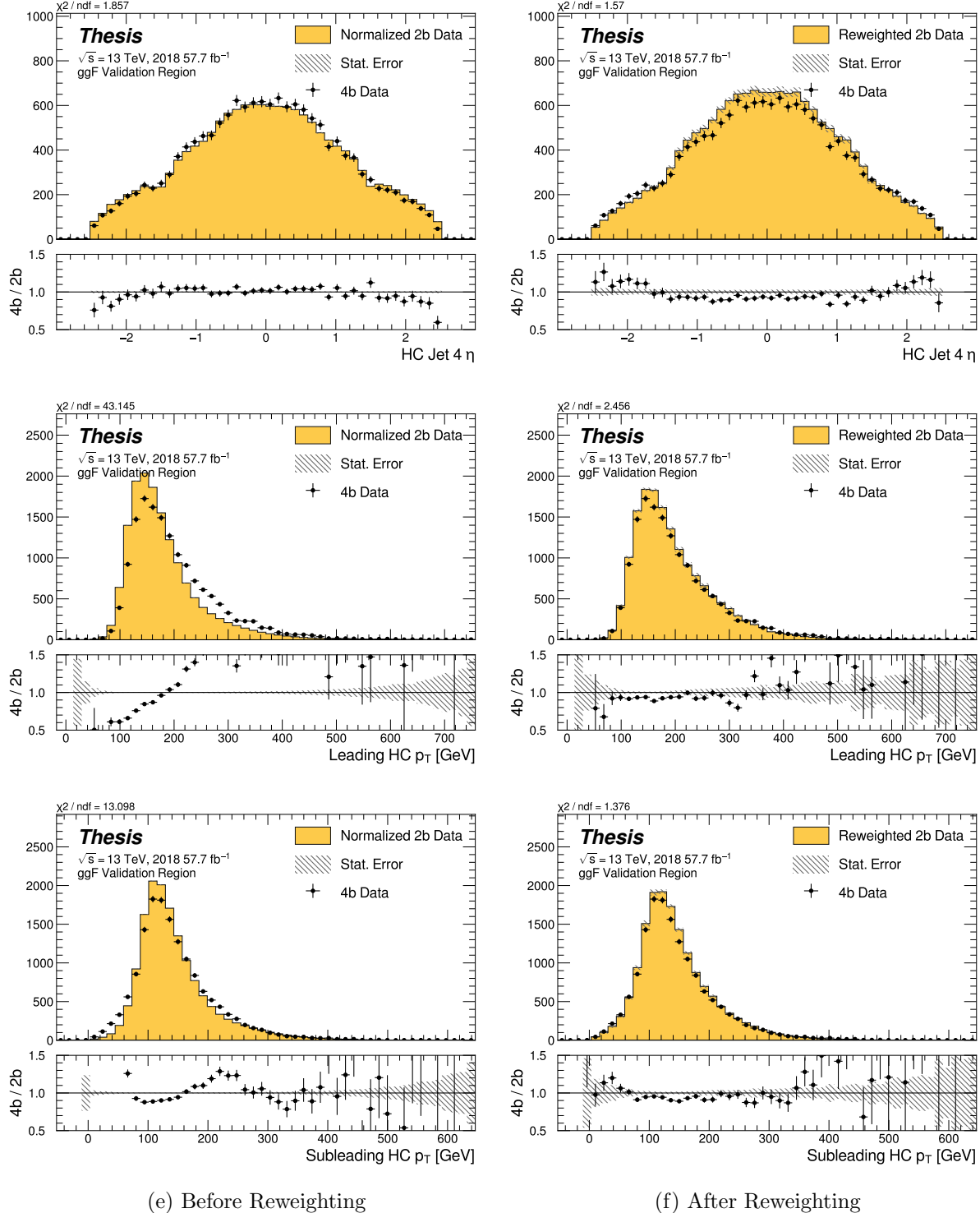


Figure 7.38: **Non-resonant Search (4b):** Distributions of  $\eta$  of the 4th leading Higgs Candidate jet and the  $p_T$  of the leading and subleading Higgs candidates before and after CR derived reweighting for the 2018 4b Validation Region.

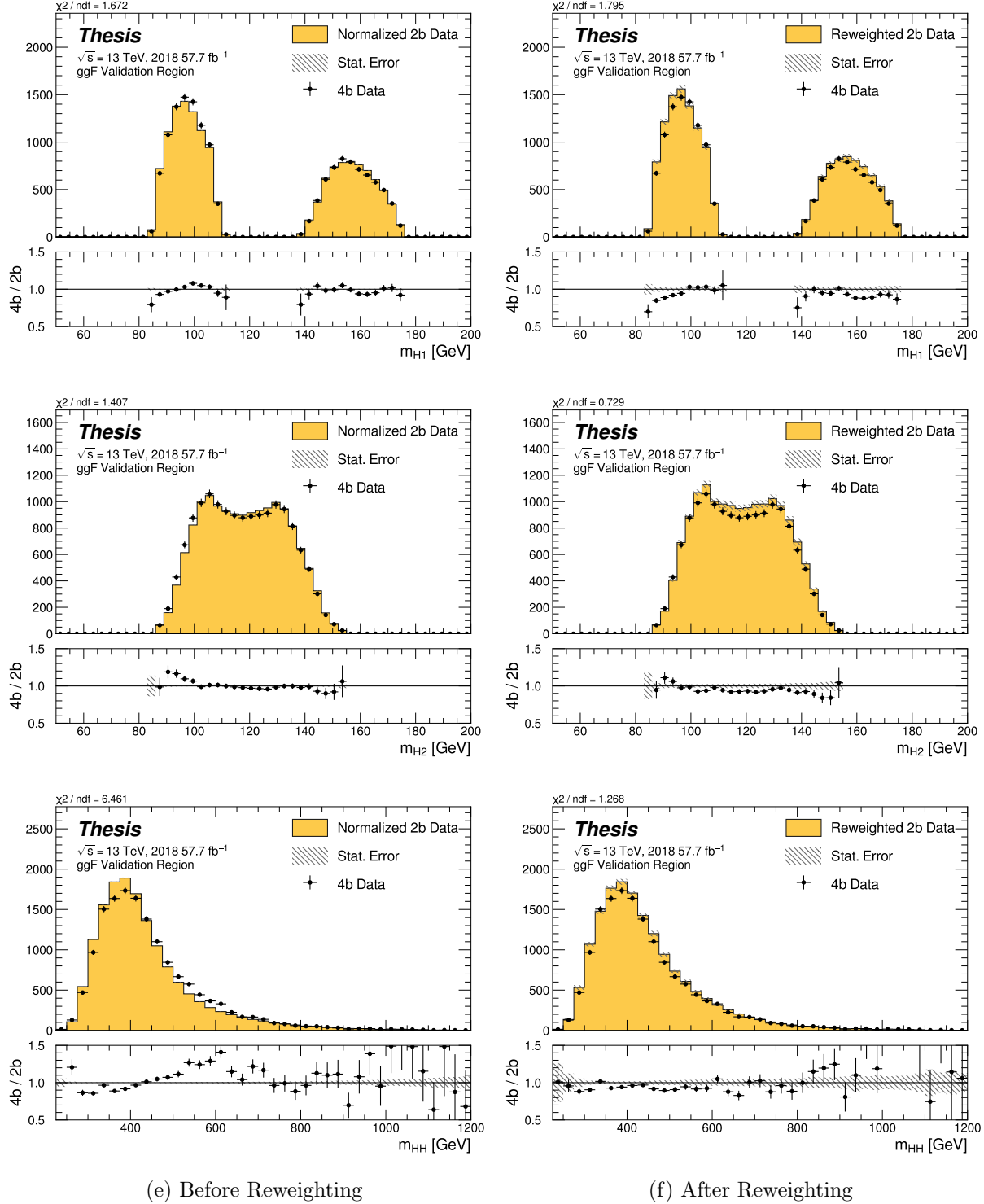


Figure 7.39: **Non-resonant Search (4b):** Distributions of mass of the leading and subleading Higgs candidates and of the di-Higgs system before and after CR derived reweighting for the 2018 4b Validation Region.

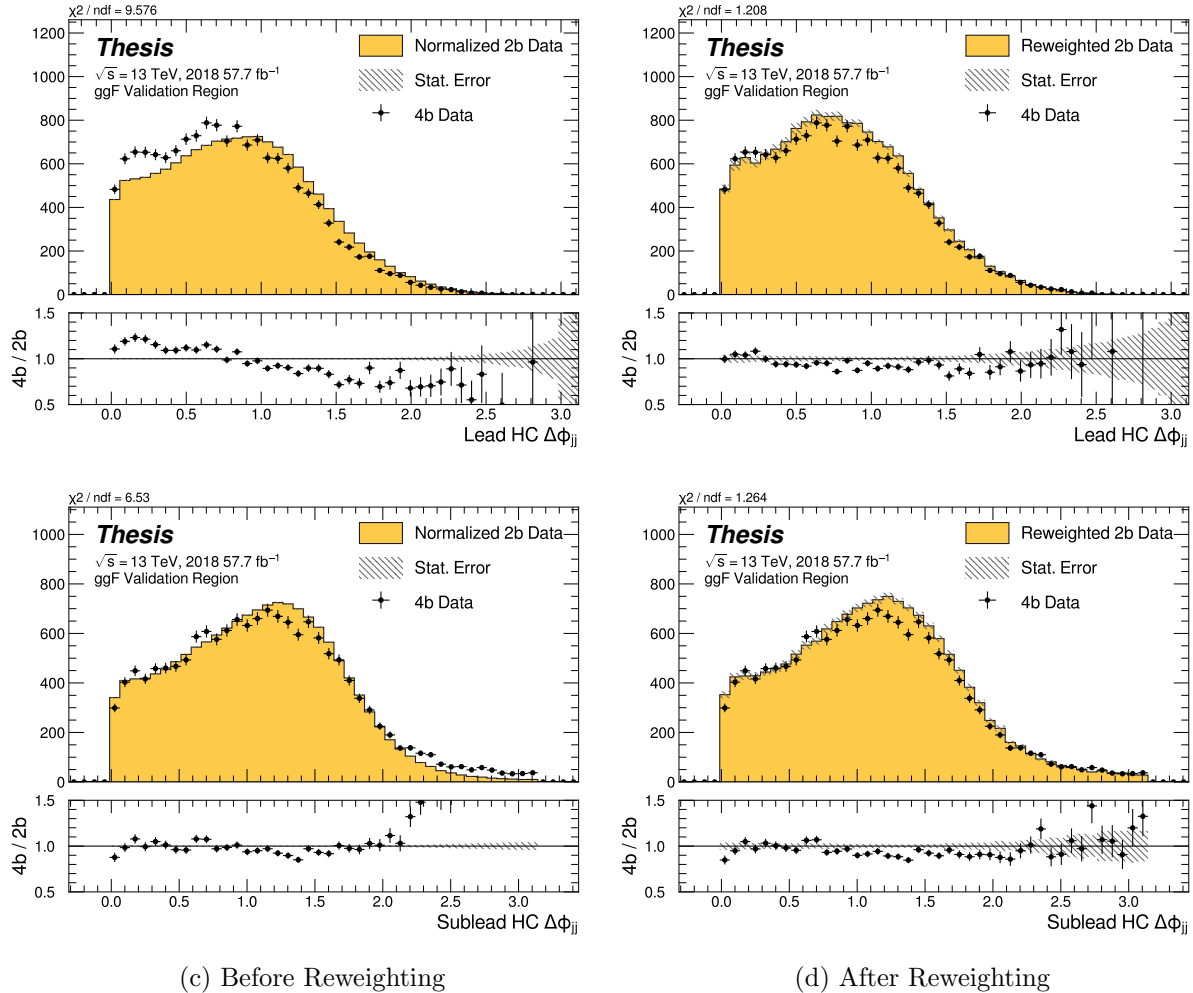


Figure 7.40: **Non-resonant Search (4b):** Distributions of  $\Delta\phi$  between jets in the leading and subleading Higgs candidates before and after CR derived reweighting for the 2018 4b Validation Region.

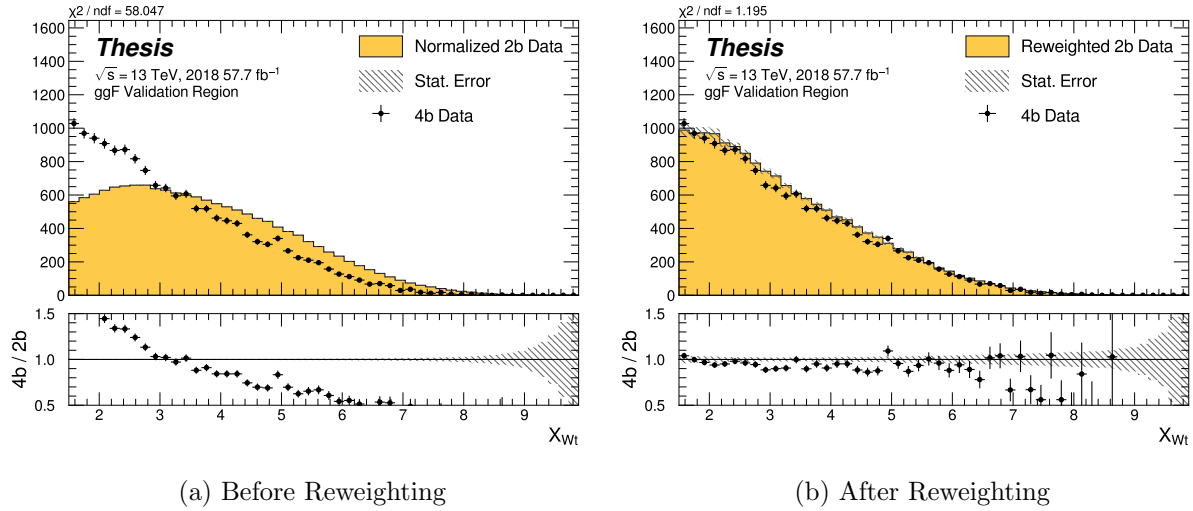


Figure 7.41: **Non-resonant Search (4b):** Distributions of the top veto variable,  $X_{Wt}$ , before and after CR derived reweighting for the 2018 4b Validation Region. Reweighting is done after the cut on this variable is applied.

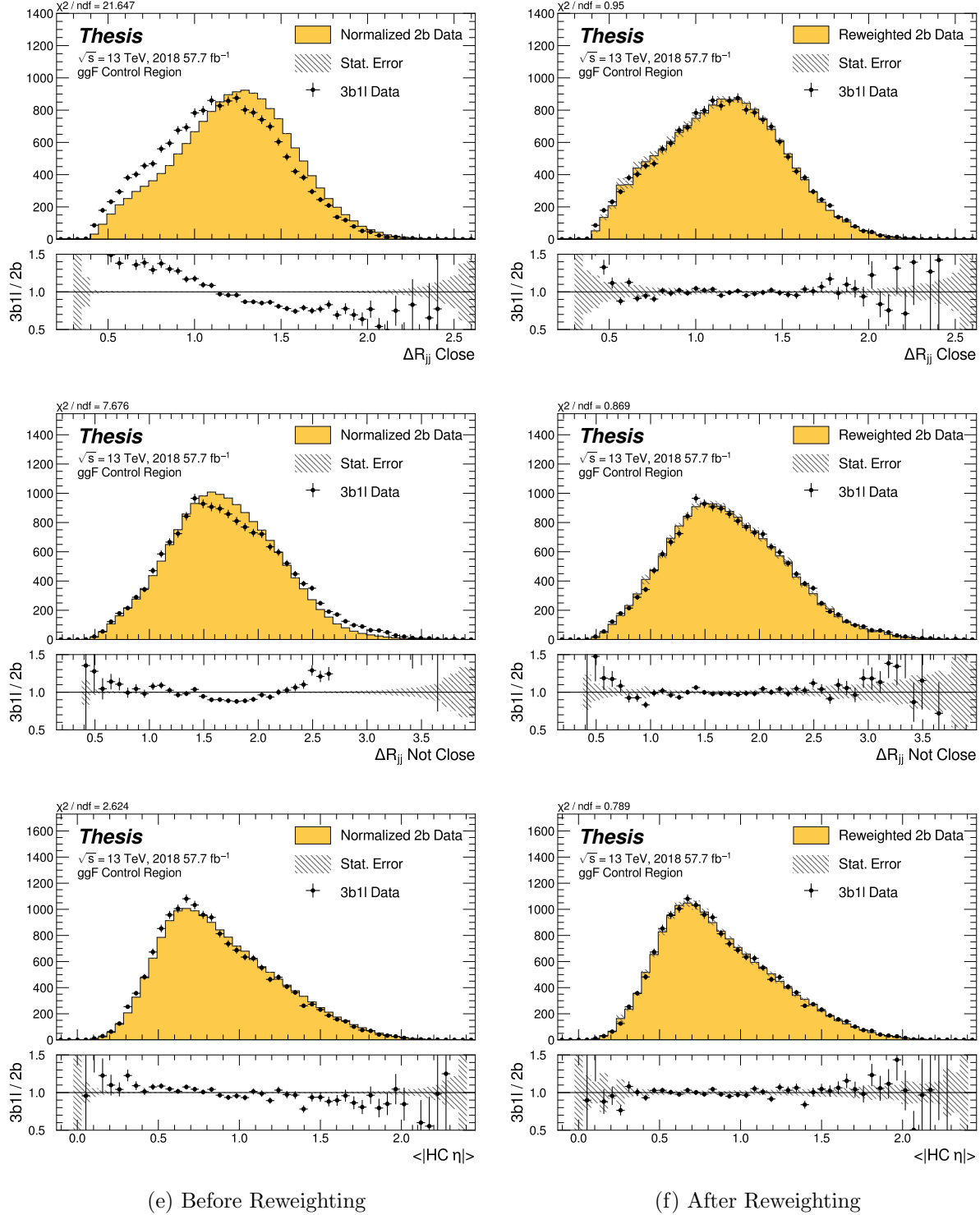


Figure 7.42: **Non-resonant Search (3b1l):** Distributions of  $\Delta R$  between the closest Higgs Candidate jets,  $\Delta R$  between the other two, and average absolute value of HC jet  $\eta$  before and after CR derived reweighting for the 2018 3b1l Control Region.

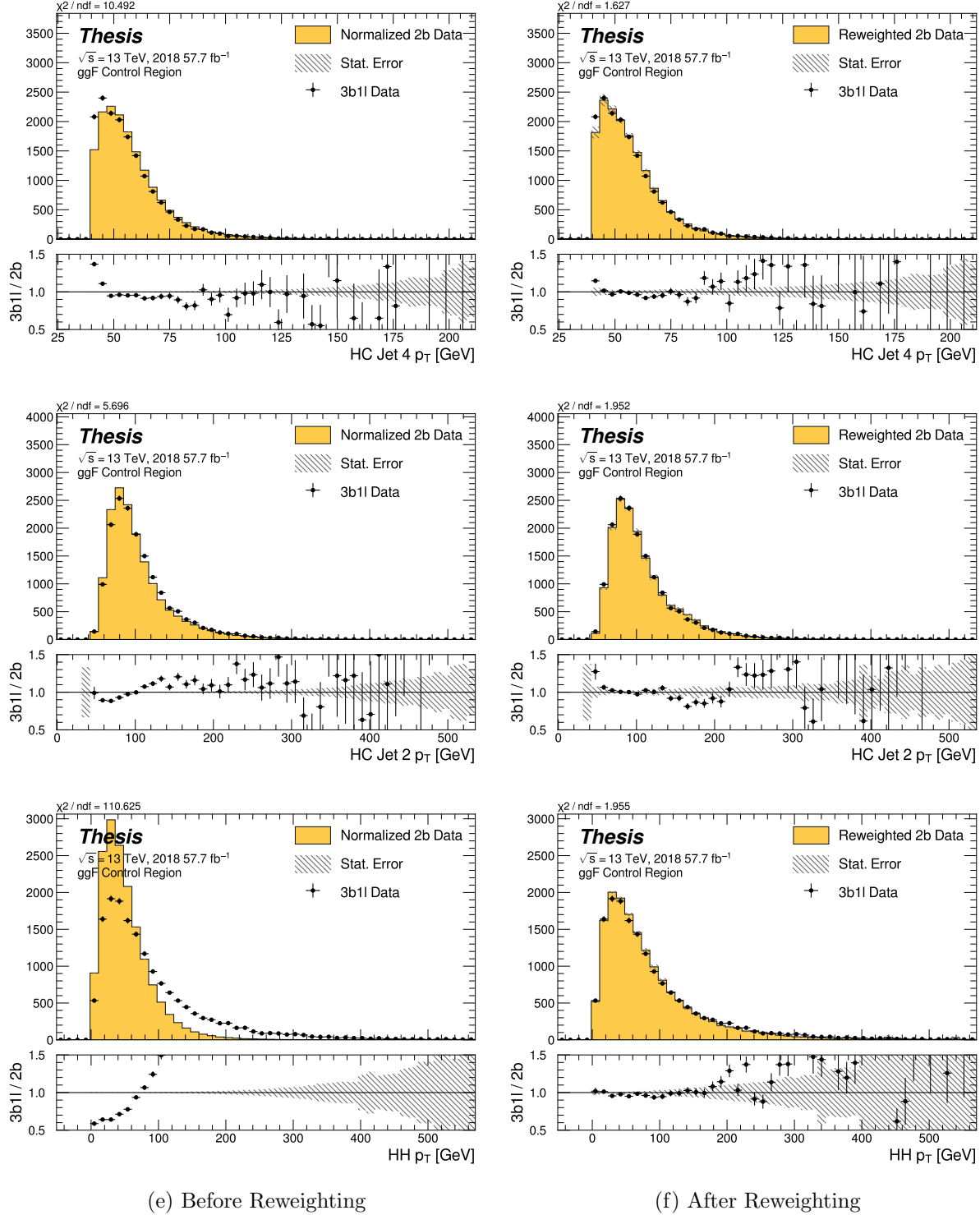


Figure 7.43: **Non-resonant Search (3b1l):** Distributions of  $p_T$  of the 2nd and 4th leading Higgs Candidate jets and the  $p_T$  of the di-Higgs system before and after CR derived reweighting for the 2018 3b1l Control Region.

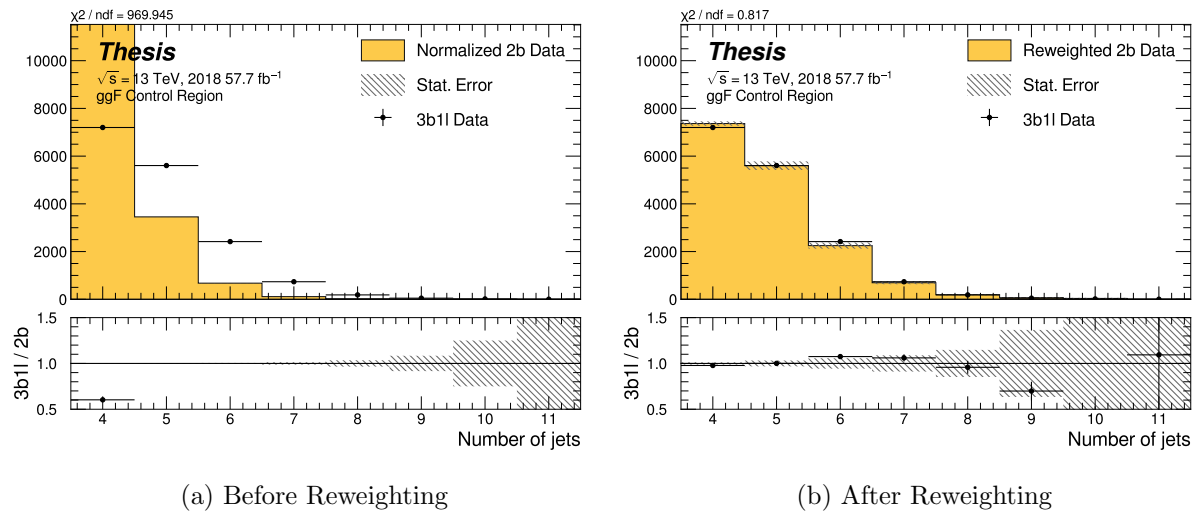


Figure 7.44: **Non-resonant Search (3b1l):** Distributions of the number of jets before and after CR derived reweighting for the 2018 3b1l Control Region. A minimum of 4 jets is required in each event in order to form Higgs candidates.

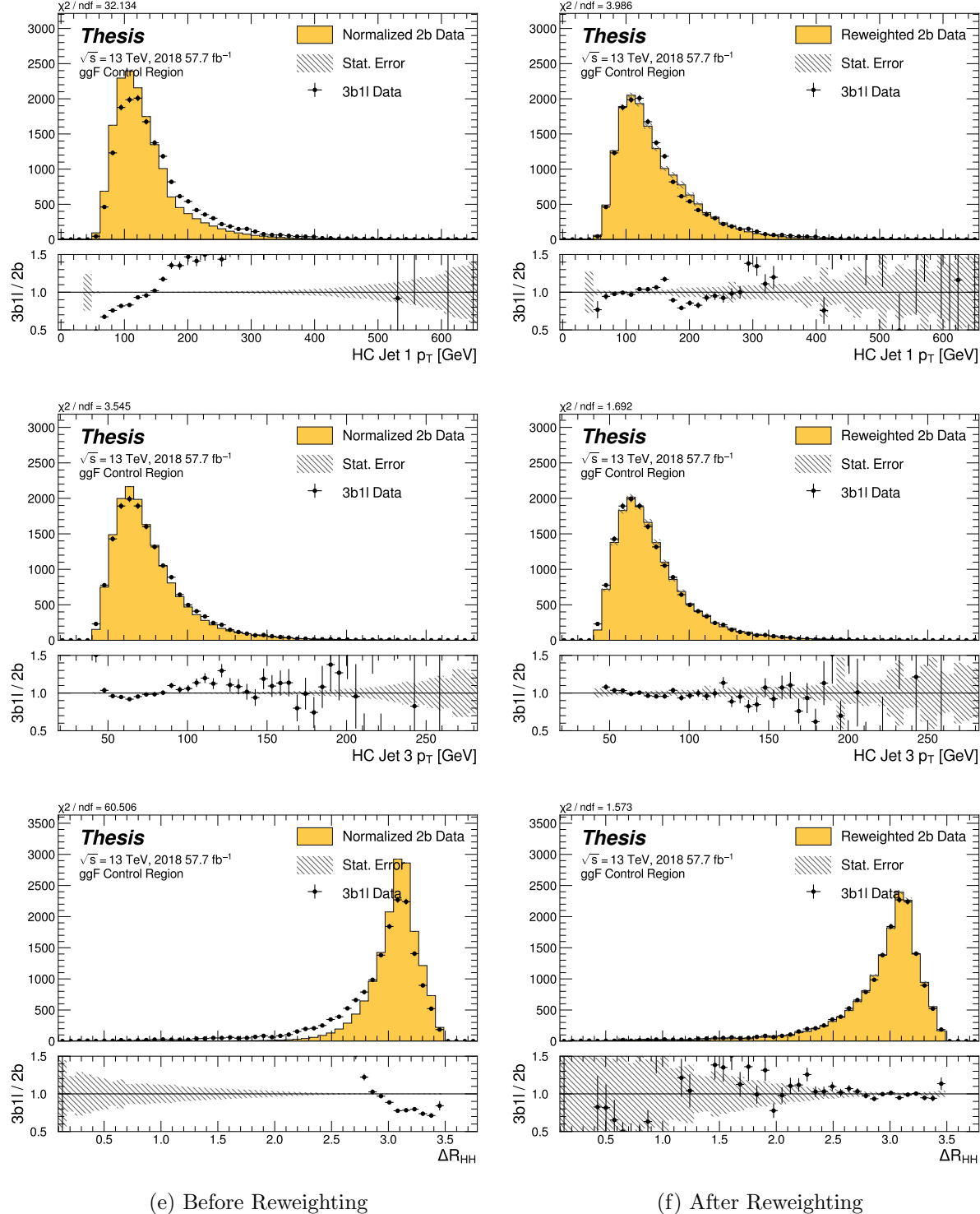


Figure 7.45: **Non-resonant Search (3b1l):** Distributions of  $p_T$  of the 1st and 3rd leading Higgs Candidate jets and  $\Delta R$  between Higgs candidates before and after CR derived reweighting for the 2018 3b1l Control Region.

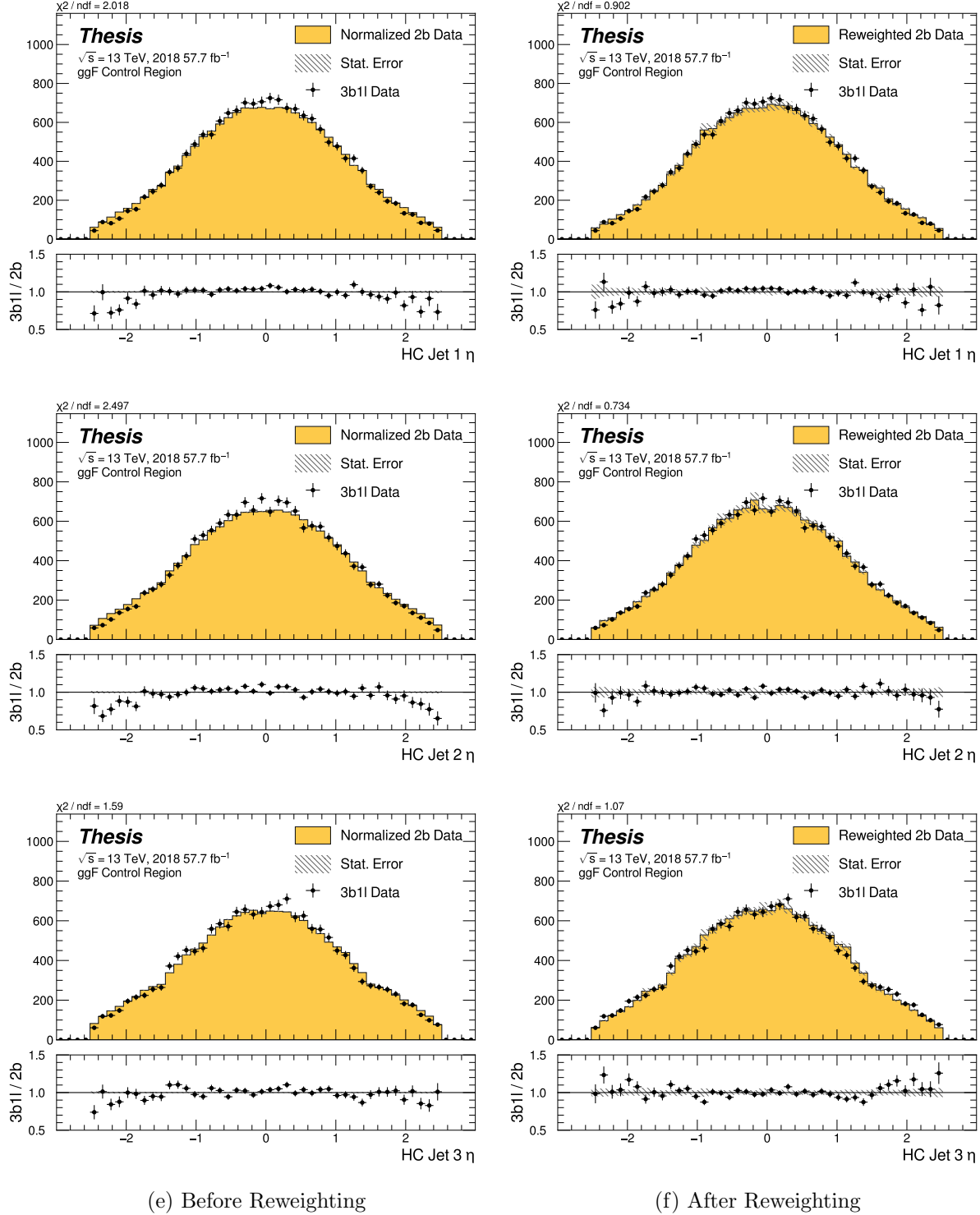


Figure 7.46: **Non-resonant Search (3b1l):** Distributions of  $\eta$  of the 1st, 2nd, and 3rd leading Higgs Candidate jets before and after CR derived reweighting for the 2018 3b1l Control Region.

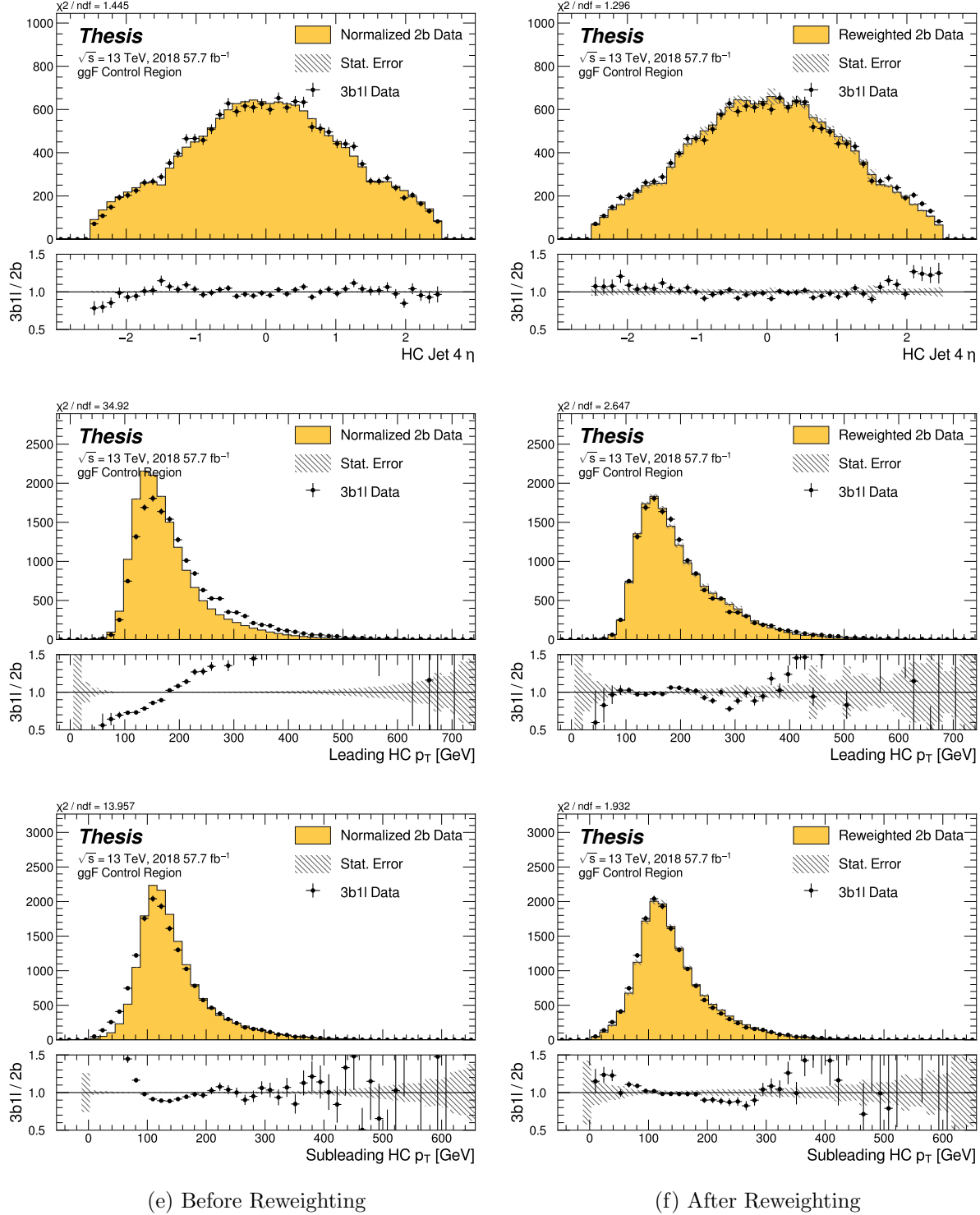


Figure 7.47: **Non-resonant Search (3b1l):** Distributions of  $\eta$  of the 4th leading Higgs Candidate jet and the  $p_T$  of the leading and subleading Higgs candidates before and after CR derived reweighting for the 2018 3b1l Control Region.

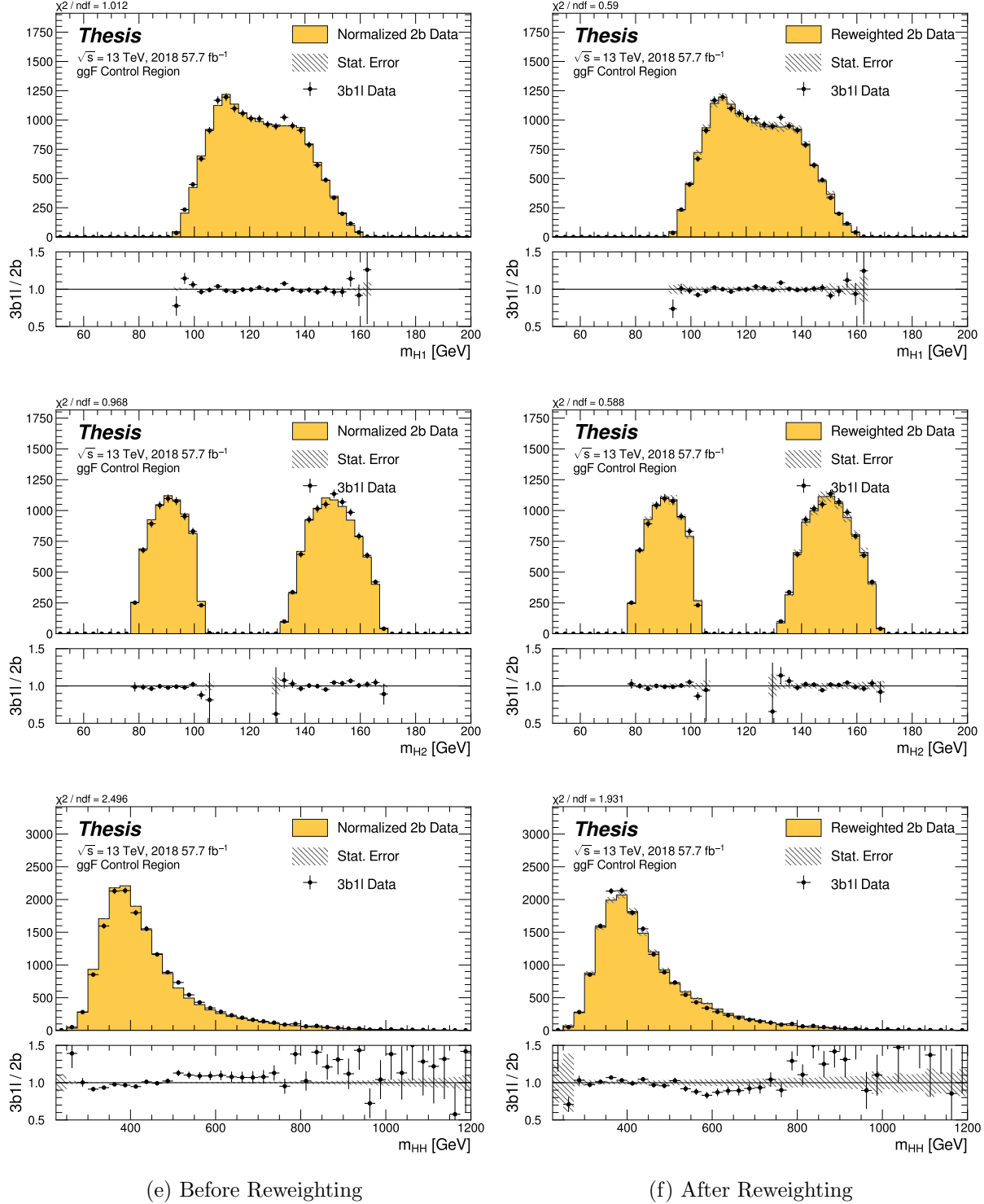


Figure 7.48: **Non-resonant Search (3b1l):** Distributions of mass of the leading and sub-leading Higgs candidates and of the di-Higgs system before and after CR derived reweighting for the 2018 3b1l Control Region.

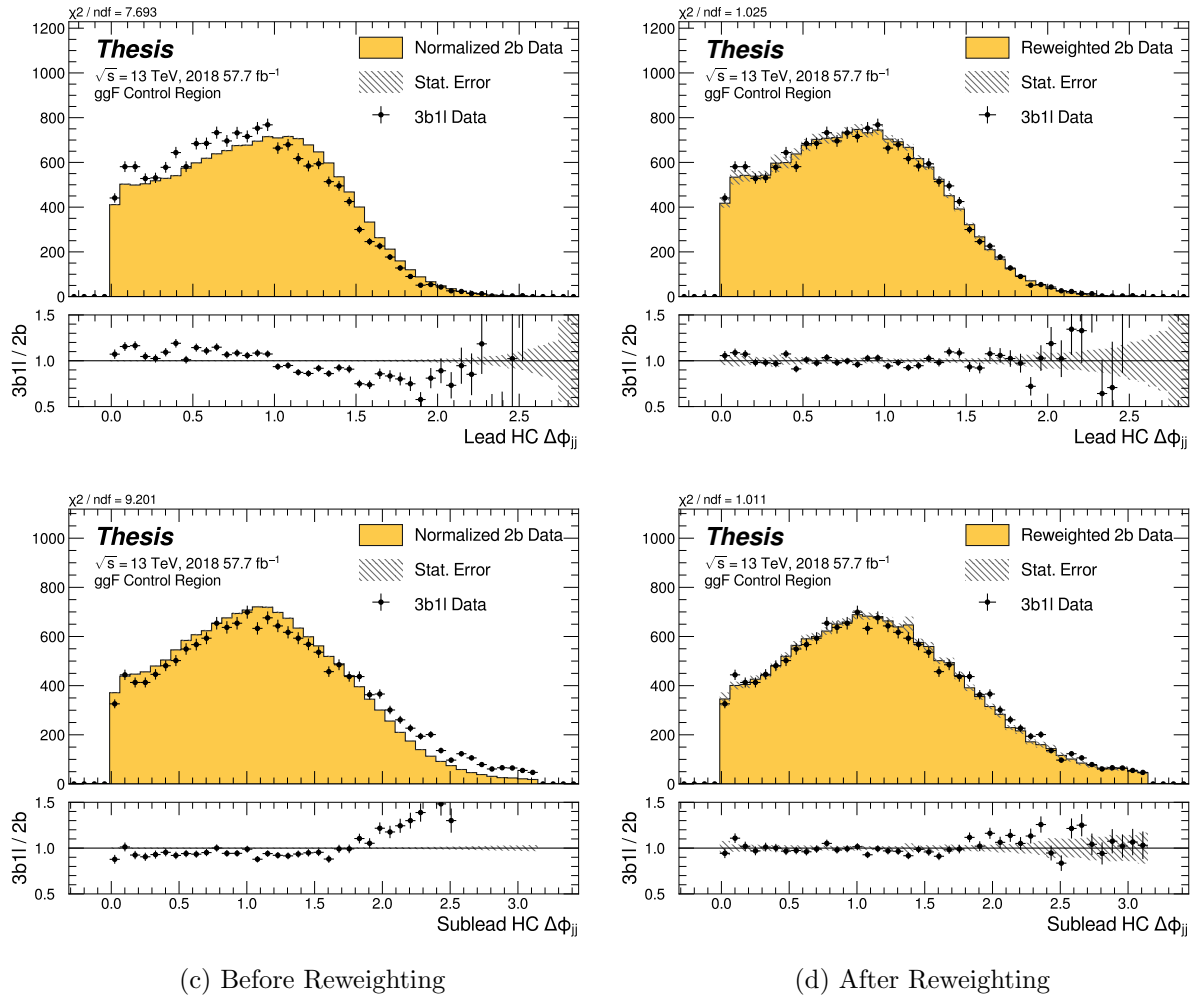


Figure 7.49: **Non-resonant Search (3b1l):** Distributions of  $\Delta\phi$  between jets in the leading and subleading Higgs candidates before and after CR derived reweighting for the 2018 3b1l Control Region.

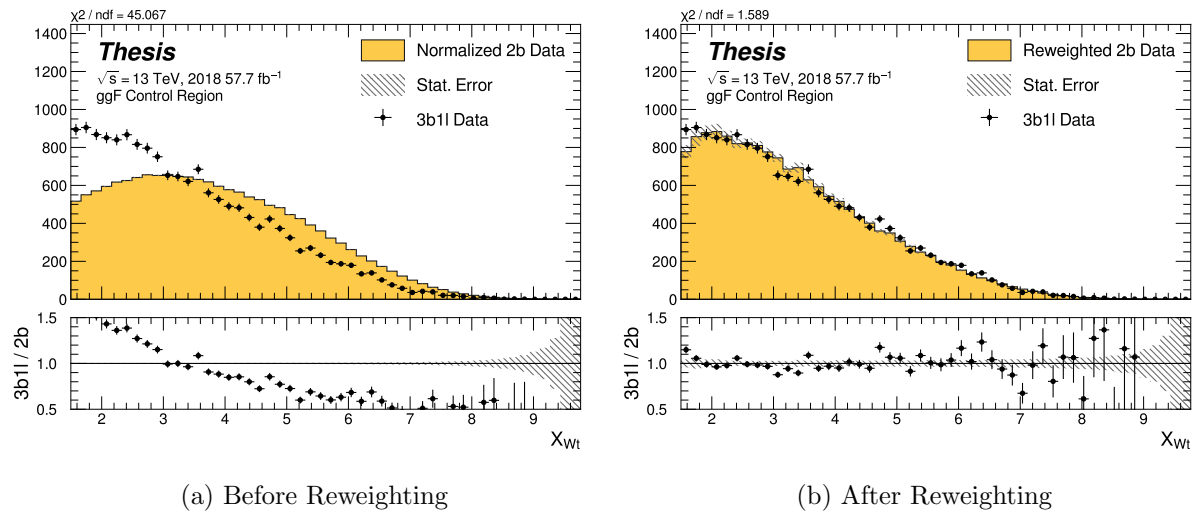


Figure 7.50: **Non-resonant Search (3b1l):** Distributions of the top veto variable,  $X_{Wt}$ , before and after CR derived reweighting for the 2018 3b1l Control Region. Reweighting is done after the cut on this variable is applied.

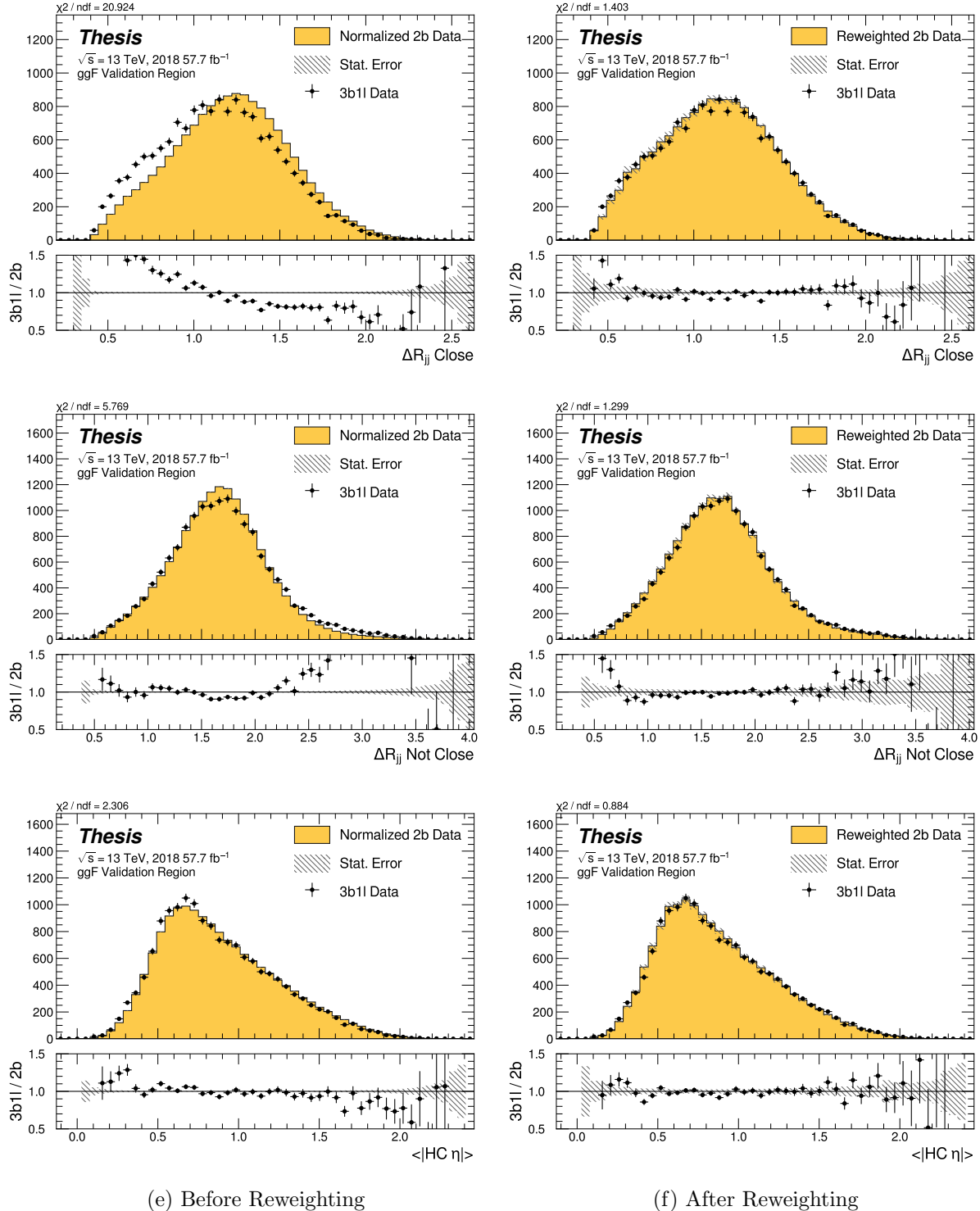


Figure 7.51: **Non-resonant Search (3b1l):** Distributions of  $\Delta R$  between the closest Higgs Candidate jets,  $\Delta R$  between the other two, and average absolute value of HC jet  $\eta$  before and after CR derived reweighting for the 2018 3b1l Validation Region.

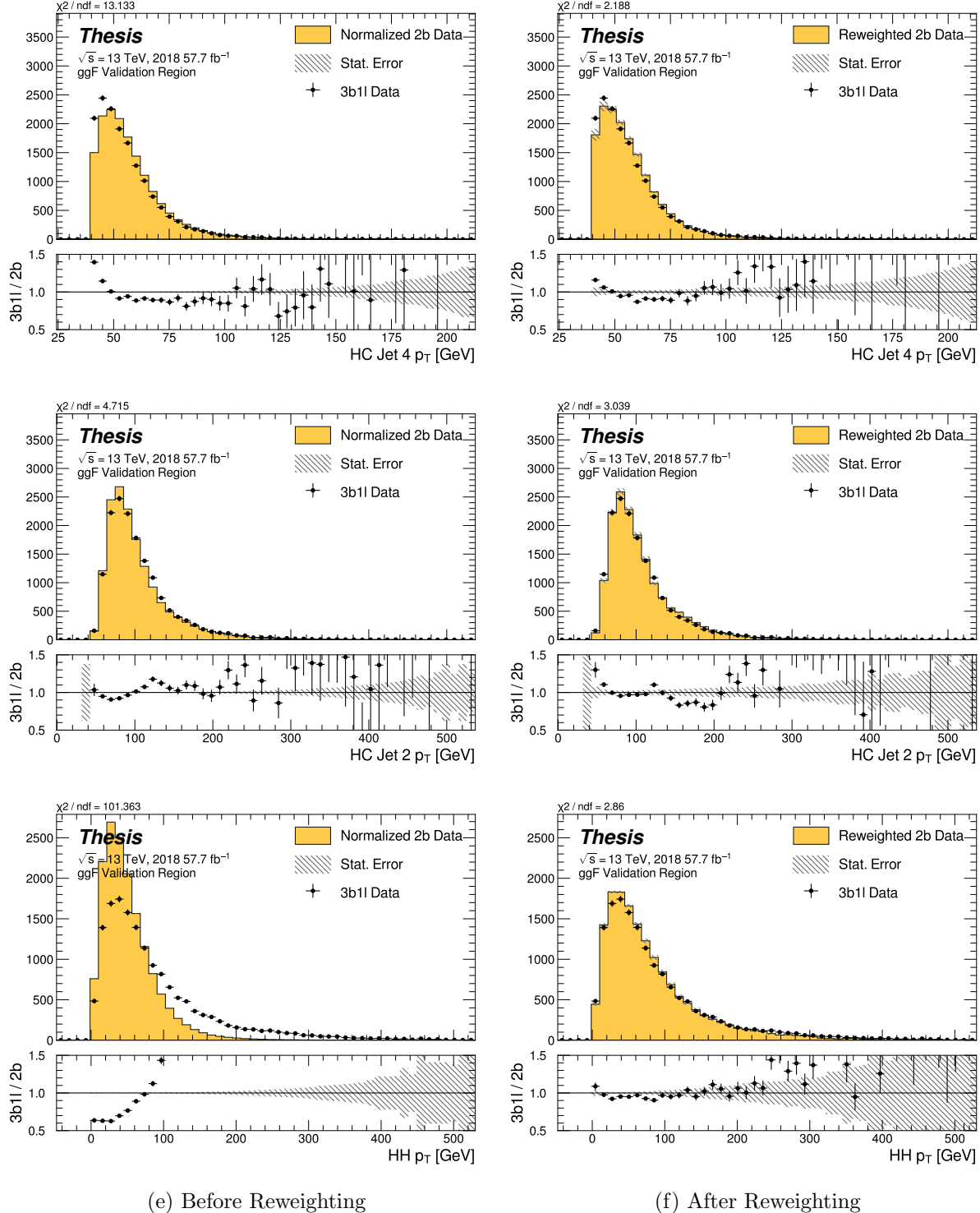


Figure 7.52: **Non-resonant Search (3b1l):** Distributions of  $p_T$  of the 2nd and 4th leading Higgs Candidate jets and the  $p_T$  of the di-Higgs system before and after CR derived reweighting for the 2018 3b1l Validation Region.

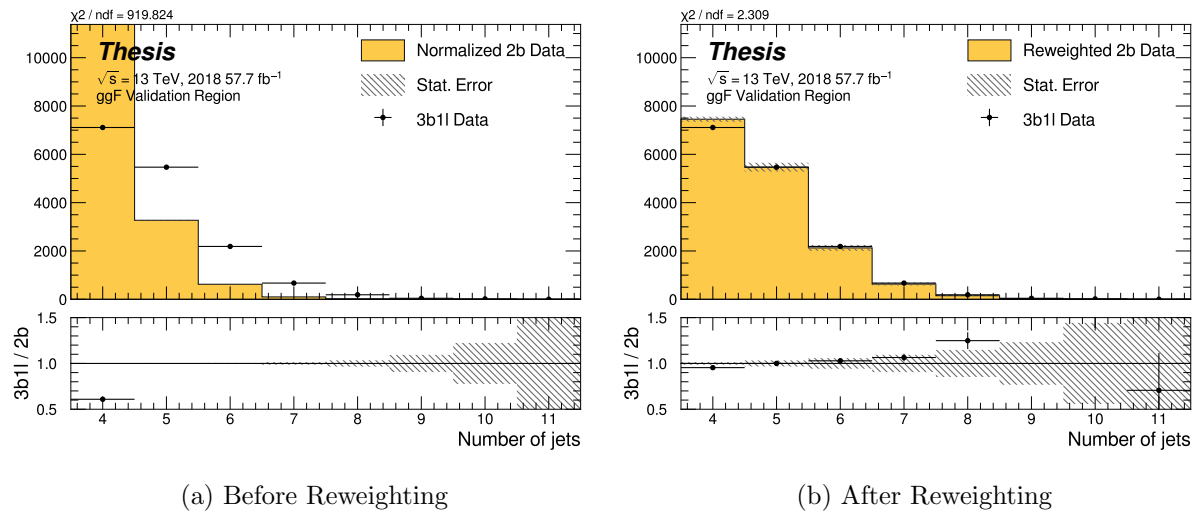


Figure 7.53: **Non-resonant Search (3b1l):** Distributions of the number of jets before and after CR derived reweighting for the 2018 3b1l Validation Region. A minimum of 4 jets is required in each event in order to form Higgs candidates.

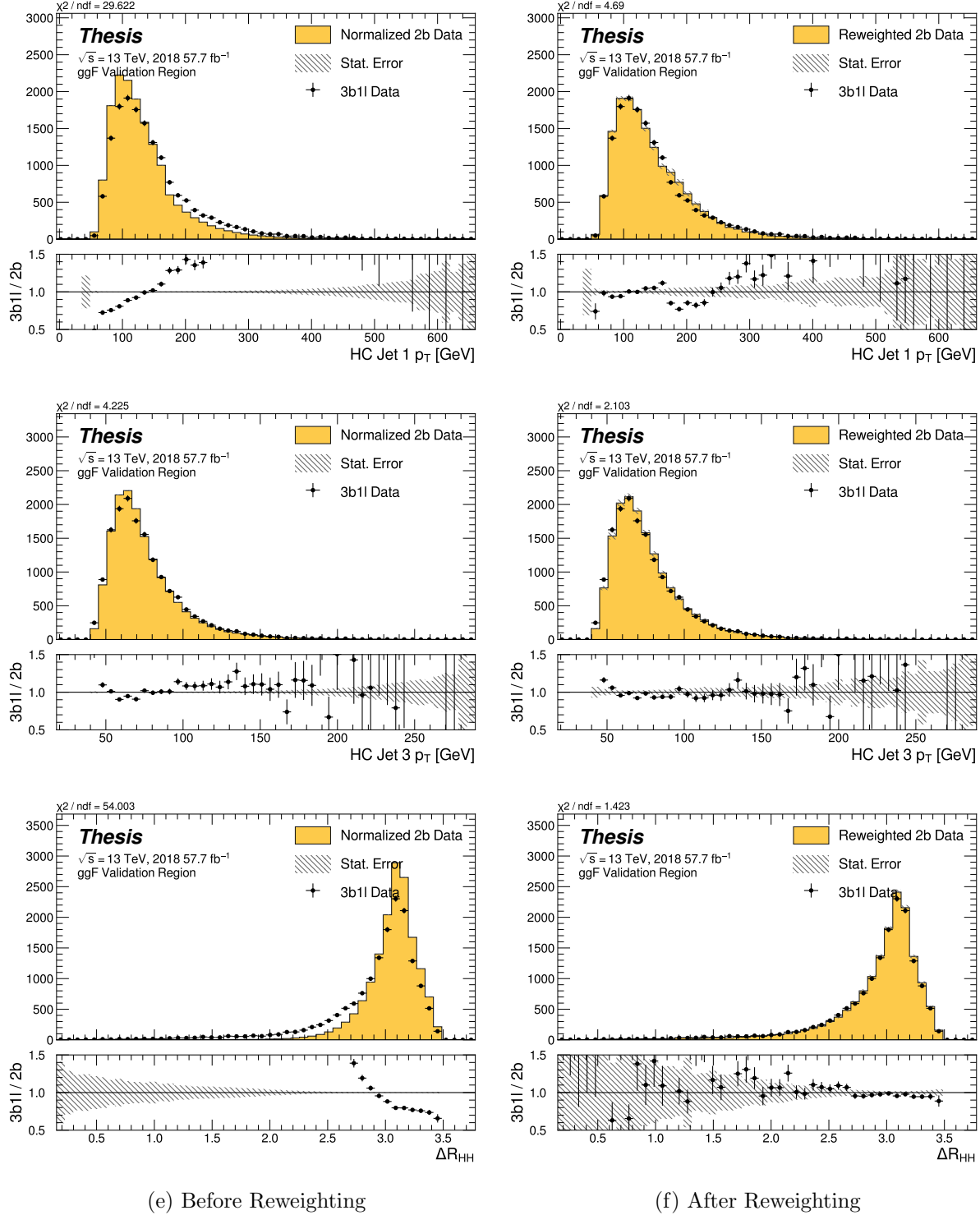


Figure 7.54: **Non-resonant Search (3b1l):** Distributions of  $p_T$  of the 1st and 3rd leading Higgs Candidate jets and  $\Delta R$  between Higgs candidates before and after CR derived reweighting for the 2018 3b1l Validation Region.

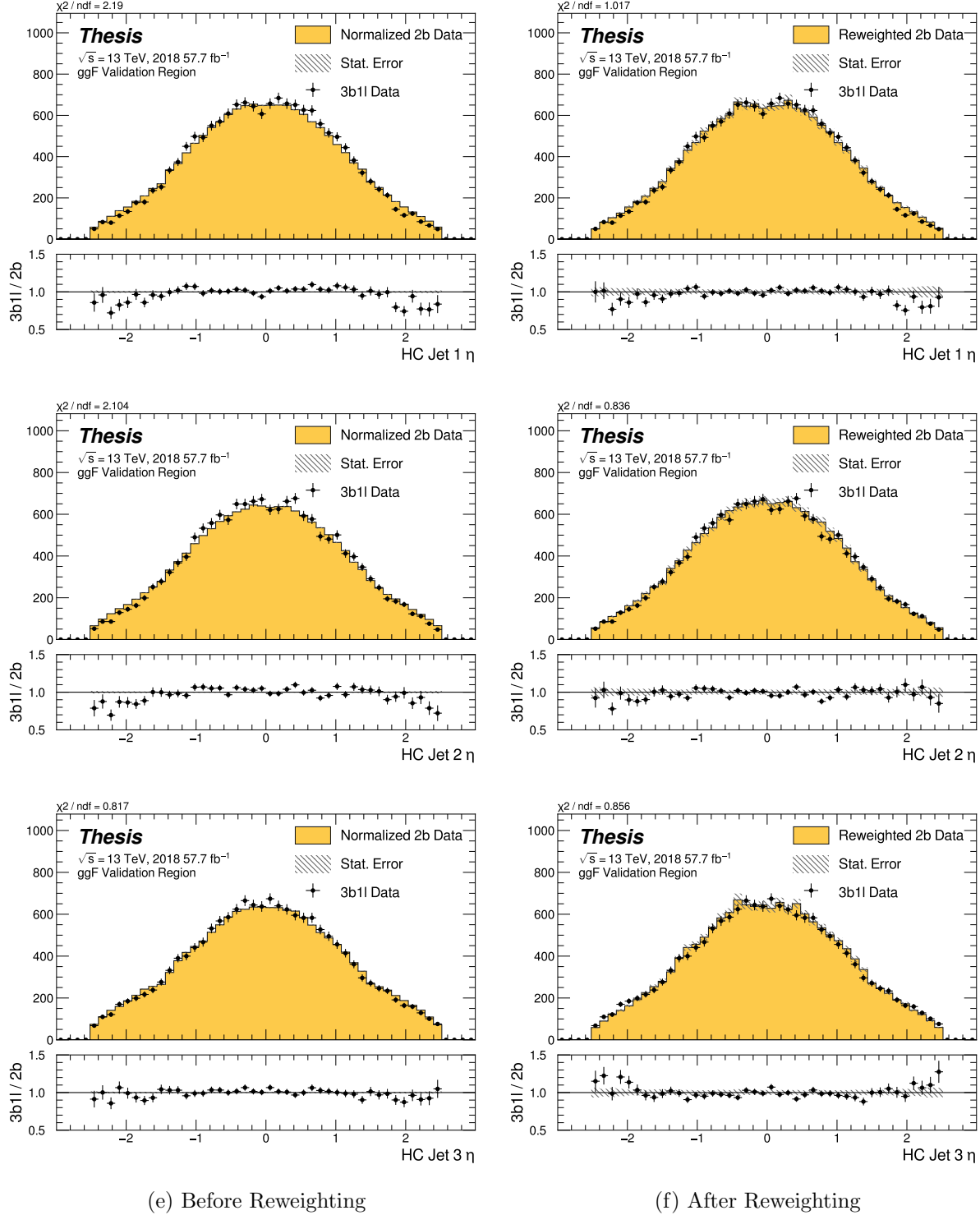


Figure 7.55: **Non-resonant Search (3b1l):** Distributions of  $\eta$  of the 1st, 2nd, and 3rd leading Higgs Candidate jets before and after CR derived reweighting for the 2018 3b1l Validation Region.

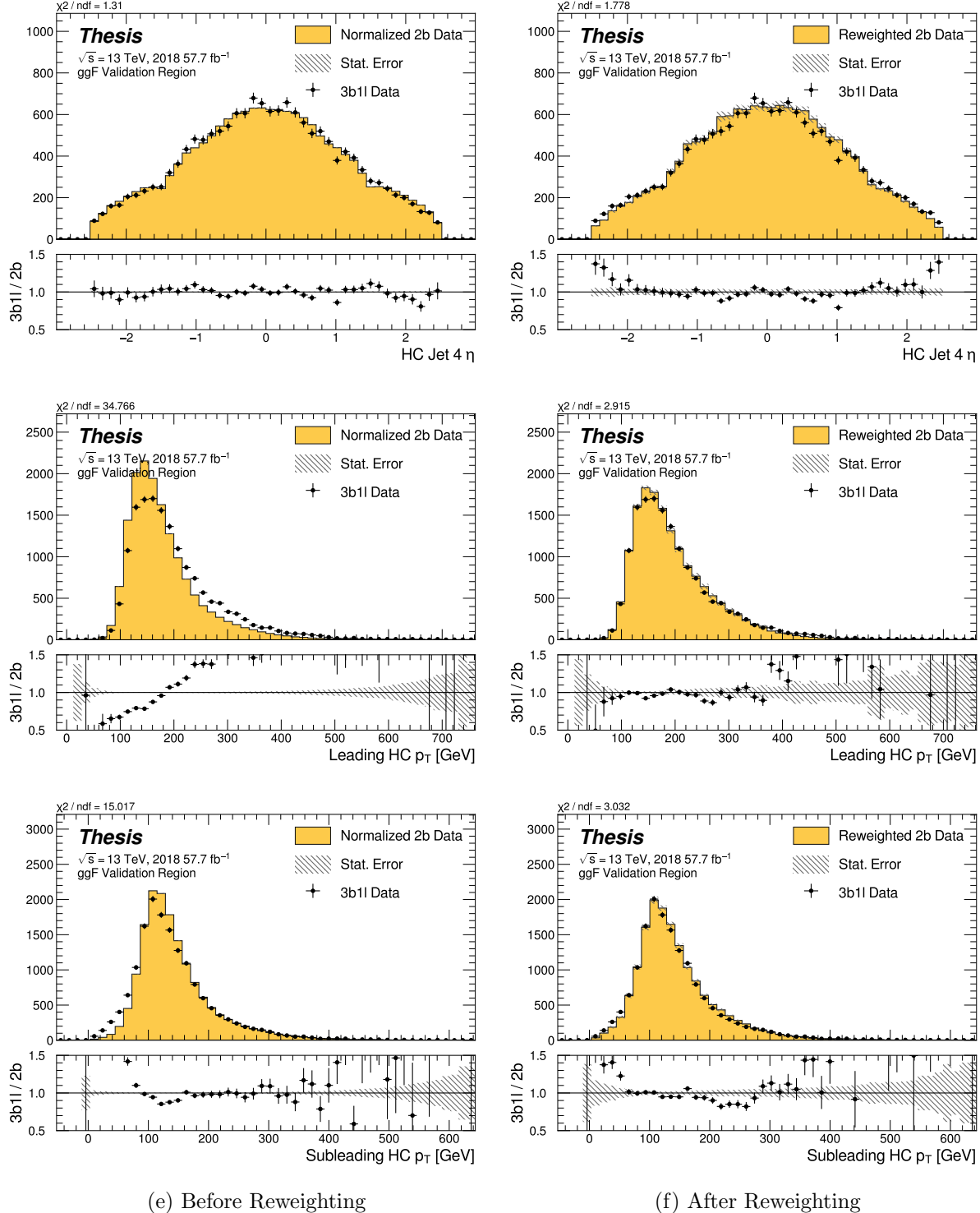


Figure 7.56: **Non-resonant Search (3b1l):** Distributions of  $\eta$  of the 4th leading Higgs Candidate jet and the  $p_T$  of the leading and subleading Higgs candidates before and after CR derived reweighting for the 2018 3b1l Validation Region.

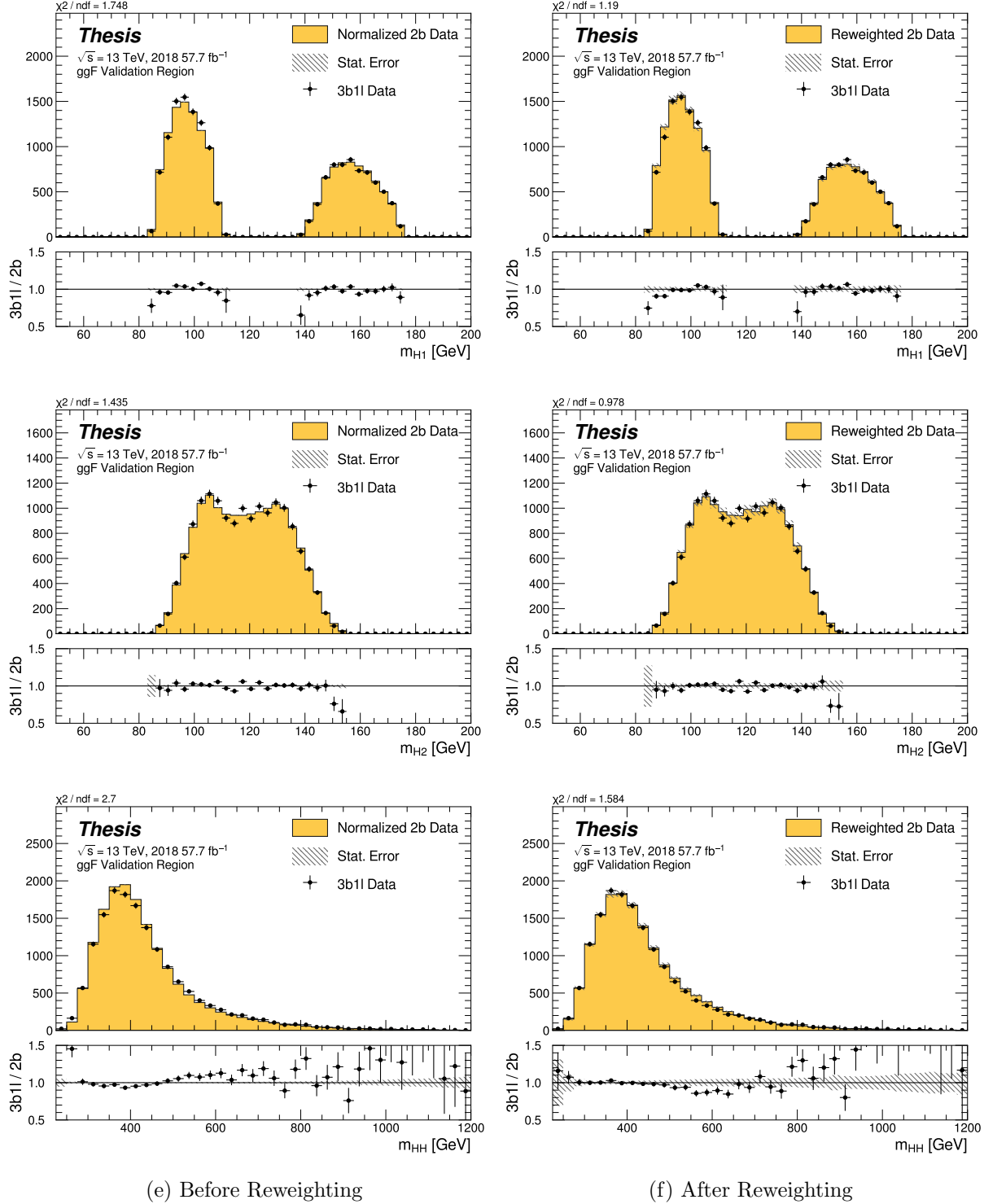


Figure 7.57: **Non-resonant Search (3b1l):** Distributions of mass of the leading and sub-leading Higgs candidates and of the di-Higgs system before and after CR derived reweighting for the 2018 3b1l Validation Region.

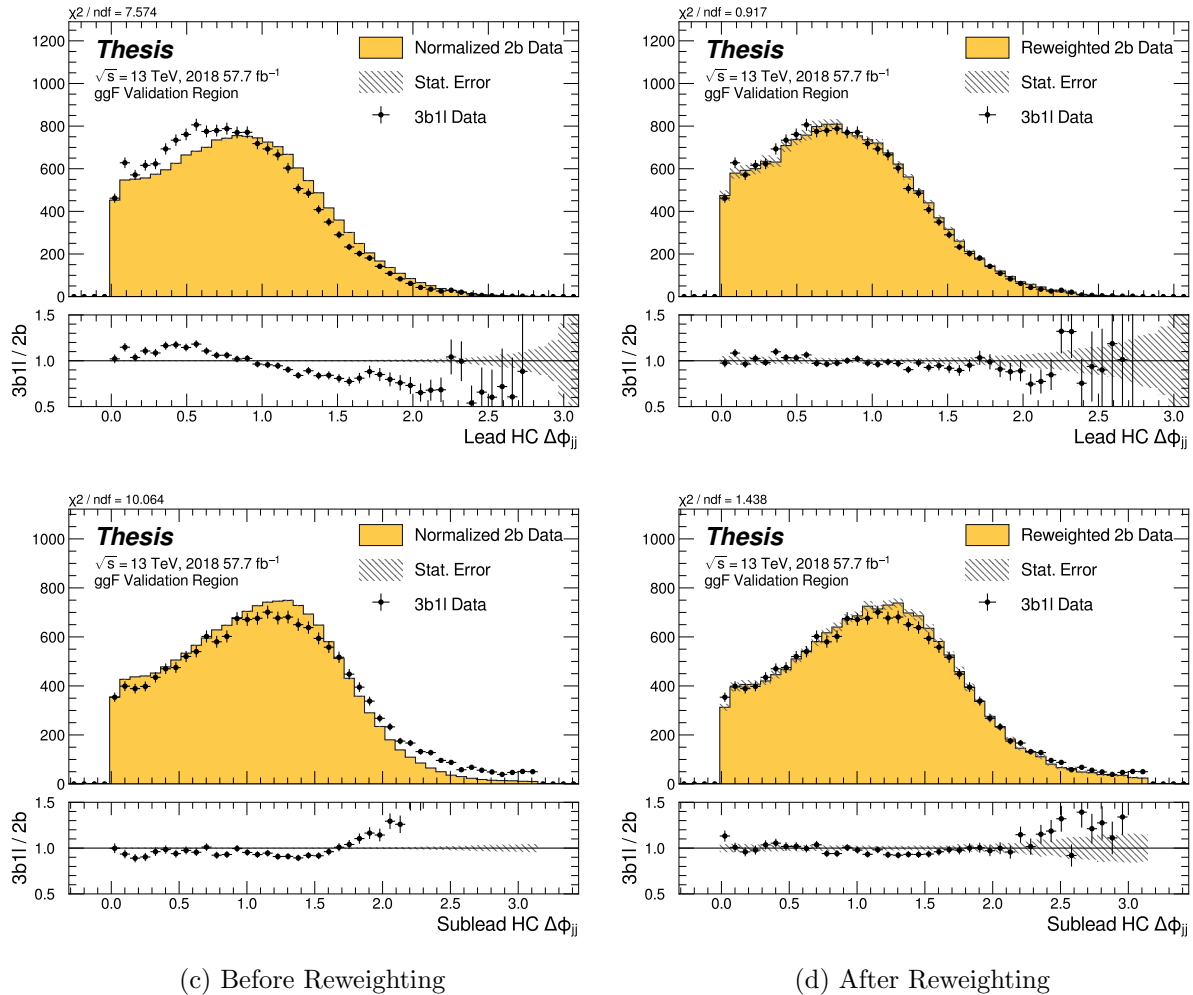


Figure 7.58: **Non-resonant Search (3b1l):** Distributions of  $\Delta\phi$  between jets in the leading and subleading Higgs candidates before and after CR derived reweighting for the 2018 3b1l Validation Region.

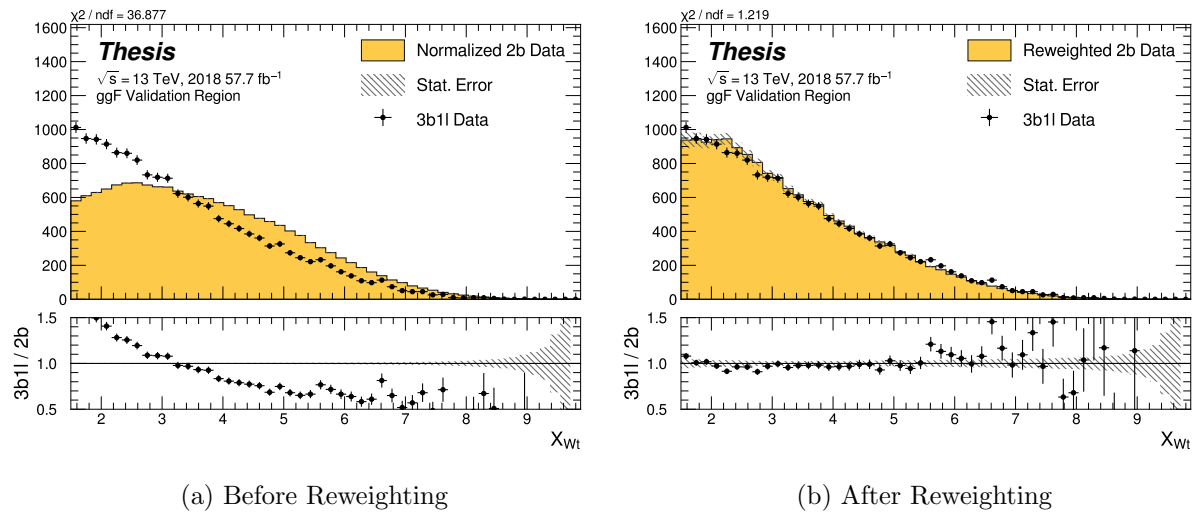


Figure 7.59: **Non-resonant Search (3b1l):** Distributions of the top veto variable,  $X_{Wt}$ , before and after CR derived reweighting for the 2018 3b1l Validation Region. Reweighting is done after the cut on this variable is applied.

2087 **7.7 Uncertainties**

2088 A variety of uncertainties are assigned to account for known biases in the underlying methods,  
2089 calibrations, and objects used for this analysis. The largest such uncertainty is associated  
2090 with the kinematic bias inherent in deriving the background estimate outside of the signal  
2091 region. However, a statistical biasing of this same estimate also has a significant impact.  
2092 Additionally, due to the use of Monte Carlo for signal modelling and  $b$ -tagging calibration,  
2093 uncertainties related to mismodellings in simulation must also be accounted for. Note that  
2094 the results for the non-resonant analysis presented here are preliminary and only include  
2095 background systematic, such that the discussion of the signal systematics *only* applies for  
2096 the resonant search. However, these background systematics are expected to be by far the  
2097 dominant uncertainties.

2098 *7.7.1 Statistical Uncertainties and Bootstrapping*

2099 There are two components to the statistical error for the neural network background estimate.  
2100 The first is standard Poisson error, i.e., a given bin,  $i$ , in the background histogram has value  
2101  $n_i = \sum_{j \in i} w_j$ , where  $w_j$  is the weight for an event  $j$  which falls in bin  $i$ . Standard techniques  
2102 then result in statistical error  $\delta n_i = \sqrt{\sum_{j \in i} w_j^2}$ , which reduces to the familiar  $\sqrt{N}$  Poisson error  
2103 when all  $w_j$  are equal to 1.

2104 However, this procedure does not take into account the statistical uncertainty on the  
2105  $w_j$  due to the finite training dataset. Due to the large size difference between the two tag  
2106 and four tag datasets, it is the statistical uncertainty due to the four tag training data that  
2107 dominates that on the background. A standard method for estimating this uncertainty is the  
2108 bootstrap resampling technique [105]. Conceptually, a set of statistically equivalent sets is  
2109 constructed by sampling with replacement from the original training set. The reweighting  
2110 network is then trained on each of these separately, resulting in a set of statistically equivalent  
2111 background estimates. Each of these sets is below referred to as a replica.

2112 In practice, as the original training set is large, the resampling procedure is able to

2113 be simplified through the relation  $\lim_{n \rightarrow \infty} \text{Binomial}(n, 1/n) = \text{Poisson}(1)$ , which dictates that  
 2114 sampling with replacement is approximately equivalent to applying a randomly distributed  
 2115 integer weight to each event, drawn from a Poisson distribution with a mean of 1.

2116 Though the network configuration itself is the same for each bootstrap training, the  
 2117 network initialization is allowed to vary. It should therefore be noted that the bootstrap  
 2118 uncertainties implicitly capture the uncertainty due to this variation in addition to the  
 2119 previously mentioned training set variation.

2120 The variation from this bootstrapping procedure is used to assign a bin-by-bin uncertainty  
 2121 which is treated as a statistical uncertainty in the fit. Due to practical constraints, a  
 2122 procedure for approximating the full bootstrap error band is developed which demonstrates  
 2123 good agreement with the full bootstrap uncertainty. This procedure is described below.

#### 2124 *Calculating the Bootstrap Error Band*

2125 The standard procedure to calculate the bootstrap uncertainty would proceed as follows: first,  
 2126 each network trained on each bootstrap replica dataset would be used to produce a histogram  
 2127 in the variable of interest. This would result in a set of replica histograms (e.g. for 100  
 2128 bootstrap replicas, 100 histograms would be created). The nominal estimate would then be  
 2129 the mean of bin values across these replica histograms, with errors set by the corresponding  
 2130 standard deviation.

2131 In practice, such an approach is inflexible and demanding both in computation and in  
 2132 storage, in so far as we would like to produce histograms in many variables, with a variety  
 2133 of different cuts and binnings. This motivates a derivation based on event-level quantities.  
 2134 However, due to non-trivial correlations between replica weights, simple linear propagation of  
 2135 event weight variation is not correct.

2136 We therefore adopt an approach which has been empirically found to produce results  
 2137 (for this analysis) in line with those produced by generating all of the histograms, as in the  
 2138 standard procedure. This approach is described below. Note that, for robustness to outliers  
 2139 and weight distribution asymmetry, the median and interquartile range (IQR) are used for

2140 the central value and width respectively (as opposed to the mean and standard deviation).

2141 The components involved in the calculation have been mentioned in Section 7.6 and are  
2142 as follows:

2143 1. Replica weight ( $w_i$ ): weight predicted for a given event by a network trained on replica  
2144 dataset  $i$ .

2145 2. Replica norm ( $\alpha_i$ ): normalization factor for replica  $i$ . This normalizes the reweighting  
2146 prediction of the network trained on replica dataset  $i$  to match the correponding target  
2147 yield.

3. Median weight ( $w_{med}$ ): median weight for a given event across replica datasets, used  
 for the nominal estimate. Defined (for 100 bootstrap replicas) as

$$w_{med} \equiv \text{median}(\alpha_1 w_1, \dots, \alpha_{100} w_{100}) \quad (7.12)$$

2148 4. Normalization correction ( $\alpha_{med}$ ): normalization factor to match the predicted yield of  
2149 the median weights ( $w_{med}$ ) to the target yield in the training region.

2150 As mentioned in Section 7.6, the *nominal estimate* is constructed from the set of median  
2151 weights and the normalization correction, i.e.  $\alpha_{med} \cdot w_{med}$ .

2152 For the bootstrap error band, a “varied” histogram is then generated by applying, for  
2153 each event, a weight equal to the median weight (with no normalization correction) plus half  
2154 the interquartile range of the replica weights:  $w_{varied} = w_{med} + \frac{1}{2} \text{IQR}(w_1, \dots, w_{100})$ .

2155 This varied histogram is scaled to match the yield of the nominal estimate. To account  
2156 for variation of the nominal estimate yield, a normalization variation is calculated from the  
2157 interquartile range of the replica norms:  $\frac{1}{2} \text{IQR}(\alpha_1, \dots, \alpha_{100})$ . This variation, multiplied into  
2158 the nominal estimate, is used to set a baseline for the varied histogram described above.

Denoting  $H(\text{weights})$  as a histogram constructed from a given set of weights,  $Y(\text{weights})$

as the predicted yield for a given set of weights, the final varied histogram is thus:

$$H(w_{med} + \frac{1}{2} \text{IQR}(w_1, \dots, w_{100})) \cdot \frac{Y(\alpha_{med} w_{med})}{Y(w_{med} + \frac{1}{2} \text{IQR}(w_1, \dots, w_{100}))} + \frac{1}{2} \text{IQR}(\alpha_1, \dots, \alpha_{100}) \cdot H(\alpha_{med} w_{med}) \quad (7.13)$$

where the first term roughly describes the behaviour of the bootstrap variation across the distribution of the variable of interest while the second term describes the normalization variation of the bootstrap replicas.

The difference between the varied histogram and the nominal histogram is then taken to be the bootstrap statistical uncertainty on the nominal histogram.

Figure 7.60 demonstrates how each of the components described above contribute to the uncertainty envelope for the non-resonant 2017 Control Region and compares this approximate band to the variation of histograms from individual bootstrap estimates. The error band constructed from the above procedure is seen to provide a good description of the bootstrap variation.

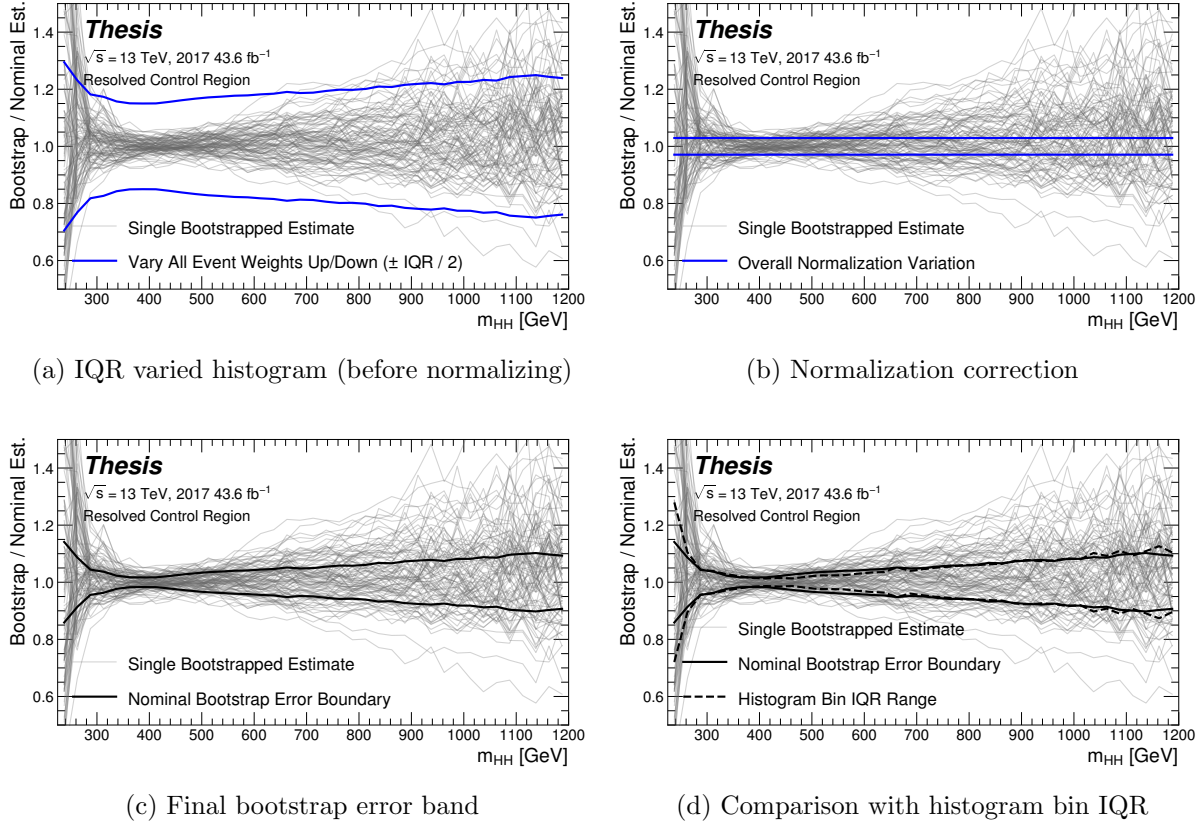


Figure 7.60: Illustration of the approximate bootstrap band procedure, shown as a ratio to the nominal estimate for the 2017 non-resonant background estimate. Each grey line is from the  $m_{HH}$  prediction for a single bootstrap training. Figure 7.60(a) shows the variation histograms constructed from median weight  $\pm$  the IQR of the replica weights. It can be seen that this captures the rough shape of the bootstrap envelope, but is not good estimate for the overall magnitude of the variation. Figure 7.60(b) demonstrates the applied normalization correction, and Figure 7.60(c) shows the final band (normalized Figure 7.60(a) + Figure 7.60(b)). Comparing this with the IQR variation for the prediction from each bootstrap in each bin in Figure 7.60(d), the approximate envelope describes a very similar variation.

2169 7.7.2 *Background Shape Uncertainties*

2170 To account for the systematic bias associated with deriving the reweighting function in the  
2171 control region and extrapolating to the signal region, an alternative background model is  
2172 derived in the validation region. Because of the fully data-driven nature of the background  
2173 model, this is an uncertainty assessed on the full background. The alternative model and  
2174 the baseline are consistent with the observed data in their training regions, and differences  
2175 between the alternative and baseline models are used to define a shape uncertainty on the  
2176  $m_{HH}$  spectrum, with a two-sided uncertainty defined by symmetrizing the difference about  
2177 the baseline.

2178 For the resonant analysis, this uncertainty is split into two components to allow for two  
2179 independent variations of the  $m_{HH}$  spectrum: : a low- $H_T$  and a high- $H_T$  component, where  
2180  $H_T$  is the scalar sum of the  $p_T$  of the four jets constituting the Higgs boson candidates, and  
2181 serves as a proxy for  $m_{HH}$ , while avoiding introducing a sharp discontinuity. The boundary  
2182 value is 300 GeV. The low- $H_T$  shape uncertainty primarily affects the  $m_{HH}$  spectrum below  
2183 400 GeV (close to the kinematic threshold) by up to around 5%, and the high- $H_T$  uncertainty  
2184 mainly  $m_{HH}$  above this by up to around 20% relative to nominal. These separate  $m_{HH}$   
2185 regimes are by design – the  $H_T$  split is introduced to prevent low mass bins from constraining  
2186 the high mass uncertainty and vice-versa.

2187 This was the *status quo* shape uncertainty decomposition from the Early Run 2 analysis.  
2188 A decomposition in terms of orthogonal polynomials, which would provide increased flexibility,  
2189 was also evaluated. This study revealed that both decompositions are able to account for the  
2190 systematic deviations between four tag data and the background estimate (evaluated in the  
2191 kinematic validation region), and produce almost identical limits. The simpler *status quo*  
2192 decomposition is therefore kept.

2193 For the non-resonant analysis, the quadrant nature of the background estimation leads to  
2194 a natural breakdown of the nuisance parameters: quadrants are defined in the signal region  
2195 along the same axes as those used for the control and validation region definitions. Variations

2196 are then assessed in each of these signal region quadrants, corresponding to regions that  
 2197 are “closer to” and “further away from” the nominal and alternate estimate regions, fully  
 2198 leveraging the power of the two equivalent but systematically different estimates.

2199 Figure 7.61 shows an example of the variation in each  $H_T$  region for the 2018 resonant  
 2200 analysis. Figure 7.62 shows the example quadrant variation for the 2018 4 $b$  non-resonant  
 analysis.

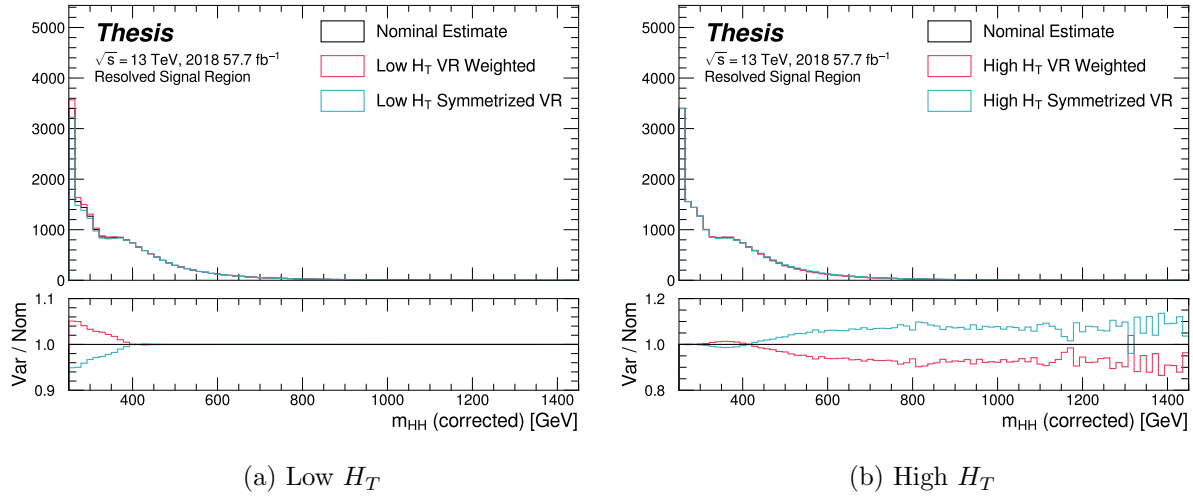
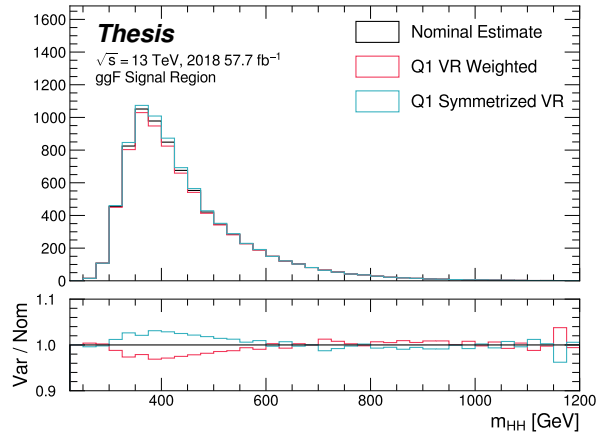
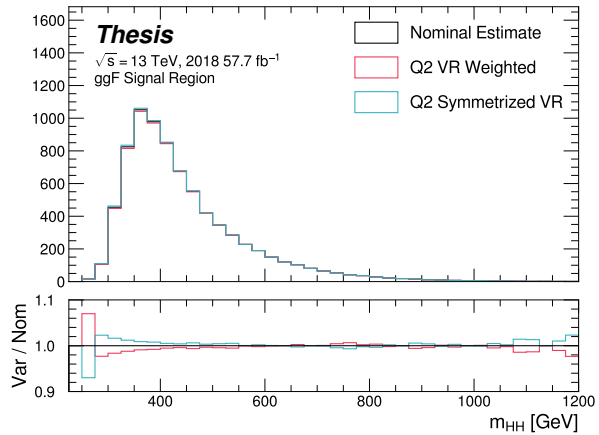


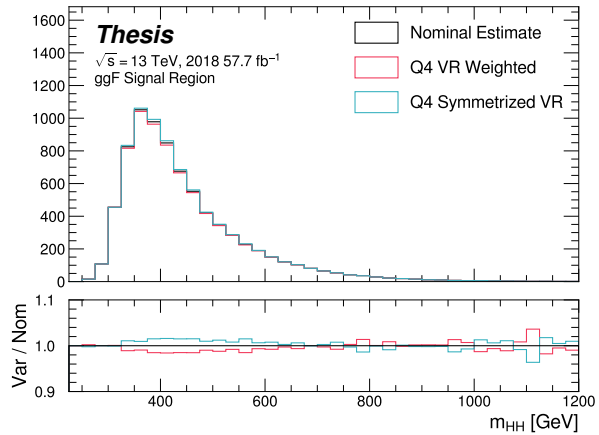
Figure 7.61: **Resonant Search:** Example of CR vs VR variation in each  $H_T$  region for 2018.  
 The variation nicely factorizes into low and high mass components.



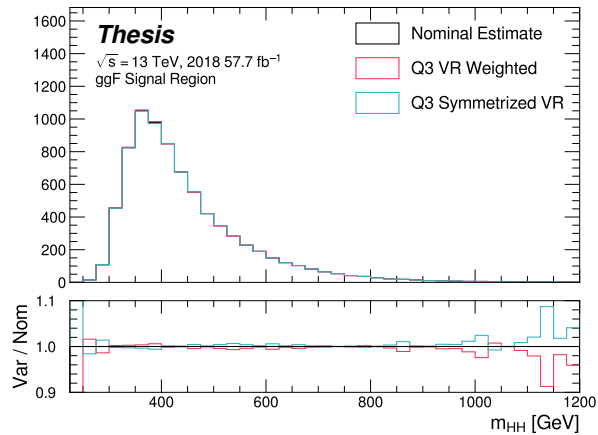
(a) Q1 (top)



(b) Q2 (left)



(c) Q4 (right)



(d) Q3 (bottom)

Figure 7.62: **Non-resonant Search (4b):** Example of CR vs VR variation in each signal region quadrant for 2018. Significantly different behavior is seen between quadrants, with the largest variation in quadrant 1 and the smallest in quadrant 4.

2202    7.7.3 *Signal Uncertainties*

2203    A variety of uncertainties are assessed on the the signal Monte Carlo simulation. As the  
 2204    background estimate is fully data driven, such uncertainties are not needed for the background  
 2205    estimate. Note again that the results presented for the non-resonant search only include the  
 2206    background systematics described above.

2207    Detector modeling and reconstruction uncertainties account for differences between Monte  
 2208    Carlo simulation and real data due to mismodelling of the detector as well as due to the  
 2209    different performance of algorithms on simulation compared to data. In this analysis they  
 2210    consist of uncertainties related to jet properties and uncertainties stemming from the flavor  
 2211    tagging procedure. The jet uncertainties are treated according to the prescription in [106] and  
 2212    are implemented as variations of the jet properties. These cover uncertainty in jet energy scale  
 2213    and resolution. Uncertainties in  $b$ -tagging efficiency are treated according to the prescription  
 2214    in Ref. [77] and implemented as scale factors applied to the Monte Carlo event weights. A  
 2215    systematic related to the PtReco  $b$ -jet energy correction has been studied in the  $HH \rightarrow \gamma\gamma b\bar{b}$   
 2216    analysis [107] and found to be negligible compared to the other jet uncertainties. Following  
 2217    this example, such a systematic is therefore neglected here.

2218    Trigger uncertainties stem from imperfect knowledge of the ratio between the efficiency of  
 2219    a given trigger in data to its efficiency in Monte Carlo simulation. This ratio is applied as a  
 2220    scale factor to all simulated events, with the systematic variations produced by varying the  
 2221    scale factor up or down by one sigma. Such variations are evaluated based on measurements  
 2222    of per-jet online efficiencies for both jet reconstruction and  $b$ -tagging, and these are used to  
 2223    compute event-level uncertainties. These are then applied as overall weight variations on the  
 2224    simulated events.

2225    An uncertainty on the total integrated luminosity used in this analysis is also applied, ans  
 2226    is measured to be 1.7% [95], obtained using the LUCID-2 detector for the primary luminosity  
 2227    measurements [108].

2228    A variety of theoretical uncertainties are also assessed on the signal. Such uncertainties

are assessed by generating samples following the configuration of the baseline samples, but with modifications to probe various aspects of the simulation. These include uncertainties in the parton density functions (PDFs); uncertainties due to missing higher order terms in the matrix elements; and uncertainties in the modelling of the underlying event, which includes multi-parton interactions, of hadronic showers and of initial and final state radiation.

Uncertainties due to modelling of the parton shower and the underlying event are evaluated by comparing results from using two different generators, namely HERWIG 7.1.3 and PYTHIA 8.235. No significant dependence on the variable of interest,  $m_{HH}$ , is observed. Therefore, a 5% flat systematic uncertainty is assigned to all signal samples, extracted from the acceptance comparison for the full 4-tag selection.

Uncertainties in the matrix element calculation are evaluated by varying the factorization and renormalization scales used in the generator up and down by a factor of two, both independently and simultaneously. This results in an effect smaller than 1% for all variations and all masses; the impact of such uncertainties is therefore neglected.

PDF uncertainties are evaluated using the PDF4LHC\_NLO\_MC set [96] by calculating the signal acceptance for each PDF replica and taking the standard deviation. In all cases, these uncertainties result in an effect smaller than 1% on the signal acceptance; therefore these are also neglected.

Theoretical uncertainties on the  $H \rightarrow b\bar{b}$  branching ratio [109] are also included.

2248 **7.8 Background Validation**

2249 In addition to checking the performance of the background estimate in the control and  
2250 validation regions, a variety of alternative selections are defined to allow for a full “dress  
2251 rehearsal” of the background estimation procedure.

2252 Both the resonant and non-resonant analyses make use of a *reversed*  $\Delta\eta$  region, in which  
2253 the kinematic cut on  $\Delta\eta_{HH}$  is reversed, so that events are required to have  $\Delta\eta_{HH} > 1.5$ .  
2254 This is orthogonal to the nominal signal region and has minimal sensitivity, allowing for the  
2255 comparison of the background estimate  $4b$  data in the corresponding “signal region”. For  
2256 this validation, a new reweighting is trained following nominal procedures, but entirely in the  
2257  $\Delta\eta_{HH} > 1.5$  region.

2258 The non-resonant analysis additionally makes use of the  $3b + 1$  fail region mentioned  
2259 above, which again is orthogonal to the nominal signal regions and has minimal sensitivity.  
2260 The reweighting in this case is between  $2b$  and  $3b + 1$  fail events rather than between  $2b$   
2261 and  $3b + 1$  loose or  $2b$  and  $4b$ . However, the kinematic selections of signal region events are  
2262 otherwise identical, allowing for a complementary test of the background estimate.

2263 *TODO: Add shifted regions if they’re ready*

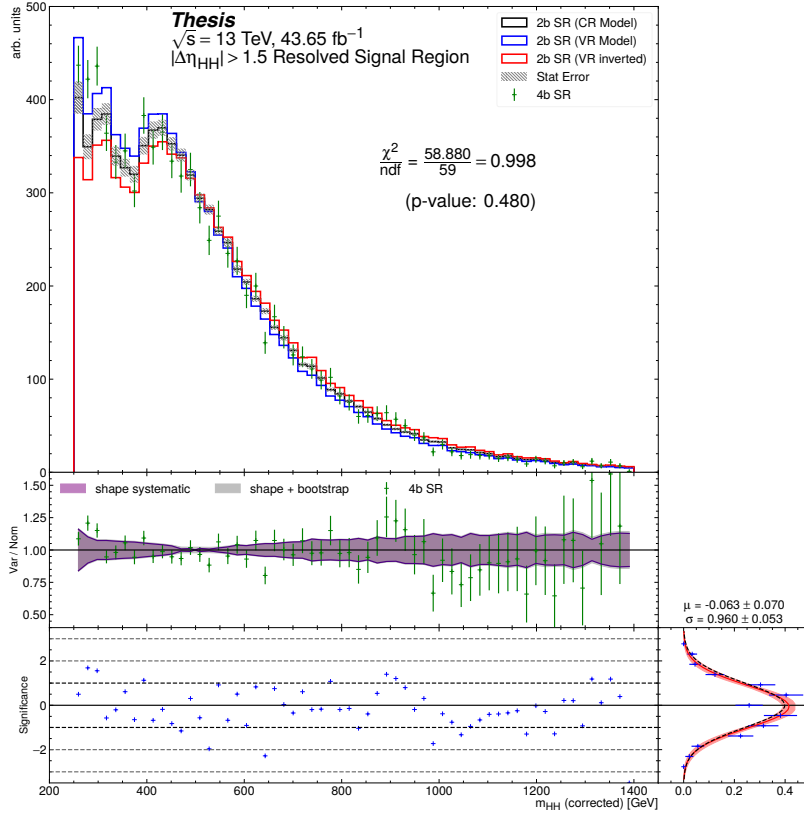


Figure 7.63: **Resonant Search:** Performance of the background estimation method in the resonant analysis reversed  $\Delta\eta_{HH}$  kinematic signal region. A new background estimate is trained following nominal procedures entirely within the reversed  $\Delta\eta_{HH}$  region, and the resulting model, including uncertainties, is compared with  $4b$  data in the corresponding signal region. Good agreement is shown. The quoted  $p$ -value uses the  $\chi^2$  test statistic, and demonstrates no evidence that the data differs from the assessed background.

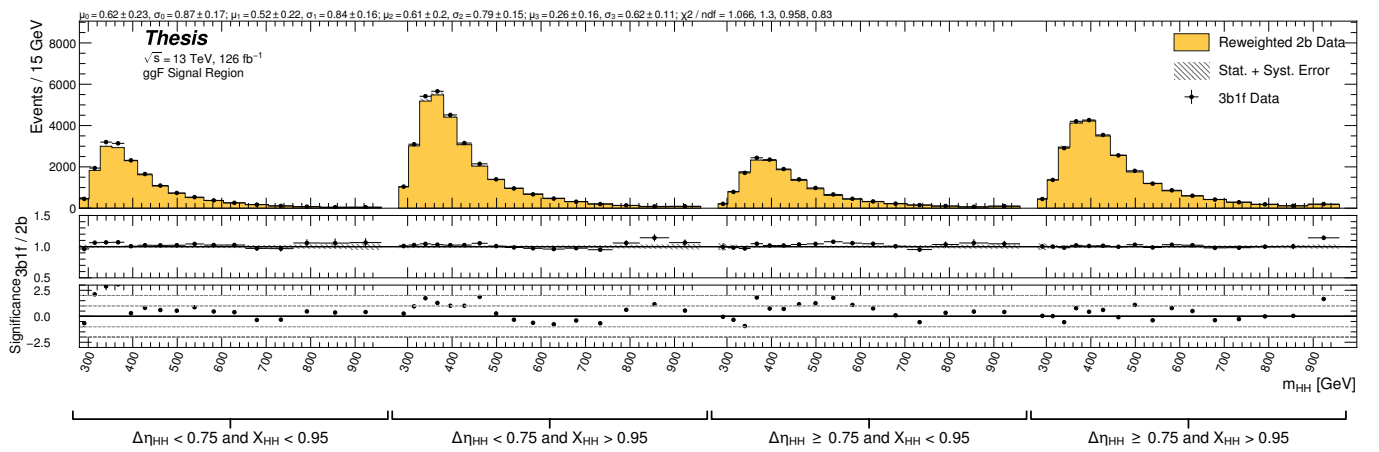


Figure 7.64: **Non-resonant Search:** Performance of the background estimation method in the  $3b + 1$  fail validation region. A new background estimate is trained following nominal procedures but with a reweighting from  $2b$  to  $3b + 1$  fail events. Generally good agreement is seen, though there is some deviation at very low masses in the low  $\Delta\eta_{HH}$  low  $X_{HH}$  category.

2264 **7.9 Overview of Other  $b\bar{b}b\bar{b}$  Channels**

2265 The results discussed above have been developed in conjunction with (1) a boosted channel  
2266 for the resonant search and (2) a vector boson fusion (VBF) channel for the non-resonant  
2267 search. Detailed discussions of these two channels are beyond the scope of this thesis, though  
2268 a combined set of resolved and boosted results are presented below. The VBF results are not  
2269 included in this thesis, but much of this thesis work has been useful in the development of  
2270 that result. For completeness, we therefore briefly summarize both analyses here.

2271 **7.9.1 Resonant: Boosted Channel**

2272 The boosted analysis selection targets resonance masses from 900 GeV to 5 TeV. In such  
2273 events,  $H$  decays have a high Lorentz boost, such that the  $b\bar{b}$  decays are very collimated. The  
2274 resolved analysis fails to reconstruct such  $HH$  events, as the  $R = 0.4$  jets start to overlap.

2275 The boosted analysis instead reconstructs  $H$  decays as large radius,  $R = 1.0$  jets, with  
2276 corresponding  $b$ -quarks identified with variable radius subjets, that is jets with a radius that  
2277 scales as  $\rho/p_T$ , the  $p_T$  is that of the jet in question, and  $\rho$  is a fixed parameter, here chosen  
2278 to be 30 GeV, which is optimized to maintain truth-level double  $b$ -labelling efficiency across  
2279 the full range of Higgs jet  $p_T$  [73].

2280 Due to limited boosted  $b$ -tagging efficiency and to maintain sensitivity even when  $b$ -jets  
2281 are highly collimated, the boosted analysis is divided into three categories based on the  
2282 number of  $b$ -tagged jets associated to each large radius jet:

- 2283 • 4 $b$  category: two  $b$ -tagged jets in each
- 2284 • 2 $b - 1$  category: two  $b$ -tagged jets in one, one in the other
- 2285 • 1 $b - 1$  category: one  $b$ -tagged jet in each

2286 The analysis then proceeds in each of these categories.

2287 The resolved and boosted channels are combined for resonance masses from 900 GeV to  
2288 1.5 TeV inclusive. To keep the channels statistically independent, the boosted channel vetos  
2289 events passing the resolved analysis selection.

2290 *7.9.2 Non-resonant: VBF Channel*

2291 The vector boson fusion channel is only considered for the non-resonant search. While the  
2292 sensitivity is in general much more limited than the gluon-gluon fusion analysis due to the  
2293 much smaller production cross section, VBF is sensitive to a variety of Beyond the Standard  
2294 Model physics, both complementary and orthogonal to the theoretical scope of gluon-gluon  
2295 fusion.

2296 The VBF channel proceeds very similarly to the ggF, with the primary differences being  
2297 the kinematic selections and the categorization, which are impacted by the presence of two  
2298 *VBF jets*, resulting from the two initial state quarks. The ggF channel result presented here  
2299 includes a veto on VBF events, such that if events pass the full VBF selection, they are not  
2300 included in the set of events considered for the ggF result.

2301 Beginning with the assumption of four  $HH$  jets and two VBF jets, the VBF channel first  
2302 requires an event to have a minimum six jets. The VBF jets are reconstructed as the two jets  
2303 with the highest di-jet invariant mass,  $m_{jj}$ , out of the set of all non-tagged jets in the event.  
2304 If no such pair exists (i.e., there are less than two non-tagged jets), the event is placed in the  
2305 ggF channel. To reduce the number of background events, three cuts are then applied, VBF  
2306 jets are required to have  $\Delta\eta > 3$  and a combined invariant mass of  $m_{jji} < 1000$  GeV.  $HH$  jets  
2307 are identified as in the ggF channel, and the vector sum of the  $p_T$  of the  $HH$  and VBF jets is  
2308 required to be less than 65 GeV. The remainder of the analysis proceeds similarly to the ggF  
2309 channel, and events failing any stage of this selection are considered for ggF.

2310 Note that the background estimation for the VBF channel is inherited from the resonant  
2311 and ggF analyses, an ancillary, but significant, contribution of this thesis work.

2312 **7.10  $m_{HH}$  Distributions**

2313 *7.10.1 Resonant Search*

2314 The final discriminant used for the resonant search is corrected  $m_{HH}$ . Histogram binning  
2315 was optimized for the resonant search to be 84 equal width bins from 250 GeV to 1450 GeV,  
2316 corresponding to a bin width of 14.3 GeV, and overflow events (events above 1450 GeV) are  
2317 included in the last bin. A demonstration of the performance of the reweighting on this  
2318 distribution is shown in Figure 7.65 for the control region and Figure 7.66 for the validation region. A background-only profile likelihood fit is run for the distribution in the  
2319 signal region, and results with spin-0 signals overlaid are shown in Figure 7.67. Note that the  
2320 plots show the sum across all years, but the signal extraction fit and background estimate  
2321 are run with the years separately. Agreement is generally good throughout.  
2322

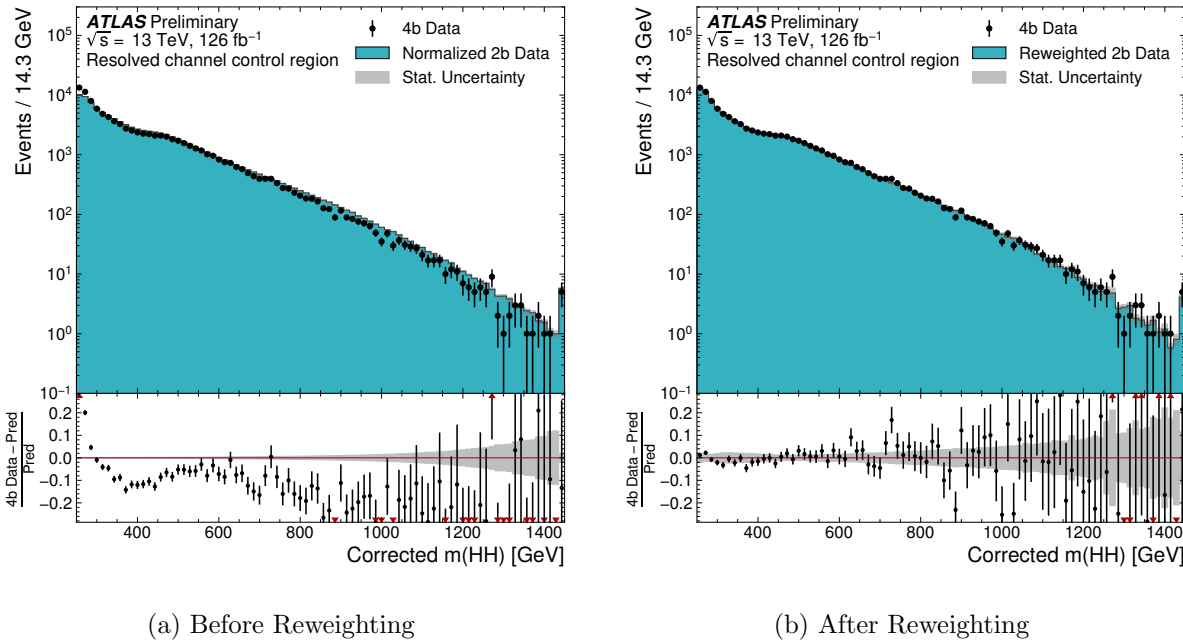


Figure 7.65: **Resonant Search:** Demonstration of the performance of the nominal reweighting in the control region on corrected  $m_{HH}$ , with Figure 7.65(a) showing  $2b$  events normalized to the total  $4b$  yield and Figure 7.65(b) applying the reweighting procedure. Agreement is much improved with the reweighting. Note that overall reweighted  $2b$  yield agrees with  $4b$  yield in the control region by construction.

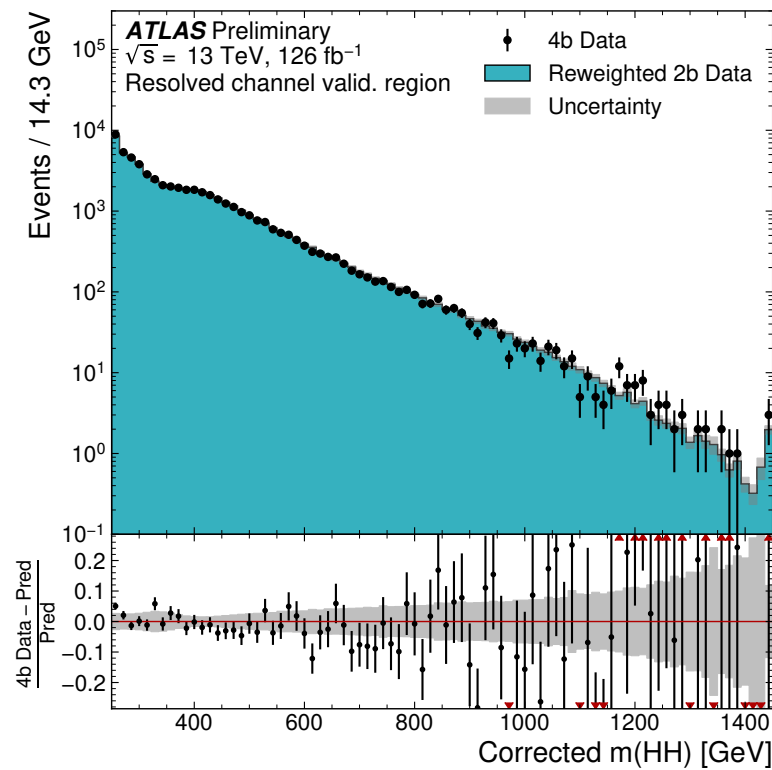


Figure 7.66: **Resonant Search:** Demonstration of the performance of the control region derived reweighting in the validation region on corrected  $m_{HH}$ . Agreement is generally good for this extrapolated estimate. Note that the uncertainty band includes the extrapolation systematic, which is defined by a reweighting trained in the validation region.

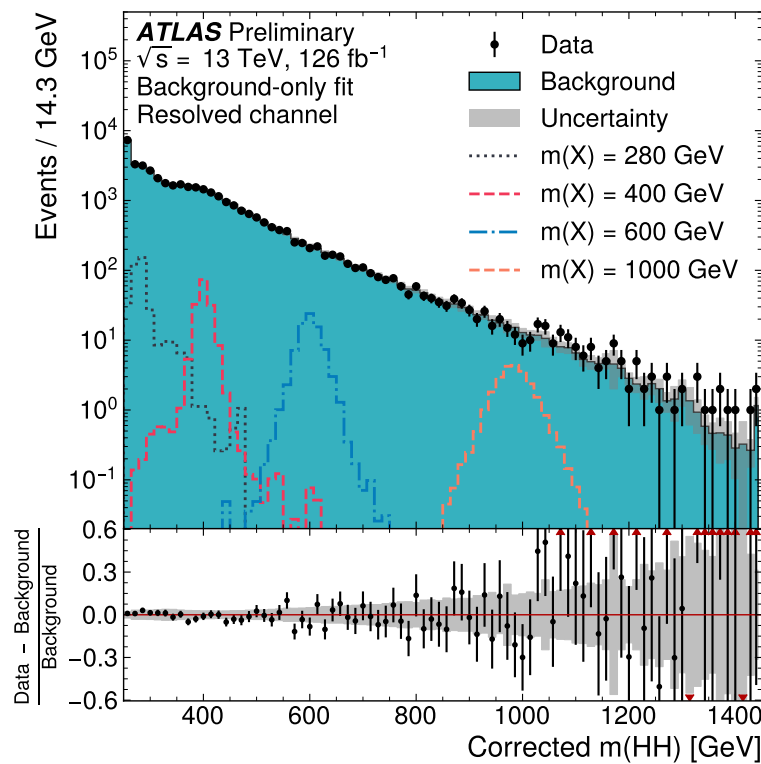


Figure 7.67: **Resonant Search:** Signal region agreement of the background estimate and observed data after a background-only profile likelihood fit. The closure is generally quite good, though there is an evident deficit in the background estimate relative to the data for higher values of corrected  $m_{HH}$ .

2323 7.10.2 Non-resonant Search

As discussed above, the non-resonant search splits the signal extraction into two categories of  $\Delta\eta_{HH}$  ( $0 \leq \Delta\eta_{HH} < 0.75$  and  $0.75 \leq \Delta\eta_{HH} < 1.5$ ), and two categories of  $X_{HH}$  ( $0 \leq X_{HH} < 0.95$  and  $0.95 \leq X_{HH} < 1.6$ ). To maintain reasonable statistics in each bin entering the signal extraction fit, a variable width binning is considered defined by a resolution parameter,  $r$ , and a set range in  $m_{HH}$ , where bin edges are determined iteratively as

$$b_{low}^{i+1} = b_{low}^i + r \cdot b_{low}^i, \quad (7.14)$$

2324 where  $b_{low}^i$  is the low edge of bin  $i$ . The parameters used here are  $r = 0.08$  over a range  
2325 from 280 GeV to 975 GeV, and underflow and overflow are included in the intial and final  
2326 bin contents respectively.  $m_{HH}$  with no correction is used as the final discriminant in each  
2327 category.

2328 A demonstration of the performance of the reweighting on distributions unrolled across  
2329 categories is shown in Figures 7.68 and 7.69 for the the control region and Figures 7.70  
2330 and 7.71 for the validation region. A background-only profile likelihood fit is run for the  
2331 distribution in the signal region, and results with the Standard Model  $HH$  signal and  $\kappa_\lambda = 6$   
2332 signal overlaid are shown for  $4b$  in Figure 7.72 and  $3b1l$  in Figure 7.73. Note that the plots  
2333 show the sum across all years, but the signal extraction fit and background estimate are run  
2334 with the years separately. All bins are normalized to represent a density of Events / 15 GeV.

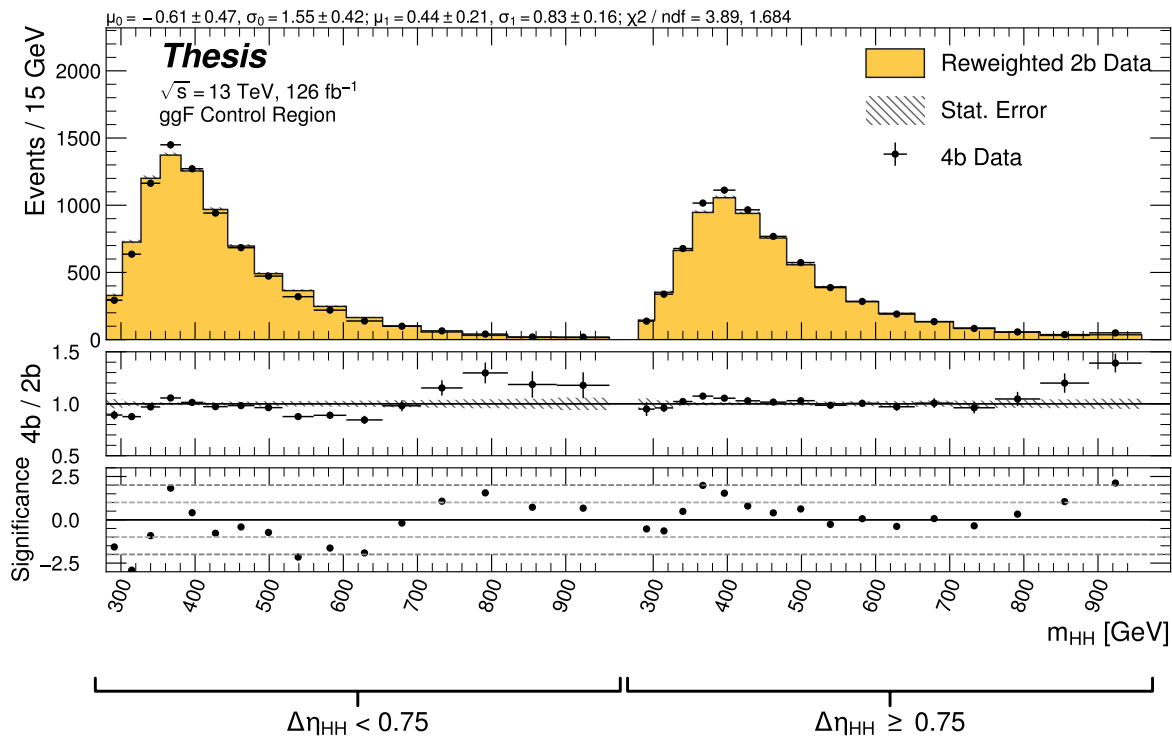


Figure 7.68: **Non-resonant Search (4b)**: Demonstration of the performance of the nominal reweighting in the control region on  $m_{HH}$ , split into the two  $\Delta\eta_{HH}$  regions. Closure is generally good, with some residual mismodeling in the low  $\Delta\eta_{HH}$  region near 600 GeV.

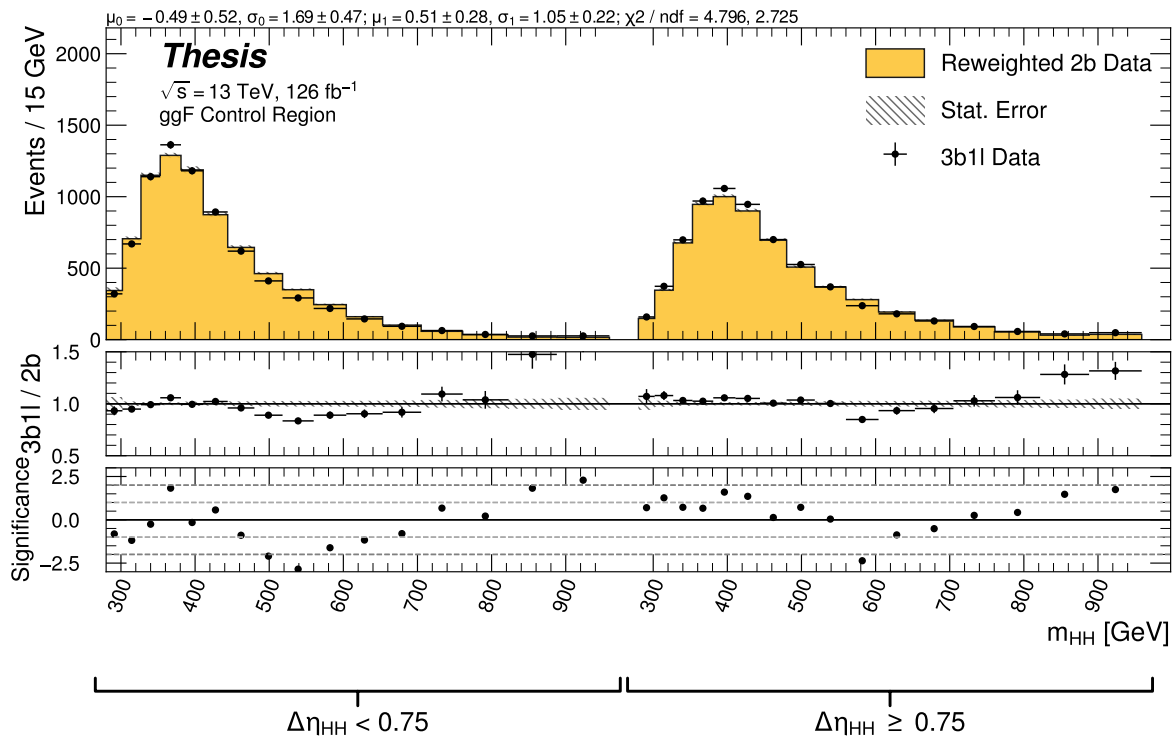


Figure 7.69: **Non-resonant Search (3b1l):** Demonstration of the performance of the nominal reweighting in the control region on  $m_{HH}$ , split into the two  $\Delta\eta_{HH}$  regions. Closure is generally good, with similar conclusions as for the  $4b$  region.

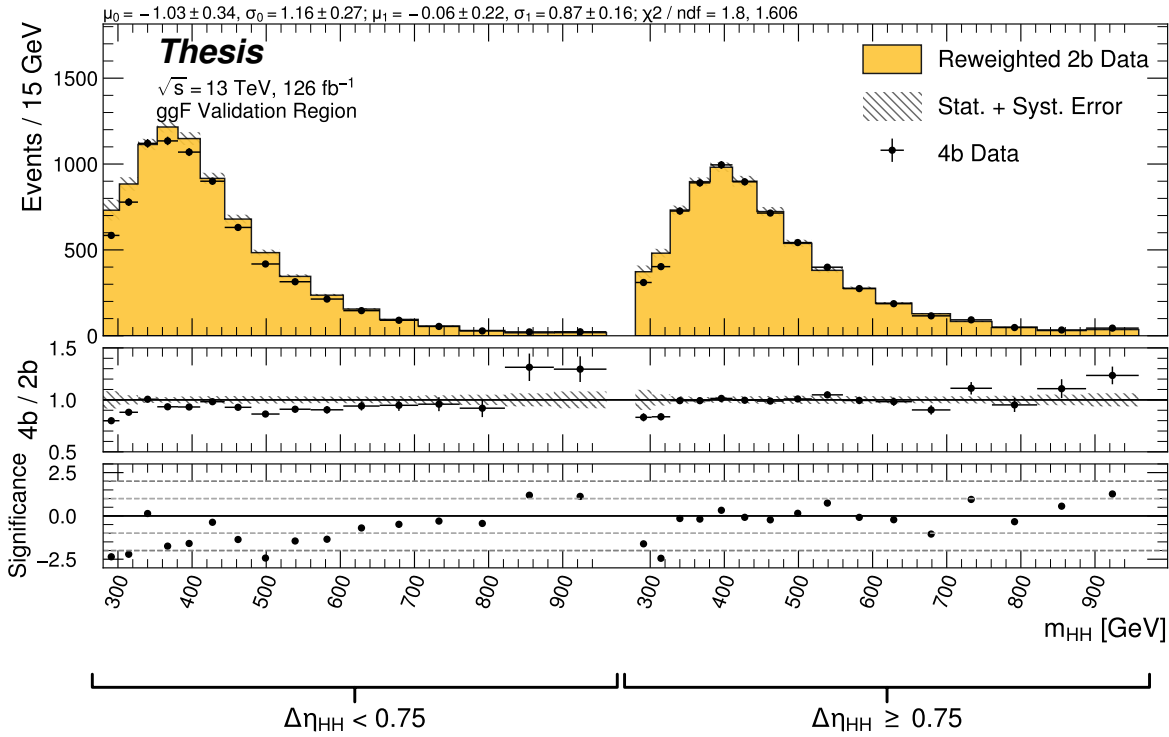


Figure 7.70: **Non-resonant Search (4b)**: Demonstration of the performance of the nominal reweighting in the validation region on  $m_{HH}$ , split into the two  $\Delta\eta_{HH}$  regions. The low  $\Delta\eta_{HH}$  region is consistently overestimated, but, systematic uncertainties are defined via the difference between VR and CR estimates.

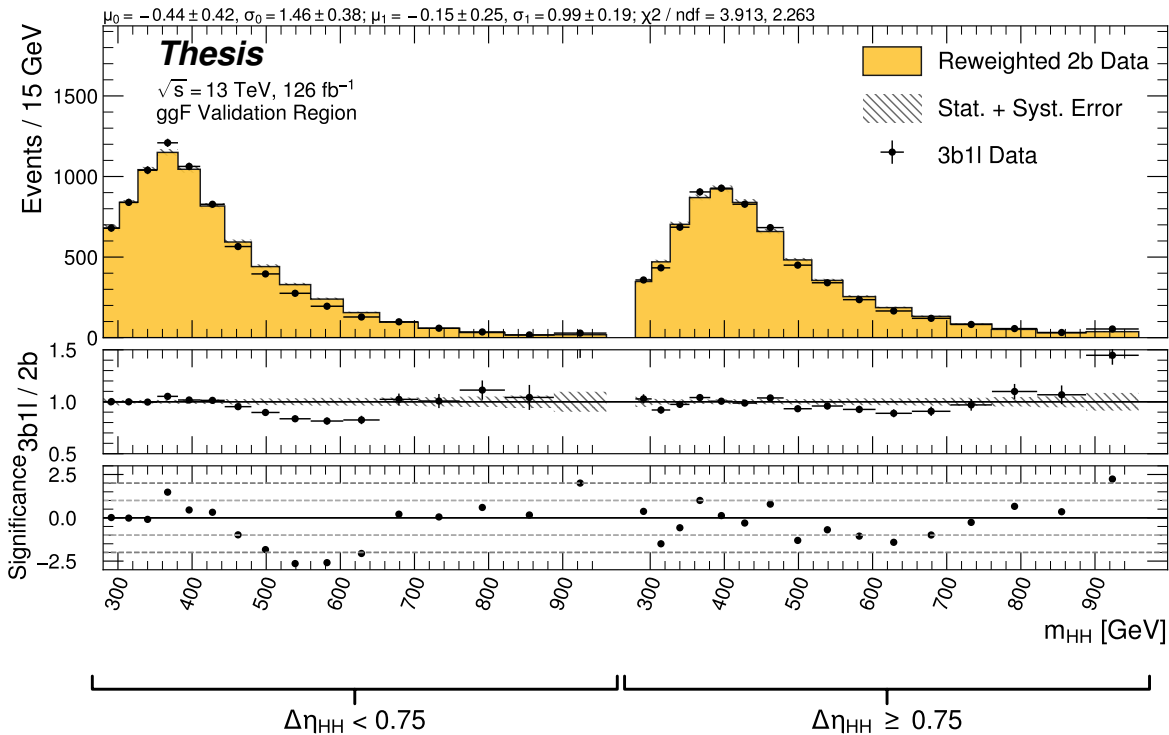


Figure 7.71: **Non-resonant Search (3b1l):** Demonstration of the performance of the nominal reweighting in the validation region on  $m_{HH}$ , split into the two  $\Delta\eta_{HH}$  regions. A deficit is present near 600 GeV, but agreement is fairly good otherwise.

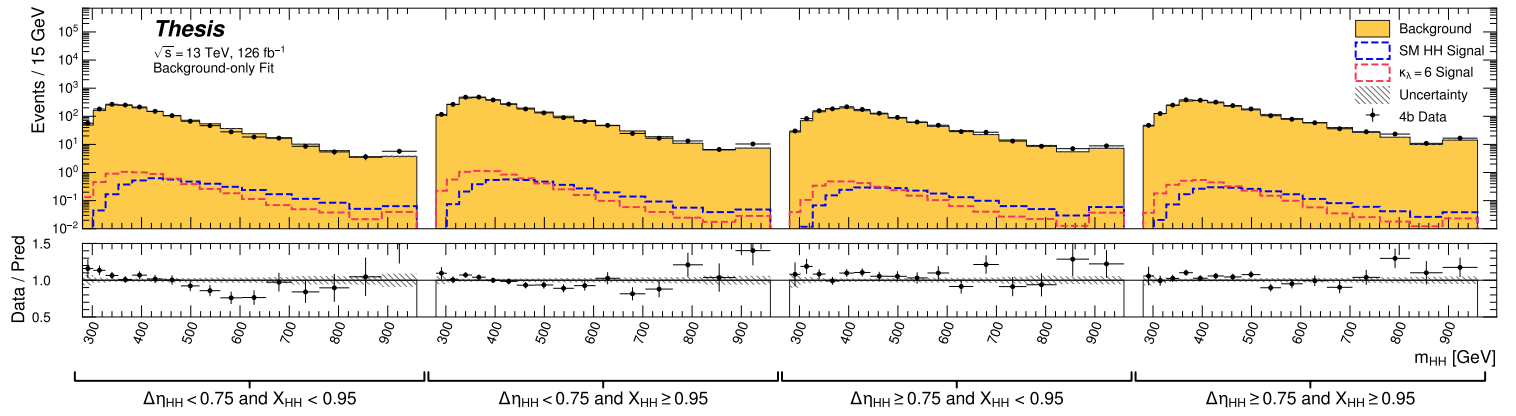


Figure 7.72: **Non-resonant Search (4b):** Signal region agreement of the background estimate and observed data after a background-only profile likelihood fit for the  $4b$  channels, with Standard Model and  $\kappa_\lambda = 6$  signal overlaid for reference. Modeling is generally quite good near the Standard Model peak, but disagreements are seen at very low and high masses. A deficit is present in low  $\Delta\eta_{HH}$  bins near 600 GeV.

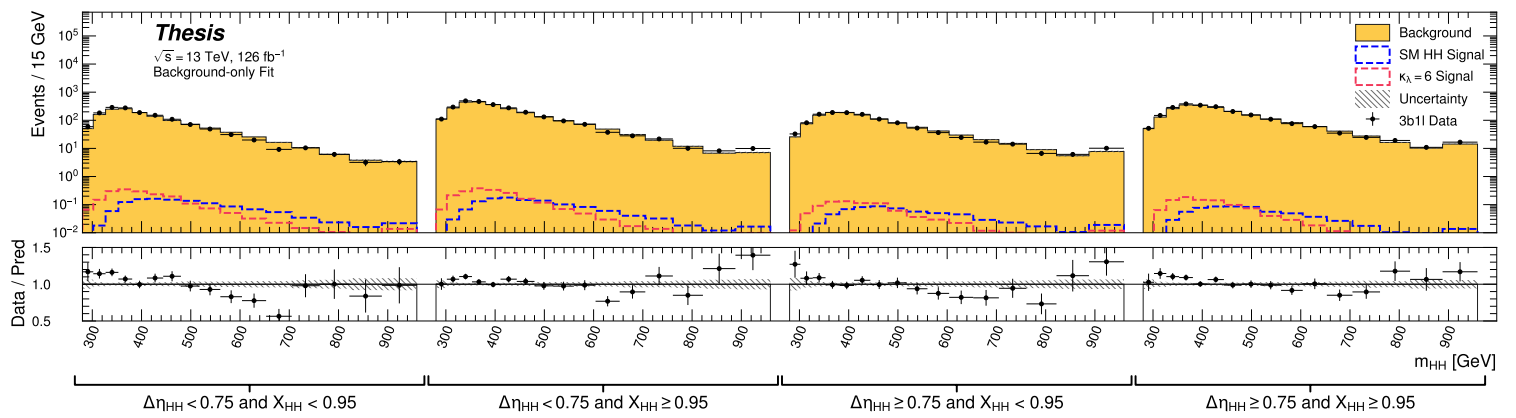


Figure 7.73: **Non-resonant Search (3b1l):** Signal region agreement of the background estimate and observed data after a background-only profile likelihood fit for the 3b1l channels, with Standard Model and  $\kappa_\lambda = 6$  signal overlaid for reference. Conclusions are very similar to the 4b channels, with generally good modeling near the Standard Model peak, but disagreements at very low and high masses. A deficit is present near 600 GeV.

2335 **7.11 Statistical Analysis**

2336 The resonant analysis is used to set a 95% confidence level upper limit on the  $pp \rightarrow X \rightarrow$   
2337  $HH \rightarrow b\bar{b}b\bar{b}$  and  $pp \rightarrow G_{KK}^* \rightarrow HH \rightarrow b\bar{b}b\bar{b}$  cross-sections, while the non-resonant analysis  
2338 is used to set a 95% confidence level upper limit on the  $pp \rightarrow HH \rightarrow b\bar{b}b\bar{b}$  cross sections for  
2339 a variety of values of the trilinear Higgs coupling.

2340 The upper limit is extracted using the  $CL_s$  method [110]. The test statistic used is  $q_\mu$  [111],  
2341 where  $\mu$  is the signal strength, and  $\theta$  represents the nuisance parameters. Due to the use of  
2342 signals normalized to 1 fb,  $\mu$  is also the signal cross-section in fb. A single hat represents the  
2343 maximum likelihood estimate of a parameter, while  $\hat{\theta}(x)$  represents the conditional maximum  
2344 likelihood estimate of the nuisance parameters if the signal cross-section is fixed at  $x$ .

$$q_\mu = \begin{cases} -2 \ln \left( \frac{\mathcal{L}(\mu, \hat{\theta}(\mu))}{\mathcal{L}(\hat{\mu}, \hat{\theta})} \right) & \hat{\mu} \leq \mu \\ 0 & \hat{\mu} > \mu \end{cases} \quad (7.15)$$

2345  $CL_s$  for some test value of  $\mu$  is then defined by

$$CL_s = \frac{CL_{s+b}}{CL_b} = \frac{p(q_\mu \geq q_{\mu, \text{obs}} | s+b)}{p(q_\mu \geq q_{\mu, \text{obs}} | b)}, \quad (7.16)$$

2346 where the  $p$ -values are calculated in the asymptotic approximation [111], which is valid in  
2347 the large sample limit.

2348 The signal cross-section  $\mu$  fb is excluded at the 95% confidence level if  $CL_s < 0.05$ .

Observed	$-2\sigma$	$-1\sigma$	Expected	$+1\sigma$	$+2\sigma$
<b>4.4</b>	3.1	4.2	<b>5.9</b>	8.2	11.0

Table 7.1: Limits on Standard Model  $HH \rightarrow b\bar{b}b\bar{b}$  production, presented in units of the predicted Standard Model cross section. Results include background systematics only.

## 2349 7.12 Results

2350 Figure 7.74 shows the expected limit for the spin-0 and spin-2 resonant search. The resolved  
 2351 channel covers the range between 251 and 1500 GeV and is combined with the boosted channel  
 2352 between 900 and 1500 GeV. The boosted channel then extends to 3 TeV. The most significant  
 2353 excess is seen for a signal mass of 1100 GeV, with local significance of  $2.6\sigma$  for the spin-0  
 2354 signal and  $2.7\sigma$  for the spin-2 signal. This is reduced to  $1.0\sigma$  and  $1.2\sigma$  globally.

2355 The spin-2 bulk Randall-Sundrum model with  $k/\overline{M}_{\text{Pl}} = 1$  is excluded for graviton masses  
 2356 between 298 and 1440 GeV.

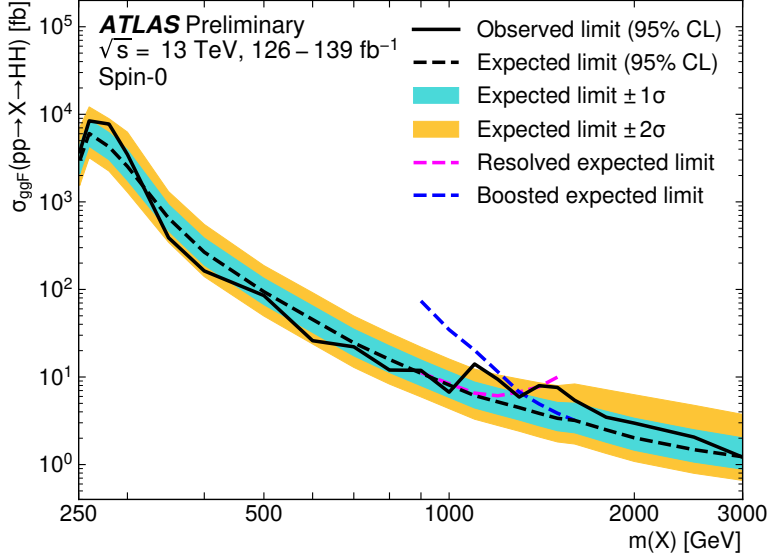
2357 Preliminary results are presented here for the gluon-gluon fusion non-resonant search,  
 2358 combining results from the  $4b$  and  $3b + 1l$  signal regions in the  $2 \times 2$  category scheme in  
 2359  $\Delta\eta_{HH}$  and  $X_{HH}$ . These results will be further combined with a VBF channel as discussed,  
 2360 but this is left for future work. Results shown here include background systematics only.  
 2361 Limits are set for  $\kappa_\lambda$  values from  $-20$  to  $20$ . The cross section limit for  $HH$  production is set  
 2362 at  $140 \text{ fb}$  ( $180 \text{ fb}$ ) observed (expected), corresponding to an observed (expected) limit of  $4.4$   
 2363 ( $5.9$ ) times the Standard Model prediction (see Table 7.1).  $\kappa_\lambda$  is constrained to be within the  
 2364 range  $-4.9 \leq \kappa_\lambda \leq 14.4$  observed ( $-3.9 \leq \kappa_\lambda \leq 10.9$  expected). These results are shown in  
 2365 Figure 7.75.

2366 We note that this is a significant improvement over the early Run 2 result, which achieved  
 2367 an observed (expected) limit of  $12.9$  ( $20.7$ ) times the Standard Model prediction. The dataset  
 2368 is 4.6 times larger, and a naive scaling of the early Run 2 result (Poisson statistics  $\implies$  a factor  
 2369 of  $1/\sqrt{4.6}$ ) would predict an observed (expected) limit of  $6.0$  ( $9.7$ ) times the Standard Model.

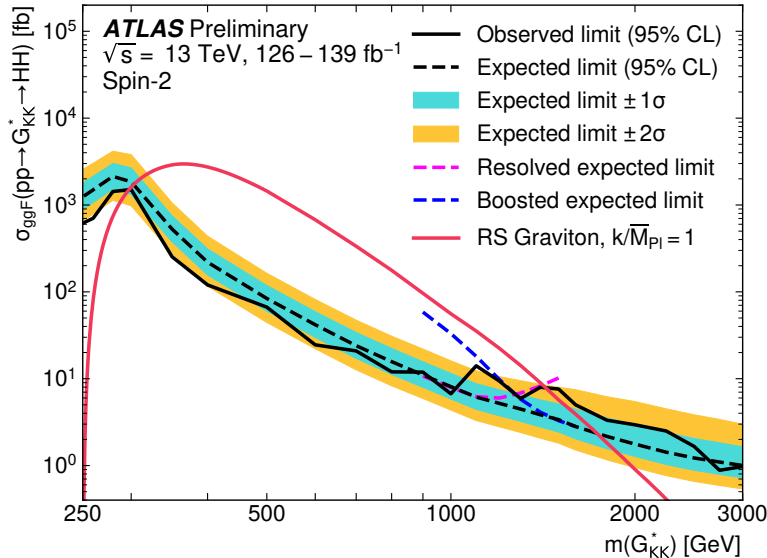
2370 The result of 4.4 (5.9) observed (expected) presented here is therefore both an improvement  
 2371 by a factor of 3 (3.5) over the previous result and also beats the statistical scaling by around  
 2372 30 (40) %, demonstrating the impact of the various analysis improvements presented here.  
 2373 We note again that these results do not include the complete set of uncertainties – however  
 2374 we expect the addition of the remaining uncertainties to have no more than a few percent  
 2375 impact.

2376 The observed limits presented in Figure 7.75 are consistently above the  $2\sigma$  band for values  
 2377 of  $\kappa_\lambda \geq 5$ , peaking at a local significance of  $3.8\sigma$  for  $\kappa_\lambda = 6$ . As this analysis is optimized for  
 2378 points near the Standard Model, and as there is no excess present in more sensitive channels  
 2379 in this same region (e.g.  $HH \rightarrow bb\gamma\gamma$  *TODO: include comparison*), we do not believe this is a  
 2380 real effect, but is rather due to a mis-modeling of the background at low mass, where the  
 2381 min  $\Delta R$  pairing has poor signal efficiency and the assumption of well behaved background in  
 2382 the mass plane breaks down. This is consistent with the location of the  $\kappa_\lambda = 6$  signal in  $m_{HH}$ ,  
 2383 as shown in Figures 7.72 and 7.73. It was considered, but not implemented, for this analysis  
 2384 to impose a cut on  $m_{HH}$  near 350 or 400 GeV to avoid such a low mass modeling issue.

2385 To check the impact of if we would have imposed such a cut, and to verify that the excess  
 2386 is due to the low mass regime, we therefore run the same set of limits without the low mass  
 2387 bins. In this case, we choose to simply drop the first few bins in  $m_{HH}$  such that everything  
 2388 else, including the higher mass bin edges, is kept the same. Due to the variable width binning,  
 2389 this corresponds to an  $m_{HH}$  cut of 381 GeV. The results of this check are shown in Figure  
 2390 7.76, overlaid with the limits of Figure 7.75 for reference. With the  $m_{HH}$  cut imposed, there  
 2391 is a slight degradation in the expected limits for larger positive and negative values of  $\kappa_\lambda$ ,  
 2392 but the points near the Standard Model are nearly identical. Further, the observed excess is  
 2393 significantly reduced, with observed limits for  $\kappa_\lambda \geq 5$  now falling entirely within the expected  
 2394  $1\sigma$  band. Due to the preliminary nature of these results, further study is left for future  
 2395 work. However, we believe, in conjunction with the  $HH \rightarrow bb\gamma\gamma$  results and our expectations  
 2396 about the difficulty of the background estimation at low mass, that this is demonstrative of a  
 2397 mismodeling rather than a real excess.



(a)



(b)

Figure 7.74: Expected (dashed black) and observed (solid black) 95% CL upper limits on the cross-section times branching ratio of resonant production for spin-0 ( $X \rightarrow HH$ ) and spin-2  $G_{KK}^* \rightarrow HH$ . The  $\pm 1\sigma$  and  $\pm 2\sigma$  ranges for the expected limits are shown in the colored bands. The resolved channel expected limit is shown in dashed pink and covers the range from 251 and 1500 GeV. It is combined with the boosted channel (dashed blue) between 900 and 1500 GeV. The theoretical prediction for the bulk RS model with  $k/\bar{M}_{\text{Pl}} = 1$  [20] (solid red line) is shown, with the decrease below 350 GeV due to a sharp reduction in the  $G_{KK}^* \rightarrow HH$  branching ratio. The nominal  $H \rightarrow b\bar{b}$  branching ratio is taken as 0.582.

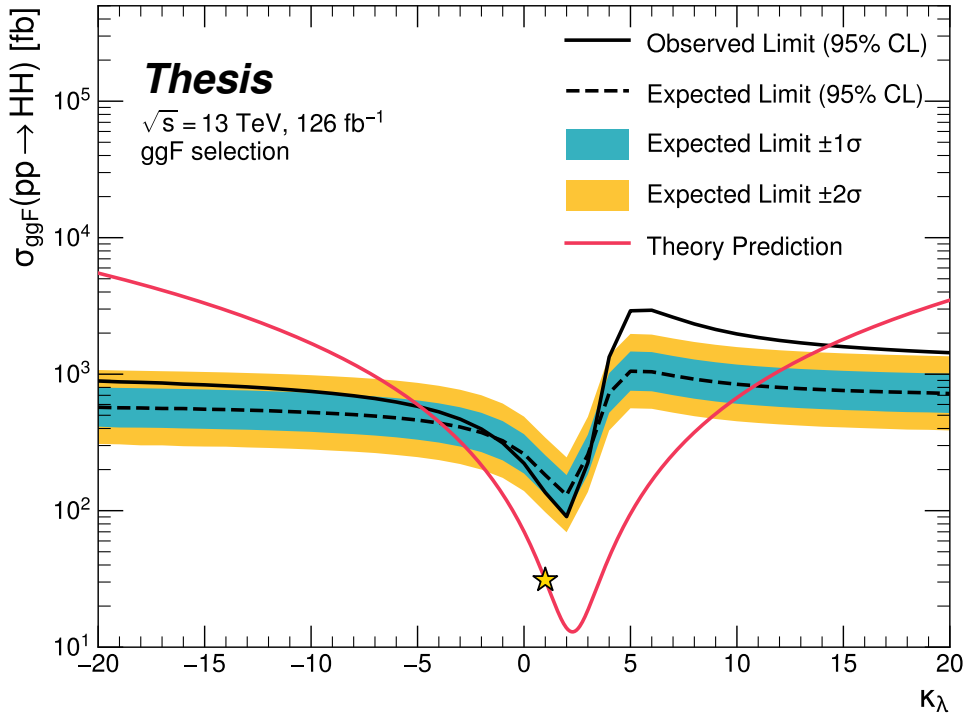


Figure 7.75: Expected (dashed black) and observed (solid black) 95% CL upper limits on the cross-section times branching ratio of non-resonant production for a range of values of the Higgs self-coupling, with the Standard Model value ( $\kappa_\lambda = 1$ ) illustrated with a star. The  $\pm 1\sigma$  and  $\pm 2\sigma$  ranges for the expected limits are shown in the colored bands. The cross section limit for  $HH$  production is set at 140 fb (180 fb) observed (expected), corresponding to an observed (expected) limit of 4.4 (5.9) times the Standard Model prediction.  $\kappa_\lambda$  is constrained to be within the range  $-4.9 \leq \kappa_\lambda \leq 14.4$  observed ( $-3.9 \leq \kappa_\lambda \leq 10.9$  expected). The nominal  $H \rightarrow b\bar{b}$  branching ratio is taken as 0.582. We note that the excess present for  $\kappa_\lambda \geq 5$  is thought to be due to a low mass background mis-modeling, present due to the optimization of this analysis for the Standard Model point, and is not present in more sensitive channels in this same region (e.g.  $HH \rightarrow bb\gamma\gamma$ ).

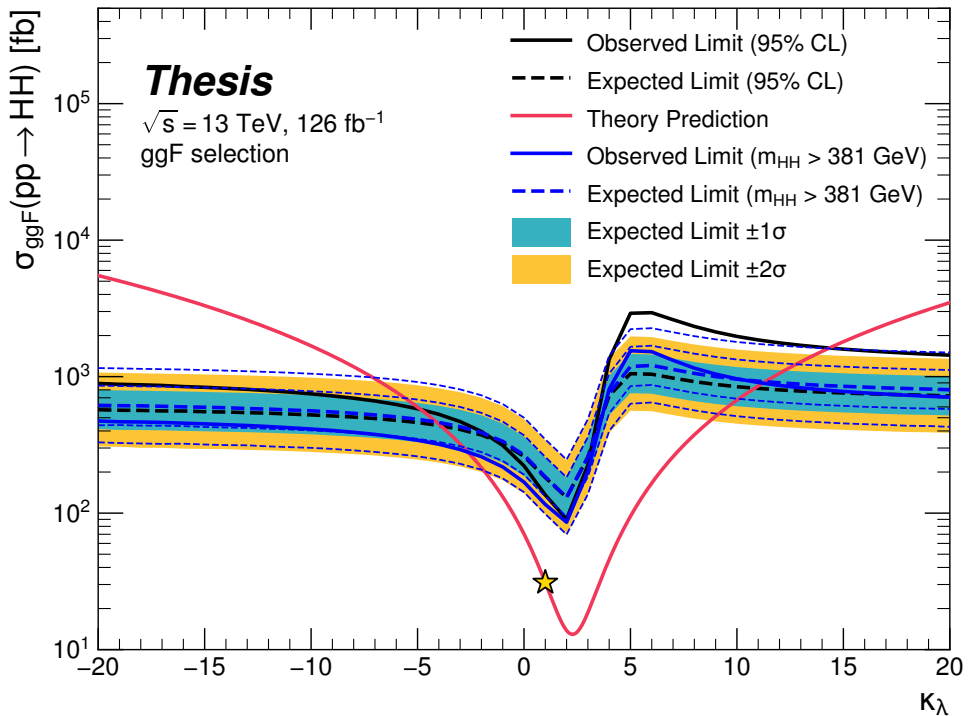


Figure 7.76: Comparison of the limits in Figure 7.75 with an equivalent set of limits that drop the  $m_{HH}$  bins below 381 GeV, with the value of 381 GeV determined by the optimized variable width binning. The expected limit band with this mass cut is shown in dashed blue, and the observed is shown in solid blue. The excess at and above  $\kappa_\lambda = 5$  is significantly reduced, demonstrating that this is driven by low mass. Notably, there is minimal impact on the expected sensitivity with this  $m_{HH}$  cut.

2398

## Chapter 8

2399

### FUTURE IDEAS FOR $HH \rightarrow b\bar{b}b\bar{b}$

2400 The searches presented in this thesis make use of a large suite of sophisticated techniques,  
 2401 selected through careful study and validation. During this process, a variety of interesting  
 2402 directions for the  $HH \rightarrow b\bar{b}b\bar{b}$  analysis were explored by this thesis author, in collaboration  
 2403 with a few others<sup>1</sup>, but were not used due to a variety of constraints. We present two  
 2404 such interesting directions here, with the hope of encouraging further exploration of these  
 2405 techniques in future work.

2406 **8.1 pairAGraph: A New Method for Jet Pairing**

2407 As discussed in Chapter 7, one of the main problems to solve is the pairing of  $b$ -jets into  
 2408 Higgs candidates. Figure 7.1 demonstrates that the choice of the pairing method, while  
 2409 important for achieving good reconstruction of signal events, also significantly impacts the  
 2410 structure of non- $HH$  events, leading to various biases in the background estimate. Evaluation  
 2411 of the pairing method therefore must take both of these factors into account. While we have  
 2412 presented some advantages in respective contexts for the pairing methods considered here,  
 2413 we of course would like to explore further improvements to this important component of the  
 2414 analysis.

2415 To that end, we note that all of the pairing methods considered here share a common  
 2416 feature: four jets are selected, and the pairing is some discrimination between the available  
 2417 three pairings of these four jets. For the methods used in this analysis, the jet selection  
 2418 proceeds via a simple  $p_T$  ordering, with  $b$ -tagged jets receiving a higher priority than non-

---

<sup>1</sup>Notably Nicole Hartman (SLAC), who spearheaded much of the development and proof of concept work, in collaboration with Michael Kagan and Rafael Teixeira De Lima.

2419 tagged jets.

2420 With the advent of a variety of machine learning methods for dealing with a variable number  
2421 of inputs (e.g. recurrent neural networks [112], deep sets [113], graph neural networks [114],  
2422 and transformers [115]), a natural place to improve on the pairing is to consider more than  
2423 just four jets. The pairing and jet selection is then performed simultaneously, allowing for  
2424 the incorporation of more event information in the pairing decision and the incorporation of  
2425 jet correlation structure in the jet selection.

2426 In practice, the majority of  $HH \rightarrow b\bar{b}b\bar{b}$  events have either four or five jets which pass the  
2427 kinematic preselection, and any gain from this additional freedom would come from events  
2428 with greater than or equal to five jets. However, this five jet topology is particularly exciting  
2429 for scenarios such as events with initial state radiation (ISR), in which the  $HH - > 4b$  jets  
2430 are offset by a single jet with  $p_T$  similar in magnitude to that of the  $HH - > 4b$  system.  
2431 Such events have explicit event level information which is not encoded with the inclusion  
2432 of only the  $HH - > 4b$  jets, and are pathological if the ISR jet happens to pass  $b$ -tagging  
2433 requirements.

2434 Additionally, with the use of lower tagged regions for background estimation and alternate  
2435 signal regions, this extra flexibility in jet selection may provide a very useful bias – since the  
2436 algorithm is trained on signal, the selected jets for the pairing will be the most “4b-like” jets  
2437 available in the considered set.

2438 For the studies considered here, a transformer [115] based architecture is used. This is  
2439 best visualized by considering the event as a graph with jets corresponding to nodes and edges  
2440 corresponding to potential connections – for this reason, we term this algorithm “pairAGraph”.  
2441 The approach is as follows: each jet,  $i$ , is represented by some vector of input variables,  $\vec{x}_i$ ,  
2442 in our case the four-vector information,  $(p_T, \eta, \phi, E)$  of each jet, plus information on the  
2443  $b$ -tagging decision. A multi-layer perceptron (MLP) is used to create a latent embedding,  
2444  $\mathbf{h}(\vec{x}_i)$ , of this input vector.

To describe the relationship between various jets in the event, we then define a vector  $\vec{z}_i$

for each jet as

$$\vec{z}_i = \sum_j w_{ij} \mathbf{h}(\vec{x}_j) \quad (8.1)$$

where  $j$  runs over all jets in the event (including  $i = j$ ), the  $w_{ij}$  can be thought of as edge weights, and  $\mathbf{h}(\vec{x}_j)$  is the latent embedding for jet  $j$  mentioned above.

Within this formula, both  $\mathbf{h}$  and the  $w_{ij}$  are learnable. To learn an appropriate latent mapping and set of edge weights, we define a similarity metric corresponding to each possible jet pairing:

$$\vec{z}_{1a} \cdot \vec{z}_{1b} + \vec{z}_{2a} \cdot \vec{z}_{2b} \quad (8.2)$$

where subscripts  $1a$  and  $1b$  correspond to the two jets in pair 1,  $2a$  and  $2b$  to the jets in pair 2 for a given pairing of four distinct jets.

This similarity metric is calculated for all possible pairings, which are then passed through a softmax [116] activation function, which compresses these scores to between 0 and 1 with sum of 1, lending an interpretation as probability of each pairing.

In training, the ground truth pairing is set by *truth matching* jets to the  $b$ -jets in the  $HH$  signal simulation – a jet is considered to match if it is  $< 0.3$  in  $\Delta R$  away from a  $b$ -jet in the simulation record. Given this ground truth, a cross-entropy loss *TODO: cite* is used on the softmax outputs, and  $w_{ij}$  and  $\mathbf{h}$  are updated correspondingly. Training in such a way corresponds to updating  $w_{ij}$  and  $\mathbf{h}$  to maximize the similarity metric for the correct pairing.

In evaluation, the pairings with a higher score (and therefore higher softmax output) given the trained  $h$  and  $w_{ij}$  therefore correspond to the pairings that are most “ $HH$ -like”. The maximum over these scores is therefore the pairing used as the predicted result from the algorithm.

Because the majority of  $HH \rightarrow b\bar{b}b\bar{b}$  events have either four or five jets, it was found to be sufficient to only consider a maximum of 5 jets. Consideration of more is in principle possible, but the quickly expanding combinatorics leads to a rapidly more difficult problem. The jets considered are the five leading jets in  $p_T$ . Notably, this set of jets may include jets which are not  $b$ -tagged, even for the nominal  $4b$  region – therefore events with 4  $b$ -jets are

2466 not required to use all of them in the construction of Higgs candidates, in contrast to the  
2467 other algorithms used in this thesis.

2468 **8.2 Background Estimation with Mass Plane Interpolation**

2469 The choice of a pairing algorithm that results in a smooth mass plane (such as  $\min \Delta R$ )  
2470 opens up a variety of options for the background estimation. While the method based on  
2471 reweighting of  $2b$  events used for this thesis performs well and has been extensively studied  
2472 and validated, it also relies on several assumptions. In particular, the reweighting is derived  
2473 between e.g.,  $2b$  and  $4b$  events *outside* of the signal region and then applied to  $2b$  events *inside*  
2474 the signal region, with the assumption that the  $2b$  to  $4b$  transfer function will be sufficiently  
2475 similar in both regions of the mass plane. An uncertainty is assigned to account for the bias  
2476 due to this assumption, but the extrapolation in the mass plane is never explicitly treated in  
2477 the nominal estimate. While the approach of reweighting  $2b$  events within the signal region  
2478 does have the advantage of incorporating explicit signal region information (that is, the  $2b$   
2479 signal region events), the importance of the extrapolation bias motivates consideration of  
2480 a method that operates within the  $4b$  mass plane. This additionally removes the reliance  
2481 on lower  $b$ -tagging regions, allowing for the use of, e.g.  $3b$  triggers, and future-proofing the  
2482 analysis against trigger bandwidth constraints in the low tag regions.

The method considered here relies on the following: for a given vector of input variables (event kinematics, etc),  $\vec{x}$ , the joint probability in the  $HH$  mass plane may be written as:

$$p(\vec{x}, m_{H1}, m_{H2}) = p(\vec{x}|m_{H1}, m_{H2})p(m_{H1}, m_{H2}) \quad (8.3)$$

2483 by the chain rule of probability. This means that the full dynamics of events in the  $HH$  mass  
2484 plane may be described by (1) the conditional probability of considered variables  $\vec{x}$ , given  
2485 values of  $m_{H1}$  and  $m_{H2}$ , and (2) the density of the mass plane itself.

2486 We present here an approach which uses normalizing flows *TODO: cite* to model the  
2487 conditional probabilities of events in the mass plane and Gaussian processes to model the  
2488 mass plane density. These models are trained in a region around, but not including, the

2489 signal region, and the trained models are then used to construct an *interpolated* estimate of  
 2490 the signal region kinematics. This approach therefore explicitly treats event behavior within  
 2491 the mass plane, avoiding the concerns associated with a reweighted estimate. Validation of  
 2492 such a method, as well as assessing of closure and biases of the method, may be done in  
 2493 alternate  $b$ -tagging or kinematic regions, notably the now unused  $2b$  region, results of which  
 2494 are shown below.

2495 *8.2.1 Normalizing Flows*

Normalizing flows model observed data  $x \in X$ , with  $x \sim p_X$ , as the output of an invertible,  
 differentiable function  $f : X \rightarrow Z$ , with  $z \in Z$  a latent variable with a simple prior probability  
 distribution (often standard normal),  $z \sim p_Z$ . From a change of variables, given such a  
 function, we may write

$$p_X(x) = p_Z(f(x)) \left| \det \left( \frac{d(f(x))}{dx} \right) \right| \quad (8.4)$$

2496 where  $\left( \frac{d(f(x))}{dx} \right)$  is the Jacobian of  $f$  at  $x$ .

2497 The problem of normalizing flows then reduces to (1) choosing sets of  $f$  which are both  
 2498 tractable and sufficiently expressive to describe observed data, and (2) optimizing associated  
 2499 sets of functional parameters on observed data via maximum likelihood estimation using  
 2500 the above formula. Sampling from the learned density is done by drawing from the latent  
 2501 distribution  $z \sim p_Z$  (cf. inverse transform sampling) – the corresponding sample is then  
 2502  $x \sim p_X$  with  $x = f^{-1}(z)$ .

2503 A standard approach to the definition of these  $f$  is as a composition of affine transfor-  
 2504 mations (e.g. RealNVP [117]), that is, transformations of the form  $\alpha z + \beta$ , with  $\alpha$  and  $\beta$   
 2505 learnable parameter vectors. This can roughly be thought of as shifting and squeezing the  
 2506 input prior density in order to match the data density. However, this has somewhat  
 2507 limited expressivity, for instance in the case of a multi-modal density.

This work thus instead relies on neural spline flows [118] in which the functions considered  
 are monotonic rational-quadratic splines, which have an analytic inverse. A rational quadratic

function has the form of a quotient of two quadratic polynomials, namely,

$$f_j(x_i) = \frac{a_{ij}x_i^2 + b_{ij}x_{ij} + c_{ij}}{d_{ij}x_i^2 + e_{ij}x_i + f_{ij}} \quad (8.5)$$

with six associated parameters ( $a_{ij}$  through  $f_{ij}$ ) per each piecewise bin  $j$  of the spline and each input dimension  $i$ . This is explicitly more flexible and expressive than a simple affine transformation, allowing, e.g., the treatment of multi-modality via the piecewise nature of the spline.

The rational quadratic spline is defined on an set interval. The transformation outside of this interval is set to the identity, with these linear tails allowing for unconstrained inputs. The boundaries between bins of the spline are set by coordinates scalled *knots*, with  $K + 1$  knots for  $K$  bins – the two endpoints for the spline interval plus the  $K - 1$  internal boundaries. The derivatives at these points are constrained to be positive for the internal knots, and boundary derivatives are set to 1 to match the linear tails.

The bin widths and heights are learnable ( $2 \cdot K$  parameters) as are the internal knot derivatives ( $K - 1$  parameters), and these  $3K - 1$  ouputs of the neural network are sufficient to define a monotonic rational-quadratic spline which passes through each knot and has the given derivative value at each knot.

In the context of the  $HH \rightarrow 4b$  analysis, a neural spline flow is used to model the four vector information of each Higgs candidate, conditional on their respective masses. The resulting flow is therefore five dimensional, with inputs  $x = (p_{T,H1}, p_{T,H2}, \eta_{H1}, \eta_{H2}, \Delta\phi_{HH})$ , where the ATLAS  $\phi$  symmetry has been encdoded by assuming  $\phi_{H1} = 0$ . Conditional variables  $m_{H1}$  and  $m_{H2}$  are not modeled by the flow, but “come along for the ride”. A standard normal distribution in 5 dimensions is used for the underlying prior. Modeling of the four vectors was chosen in order to reduce bias from modeling  $m_{HH}$  directly.

The trained flow model then gives a model for  $p(x|m_{H1}, m_{H2})$  which may be sampled from to reconstruct distributions of  $HH$  kinematics given values of  $m_{H1}$  and  $m_{H2}$ .

2531 8.2.2 Gaussian Processes

2532 The second piece of this background estimate is the modeling of the mass plane density,  
 2533  $p(m_{H1}, m_{H2})$ . This is done using Gaussian process regression – note that a similar procedure  
 2534 is used to define a systematic in the boosted 4 $b$  analysis. Generally, Gaussian processes  
 2535 are a collection of random variables in which every finite collection of said variables is  
 2536 distributed according to a multivariate normal distribution. For the context of Gaussian  
 2537 process regression, what we consider is a Gaussian process over function space, that is, for a  
 2538 collection of points,  $x_1, \dots, x_N$ , the space of corresponding function values,  $(f(x_1), \dots, f(x_N))$   
 2539 is Gaussian process distributed, that is, described by an  $N$  dimensional normal distribution  
 2540 with mean  $\mu$ , covariance matrix  $\Sigma$ .

2541 For a single point, this would correspond to a function space described entirely by a  
 2542 normal distribution, with various samples from that distribution yielding various candidate  
 2543 functions. For multiple points, a covariance matrix describes the relationship between each  
 2544 pair of points – correspondingly, it is represented via a *kernel function*,  $K(x, x')$ . As, in  
 2545 practice,  $\mu$  may always be set to 0 via a centering of the data, the kernel function fully defines  
 2546 the considered family of functions.

The considered family of functions describes a Bayesian *prior* for the data. This prior may be conditioned on a set of training data points  $(X_1, \vec{y}_1)$ . This conditional *posterior* may then be used to make predictions  $\vec{y}_2 = f(X_2)$  at a set of new points  $X_2$ . Because of the Gaussian process prior assumption,  $\vec{y}_1$  and  $\vec{y}_2$  are assumed to be jointly Gaussian. We may therefore write

$$\begin{pmatrix} \vec{y}_1 \\ \vec{y}_2 \end{pmatrix} \sim \mathcal{N} \left( \begin{pmatrix} 0 \\ 0 \end{pmatrix}, \begin{pmatrix} K(X_1, X_1) & K(X_1, X_2) \\ K(X_1, X_2) & K(X_2, X_2) \end{pmatrix} \right) \quad (8.6)$$

2547 where we have used that the kernel function is symmetric and assumed prior mean 0.

By standard conditioning properties of Gaussian distributions,

$$\vec{y}_2 | \vec{y}_1 \sim \mathcal{N}(K(X_2, X_1)K(X_1, X_1)^{-1}\vec{y}_1, K(X_2, X_2) - K(X_2, X_1)K(X_1, X_1)^{-1}K(X_1, X_2)) \quad (8.7)$$

2548 which is the sampling distribution for a Gaussian process given kernel  $K$ . In practice, the  
 2549 mean of this sampling distribution is used as the function estimate, with an uncertainty from  
 2550 the predicted variance at a given point.

The choice of kernel function has a very strong impact on the fitted curve, and must therefore be chosen to express the expected dynamics of the data. A common such choice is a radial basis function (RBF) kernel, which takes the form

$$K(x, x') = \exp\left(-\frac{d(x, x')^2}{2l^2}\right) \quad (8.8)$$

2551 where  $d(\cdot, \cdot)$  is the Euclidean distance and  $l > 0$  is a length scale parameter. Conceptually, as  
 2552 distances  $d(x, x')$  increase relative to the chosen length scale, the kernel smoothly dies off –  
 2553 further away points influence each other less.

2554 Coming back to our case of the mass plane, the procedure runs as follows:

2555 1. A binned 2d histogram of the blinded mass plane is created in a window around the  
 2556 “standard” analysis regions. Bins which have any overlap with the signal region are  
 2557 excluded.

2558 2. A Gaussian process is trained using the bin centers, values as training points. The  
 2559 scikit-learn implementation [119] is used, with RBF kernel with anisotropic length scale  
 2560 ( $l$  is dimension 2). The length scale is initialized to  $(50, 50)$  to cover the signal region,  
 2561 and optimized by minimizing the negative log-marginal likelihood on the training data,  
 2562  $-\log p(\vec{y}|\theta)$ . Training data is centered and scaled to mean 0, variance 1, and a statistical  
 2563 error is included in the fit.

2564 3. The Gaussian process is then used to predict the density  $p(m_{H1}, m_{H2})$  in the signal  
 2565 region. This may then be sampled from via an inverse transform sampling to generate  
 2566 values  $(m_{H1}, m_{H2})$  according to the density (specifically, according to the mean of the  
 2567 Gaussian process posterior). Though in principle the Gaussian process sampling is not  
 2568 limited to bin centers, this is kept for simplicity, with a uniform smearing applied within

2569 each sampled bin to approximate the continuous estimate, namely, if a bin is sampled  
 2570 from, the returned value is drawn uniformly at random within the sampled bin.

4. The sampling in the previous step can be arbitrary – to set the overall normalization, a Monte Carlo sampling of the Gaussian process is done to approximate the relative fraction of events predicted both inside ( $f_{in}$ ) and outside ( $f_{out}$ ) of the signal region, within the training box. The number of events outside of the signal region ( $n_{out}$ ) is known, therefore, the number of events inside of the signal region,  $n_{in}$ , may be estimated as

$$n_{in} = \frac{n_{out}}{f_{out}} \cdot f_{in}. \quad (8.9)$$

2571 Note that the Monte Carlo sampling procedure is simply a set of samples of the Gaussian  
 2572 process from uniformly random values of  $m_{H1}, m_{H2}$ , and is the most convenient approach  
 2573 given the irregular shape of the signal region.

2574 This procedure results in a generated set of predicted  $m_{H1}, m_{H2}$  values for signal region  
 2575 background events, along with an overall yield prediction.

### 2576 8.2.3 The Full Prediction

2577 Given the normalizing flow parametrization of  $p(x|m_{H1}, m_{H2})$  and the Gaussian process  
 2578 generation of  $(m_{H1}, m_{H2}) \sim p(m_{H1}, m_{H2})$  and prediction of the signal region yield, all of the  
 2579 pieces are in place to construct an interpolation background estimate. Namely

- 2580 1. Gaussian process sampled  $(m_{H1}, m_{H2})$  values are provided to the normalizing flow to  
 2581 predict the other variables for the Higgs candidate four-vectors. These are used to  
 2582 construct the  $HH$  system (notably  $m_{HH}, \cos \theta^*$ ).
- 2583 2. These final distributions are normalized according to the predicted background yield.

2584 *8.2.4 Results*

2585 The Gaussian process sampling procedure is trained on a small fraction (0.01) of  $2b$  data to  
 2586 mimic the available  $4b$  statistics. This fraction of  $2b$  data is blinded, and the prediction of the  
 2587 estimate trained on this blinded region may then be compared to real  $2b$  data in the signal  
 2588 region. The predictions for signal region  $m_{H_1}$  and  $m_{H_2}$  individually are shown in Figure 8.1,  
 and the resulting mass planes are compared in Figure 8.2. Good agreement is seen.

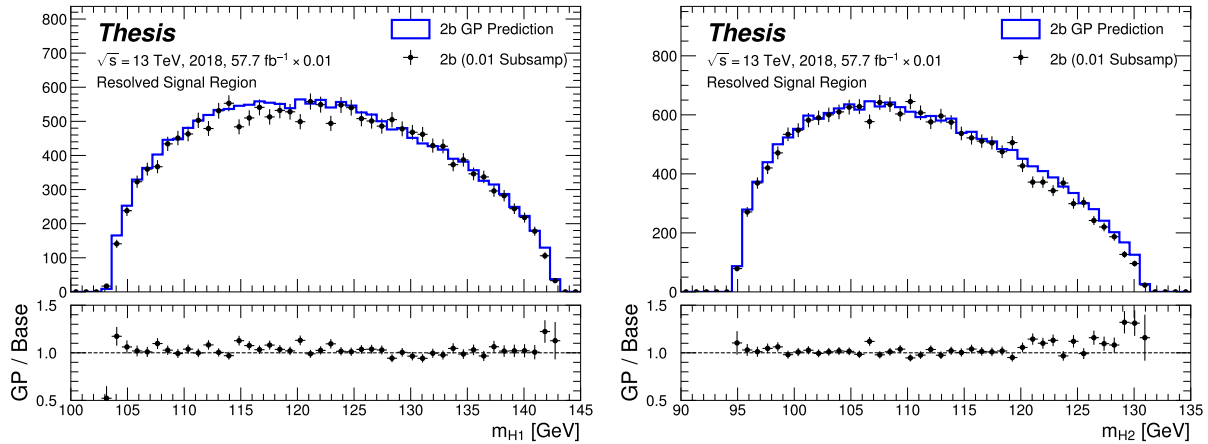


Figure 8.1: Gaussian process sampling prediction of marginals  $m_{H_1}$  and  $m_{H_2}$  for  $2b$  signal region events compared to real  $2b$  signal region events for the 2018 dataset. Good agreement is seen. Only a small fraction (0.01) of the  $2b$  dataset is used for both training and this final comparison to mimic  $4b$  statistics.

2589

2590 The  $4b$  region is kept blinded for this work, meaning that a direct comparison of the  
 2591 Gaussian process estimate in the  $4b$  signal region is not done. However, a Gaussian process is  
 2592 trained on the blinded  $4b$  region and compared to the corresponding reweighted  $2b$  estimate,  
 2593 trained per the nominal procedures from the analyses above. The predictions for signal  
 2594 region  $m_{H_1}$  and  $m_{H_2}$  individually are shown in Figure 8.3, compared to both the control and  
 2595 validation region derived reweighting estimates, and the resulting signal region mass planes  
 2596 are compared in Figure 8.4. The estimates are seen to be compatible.

2597 *8.2.5 Outstanding Points*

2598 While good performance is demonstrated from the nominal interpolated background estimate,  
2599 various uncertainties must be assigned according to the various stages of the estimate. These  
2600 notably include

- 2601     • Assessing a statistical uncertainty on the normalizing flow training (cf. bootstrap  
2602       uncertainty).
- 2603     • Propagation of the Gaussian process uncertainty through the sampling procedure.
- 2604     • Validation of the resulting estimate and assessment of necessary systematic uncertainties  
2605       (e.g. from validation region non-closure).

2606 These are all quite tractable, but some, especially the choice of an appropriate systematic  
2607 uncertainty, are certainly not obvious and require detailed study. In this respect, the  
2608 reweighting validation work of the non-resonant analysis is certainly quite useful as a starting  
2609 place in terms of the available regions and their correspondence to the nominal  $4b$  signal  
2610 region.

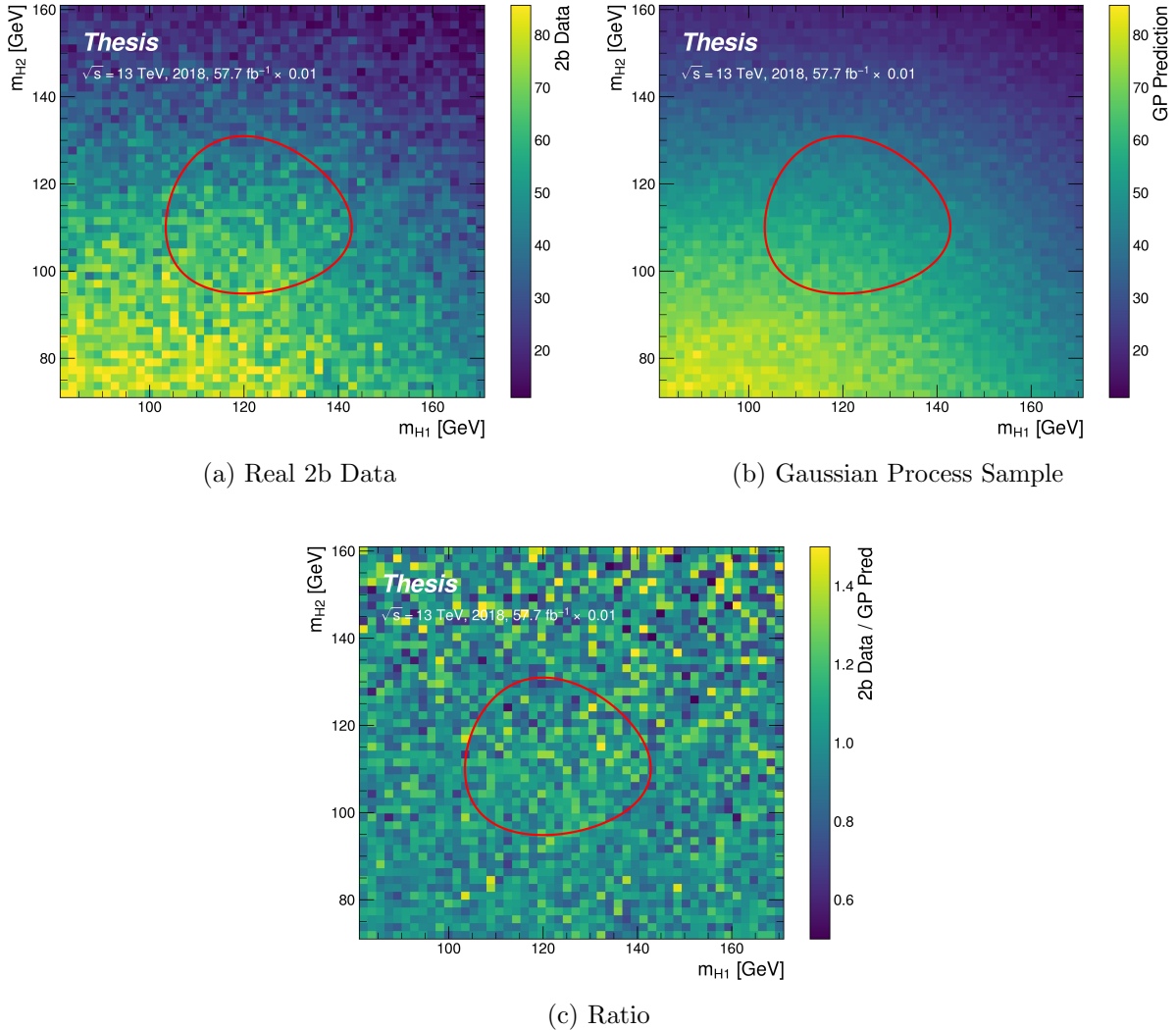


Figure 8.2: Gaussian process sampling prediction for the mass plane compared to the real 2b dataset for 2018. Only a small fraction (0.01) of the 2b dataset is used for both training and this final comparison to mimic 4b statistics. Good agreement is seen.

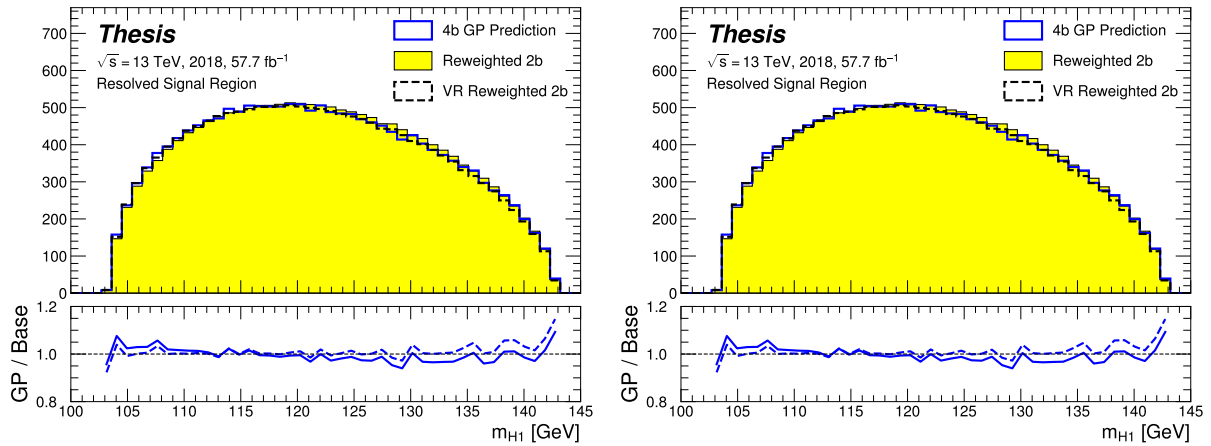


Figure 8.3: Gaussian process sampling prediction of marginals  $m_{H1}$  and  $m_{H2}$  for 4b signal region events compared to both control and validation reweighting predictions. While there are some differences, the estimates are compatible.

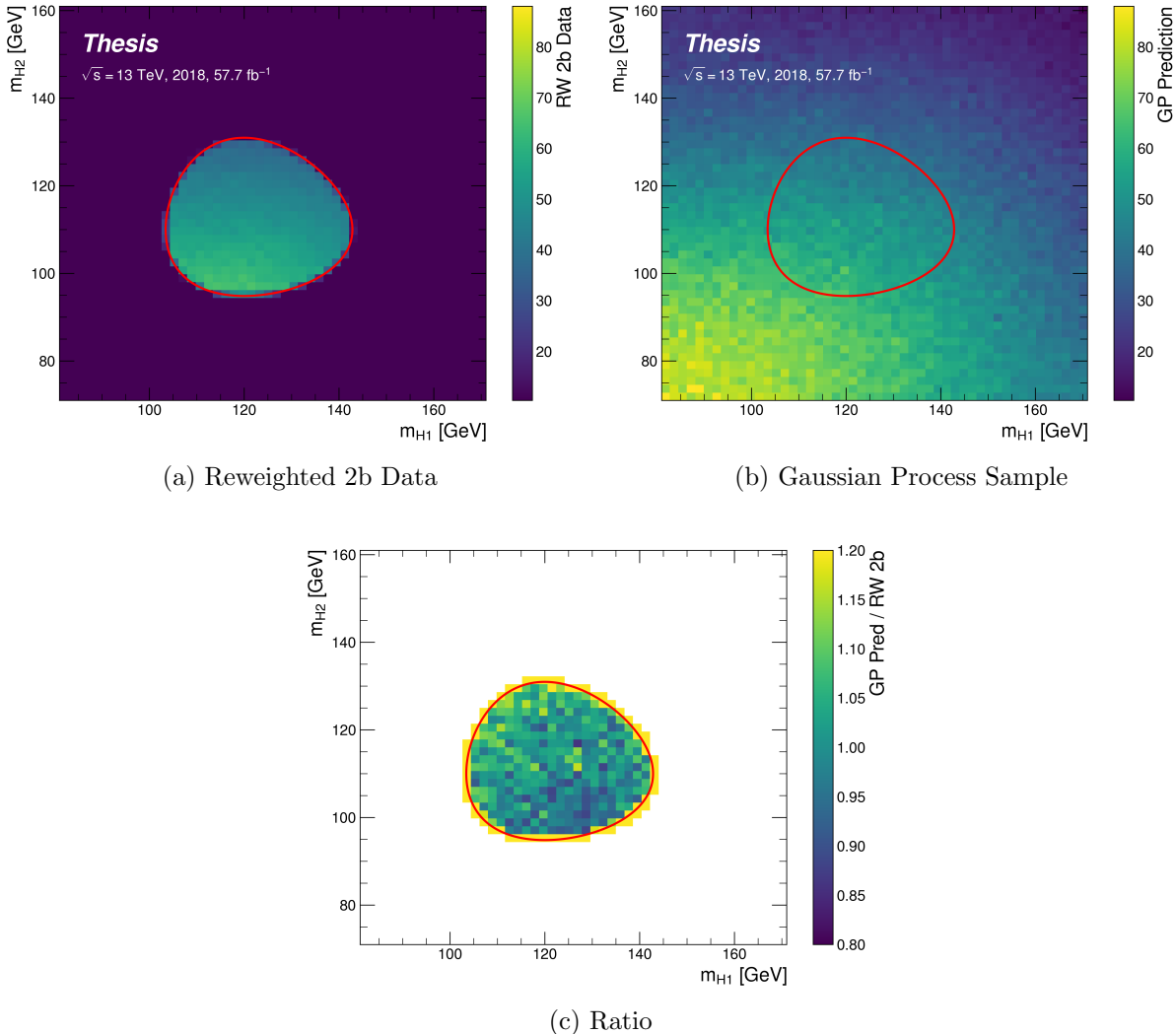


Figure 8.4: Gaussian process sampling prediction for the  $4b$  mass plane compared to the reweighted  $2b$  estimate in the signal region. Both estimates are compatible.

2611

## Chapter 9

2612

### CONCLUSIONS

2613 This thesis has provided an overview of the Standard Model, with an emphasis on pair  
2614 production of Higgs bosons and how this process may be used to both verify the Standard  
2615 Model and to search for new physics. An overview of the Large Hadron Collider and the  
2616 ATLAS detector has been provided, and the design and use of simulation infrastructure  
2617 has been explained, including work to improve hadronic shower modeling in fast detector  
2618 simulation. The translation of detector level information to analysis level information has  
2619 been explained, with an emphasis on jets and the identification of  $B$  hadron decay. Finally,  
2620 two searches for Higgs boson pair production have been presented, with a complete set of  
2621 results for resonant production included, focusing on searches beyond the Standard Model,  
2622 and a preliminary set of results for non-resonant production, targeting Standard Model  
2623 production, with variations of the Higgs self-coupling. Two advanced techniques for the  
2624 future of these analyses are further presented, along with proof-of-concept results.

2625

## BIBLIOGRAPHY

- [1] *A New Map of All the Particles and Forces*, <https://www.quantamagazine.org/a-new-map-of-the-standard-model-of-particle-physics-20201022/>, Accessed: 2021-07-23 (cit. on p. 3).
- [2] J. D. Jackson, *Classical electrodynamics; 2nd ed.* Wiley, 1975 (cit. on p. 2).
- [3] M. Thomson, *Modern particle physics*, Cambridge University Press, 2013, ISBN: 978-1-107-03426-6 (cit. on p. 2).
- [4] M. Srednicki, *Quantum Field Theory*, Cambridge Univ. Press, 2007 (cit. on p. 2).
- [5] M. Gell-Mann, *A schematic model of baryons and mesons*, Physics Letters **8** (1964) 214, ISSN: 0031-9163, URL: <https://www.sciencedirect.com/science/article/pii/S0031916364920013> (cit. on p. 11).
- [6] G. Zweig, *An  $SU_3$  model for strong interaction symmetry and its breaking; Version 1*, tech. rep., CERN, 1964, URL: <https://cds.cern.ch/record/352337> (cit. on p. 11).
- [7] O. W. Greenberg, *Spin and Unitary-Spin Independence in a Paraquark Model of Baryons and Mesons*, Phys. Rev. Lett. **13** (20 1964) 598, URL: <https://link.aps.org/doi/10.1103/PhysRevLett.13.598> (cit. on p. 11).
- [8] M. Y. Han and Y. Nambu, *Three-Triplet Model with Double  $SU(3)$  Symmetry*, Phys. Rev. **139** (4B 1965) B1006, URL: <https://link.aps.org/doi/10.1103/PhysRev.139.B1006> (cit. on p. 11).
- [9] F. L. Wilson, *Fermi's Theory of Beta Decay*, American Journal of Physics **36** (1968) 1150, eprint: <https://doi.org/10.1119/1.1974382>, URL: <https://doi.org/10.1119/1.1974382> (cit. on p. 14).

- 2647 [10] *The Nobel Prize in Physics 1979*, <https://www.nobelprize.org/prizes/physics/1979/summary/>, Accessed: 2021-07-23 (cit. on p. 15).
- 2648
- 2649 [11] F. Englert and R. Brout, *Broken Symmetry and the Mass of Gauge Vector Mesons*,  
2650 Phys. Rev. Lett. **13** (9 1964) 321, URL: <https://link.aps.org/doi/10.1103/PhysRevLett.13.321> (cit. on p. 20).
- 2651
- 2652 [12] P. W. Higgs, *Broken Symmetries and the Masses of Gauge Bosons*, Phys. Rev. Lett.  
2653 **13** (16 1964) 508, URL: <https://link.aps.org/doi/10.1103/PhysRevLett.13.508>  
2654 (cit. on p. 20).
- 2655
- 2656 [13] G. S. Guralnik, C. R. Hagen, and T. W. B. Kibble, *Global Conservation Laws and  
2657 Massless Particles*, Phys. Rev. Lett. **13** (20 1964) 585, URL: <https://link.aps.org/doi/10.1103/PhysRevLett.13.585> (cit. on p. 20).
- 2658
- 2659 [14] ATLAS Collaboration, *Observation of a new particle in the search for the Standard  
2660 Model Higgs boson with the ATLAS detector at the LHC*, Phys. Lett. B **716** (2012) 1,  
arXiv: [1207.7214 \[hep-ex\]](https://arxiv.org/abs/1207.7214) (cit. on p. 20).
- 2661
- 2662 [15] CMS Collaboration, *Observation of a new boson at a mass of 125 GeV with the CMS  
2663 experiment at the LHC*, Phys. Lett. B **716** (2012) 30, arXiv: [1207.7235 \[hep-ex\]](https://arxiv.org/abs/1207.7235)  
(cit. on p. 20).
- 2664
- 2665 [16] S. Weinberg, *A Model of Leptons*, Phys. Rev. Lett. **19** (21 1967) 1264, URL: <https://link.aps.org/doi/10.1103/PhysRevLett.19.1264> (cit. on p. 25).
- 2666
- 2667 [17] ATLAS Collaboration, *Search for the  $HH \rightarrow b\bar{b}b\bar{b}$  process via vector-boson fusion  
2668 production using proton–proton collisions at  $\sqrt{s} = 13$  TeV with the ATLAS detector*,  
JHEP **07** (2020) 108, arXiv: [2001.05178 \[hep-ex\]](https://arxiv.org/abs/2001.05178) (cit. on pp. 28, 76, 96), Erratum:  
2669 JHEP **01** (2021) 145.
- 2670
- 2671 [18] G. Branco et al., *Theory and phenomenology of two-Higgs-doublet models*, Physics Reports **516** (2012) 1, Theory and phenomenology of two-Higgs-doublet models,

- 2672 ISSN: 0370-1573, URL: <http://www.sciencedirect.com/science/article/pii/S0370157312000695> (cit. on pp. 29, 30).
- 2673
- 2674 [19] K. Agashe, H. Davoudiasl, G. Perez, and A. Soni, *Warped gravitons at the CERN*  
2675 *LHC and beyond*, Phys. Rev. D **76** (3 2007) 036006, URL: <https://link.aps.org/doi/10.1103/PhysRevD.76.036006> (cit. on pp. 29, 30).
- 2676
- 2677 [20] A. Carvalho, *Gravity particles from Warped Extra Dimensions, predictions for LHC*,  
2678 2018, arXiv: [1404.0102 \[hep-ph\]](https://arxiv.org/abs/1404.0102) (cit. on pp. 29, 30, 185).
- 2679 [21] ATLAS Collaboration, *Combination of searches for Higgs boson pairs in pp collisions*  
2680 *at  $\sqrt{s} = 13 \text{ TeV}$  with the ATLAS detector*, Phys. Lett. B **800** (2020) 135103, arXiv:  
2681 [1906.02025 \[hep-ex\]](https://arxiv.org/abs/1906.02025) (cit. on pp. 30, 33, 76).
- 2682 [22] P. D. Group et al., *Review of Particle Physics*, Progress of Theoretical and Experimental  
2683 Physics **2020** (2020), 083C01, ISSN: 2050-3911, eprint: <https://academic.oup.com/ptep/article-pdf/2020/8/083C01/34673722/ptaa104.pdf>, URL: <https://doi.org/10.1093/ptep/ptaa104> (cit. on p. 32).
- 2684
- 2685 [23] T. van Ritbergen and R. G. Stuart, *On the precise determination of the Fermi coupling*  
2686 *constant from the muon lifetime*, Nuclear Physics B **564** (2000) 343, ISSN: 0550-3213,  
2687 URL: [http://dx.doi.org/10.1016/S0550-3213\(99\)00572-6](https://dx.doi.org/10.1016/S0550-3213(99)00572-6) (cit. on p. 32).
- 2688
- 2689 [24] S. Dawson, A. Ismail, and I. Low, *What's in the loop? The anatomy of double Higgs*  
2690 *production*, Physical Review D **91** (2015), ISSN: 1550-2368, URL: [http://dx.doi.org/10.1103/PhysRevD.91.115008](https://dx.doi.org/10.1103/PhysRevD.91.115008) (cit. on p. 32).
- 2691
- 2692 [25] A. M. Sirunyan et al., *Measurement of the top quark Yukawa coupling from  $t\bar{t}$  kinematic*  
2693 *distributions in the dilepton final state in proton-proton collisions at  $\sqrt{s}=13 \text{ TeV}$* ,  
2694 Physical Review D **102** (2020), ISSN: 2470-0029, URL: [http://dx.doi.org/10.1103/PhysRevD.102.092013](https://dx.doi.org/10.1103/PhysRevD.102.092013) (cit. on p. 32).
- 2695

- 2696 [26] S. Dawson, S. Dittmaier, and M. Spira, *Neutral Higgs-boson pair production at hadron*  
 2697 *colliders: QCD corrections*, Physical Review D **58** (1998), ISSN: 1089-4918, URL:  
 2698 <http://dx.doi.org/10.1103/PhysRevD.58.115012> (cit. on p. 33).
- 2699 [27] S. Borowka et al., *Higgs Boson Pair Production in Gluon Fusion at Next-to-Leading*  
 2700 *Order with Full Top-Quark Mass Dependence*, Physical Review Letters **117** (2016),  
 2701 ISSN: 1079-7114, URL: <http://dx.doi.org/10.1103/PhysRevLett.117.012001>  
 2702 (cit. on p. 33).
- 2703 [28] J. Baglio et al., *Gluon fusion into Higgs pairs at NLO QCD and the top mass*  
 2704 *scheme*, The European Physical Journal C **79** (2019), ISSN: 1434-6052, URL: <http://dx.doi.org/10.1140/epjc/s10052-019-6973-3> (cit. on p. 33).
- 2706 [29] D. de Florian and J. Mazzitelli, *Higgs Boson Pair Production at Next-to-Next-to-*  
 2707 *Leading Order in QCD*, Physical Review Letters **111** (2013), ISSN: 1079-7114, URL:  
 2708 <http://dx.doi.org/10.1103/PhysRevLett.111.201801> (cit. on p. 33).
- 2709 [30] D. Y. Shao, C. S. Li, H. T. Li, and J. Wang, *Threshold resummation effects in Higgs*  
 2710 *boson pair production at the LHC*, Journal of High Energy Physics **2013** (2013), ISSN:  
 2711 1029-8479, URL: [http://dx.doi.org/10.1007/JHEP07\(2013\)169](http://dx.doi.org/10.1007/JHEP07(2013)169) (cit. on p. 33).
- 2712 [31] D. de Florian and J. Mazzitelli, *Higgs pair production at next-to-next-to-leading*  
 2713 *logarithmic accuracy at the LHC*, 2015, arXiv: [1505.07122 \[hep-ph\]](https://arxiv.org/abs/1505.07122) (cit. on p. 33).
- 2714 [32] M. Grazzini et al., *Higgs boson pair production at NNLO with top quark mass effects*,  
 2715 Journal of High Energy Physics **2018** (2018), ISSN: 1029-8479, URL: [http://dx.doi.org/10.1007/JHEP05\(2018\)059](http://dx.doi.org/10.1007/JHEP05(2018)059) (cit. on p. 33).
- 2717 [33] J. Baglio et al., *gg → HH: Combined uncertainties*, Physical Review D **103** (2021),  
 2718 ISSN: 2470-0029, URL: <http://dx.doi.org/10.1103/PhysRevD.103.056002> (cit. on  
 2719 p. 33).

- 2720 [34] F. Dulat, A. Lazopoulos, and B. Mistlberger, *iHixs 2 — Inclusive Higgs cross sections*,  
 2721 Computer Physics Communications **233** (2018) 243, ISSN: 0010-4655, URL: <http://dx.doi.org/10.1016/j.cpc.2018.06.025> (cit. on p. 34).
- 2723 [35] ATLAS Collaboration, *Measurement prospects of the pair production and self-coupling*  
 2724 *of the Higgs boson with the ATLAS experiment at the HL-LHC*, ATL-PHYS-PUB-  
 2725 2018-053, 2018, URL: <https://cds.cern.ch/record/2652727> (cit. on p. 34).
- 2726 [36] D. de Florian, I. Fabre, and J. Mazzitelli, *Triple Higgs production at hadron colliders*  
 2727 *at NNLO in QCD*, Journal of High Energy Physics **2020** (2020), ISSN: 1029-8479, URL:  
 2728 [http://dx.doi.org/10.1007/JHEP03\(2020\)155](http://dx.doi.org/10.1007/JHEP03(2020)155) (cit. on p. 34).
- 2729 [37] A. Papaefstathiou, T. Robens, and G. Tetlamatzi-Xolocotzi, *Triple Higgs boson*  
 2730 *production at the Large Hadron Collider with Two Real Singlet scalars*, Journal of  
 2731 High Energy Physics **2021** (2021), ISSN: 1029-8479, URL: [http://dx.doi.org/10.1007/JHEP05\(2021\)193](http://dx.doi.org/10.1007/JHEP05(2021)193) (cit. on p. 34).
- 2733 [38] T. Robens, T. Stefaniak, and J. Wittbrodt, *Two-real-scalar-singlet extension of the*  
 2734 *SM: LHC phenomenology and benchmark scenarios*, The European Physical Journal C  
 2735 **80** (2020), ISSN: 1434-6052, URL: <http://dx.doi.org/10.1140/epjc/s10052-020-7655-x> (cit. on p. 34).
- 2737 [39] D. Egana-Ugrinovic, S. Homiller, and P. Meade, *Multi-Higgs boson production probes*  
 2738 *Higgs sector flavor*, Physical Review D **103** (2021), ISSN: 2470-0029, URL: <http://dx.doi.org/10.1103/PhysRevD.103.115005> (cit. on p. 34).
- 2740 [40] CERN, *CERN’s accelerator complex*, <https://home.cern/science/accelerators/accelerator-complex>, Accessed: 27 July 2021 (cit. on p. 36).
- 2742 [41] J. Pequenao, “Computer generated image of the whole ATLAS detector”, 2008, URL:  
 2743 <https://cds.cern.ch/record/1095924> (cit. on p. 38).
- 2744 [42] ATLAS Collaboration, *The ATLAS Experiment at the CERN Large Hadron Collider*,  
 2745 JINST **3** (2008) S08003 (cit. on p. 39).

- 2746 [43] J. Pequenao and P. Schaffner, “How ATLAS detects particles: diagram of particle  
 2747 paths in the detector”, 2013, URL: <https://cds.cern.ch/record/1505342> (cit. on  
 2748 p. 40).
- 2749 [44] ATLAS Collaboration, *ATLAS Insertable B-Layer: Technical Design Report*, ATLAS-  
 2750 TDR-19; CERN-LHCC-2010-013, 2010, URL: <https://cds.cern.ch/record/1291633> (cit. on p. 41), Addendum: ATLAS-TDR-19-ADD-1; CERN-LHCC-2012-009,  
 2751 2012, URL: <https://cds.cern.ch/record/1451888>.
- 2752 [45] B. Abbott et al., *Production and integration of the ATLAS Insertable B-Layer*, JINST  
 2753 **13** (2018) T05008, arXiv: [1803.00844 \[physics.ins-det\]](https://arxiv.org/abs/1803.00844) (cit. on p. 41).
- 2754 [46] A. Outreach, “ATLAS Fact Sheet : To raise awareness of the ATLAS detector and  
 2755 collaboration on the LHC”, 2010, URL: <https://cds.cern.ch/record/1457044>  
 2756 (cit. on p. 43).
- 2757 [47] ATLAS Collaboration, *Performance of the ATLAS trigger system in 2015*, Eur. Phys.  
 2758 J. C **77** (2017) 317, arXiv: [1611.09661 \[hep-ex\]](https://arxiv.org/abs/1611.09661) (cit. on p. 44).
- 2759 [48] ATLAS Collaboration, *The ATLAS Collaboration Software and Firmware*, ATL-SOFT-  
 2760 PUB-2021-001, 2021, URL: <https://cds.cern.ch/record/2767187> (cit. on p. 44).
- 2761 [49] P. Nason, *A New method for combining NLO QCD with shower Monte Carlo algorithms*,  
 2762 JHEP **11** (2004) 040, arXiv: [hep-ph/0409146 \[hep-ph\]](https://arxiv.org/abs/hep-ph/0409146) (cit. on pp. 48, 79).
- 2763 [50] S. Frixione, P. Nason and C. Oleari, *Matching NLO QCD computations with parton  
 2764 shower simulations: the POWHEG method*, JHEP **11** (2007) 070, arXiv: [0709.2092  
 2765 \[hep-ph\]](https://arxiv.org/abs/0709.2092) (cit. on pp. 48, 79).
- 2766 [51] S. Alioli, P. Nason, C. Oleari, and E. Re, *A general framework for implementing NLO  
 2767 calculations in shower Monte Carlo programs: the POWHEG BOX*, JHEP **06** (2010)  
 2768 043, arXiv: [1002.2581 \[hep-ph\]](https://arxiv.org/abs/1002.2581) (cit. on pp. 48, 79).
- 2769

- 2770 [52] J. Alwall et al., *The automated computation of tree-level and next-to-leading order*  
 2771 *differential cross sections, and their matching to parton shower simulations*, Journal of  
 2772 High Energy Physics **2014** (2014), URL: [https://doi.org/10.1007/jhep07\(2014\)](https://doi.org/10.1007/jhep07(2014)079)  
 2773 (cit. on pp. 48, 78).
- 2774 [53] J. Bellm et al., *Herwig 7.0/Herwig++ 3.0 release note*, The European Physical Journal  
 2775 C **76** (2016), URL: <https://doi.org/10.1140/epjc/s10052-016-4018-8> (cit. on  
 2776 pp. 48, 78).
- 2777 [54] M. Bähr et al., *Herwig++ physics and manual*, The European Physical Journal C  
 2778 **58** (2008) 639, URL: <https://doi.org/10.1140/epjc/s10052-008-0798-9> (cit. on  
 2779 pp. 48, 78).
- 2780 [55] T. Sjöstrand et al., *An introduction to PYTHIA 8.2*, Computer Physics Communi-  
 2781 cations **191** (2015) 159, ISSN: 0010-4655, URL: <https://www.sciencedirect.com/science/article/pii/S0010465515000442> (cit. on pp. 48, 78).
- 2783 [56] D. J. Lange, *The EvtGen particle decay simulation package*, Nucl. Instrum. Meth. A  
 2784 **462** (2001) 152 (cit. on pp. 48, 78).
- 2785 [57] S. Höche, *Introduction to parton-shower event generators*, 2015, arXiv: [1411.4085](https://arxiv.org/abs/1411.4085)  
 2786 [[hep-ph](#)] (cit. on p. 49).
- 2787 [58] S. Agostinelli et al., *Geant4—a simulation toolkit*, Nuclear Instruments and Methods  
 2788 in Physics Research Section A: Accelerators, Spectrometers, Detectors and Associated  
 2789 Equipment **506** (2003) 250, ISSN: 0168-9002, URL: <https://www.sciencedirect.com/science/article/pii/S0168900203013688> (cit. on p. 50).
- 2791 [59] P. Calafiura, J. Catmore, D. Costanzo, and A. Di Girolamo, *ATLAS HL-LHC Com-  
 2792 puting Conceptual Design Report*, tech. rep., CERN, 2020, URL: <https://cds.cern.ch/record/2729668> (cit. on p. 50).

- 2794 [60] A. Collaboration, *Computing and Software - Public Results*, <https://twiki.cern.ch/twiki/bin/view/AtlasPublic/ComputingandSoftwarePublicResults>, Accessed:  
 2795  
 2796 27 July 2021 (cit. on p. 51).
- 2797 [61] ATLAS Collaboration, *The ATLAS Simulation Infrastructure*, *Eur. Phys. J. C* **70**  
 2798 (2010) 823, arXiv: [1005.4568 \[physics.ins-det\]](https://arxiv.org/abs/1005.4568) (cit. on pp. 50, 78).
- 2799 [62] ATLAS Collaboration, *The new Fast Calorimeter Simulation in ATLAS*, ATL-SOFT-  
 2800 PUB-2018-002, 2018, URL: <https://cds.cern.ch/record/2630434> (cit. on pp. 52,  
 2801 53).
- 2802 [63] ROOT, *TPrincipal Class Reference*, <https://root.cern.ch/doc/master/classTPrincipal.html>, Accessed: 27 July 2021 (cit. on p. 52).
- 2803  
 2804 [64] M. Aharrouche et al., *Energy linearity and resolution of the ATLAS electromagnetic*  
 2805 *barrel calorimeter in an electron test-beam*, *Nuclear Instruments and Methods in*  
 2806 *Physics Research Section A: Accelerators, Spectrometers, Detectors and Associated*  
 2807 *Equipment* **568** (2006) 601, ISSN: 0168-9002, URL: <http://dx.doi.org/10.1016/j.nima.2006.07.053> (cit. on p. 53).
- 2808  
 2809 [65] ATLAS Collaboration, *Evidence for prompt photon production in pp collisions at*  
 2810  $\sqrt{s} = 7 \text{ TeV}$  *with the ATLAS detector*, ATLAS-CONF-2010-077, 2010, URL: <https://cds.cern.ch/record/1281368> (cit. on p. 53).
- 2811  
 2812 [66] S. Gasiorowski and H. Gray, *Fast Calorimeter Simulation in ATLAS*, EPJ Web Conf.  
 2813 **245** (2020) 02002. 7 p, URL: <https://cds.cern.ch/record/2756298> (cit. on p. 54).
- 2814  
 2815 [67] D. P. Kingma and M. Welling, *Auto-Encoding Variational Bayes*, 2014, arXiv: [1312.6114 \[stat.ML\]](https://arxiv.org/abs/1312.6114) (cit. on p. 54).
- 2816  
 2817 [68] G. Aad et al., *Topological cell clustering in the ATLAS calorimeters and its performance*  
 2818 *in LHC Run 1*, *The European Physical Journal C* **77** (2017), ISSN: 1434-6052, URL:  
<http://dx.doi.org/10.1140/epjc/s10052-017-5004-5> (cit. on pp. 58, 59).

- 2819 [69] A. Ghosh and A. Collaboration, *Deep generative models for fast shower simulation*  
 2820 *in ATLAS*, Journal of Physics: Conference Series **1525** (2020) 012077, URL: <https://doi.org/10.1088/1742-6596/1525/1/012077> (cit. on p. 60).
- 2821  
 2822 [70] R. Di Sipio, M. F. Giannelli, S. K. Haghight, and S. Palazzo, *DijetGAN: a Generative-  
 2823 Adversarial Network approach for the simulation of QCD dijet events at the LHC*,  
 2824 Journal of High Energy Physics **2019** (2019), ISSN: 1029-8479, URL: [http://dx.doi.org/10.1007/JHEP08\(2019\)110](http://dx.doi.org/10.1007/JHEP08(2019)110) (cit. on p. 60).
- 2825  
 2826 [71] ATLAS Collaboration, *Jet reconstruction and performance using particle flow with*  
 2827 *the ATLAS Detector*, Eur. Phys. J. C **77** (2017) 466, arXiv: [1703.10485](https://arxiv.org/abs/1703.10485) [hep-ex]  
 2828 (cit. on pp. 63, 77).
- 2829  
 2830 [72] ATLAS Collaboration, *Topological cell clustering in the ATLAS calorimeters and*  
 2831 *its performance in LHC Run 1*, Eur. Phys. J. C **77** (2017) 490, arXiv: [1603.02934](https://arxiv.org/abs/1603.02934)  
 [hep-ex] (cit. on p. 63).
- 2832  
 2833 [73] ATLAS Collaboration, *Variable Radius, Exclusive- $k_T$ , and Center-of-Mass Subjet*  
 2834 *Reconstruction for Higgs( $\rightarrow b\bar{b}$ ) Tagging in ATLAS*, ATL-PHYS-PUB-2017-010, 2017,  
 URL: <https://cds.cern.ch/record/2268678> (cit. on pp. 63, 169).
- 2835  
 2836 [74] M. Cacciari, G. P. Salam, and G. Soyez, *The anti- $k_T$  jet clustering algorithm*, Journal  
 2837 of High Energy Physics **2008** (2008) 063, ISSN: 1029-8479, URL: <http://dx.doi.org/10.1088/1126-6708/2008/04/063> (cit. on p. 63).
- 2838  
 2839 [75] G. P. Salam, *Towards jetography*, The European Physical Journal C **67** (2010) 637,  
 ISSN: 1434-6052, URL: <http://dx.doi.org/10.1140/epjc/s10052-010-1314-6>  
 (cit. on p. 63).
- 2840  
 2841 [76] A. Collaboration, *Configuration and performance of the ATLAS b-jet triggers in Run*  
 2842 *2*, 2021, arXiv: [2106.03584](https://arxiv.org/abs/2106.03584) [hep-ex] (cit. on p. 67).

- 2843 [77] ATLAS Collaboration, *ATLAS b-jet identification performance and efficiency mea-*  
 2844 *surement with  $t\bar{t}$  events in pp collisions at  $\sqrt{s} = 13$  TeV*, Eur. Phys. J. C **79** (2019)  
 2845 970, arXiv: 1907.05120 [hep-ex] (cit. on pp. 66, 77, 164).
- 2846 [78] ATLAS Collaboration, *Topological b-hadron decay reconstruction and identification*  
 2847 *of b-jets with the JetFitter package in the ATLAS experiment at the LHC*, ATL-  
 2848 PHYS-PUB-2018-025, 2018, URL: <https://cds.cern.ch/record/2645405> (cit. on  
 2849 p. 69).
- 2850 [79] R. Frühwirth, *Application of Kalman filtering to track and vertex fitting*, Nuclear  
 2851 Instruments and Methods in Physics Research Section A: Accelerators, Spectrometers,  
 2852 Detectors and Associated Equipment **262** (1987) 444, ISSN: 0168-9002, URL: <https://www.sciencedirect.com/science/article/pii/0168900287908874> (cit. on  
 2853 p. 69).
- 2854 [80] ATLAS Collaboration, *Identification of Jets Containing b-Hadrons with Recurrent*  
 2855 *Neural Networks at the ATLAS Experiment*, ATL-PHYS-PUB-2017-003, 2017, URL:  
 2856 <https://cds.cern.ch/record/2255226> (cit. on p. 70).
- 2857 [81] *Expected performance of the 2019 ATLAS b-taggers*, <http://atlas.web.cern.ch/Atlas/GROUPS/PHYSICS/PLOTS/FTAG-2019-005/>, Accessed: 2021-07-14 (cit. on  
 2858 p. 72).
- 2859 [82] ATLAS Collaboration, *Search for pair production of Higgs bosons in the  $b\bar{b}b\bar{b}$  final*  
 2860 *state using proton–proton collisions at  $\sqrt{s} = 13$  TeV with the ATLAS detector*, JHEP  
 2861 **01** (2019) 030, arXiv: 1804.06174 [hep-ex] (cit. on pp. 76, 90, 96).
- 2862 [83] ATLAS Collaboration, *Search for Higgs boson pair production in the  $b\bar{b}WW^*$  decay*  
 2863 *mode at  $\sqrt{s} = 13$  TeV with the ATLAS detector*, JHEP **04** (2019) 092, arXiv: 1811.  
 2864 04671 [hep-ex] (cit. on p. 76).
- 2865 [84] ATLAS Collaboration, *A search for resonant and non-resonant Higgs boson pair*  
 2866 *production in the  $b\bar{b}\tau^+\tau^-$  decay channel in pp collisions at  $\sqrt{s} = 13$  TeV with the*

- 2869        *ATLAS detector*, Phys. Rev. Lett. **121** (2018) 191801, arXiv: [1808.00336 \[hep-ex\]](#)  
 2870        (cit. on p. 76), Erratum: Phys. Rev. Lett. **122** (2019) 089901.
- 2871        [85] ATLAS Collaboration, *Search for Higgs boson pair production in the  $WW^{(*)}WW^{(*)}$*   
 2872        *decay channel using ATLAS data recorded at  $\sqrt{s} = 13 \text{ TeV}$* , JHEP **05** (2019) 124,  
 2873        arXiv: [1811.11028 \[hep-ex\]](#) (cit. on p. 76).
- 2874        [86] ATLAS Collaboration, *Search for Higgs boson pair production in the  $\gamma\gamma b\bar{b}$  final state*  
 2875        *with 13 TeV pp collision data collected by the ATLAS experiment*, JHEP **11** (2018)  
 2876        040, arXiv: [1807.04873 \[hep-ex\]](#) (cit. on p. 76).
- 2877        [87] ATLAS Collaboration, *Search for Higgs boson pair production in the  $\gamma\gamma WW^*$  channel*  
 2878        *using pp collision data recorded at  $\sqrt{s} = 13 \text{ TeV}$  with the ATLAS detector*, Eur. Phys.  
 2879        J. C **78** (2018) 1007, arXiv: [1807.08567 \[hep-ex\]](#) (cit. on p. 76).
- 2880        [88] ATLAS Collaboration, *Reconstruction and identification of boosted di- $\tau$  systems in*  
 2881        *a search for Higgs boson pairs using 13 TeV proton–proton collision data in ATLAS*,  
 2882        JHEP **11** (2020) 163, arXiv: [2007.14811 \[hep-ex\]](#) (cit. on p. 76).
- 2883        [89] ATLAS Collaboration, *Search for non-resonant Higgs boson pair production in the*  
 2884         *$b\bar{b}\ell\nu\ell\nu$  final state with the ATLAS detector in pp collisions at  $\sqrt{s} = 13 \text{ TeV}$* , Phys.  
 2885        Lett. B **801** (2020) 135145, arXiv: [1908.06765 \[hep-ex\]](#) (cit. on p. 76).
- 2886        [90] ATLAS Collaboration, *Search for Higgs boson pair production in the two bottom quarks*  
 2887        *plus two final state with in pp collisions at  $\sqrt{s} = 13 \text{ TeV}$  with the ATLAS detector*,  
 2888        ATLAS-CONF-2021-016, 2021, URL: <https://cds.cern.ch/record/2759683> (cit. on  
 2889        p. 76).
- 2890        [91] CMS Collaboration, *Search for heavy resonances decaying to two Higgs bosons in final*  
 2891        *states containing four b quarks*, Eur. Phys. J. C **76** (2016) 371, arXiv: [1602.08762](#)  
 2892        [hep-ex] (cit. on p. 77).

- 2893 [92] CMS Collaboration, *Search for production of Higgs boson pairs in the four b quark*  
 2894 *final state using large-area jets in proton–proton collisions at  $\sqrt{s} = 13 \text{ TeV}$* , JHEP **01**  
 2895 (2019) 040, arXiv: [1808.01473 \[hep-ex\]](https://arxiv.org/abs/1808.01473) (cit. on p. 77).
- 2896 [93] CMS Collaboration, *Combination of Searches for Higgs Boson Pair Production in*  
 2897 *Proton–Proton Collisions at  $\sqrt{s} = 13 \text{ TeV}$* , Phys. Rev. Lett. **122** (2019) 121803, arXiv:  
 2898 [1811.09689 \[hep-ex\]](https://arxiv.org/abs/1811.09689) (cit. on p. 77).
- 2899 [94] G. Bartolini et al., *Performance of the ATLAS b-jet trigger in  $p\ p$  collisions at  $\sqrt{s} =$*   
 2900  *$13 \text{ TeV}$* , tech. rep. ATL-COM-DAQ-2019-150, CERN, 2019, URL: <https://cds.cern.ch/record/2688819> (cit. on p. 77).
- 2902 [95] ATLAS Collaboration, *Luminosity determination in  $pp$  collisions at  $\sqrt{s} = 13 \text{ TeV}$  using the ATLAS detector at the LHC*, ATLAS-CONF-2019-021, 2019, URL: <https://cds.cern.ch/record/2677054> (cit. on pp. 78, 164).
- 2905 [96] J. Butterworth et al., *PDF4LHC recommendations for LHC Run II*, J. Phys. G **43**  
 2906 (2016) 023001, arXiv: [1510.03865 \[hep-ph\]](https://arxiv.org/abs/1510.03865) (cit. on pp. 79, 165).
- 2907 [97] M. Bahr et al., *Herwig++ Physics and Manual*, Eur. Phys. J. **C58** (2008) 639, arXiv:  
 2908 [0803.0883 \[hep-ph\]](https://arxiv.org/abs/0803.0883) (cit. on p. 79).
- 2909 [98] T. Head et al., *scikit-optimize/scikit-optimize: v0.5.2*, version v0.5.2, 2018, URL: <https://doi.org/10.5281/zenodo.1207017> (cit. on p. 84).
- 2911 [99] A. Carvalho et al., *Higgs pair production: choosing benchmarks with cluster analysis*,  
 2912 Journal of High Energy Physics **2016** (2016) 1, ISSN: 1029-8479, URL: [http://dx.doi.org/10.1007/JHEP04\(2016\)126](http://dx.doi.org/10.1007/JHEP04(2016)126) (cit. on p. 94).
- 2914 [100] A. Rogozhnikov, *Reweighting with Boosted Decision Trees*, Journal of Physics: Conference Series **762** (2016) 012036, ISSN: 1742-6596, URL: <http://dx.doi.org/10.1088/1742-6596/762/1/012036> (cit. on p. 96).
- 2917 [101] G. V. Moustakides and K. Basioti, *Training Neural Networks for Likelihood/Density*  
 2918 *Ratio Estimation*, 2019, arXiv: [1911.00405 \[eess.SP\]](https://arxiv.org/abs/1911.00405) (cit. on p. 97).

- 2919 [102] T. Kanamori, S. Hido, and M. Sugiyama, *A Least-Squares Approach to Direct Im-*  
 2920 *portance Estimation*, J. Mach. Learn. Res. **10** (2009) 1391, ISSN: 1532-4435 (cit. on  
 2921 p. 97).
- 2922 [103] A. Andreassen and B. Nachman, *Neural networks for full phase-space reweighting*  
 2923 *and parameter tuning*, Physical Review D **101** (2020), ISSN: 2470-0029, URL: <http://dx.doi.org/10.1103/PhysRevD.101.091901> (cit. on p. 98).
- 2925 [104] S. Fort, H. Hu, and B. Lakshminarayanan, *Deep Ensembles: A Loss Landscape Per-*  
 2926 *spective*, 2020, arXiv: [1912.02757 \[stat.ML\]](https://arxiv.org/abs/1912.02757) (cit. on p. 99).
- 2927 [105] B. Efron, *Bootstrap Methods: Another Look at the Jackknife*, Ann. Statist. **7** (1979) 1,  
 2928 URL: <https://doi.org/10.1214/aos/1176344552> (cit. on p. 156).
- 2929 [106] ATLAS Collaboration, *Jet energy scale and resolution measured in proton–proton*  
 2930 *collisions at  $\sqrt{s} = 13 \text{ TeV}$  with the ATLAS detector*, (2020), arXiv: [2007 . 02645](https://arxiv.org/abs/2007.02645)  
 2931 [[hep-ex](#)] (cit. on p. 164).
- 2932 [107] J. Adelman et al., *Search for Higgs boson pair production in the  $b\bar{b}\gamma\gamma$  final state with*  
 2933 *the full Run 2 13 TeV pp collision data collected by the ATLAS Experiment Supporting*  
 2934 *note.*, tech. rep., CERN, 2020, URL: <https://cds.cern.ch/record/2711865> (cit. on  
 2935 p. 164).
- 2936 [108] G. Avoni et al., *The new LUCID-2 detector for luminosity measurement and monitoring*  
 2937 *in ATLAS*, JINST **13** (2018) P07017. 33 p, URL: <https://cds.cern.ch/record/2633501> (cit. on p. 164).
- 2939 [109] D. de Florian et al., *Handbook of LHC Higgs Cross Sections: 4. Deciphering the Nature*  
 2940 *of the Higgs Sector*, CERN Yellow Reports: Monographs, 869 pages, 295 figures, 248 ta-  
 2941 *bles and 1645 citations*. Working Group web page: <https://twiki.cern.ch/twiki/bin/view/LHCPhysics/>  
 2942 CERN, 2016, URL: <https://cds.cern.ch/record/2227475> (cit. on p. 165).
- 2943 [110] A. L. Read, *Presentation of search results: the CLs technique*, Journal of Physics G:  
 2944 Nuclear and Particle Physics **28** (2002) 2693, ISSN: 0954-3899 (cit. on p. 182).

- 2945 [111] G. Cowan, K. Cranmer, E. Gross, and O. Vitells, *Asymptotic formulae for likelihood-*  
2946 *based tests of new physics*, *The European Physical Journal C* **71** (2011), ISSN: 1434-6052  
2947 (cit. on p. 182).
- 2948 [112] A. Sherstinsky, *Fundamentals of Recurrent Neural Network (RNN) and Long Short-*  
2949 *Term Memory (LSTM) network*, *Physica D: Nonlinear Phenomena* **404** (2020) 132306,  
2950 ISSN: 0167-2789, URL: <http://dx.doi.org/10.1016/j.physd.2019.132306> (cit. on  
2951 p. 189).
- 2952 [113] M. Zaheer et al., *Deep Sets*, 2018, arXiv: [1703.06114 \[cs.LG\]](https://arxiv.org/abs/1703.06114) (cit. on p. 189).
- 2953 [114] J. Zhou et al., *Graph Neural Networks: A Review of Methods and Applications*, 2021,  
2954 arXiv: [1812.08434 \[cs.LG\]](https://arxiv.org/abs/1812.08434) (cit. on p. 189).
- 2955 [115] A. Vaswani et al., *Attention Is All You Need*, 2017, arXiv: [1706.03762 \[cs.CL\]](https://arxiv.org/abs/1706.03762)  
2956 (cit. on p. 189).
- 2957 [116] I. Goodfellow, Y. Bengio, and A. Courville, *Deep Learning*, <http://www.deeplearningbook.org>,  
2958 MIT Press, 2016 (cit. on p. 190).
- 2959 [117] L. Dinh, J. Sohl-Dickstein, and S. Bengio, *Density estimation using Real NVP*, 2017,  
2960 arXiv: [1605.08803 \[cs.LG\]](https://arxiv.org/abs/1605.08803) (cit. on p. 192).
- 2961 [118] C. Durkan, A. Bekasov, I. Murray, and G. Papamakarios, *Neural Spline Flows*, 2019,  
2962 arXiv: [1906.04032 \[stat.ML\]](https://arxiv.org/abs/1906.04032) (cit. on p. 192).
- 2963 [119] F. Pedregosa et al., *Scikit-learn: Machine Learning in Python*, *Journal of Machine*  
2964 *Learning Research* **12** (2011) 2825 (cit. on p. 195).